ZEOLITIC IMIDAZOLATE FRAMEWORK (ZIF)-BASED MEMBRANES AND SORBENTS FOR ADVANCED OLEFIN/PARAFFIN SEPARATIONS

A Dissertation
Presented to
The Academic Faculty

by

Chen Zhang

In Partial Fulfillment
of the Requirements for the Degree
Doctor of Philosophy in the
School of Chemical and Biomolecular Engineering

Georgia Institute of Technology
May 2014

ZEOLITIC IMIDAZOLATE FRAMEWORK (ZIF)-BASED MEMBRANES AND SORBENTS FOR ADVANCED OLEFIN/PARAFFIN SEPARATIONS

Approved by:

Dr. William J. Koros, Advisor
School of Chemical and Biomolecular Engineering
Georgia Institute of Technology

Dr. Krista S. Walton
School of Chemical and Biomolecular Engineering
Georgia Institute of Technology

Dr. Christopher W. Jones
School of Chemical and Biomolecular Engineering
Georgia Institute of Technology

Dr. Anselm Griffin
School of Materials Science and Engineering
Georgia Institute of Technology

Dr. Sankar Nair
School of Chemical and Biomolecular Engineering
Georgia Institute of Technology

Date Approved: January 24, 2014

To my parents and grandmothers

They always say time changes things, but you actually have to change them yourself.

-Andy Warhol

ACKNOWLEDGEMENT

It wasn't until the moment I started drafting this section that I realized I was actually leaving graduate school, by recalling those acknowledgeable names in the past four years at Georgia Tech.

First and foremost, I must thank my advisor Professor Bill Koros for his guidance and endless support in my PhD study. His encouragements and constantly positive attitude have been like a lighthouse to guide me through those difficult moments. I feel lucky to have worked for him. He has been not only a supervisor but also a mentor who has educated me both on a professional and personal level. His enthusiasm towards research, strong work ethic, and relentless dedication will continue to be a valuable source of inspiration in the rest of my life. I would also like to thank my committee members: Professor Christopher Jones, Professor Sankar Nair, Professor Krista Walton, and Professor Anselm Griffin for their valuable time and insights. Sponsorship from KAUST is greatly appreciated.

The whole Koros group has been a pleasure to work with. Almost everyone in the team deserves thanks. I want to specially thank Dr. Junqiang Liu for introducing me to the team and the endless help afterwards. Technical support from Dr. JR Johnson and Dr. Oguz Karvan is highly appreciated. The entire Chapter 5 and part of Chapter 6 would not have been possible without the highly sensitive sorption cells that they crafted. Special credits go to Xue Ning, Dr. Ying Labreche, and Dr. Liren Xu for taking care of me, both

technically and non-technically. Additionally, I would like to thank Professor Ryan Lively, Dr. Ke Zhang, Steven Burgess, Dr. Kuang Zhang, Dr. Meha Rungta, Dr. Brian Kraftschik, and Graham Wenz for their valuable collaborations. I want to specially thank Professor Ryan Lively and Dr. Liren Xu for their contributions to Chapter 4 and 7, respectively. Correspondence with Dr. Mita Das in the early days of my research is appreciated. Other names that I feel obliged to mention are: Dr. Wulin Qiu, Dr. Omoyemen Esekhile, Dr. Chien-Chiang Chen, Dr. Surendar Venna, Dr. Justin Vaughn, Lucy Liu, Dr. Ali Rownaghi, and Dr. Zhiming Mao.

Thanks to Dr. Josh Thompson for help with zeolite synthesis at the early stage of my research and Dr. Megan Lydon for generous assistance with sample TEM imaging. The friends I have made in Atlanta helped me stay motivated throughout my PhD study. Thanks go out especially to Hongzhi Wang, Wei-Ming Yeh, Yang Cai, and Elaine Tang.

TABLE OF CONTENTS

LIST OF TABLES

LIST OF FIGURES

SUMMARY

Propylene is one of the most important feedstocks of the petrochemical industry with an estimated 2015 worldwide demand of 100 million tons. Retrofitting conventional C_3 splitters is highly desirable due to the huge amount of thermal energy required to separate propylene from propane. Membrane separation is among the alternatives that both academia and industry have actively studied during the past decades, however; many challenges remain to advance membrane separation as a scalable technology for energy-efficient propylene/propane separations.

The overarching goal of this research is to provide a framework for development of scalable ZIF-based mixed-matrix membrane that is able to deliver attractive transport properties for advanced gas separations. Zeolitic imidazolate frameworks (ZIFs) were pursued instead of conventional molecular sieves (zeolites and carbon molecular sieves) to form mixed-matrix membrane due to their intrinsic compatibility with high T_g glassy polymers. A systematic study of adsorption and diffusion in zeolitic imidazolate framework-8 (ZIF-8) suggests that this material is remarkably kinetically selective for C_3 and C_4 hydrocarbons and therefore promising for membrane-based gas separation and adsorptive separation. As a result, ZIF-8 was used to form mixed-matrix dense film membranes with polyimide 6FDA-DAM at varied particle loadings and it was found that ZIF-8 significantly enhanced propylene/propane separation performance beyond the "permeability-selectivity" trade-off curve for polymeric materials. Eventually, this research advanced ZIF-based mixed-matrix membrane into a scalable technology by successfully forming high-loading dual-layer ZIF-8/6FDA-DAM asymmetric mixed-matrix hollow fiber membranes with attractive propylene/propane selectivity.

CHAPTER 1

INTRODUCTION

1.1 An Overview of Olefin Manufacture

Light olefins (ethylene, propylene, butadiene, and butylene isomers) are consumed as feedstocks to produce a variety of chemicals that are critical to the petrochemical industry. Propylene is the second largest organic feedstock produced in the United States after ethylene. Propylene worldwide capacity was 68 million tons in 2005 and is expected to approach 100 million tons in 2015 [1]. Three grades of propylene are commercially available: refinery grade (50-70%), chemical grade (92-94%), and polymer grade (>99.5%). Approximately 50% of propylene consumption was used to manufacture polypropylene plastics, which requires polymer grade propylene with high purity. Other important derivatives of propylene include propylene oxide, isopropyl alcohol, acrylonitrile, and cumene, etc. Propylene is commercially produced by three methods [2]: (1) co-product of ethylene manufacturing by steam cracking of paraffinic hydrocarbons (2) by-product of gasoline refining (3) on-purpose manufacture via catalytic dehydrogenation of propane.

In the United States, more than 50% of propylene is produced by steam cracking as a co-product of ethylene manufacturing. Steam cracking processes paraffinic hydrocarbon feedstocks including natural gas liquids (NGLs), naphtha, gas oils or simply ethane. The composition of the cracking product depends on the composition of the feedstock and cracking conditions. The flow scheme [2] of a typical olefin plant is shown

in Figure 1.1. The feedstocks are fed into a pyrolysis (steam cracking) furnace, where they are combined with steam and heated to temperatures between approximately 790-870 ℃. Within this temperature range, the feedstock molecules are cracked to produce methane, hydrogen, ethylene, propylene, butadiene, butylenes, benzene, toluene, and other co-products. After the pyrolysis reaction is quenched, the rest of the plant separates the desired products into streams that meet various product specifications. The most energy intensive separations in the olefin plant shown in Figure 1.1 are separation of ethylene/ethane and propylene/propane, which are traditionally done by fractional distillation under high pressure and cryogenic temperature. Recovery of butadiene from the crude C_4 stream is usually achieved by extractive distillation [3].

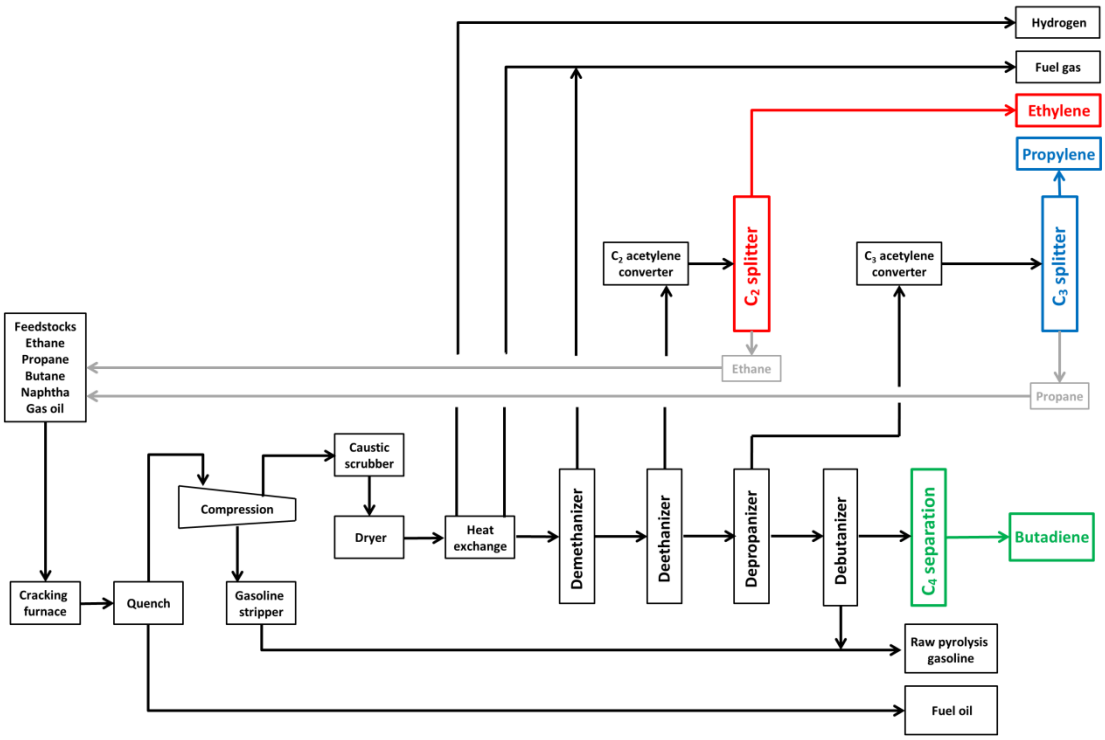

Figure 1.1: Flow paths of ethylene, propylene, and butadiene in a typical olefin plant [2].

The second largest source of propylene is from fluid catalytic cracking (FCC) units. Refineries rely on FCC units to produce gasoline from heavy gas oils. The C_3 (propane/propylene) stream produced from FCC typically varies from 7-13%, with propylene accounting for 5-9%. The actual percentage of propylene from any particular refinery depends on several variables, such as type of reactor, feedstock composition and type of catalyst, as well as on operating conditions.

Production of propylene from steam cracking and FCC strongly depends on the market demand of ethylene and gasoline. Increasing worldwide demand of propylene has created the incentives to develop on-purpose propylene production. There have been several commercial methods to produce propylene using catalytic dehydrogenation of propane, such as the Oleflex process licensed by Honeywell UOP.

None of the above three processes produces pure propylene and it has to be separated, mostly from propane, to achieve sufficient purity for downstream applications. Distillation has been the dominant technology utilized for C_3H_6/C_3H_8 separation. While distillation can be carried out at ambient temperature, it is sometimes operated at cryogenic temperature with a refrigerated overhead vapor [4]. The relative volatility of the C_3H_6/C_3H_8 mixture is very close to unity (1.09-1.15 depending on composition and pressure). Consequently, very large-sized distillation columns (C_3 splitters) with 100-300 trays have to be used and the separation needs to be carried out under high reflux ratio (12-20) to produce polymer grade (>99.5%) propylene. The capital cost for a typical C_3 splitter is in the range of 40 million to 60 million dollars. A U.S. Department of Energy

study estimated that 1.2×10^{14} BTU are used for olefin/paraffin separations each year and C_3H_6/C_3H_8 separation is the most energy-intensive distillation practiced commercially. This large capital expense and energy cost have created huge incentives to seek alternative olefin/paraffin separation technologies that are more energy-efficient.

1.2 Alternatives for Olefin/Paraffin Separation

Separation of a two components or multicomponent mixture is based on the differences in the components' thermodynamic or transport properties, which can be vapor pressure, solubility/adsorptivity, and diffusivity, etc. The differences in these macroscopic properties are traced back to differences on the molecular level such as polarizability, dipole or multipole moments, molecular size/shape, and molecular functionalities. According to Seader [5] et al, separation processes are categorized into five basic techniques: (I) phase creation (e.g. distillation and crystallization), (II) phase addition (e.g. absorptive separation and extraction), (III) barrier (membrane separation), (IV) solid agent (e.g. adsorptive separation and ion exchange), and (V) force field or gradient (e.g. centrifugation and electrolysis). Distillation is the conventional technique to separate olefin from paraffin and is based on different vapor pressure using an energy-separating agent (heat).

Figure 1.2 presents alternative C_3H_6/C_3H_8 separation techniques. The column on the left shows molecular properties of C_3H_6 and C_3H_8. The olefin's C=C double bond (133 pm) is planar and shorter than the paraffin's C-C single bond (154 pm). As a result, olefin is both slimmer in shape and shorter in length and diffuses faster in almost all

media than the corresponding paraffin. Based on the differences in diffusivity, olefin can be separated from paraffin by either kinetic selectivity-based adsorptive separation or membrane.

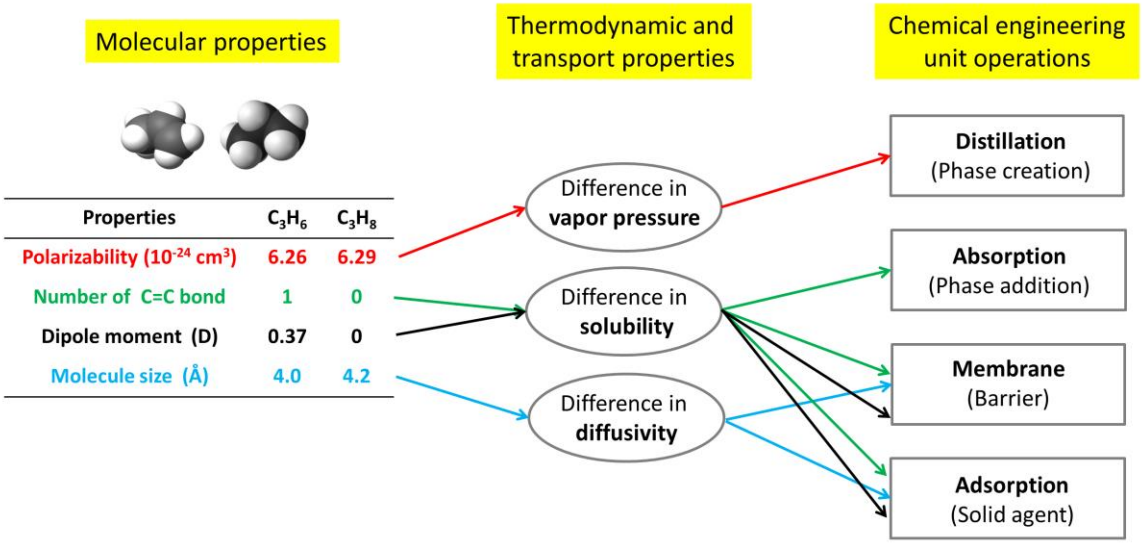

Figure 1.2: Alternatives for olefin/paraffin separation.

The separation can also be realized on the basis of different solubility/adsorptivity employing adsorbent, absorbent, or membrane. The polarizability [6] of C_3H_6 (6.26×10^{-24} cm^3) and C_3H_8 (6.29×10^{-24} cm^3) are almost identical and therefore energy-efficient separation simply based on van der Waals forces is very unlikely. A moderate equilibrium selectivity (10~20) can be achieved for C_3H_6/C_3H_8 at low partial pressure employing cationic zeolites [7] or MOFs [8] with open metals sites due to favorable electrostatic interactions with the olefin. However, the selectivity diminishes quickly as the surface becomes saturated and eventually becomes unattractive at higher partial pressure. In addition to physical interactions, certain transition metal salts (e.g. silver salts

and cuprous salts) reversibly form electron donor/acceptor complexes with olefins through interactions of the olefin π-orbitals with the metal ion [9]. These metals typically do not strongly interact with paraffins. As a result, attractive equilibrium selectivity can be achieved for olefin over paraffin.

1.2.1 Chemical Absorption

Chemical (reactive) absorption has been commercialized to remove CO_2 and H_2S from raw natural gas streams on the basis of reversible reaction between these acid gases and dissolved amines. A similar process has been designed and developed for olefin/paraffin separation using the above mentioned metal salt solution as the absorbent [10, 9]. The gaseous olefin/paraffin mixture is contacted with the salt solution that selectively and reversibly complexes the olefin. After separation of the phases, the weakly bonded olefin is displaced from the salt solution by temperature swing and/or pressure swing, and the unaltered absorbent is recovered.

Chemical absorption based on π-complexation remains one of the few, if not only, non-distillation olefin/paraffin separations that have gained considerable and continuing attention from the petrochemical industry. Serious efforts have been made to bring chemical absorption to large-scale commercial application [9]. Several attempts were even extended to pilot-plant scales. However, few processes are currently used at commercial scale due to genuine technical deficiencies of the technology. The largest one is probably stability of the absorbent. The metal salts are subject to reduction and

deactivation by impurities in the olefin/paraffin feed mixture, such as hydrogen, sulfurs, and alkynes [11].

1.2.2 Adsorptive Separation

Adsorptive separation of two components A and B can be achieved based on differences in either strength of adsorption [4] (equilibrium selectivity-based adsorptive separation) or rate of diffusion (kinetic selectivity-based adsorptive separation) [12]. The feed mixture is brought in contact with porous solid adsorbents before the system is depressurized or heated up to yield a retentate stream and a desorbate stream. Different components in the feed mixture may physically/chemically adsorb on the adsorbent surface with different strength, or diffuse in the adsorbent's porous network with different diffusivity [12]. If the desired component interacts with adsorbent surface less strongly, it will be enriched in the retentate stream, and vice versa in the desorbate stream. Table 1.1 gives several examples of adsorptive separations and purifications. Most commercialized adsorptive separations are based on equilibrium selectivity. Kinetic selectivity-based adsorptive separation is practiced much less extensively. Removal of O_2 from air using carbon molecular sieve is one of the few examples.

Table 1.1: Examples of adsorptive separations based on equilibrium or kinetic selectivity. The items shown in red are commercialized processes.

Separation	Adsorbent material
Equilibrium selectivity-based adsorptive separation	
N_2/O_2	Zeolite LiX [12]
Hydrocarbon dehydration	Zeolites, alumina, silica
CO_2/N_2	Silica-supported amine
C_3H_6/C_3H_8	Silica-supported $AgNO_3$/CuCl [13, 12]
Kinetic selectivity-based adsorptive separation	
O_2/N_2	Carbon molecular sieve [14]
N_2/CH_4	Zeolite ETS-4 [15]
C_3H_6/C_3H_8	Zeolite CHA, 4A, DDR, AlPO-14 [7]

Both equilibrium selectivity-based and kinetic selectivity-based adsorptive separations have been studied for C_3H_6/C_3H_8 separation. Examples of equilibrium selective adsorbents are cationic zeolites [4], MOF with open metal sites, and silica-supported $AgNO_3$ or CuCl. Kinetically selective adsorbents include eight ring small pore zeolites such as Chabazite (CHA), 4A, DDR, and AlPO-14. In these adsorbents, C_3H_6 either adsorbs stronger or diffuses faster and therefore has to be recovered as desorbate. Despite intensive research efforts, no commercially viable adsorptive separation processes have emerged for C_3H_6/C_3H_8 separation [7].

1.2.3 Membrane-Based Gas Separation

Membrane separation offers the advantages of energy-efficiency, compactness, smaller footprints, and flexibility [16]. Membrane-based gas separation is not as well-developed as membrane-based water purification, i.e. microfiltration, ultrafiltration, and

desalination. In membrane-based gas separation, a pressurized gaseous mixture is passed across the surface of a membrane that is selectively permeable to one component of the feed mixture to another. The fast permeating component is enriched in the permeate at the downstream side of the membrane, and the slower permeating component is enriched in the retentate at the upstream side of the membrane. The simplified flow scheme is illustrated in Figure 1.3.

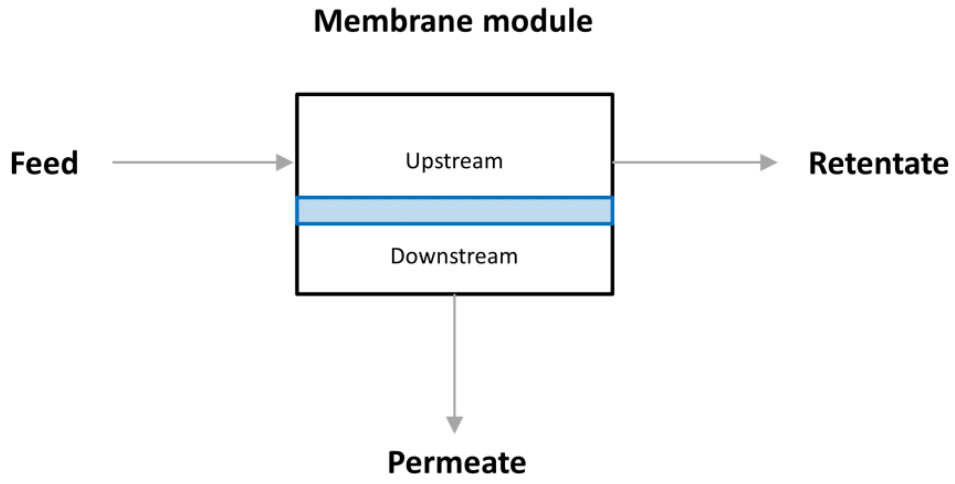

Figure 1.3: Simplified flow scheme of membrane-based gas separation process.

The gas separation membrane market was $150 million/year in 2000, and is expected to reach $760 million/year by 2020 [17]. A percentage breakdown of the total membrane market by major separation categories in 2000 and 2020 (predicted) is shown in Figure 1.4. The major industrial applications of gas separation membranes include air separation, hydrogen separation, and acid gas removal from natural gas. Extensive research efforts have been made in both academia and industry to explore more opportunities such as olefin/paraffin separations, NGL recovery from natural gas, and

post-combustion CO_2 capture. The refinery/petrochemical sector is expected to increase from 6% in 2000 to 24% in 2020.

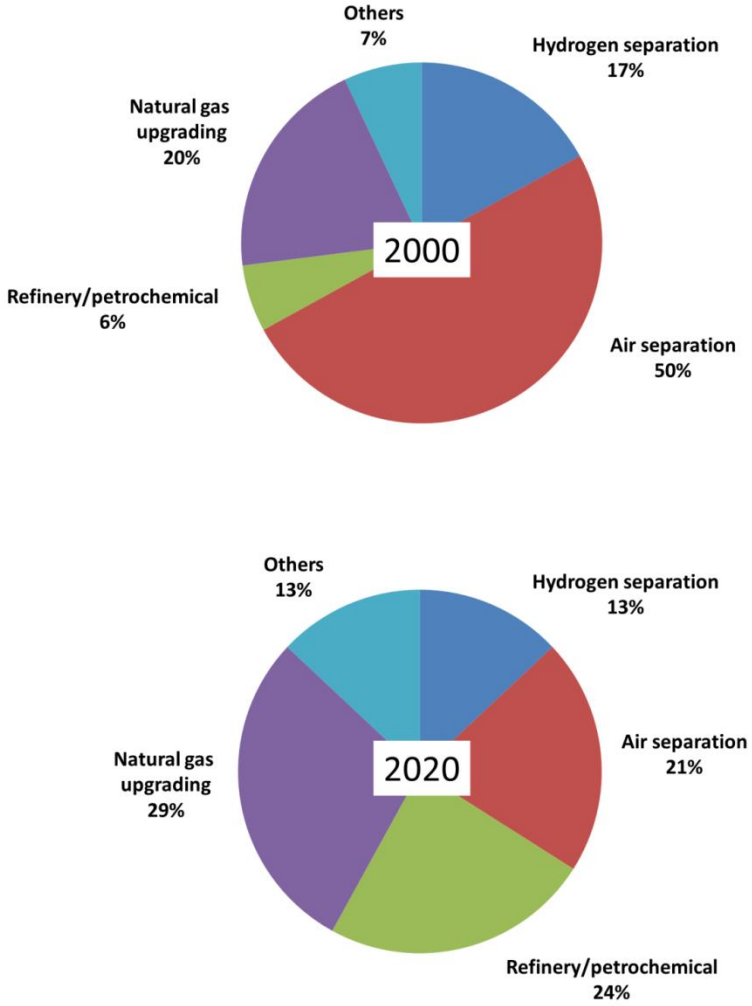

Figure 1.4: Percentage breakdown of membrane market in 2000 and 2020 (predicted) [17].

Transport in dense membranes or microporous membranes with pore dimension comparable with the size of permeating molecules follows the solution-diffusion mechanism, the details of which will be described in Chapter 2. Examples of membrane

separations based on diffusion selectivity and/or sorption selectivity are shown in Table 1.2.

Table 1.2: Examples of membrane separation based on diffusion or/and sorption selectivity [18-19]. The items shown in red are commercialized processes.

Separation	Membrane material
I. Separation based on ***sorption*** selectivity	
C_3H_6/N_2	Silicone rubber
Ethanol/water	Zeolite 4A
CO_2/N_2	Zeolite NaY
C_4H_{10}/CH_4	Silicone rubber
II. Separation based on ***diffusion*** selectivity	
O_2/N_2	Polyimide
H_2/CH_4	Polyaramide
C_2H_4/C_2H_6	Caron molecular sieve
C_3H_6/C_3H_8	ZIF-8
III. Separation based on ***sorption*** and ***diffusion*** selectivity	
CO_2/CH_4	Cellulose acetate
Methanol/MTBE	Cellulose acetate
n/iso-C_4H_{10}	Zeolite 5A
Water/acetone	PVA

For a given membrane material, the diffusivity is determined by size and shape of the diffusing molecule. Therefore, the diffusion selectivity of component A and B in a given membrane depends on how much they differ in molecular size and shape. Separation of C_3H_6/C_3H_8 based on diffusion selectivity is challenging due to the small size difference (0.2 Å) between C_3H_6 and C_3H_8 [20]. Table 1.3 compares the molecular size difference of C_3H_6/C_3H_8 with several other separations (microfiltration, ultrafiltration, desalination, hydrogen purification, and natural gas purification) that have

already been practiced commercially by membranes [18]. Obviously the molecular size difference of C_3H_6/C_3H_8 is much smaller and attractive diffusion selectivity is more challenging to be achieved. This is also demonstrated by the position of permeability-selectivity trade-off curves of polymeric materials. As shown in Figure 1.5, the trade-off curve for C_3H_6/C_3H_8 separation [21] is much lower than that of H_2/CH_4 and CO_2/CH_4 separation [22].

Table 1.3: Comparison of molecular size differences for different membrane-based separations [18, 23]

Application	Separation	Difference in molecular diameter (Å)
Microfiltration	H_2O/bacteria	$>10^4$
Ultrafiltration	H_2O/virus	$>10^3$
Desalination	H_2O/hydrated ion	>3
Gas separation	H_2/CH_4	0.9
	CO_2/CH_4	0.5
	C_3H_6/C_3H_8	0.2

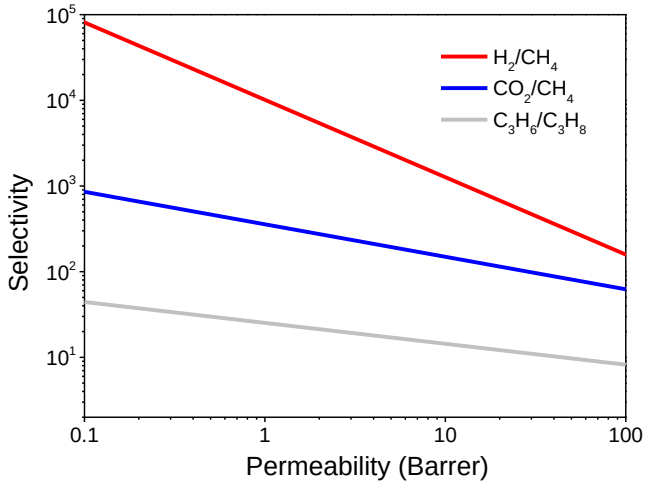

Figure 1.5: Upper bound correlations for H_2/CH_4, CO_2/CH_4, and C_3H_6/C_3H_8 separations [21-22].

With the exception of facilitated transport membranes, which have not been proved to be commercial, there do not exist membrane materials that have displayed sufficiently high C_3H_6/C_3H_8 separation performance to replace the C_3 splitter with a single pass. Colling and co-workers [24] studied the possibility of replacing the C_3 splitter with a multi-stage membrane separator. Their results show that by carefully designing the membrane sequences, without the C_3 splitter, it was possible to produce polymer grade C_3H_6 and liquefied petroleum gas (LPG) using moderately selective membrane with reasonable membrane area. However, their calculations were based on hypothetical hollow fiber membranes and the economic competitiveness of the process was not evaluated and compared with cryogenic distillation.

Instead of completely replacing the C_3 splitter, another option is to retrofit the separation using a membrane-distillation hybrid separation system. Several configurations have been proposed. One example is given in Figure 1.6, in which the membrane unit is used to enrich C_3H_6 in the feed stream before being introduced into the column [25]. With this design, incorporation of the membrane separator may help to decrease the required reflux ratio to produce polymer grade C_3H_6 for an existing column. The cost-effectiveness of the membrane-distillation hybrid separation system is determined by performance and cost of the membrane separator as well as detailed process design [26].

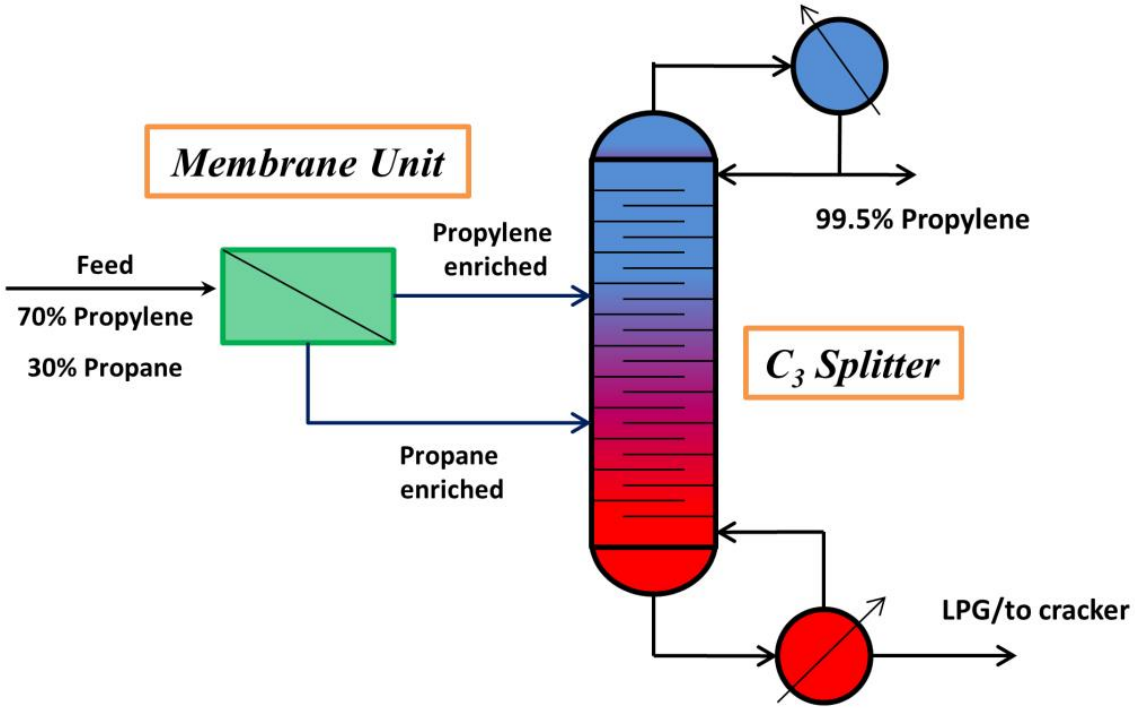

Figure 1.6: Schematic illustration of membrane-distillation hybrid separation C_3H_6/C_3H_8 system [25].

1.3 Membrane Materials

Polymer membrane is the only type of membrane that has been commercialized for large-scale gas separations and purifications [27]. Unfortunately, polymer membranes seem to be inadequate for olefin/paraffin separations due to performance and compromised stability under realistic operating conditions [21]. Due to these limitations, advanced membranes have been studied for olefin/paraffin separations, including zeolite membrane, carbon molecular sieve membrane, MOF/ZIF membrane, mixed-matrix membrane, and facilitated transport membrane. Nonetheless, none of these membranes have been commercialized for large-scale olefin/paraffin separations due to many technical challenges that have yet been overcome.

1.3.1 Polymeric Membranes

Polymeric membranes provide a baseline for advanced membrane research. Following their success in desalination since 1980s, enormous attempts have been made to advance polymer membranes as commercially viable separation devices for separations and purifications of gas mixtures. Polymers have clear advantages over "less conventional" membrane materials such as zeolites, carbon molecular sieves, and MOFs/ZIFs, which will be discussed later. Polymers are relatively inexpensive, and industry has gained significant knowledge and experiences to develop polymer membranes into large-scale modules (spiral wound and hollow fiber) with reasonable manufacture costs. Applications that are already practiced commercially by polymer membranes include hydrogen recovery, air separation, and CO_2 removal from natural gas.

After many years of development, practitioners have gained substantial understanding of the relationship between polymer structure and its gas transport properties. Glassy polymers with high *Tg* (glass transition temperature) possess both good mechanical strength, durability, and desirable gas transport properties. Figure 1.7 shows chemical structures of several commercial gas separation membranes that are based on glassy polymers, including polysulfone membrane for air separation (PRISM®, Air Products), polyimide membrane for air separation (MEDAL, Air Liquide), cellulose acetate (CA) membrane for natural gas purification (Separex®, UOP), and polyaramid membrane for hydrogen purification (MEDAL, Air Liquide).

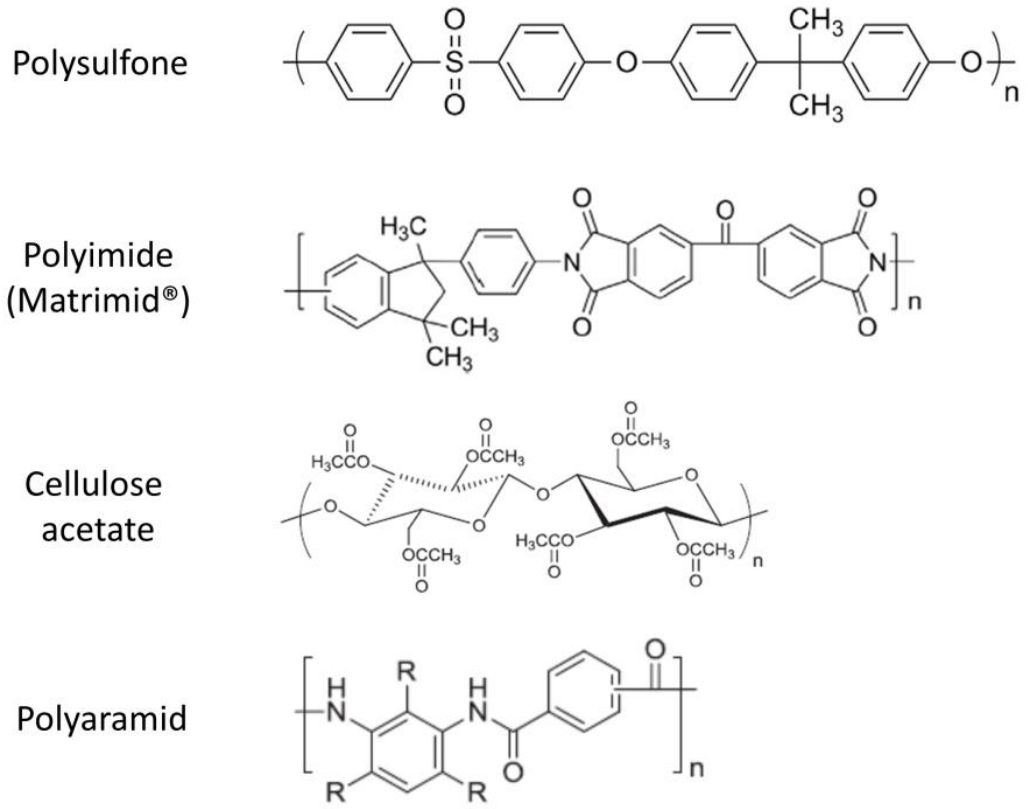

Figure 1.7: Chemical structures of several commercial gas separation membranes [18, 27].

As increasing efforts were invested to improve the gas separation performance of polymeric membrane, it became apparent that, unfortunately, a trade-off relationship [28, 22] exists between permeability and selectivity. The indication was that polymer membranes are unlikely to be attractive in the case that simultaneous high permeability and high selectivity are required to either retrofit or replace conventional separation technologies. Two examples of the permeability-selectivity trade-off are given in Figure 1.8 for CO_2/CH_4 separation [22] and C_3H_6/C_3H_8 separation [21]. In addition to inadequate performance, polymer membranes also generally suffer from plasticization problems [29].

Among the efforts that have been made to advance pure polymer membranes for C_3H_6/C_3H_8 separation, those by Air Liquide [30] were probably the most aggressive. P84-based polyimides were formed into high-quality monolithic hollow fibers. A C_3H_6/C_3H_8 separation factor as high as 15.9 was obtained, which was quite promising considering the harsh conditions that the fibers were tested (50:50 mol% C_3H_6/C_3H_8 mixture under 400 psia and 90 ^oC). Unfortunately, due to the very rigid structure of the used polyimide, the permeance was only ~0.6 GPU and apparently was not sufficiently attractive for commercialization.

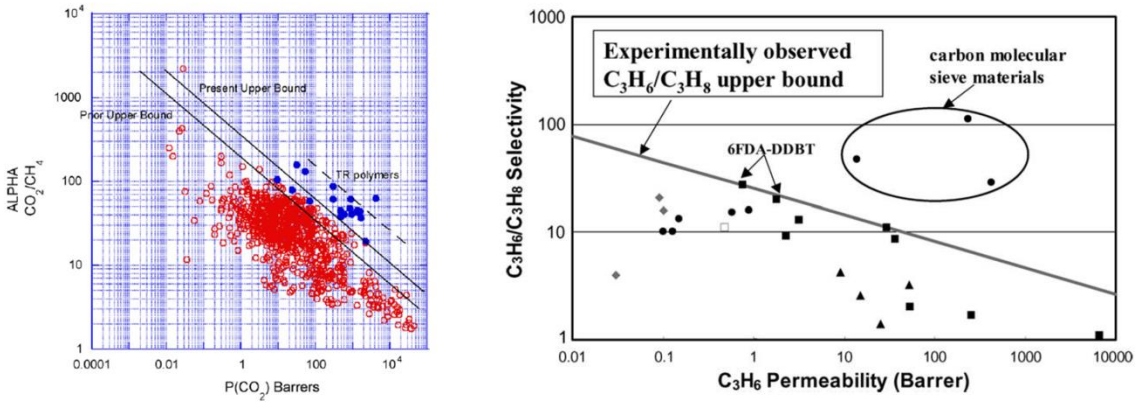

Figure 1.8: Upper bound correlations for CO_2/CH_4 separation [22] and C_3H_6/C_3H_8 separation [21]

1.3.2 Zeolite Membranes

Following their commercialization as adsorbents and catalysts, zeolites received considerable attention from both academia and industry as chemically and thermally-robust membrane materials for advanced gas separations. A coherent polycrystalline zeolite membrane can be grown on porous supports such as porous alumina. Supported

zeolite membranes formed in this way have been shown to be able to offer exceptional selectivity (and permeance as well, in some cases) that are substantially higher than polymeric membranes well above the upper bound. For example, zeolite membranes with quite attractive selectivities for separation of CO_2/CH_4, butane isomers, and butylene isomers have been successfully fabricated at lab-scale [19].

However, despite the intensive efforts that have been made over the past few decades to advance zeolite membrane as a commercially viable separation device, only one zeolite membrane process has been developed commercially, which is dehydration of water from alcohols using zeolite LTA membrane [31]. This particular separation is largely based on preferential adsorption of water over ethanol on the zeolite's hydrophilic surface. That is to say, there are no commercialized zeolite membranes for size/shape selective separations. Many challenges remain [19, 31], including difficulties to form a thin zeolite layer with minimized defects and cracks, brittleness, mismatch of thermal expansion coefficients between the zeolite layer and the underneath support, reduced selectivity and permeance under high-pressure binary or multicomponent permeation, etc. In addition to these issues that already exist for lab-scale membrane development, economical manufacture of high-quality zeolite membrane modules at large-scale has yet been proven to be practical.

1.3.3 MOF/ZIF Membranes

Following the recent explosion in research on metal-organic frameworks (MOFs) and zeolitic imidazolate frameworks (ZIFs), supported MOF and ZIF membranes have

been synthesized and characterized for gas transport properties. Examples are given by pure MOF-5 membrane and ZIF-8 membrane grown on porous alumina dishes [32-33] and tubes [33-34]. Compared with inorganic zeolitic molecular sieves, the more diversified building units (metal ions, metal oxide clusters, and organic linkers) of MOFs and ZIFs offer them flexibility to be tailored for a particular separation [31, 35].

Several studies reported successful fabrication of pure ZIF-8 membranes showing quite promising C_3H_6/C_3H_8 separation performance. However, similar to pure zeolite membranes, many challenges remain to scale up pure MOF/ZIF membranes for large-scale gas separations. MOFs and ZIFs are generally less chemically and thermally stable than zeolites. Moreover, the framework of MOFs and ZIFs is more flexible than zeolites at comparable temperature and adsorbate loading. As a result, ultrahigh diffusion selectivity or total exclusion achievable for small pore zeolites is rarely seen in MOFs and ZIFs. As will be discussed in the following sections, MOFs and ZIFs are advantageous over zeolites as membrane materials due to the fact that they are more compatible with glassy polymers and are therefore more suitable for development of mixed-matrix membranes.

1.3.4 Carbon Molecular Sieve Membranes

Compared with supported zeolite and MOF/ZIF membrane, carbon molecular sieve (CMS) membranes are more likely to evolve into a practical gas separation technology due to the possibility to be realized on the platform of hollow fibers without the need of a support [36]. CMS are amorphous, porous materials formed by the pyrolysis

of polymer precursors under controlled environments. During high temperature pyrolysis, the precursor decomposes and intrinsic pores are formed from packing imperfections between microcrystalline regions in the material, or so-called "graphene-like" sheets [37]. The slit-like structure of molecular sieve carbons is not as well defined as the above mentioned crystalline zeolites and MOFs/ZIFs.

Microstructure and gas transport properties of CMS membrane are dependent on many factors, including structure of the starting polymer precursor, pre-treatment conditions, pyrolysis conditions, and post-treatment conditions. These parameters can be tailored to form CMS membrane with desirable transport properties for a particular separation. CMS membranes have been shown to be able to deliver attractive separation performance for natural gas purification and olefin/paraffin separations [38].

1.3.5 Mixed-Matrix Membranes

The history of man-made composite materials dates back to 3000 BC when Mesopotamians first mixed mud and straw to form bricks for building construction. Composite materials consist two or more physically and/or chemically distinct, suitably arranged or distributed phases with an interface separating them. Examples (Figure 1.9) of engineering composites include concretes and fiber-reinforced plastics/metal/ceramics. Composite materials are formed to offer desirable properties that cannot be obtained by individual components. For example, glass fibers are very strong but brittle and will break if bent sharply, while plastics can be formed into complex shapes but are not sufficiently strong for demanding engineering applications. The plastics matrix holds the

glass fiber together to form fiber-reinforced plastics that are stronger than the plastics matrix and still possess shaping flexibility.

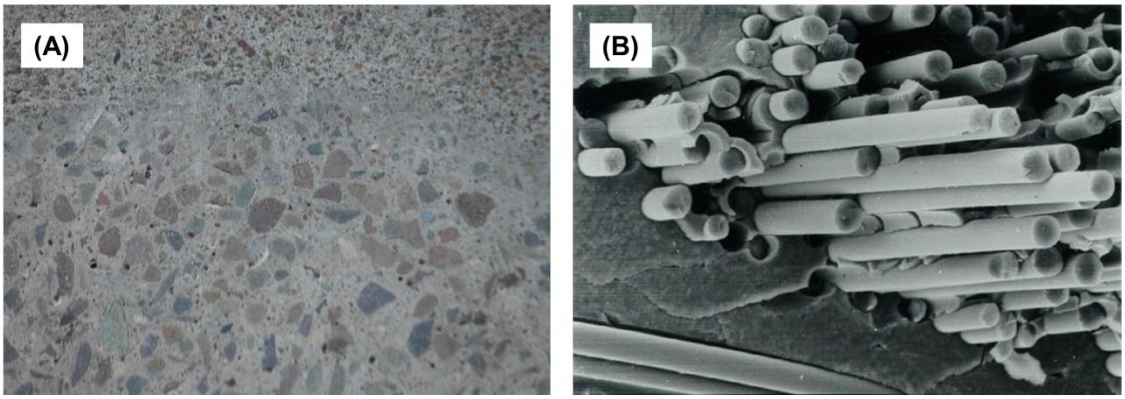

Figure 1.9: Examples of engineering composites (A) concretes formed by dispersing aggregates (sands, crushed stone, etc.) in a cement matrix (B) fiber reinforced ceramic formed by dispersing SiC fibers in a SiC matrix.

Similarly, mixed-matrix membranes (MMMs) offer an excellent compromise to address limitations of both polymeric membrane and inorganic membrane. Conventional mixed-matrix membrane is formed by dispersing fillers (particles, platelets, etc.) of porous solids in the matrix of an easily-processed polymer [39] (Figure 1.10). The dispersed fillers should be much more selective (and preferably somewhat more permeable) than the polymer matrix. Ideally, as shown in Figure 1.11, selectivity and permeability of the resulting mixed-matrix membrane should be simultaneously enhanced over the neat polymer and eventually become commercially attractive with sufficiently high particle loading. In the meantime, the membrane can be easily and inexpensively processed in the same or similar manner with polymeric membrane.

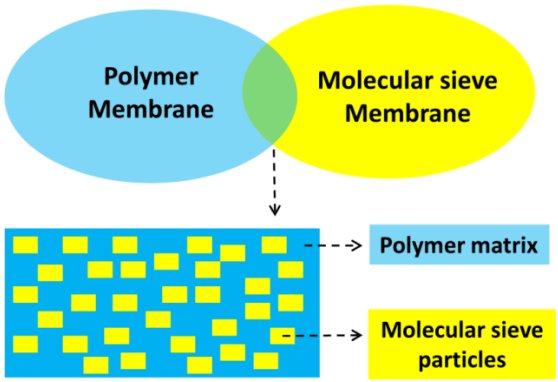

Figure 1.10: Schematic illustration of mixed-matrix membrane based on polymer and molecular sieve.

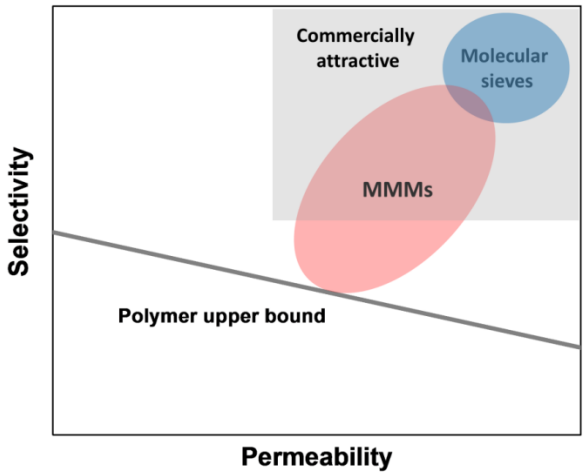

Figure 1.11: Hypothetical polymer upper bound and the capabilities of mixed-matrix membranes

Glassy polymers are favored over rubbery polymers to form mixed-matrix membrane since glassy polymers are more size/shape-selective than rubbers and can be formed into the industrially preferred self-supporting hollow fiber geometry. The dispersed particles are usually microporous adsorbents including the above mentioned

zeolites, CMS, and more recently, MOFs/ZIFs. In most cases, they enhance the permselectivity of the membrane on the basis of their exceptional diffusion selectivity. Membrane selectivity enhancement due to the filler's favorable sorption selectivity is also possible, but much less common. At practical pressures, C_3H_6/C_3H_8 sorption selectivity in most adsorbents is less than 10, which is lower than the permselectivity of 6FDA-based polyimides [21]. As a result, enhancement of C_3H_6/C_3H_8 selectivity by mixed-matrix membrane should be based on the filler's favorable diffusion selectivity. A comprehensive review of materials that have been studied for mixed-matrix membrane can be found elsewhere. The challenges to develop scalable mixed-matrix membrane will be discussed in section 2.6.

1.3.6 Facilitated Transport Membranes

In a facilitated transport membrane, passive diffusion of olefins across the membrane is supplemented with facilitated transport by carrier agents (such as metal salts) that selectively and reversibly bind with olefins but not paraffins. The most extensively studied metal salts [10] for facilitated transport membrane are silver salts (e.g. $AgNO_3$ and $AgBF_4$) and cuprous salts (e.g. $CuAlCl_4$). While the exact mechanism for transport of olefins across the membrane by complexation is complex, it has been suggested that facilitated transport occurs by either mobile diffusion of the cation-olefin complex through the membrane (for liquid membranes) or by movement of the olefin across fixed silver sites by a hopping mechanism (for solid membranes).

Due to the enhanced transport of olefin over paraffin, facilitated transport membranes have demonstrated remarkably high olefin/paraffin selectivity and attractive olefin permeance at lab- and pilot-scale. For example, a C_3H_6 permeance of 15 GPU and C_3H_6/C_3H_8 mixed-gas selectivity of 200 was seen for PDMS-$AgBF_4$ facilitated transport membrane [40]. Standard Oil even brought facilitated transport membrane to pilot-scale, using polymer hollow fiber membrane impregnated with $AgNO_3$ solution and tested C_3H_6/C_3H_8 permeation [18]. Polymer-grade (>99.5%) C_3H_6 was obtained at the beginning of the measurements with a single-stage membrane module, which is quite remarkable.

Unfortunately, in addition to reversible reaction with olefins, carrier ions irreversibly react with hydrogen, acetylenes, hydrogen sulfide and other sulfur impurities present in the olefin/paraffin feed mixtures [10]. These side reactions deactivate the carrier ions so that they are no longer able to complex olefins. As a result, although the starting olefin/paraffin separation performance of facilitated transport membranes can be far beyond the polymer upper bound, the membranes typically "degrade" progressively with substantial performance losses, thus making them questionable for practical applications. In the above mentioned Standard Oil project [18], the C_3H_6 purity decreased to ~95% after 100 days of operation even with periodical regeneration of the salt solution.

Theoretically the deactivation problem caused by poisoning impurities in the feed mixture can be solved by minimizing their concentration through pre-treatments,

however; it has been shown that silver ions are unstable even in pure olefin/paraffin feeds without impurities due to the "olefin conditioning" [41] issue that was initially identified and investigated by Membrane Technology and Research (MTR) [42]. That is to say, the development of an intrinsically stable carrier is required to make facilitated transport membranes practical for industrial implementations.

1.4 Research Objectives

Mixed-matrix membrane has received increasing attention as a promising approach to address challenging gas separations. However, many technical challenges remain to bring zeolite-based mixed-matrix membranes to commercial implementation. ZIFs is a new class of microporous adsorbent that has demonstrated interesting adsorption and diffusion properties that may enable them as advanced adsorbents or membranes. Moreover, ZIFs' intrinsic compatibility with polymers makes them particularly suitable for mixed-matrix membranes, whose scalability has been a challenge due to difficulties in achieving desirable interfacial properties between glassy polymers and zeolites.

The overarching goal of this research is **to provide a framework for development of scalable ZIF-based mixed-matrix membrane that is able to deliver attractive transport properties for advanced gas separations.** The primary objectives of this dissertation are as follows:

1. **Select membrane materials (ZIF and polymer) based on a fundamental understanding of sorption and diffusion.**

The first object of this research was to identify appropriate ZIF and polymer to form mixed-matrix membrane for C_3H_6/C_3H_8 separation. Fundamentally understand sorption and diffusion in the dispersed molecular sieve is crucial for development of mixed-matrix membrane. Solubility coefficients and transport diffusivities were obtained from equilibrium and kinetics sorption measurements, which were used to estimate the ZIF's permeability and permselectivity as well as to determine whether it will offer enhanced and attractive separation performance for the mixed-matrix membrane.

2. **Develop ZIF-based mixed-matrix dense film membranes with enhanced separation performance.**

The selected ZIF-8 and 6FDA-DAM polyimide were processed into mixed-matrix dense film membranes with particle loading up to 48wt%. Transport properties of C_3H_6/C_3H_8 and several other gases in the mixed-matrix dense film membranes were studied with both single-gas and mixed-gas permeation. Permeabilities and selectivities of these gases in ZIF-8 were estimated using Maxwell model and data from the equilibrium sorption measurements.

3. **Extend the enhanced separation performance realized in mixed-matrix dense film membranes into industrially desirable hollow fiber geometry.**

Although material selection represents a very important aspect of membrane research, processing the high-performance membrane materials to scalable membrane geometries constitutes another important aspect. Efforts were made to scale up the mixed-matrix dense film membranes in Object 2 into the industrially relevant hollow fiber geometry. Dual-layer mixed-matrix hollow fiber membranes with particle loading up to 40 wt% were formed and characterized. The effect of spinning dope compositions, spinning parameters, and post-treatments on hollow fiber morphology and transport properties were discussed.

1.5 Dissertation Organization

This dissertation is organized in the following manners. Chapter 2 provides an overview of essential background relevant to this research. Chapter 3 describes the materials, experimental procedures and equipment used throughout this research. Chapter 4 contains synthesis and characterization of ZIF-8 with controllable crystal size, which is crucial to enable convenient measurement of hydrocarbon sorption kinetics. Chapter 5 discusses selection of membrane materials based on fundamental understanding of adsorption and diffusion in ZIF-8. Chapter 6 discusses development of mixed-matrix dense film membranes with significantly enhanced C_3H_6/C_3H_8 separation performance. Chapter 7 extends the successful platform of mixed-matrix dense film membrane developed in Chapter 6 into industrially desirable hollow fiber geometry. Chapter 8

summarizes the findings of this work and also includes recommendations for future work to further advance the project.

1.6 References

[1] M. Das, PhD Dissertation, Georgia Institute of Technology, 2009.

[2] *Propylene Stewardship Guidance Manual*; American Chemistry Council: 2007

[3] *Butadiene Stewardship Guidance Manual*; American Chemistry Council: 2002

[4] H. Jarvelin and J. R. Fair, "Adsorptive separation of propylene-propane mixtures" *Industrial & Engineering Chemistry Research* **1993**, *32*, 2201-2207.

[5] J. D. Seader, E. J. Henley and D. K. Roper, *Separation Process Principles*, John Wiley & Sons, Ltd, **2011**

[6] B. E. Poling, J. M. Prausnitz and J. P. O'Connell, *The Properties of Gases and Liquids, 5th edition*, McGRAW-HILL, **2001**

[7] D. M. Ruthven and S. C. Reyes, "Adsorptive separation of light olefins from paraffins" *Microporous Mesoporous Mat.* **2007**, *104*, 59-66.

[8] E. D. Bloch, W. L. Queen, R. Krishna, J. M. Zadrozny, C. M. Brown and J. R. Long, "Hydrocarbon Separations in a Metal-Organic Framework with Open Iron(II) Coordination Sites" *Science* **2012**, *335*, 1606-1610.

[9] D. J. Safarik and R. B. Eldridge, "Olefin/Paraffin Separations by Reactive Absorption: A Review" *Industrial & Engineering Chemistry Research* **1998**, *37*, 2571-2581.

[10] R. Faiz and K. Li, "Olefin/paraffin separation using membrane based facilitated transport/chemical absorption techniques" *Chemical Engineering Science* **2012**, *73*, 261-284.

[11] D. F. Sava, M. A. Rodriguez, K. W. Chapman, P. J. Chupas, J. A. Greathouse, P. S. Crozier and T. M. Nenoff, "Capture of Volatile Iodine, a Gaseous Fission Product, by Zeolitic Imidazolate Framework-8" *Journal of the American Chemical Society* **2011**, *133*, 12398-12401.

[12] R. T. Yang, *Adsorbents: Fundamentals and Applications*, John Wiley & Sons, Inc., **2003**

[13] S. U. Rege, J. Padin and R. T. Yang, "Olefin/paraffin separations by adsorption: π-Complexation vs. kinetic separation" *AIChE Journal* **1998**, *44*, 799-809.

[14] J. Karger and D. M. Ruthven, *Diffusion in Zeolites and Other Microporous Solids.*, John Wiley & Sons, Inc., **1991**

[15] D. M. Ruthven, *Principles of Adsorption and Adsorption Processes*, John Wiley & Sons, Inc., **1984**

[16] W. J. Koros and G. K. Fleming, "Membrane-based gas separation" *Journal of Membrane Science* **1993**, *83*, 1-80.

[17] R. W. Baker, "Future directions of membrane gas separation technology" *Industrial & Engineering Chemistry Research* **2002**, *41*, 1393-1411.

[18] R. W. Baker, *Membrane Technology and Applications*, John Wiley & Sons, Ltd, **2004**

[19] J. Caro and M. Noack, "Zeolite membranes - Recent developments and progress" *Microporous Mesoporous Mat.* **2008**, *115*, 215-233.

[20] C. Zhang, R. P. Lively, K. Zhang, J. R. Johnson, O. Karvan and W. J. Koros, "Unexpected Molecular Sieving Properties of Zeolitic Imidazolate Framework-8" *The Journal of Physical Chemistry Letters* **2012**, *3*, 2130-2134.

[21] R. L. Burns and W. J. Koros, "Defining the challenges for C3H6/C3H8 separation using polymeric membranes" *Journal of Membrane Science* **2003**, *211*, 299-309.

[22] L. M. Robeson, "The upper bound revisited" *J. Membr. Sci.* **2008**, *320*, 390-400
.
[23] W. J. Koros and R. P. Lively, "Water and beyond: Expanding the spectrum of large-scale energy efficient separation processes" *Aiche Journal* **2012**, *58*, 2624-2633.

[24] C. W. Colling, G. A. Huff Jr and J. V. Bartels, Process Using Solid Perm-selective Membranes in Multiple Groups for Simultaneous Recovery of Specified Products from a Fluid Mixture. 2004.

[25] L. Xu, PhD Dissertation, Georgia Institute of Technology, 2012.

[26] J. Ploegmakers, A. R. T. Jelsma, A. G. J. van der Ham and K. Nijmeijer, "Economic Evaluation of Membrane Potential for Ethylene/Ethane Separation in a Retrofitted Hybrid Membrane-Distillation Plant Using Unisim Design" *Industrial & Engineering Chemistry Research* **2013**, *52*, 6524-6539.

[27] D. E. Sanders, Z. P. Smith, R. L. Guo, L. M. Robeson, J. E. McGrath, D. R. Paul and B. D. Freeman, "Energy-efficient polymeric gas separation membranes for a sustainable future: A review" *Polymer* **2013**, *54*, 4729-4761.

[28] L. M. Robeson, "CORRELATION OF SEPARATION FACTOR VERSUS PERMEABILITY FOR POLYMERIC MEMBRANES" *Journal of Membrane Science* **1991**, *62*, 165-185.

[29] C.-C. Chen, W. Qiu, S. J. Miller and W. J. Koros, "Plasticization-resistant hollow fiber membranes for CO2/CH4 separation based on a thermally crosslinkable polyimide" *Journal of Membrane Science* **2011**, *382*, 212-221.

[30] I. C. Roman, J. W. Simmons and O. M. Ekiner, Method of Separating Olefins from Mixtures with Paraffins. US Patent 7399897 B2, 2008.

[31] J. Karger, D. M. Ruthven and D. N. Theodorou, *Diffusion in Nanoporous Materials*, John Wiley & Sons, Ltd, **2012**

[32] H. T. Kwon and H.-K. Jeong, "In Situ Synthesis of Thin Zeolitic–Imidazolate Framework ZIF-8 Membranes Exhibiting Exceptionally High Propylene/Propane Separation" *Journal of the American Chemical Society* **2013**, *135*, 10763-10768.

[33] Y. Pan, T. Li, G. Lestari and Z. Lai, "Effective separation of propylene/propane binary mixtures by ZIF-8 membranes" *J. Membr. Sci.* **2012**, *390-391*, 93-98.

[34] Y. Pan, B. Wang and Z. Lai, "Synthesis of ceramic hollow fiber supported zeolitic imidazolate framework-8 (ZIF-8) membranes with high hydrogen permeability" *Journal of Membrane Science* **2012**, *421–422*, 292-298.

[35] A. Phan, C. J. Doonan, F. J. Uribe-Romo, C. B. Knobler, M. O'Keeffe and O. M. Yaghi, "Synthesis, Structure, and Carbon Dioxide Capture Properties of Zeolitic Imidazolate Frameworks" *Acc. Chem. Res.* **2010**, *43*, 58-67.

[36] L. R. Xu, M. Rungta and W. J. Koros, "Matrimid (R) derived carbon molecular sieve hollow fiber membranes for ethylene/ethane separation" *Journal of Membrane Science* **2011**, *380*, 138-147.

[37] M. Rungta, PhD Dissertation, Georgia Institute of Technology, 2012.

[38] M. Rungta, C. Zhang, W. J. Koros and L. Xu, "Membrane-based ethylene/ethane separation: The upper bound and beyond" *AIChE Journal* **2013**, *59*, 3475-3489.

[39] T. T. Moore, R. Mahajan, D. Q. Vu and W. J. Koros, "Hybrid membrane materials comprising organic polymers with rigid dispersed phases" *AIChE J.* **2004**, *50*, 311-321.

[40] J. H. Kim, J. Won and Y. S. Kang, "Olefin-induced dissolution of silver salts physically dispersed in inert polymers and their application to olefin/paraffin separation" *Journal of Membrane Science* **2004**, *241*, 403-407.

[41] *Separation of Olefin/Paraffin Mixtures with Carrier Facilitated Transport Membranes*; Membrane Technology and Research Inc.: 2007

[42] T. C. Merkel, R. Blanc, I. Ciobanu, B. Firat, A. Suwarlim and J. Zeid, "Silver salt facilitated transport membranes for olefin/paraffin separations: Carrier instability and a novel regeneration method" *Journal of Membrane Science* **2013**, *447*, 177-189.

CHAPTER 2

BACKGROUND AND THEORY

2.1 Overview

This chapter provides essential background materials relevant to this research. The first section describes fundamentals of diffusion, sorption, and permeation in membrane materials. The second section gives an overview of zeolites and zeolitic imidazolate frameworks. Then formation of dual-layer mixed-matrix hollow fiber membrane is described. Technical challenges to bring mixed-matrix membranes into commercialization are discussed as well.

2.2 Transport Fundamentals

2.2.1 Membrane Permeation: The Sorption-Diffusion Theory

Permeation in a dense and non-porous membrane can be described by the sorption-diffusion theory. Penetrants first sorb at the upstream side of membrane, then diffuse in the membrane by chemical potential gradient, and eventually desorb at the downstream side of the membrane. Permeability is a measure of the membrane material's intrinsic productivity and is defined as the steady-state flux (N_A) normalized by fugacity difference (Δf_A) and membrane thickness (l):

$$P_A = \frac{N_A \cdot l}{\Delta f_A} \tag{2.1}$$

In the case of ideal gases, the fugacity difference (Δf_A) in equation can be replaced by partial pressure difference (Δp_A) and equation 2.1 can be re-written as:

$$P_A = \frac{N_A \cdot l}{\Delta p_A} \tag{2.2}$$

Permeability is traditionally given in the unit of Barrer:

$$1\ Barrer = 1\times 10^{-10}\ \frac{cm^3(STP)\cdot cm}{cm^2 \cdot s \cdot cmHg}$$

For asymmetric membranes, the thickness of membrane selective layer usually cannot be reliably determined. In that case membrane productivity is described by permeance, which is simply the fugacity difference normalized flux:

$$\left(\frac{P_A}{l}\right) = \frac{N_A}{\Delta f_A} \tag{2.3}$$

"Gas permeation unit" or GPU is usually used as the unit of permeance, which is defined as:

$$1\,GPU = 10^{-6}\,\frac{cm^3(STP)}{cm^2 \cdot s \cdot cmHg}$$

Based on Fick's 1st law, permeability of a penetrant A can be decomposed into the product of a kinetic factor (diffusivity) and thermodynamic factor (sorption coefficient) [1]:

$$P_A = \tilde{D}_A \times \tilde{S}_A \tag{2.4}$$

$$\tilde{D}_A = \left[\int_{C_{A1}}^{C_{A2}} D_A(C_A)\,dC_A\right] \Big/ \left[\int_{C_{A1}}^{C_{A2}} dC_A\right] \tag{2.5}$$

$$\tilde{S}_A = (C_{A2} - C_{A1}) / (p_{A2} - p_{A1}) \tag{2.6}$$

where $\tilde{D}_A$ (cm^2/s) and $\tilde{S}_A$ (cm^3[STP] $\cdot cm^{-3} \cdot bar^{-1}$) are average diffusivity and average sorption coefficient of penetrant A in the membrane, C_{A1} (mmol/g) and C_{A2} (mmol/g) are the concentration of penetrant A at the downstream and upstream side of the membrane, p_{A1} (bar) and p_{A2} (bar) are penetrant partial pressure or fugacity in the downstream and upstream side of the membrane, respectively.

The efficiency of a membrane to separate penetrant A (faster permeating) from B (slower permeating) is characterized by permselectivity $\alpha_{A/B}$, which is defined as the ratio of permeability or permeance:

$$\alpha_{A/B} = \frac{P_A}{P_B} = \frac{(P_A/l)}{(P_B/l)} \tag{2.7}$$

When a mixture of A and B permeate through the membrane, the separation factor is:

$$\alpha_{A/B} = \frac{\left(y_A / y_B\right)}{\left(x_A / x_B\right)} \tag{2.8}$$

Where y and x are mole fractions in the downstream and upstream side of the membrane.

Based on equation 2.4, permselectivity can be further decomposed into the product of diffusion selectivity α_D and sorption selectivity α_S :

$$\alpha_{A/B} = \frac{P_A}{P_B} = \left[\frac{\tilde{D}_A}{\tilde{D}_B}\right] \times \left[\frac{\tilde{S}_A}{\tilde{S}_B}\right] = \alpha_D \times \alpha_S \tag{2.9}$$

$$\alpha_D = \left[\frac{\tilde{D}_A}{\tilde{D}_B}\right] \tag{2.10}$$

$$\alpha_S = \left[\frac{\tilde{S}_A}{\tilde{S}_B}\right] \tag{2.11}$$

That is to say, separation of penetrant A and B is based on the differences in how fast they diffuse in the membrane and how much they sorb in the membrane. In the case of C_3H_6/C_3H_8 separation, as shown in Figure 2.1, C_3H_6 usually permeate through the membrane faster than C_3H_8. As a result, when a mixture of C_3H_6 and C_3H_8 is pressurized at the upstream side of the membrane, C_3H_6 is enriched at the downstream side of the membrane while C_3H_8 is enriched at the upstream side of the membrane, and separation is achieved.

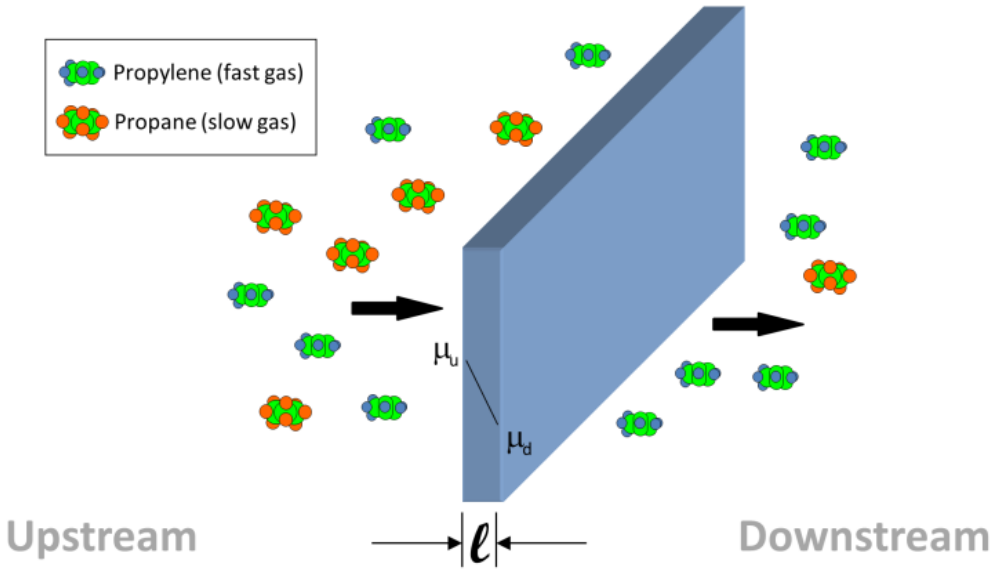

Figure 2.1: Illustration of C_3H_6/C_3H_8 separation by a permselective membrane based on solution-diffusion.

2.2.2 Sorption

Fundamentally understanding sorption and diffusion in membrane materials is crucial to design membrane devices with desirable transport properties. For physical

adsorption, the interaction potential between adsorbate molecule and adsorbent surface consists of nonspecific (non-electrostatic) van der Waals interactions (dispersion energy, close-range repulsion energy, and induction energy) supplemented by electrostatic contributions [2] (field-dipole and field gradient-quadrupole interactions):

$$\Phi_{Total} = \Phi_D + \Phi_R + \Phi_{Ind} + \Phi_{F-\mu} + \Phi_{\delta F-\mu} \qquad (2.12)$$

Where Φ_D is dispersion energy, Φ_D is close-range repulsion energy, Φ_{Ind} is induction energy, $\Phi_{F-\mu}$ represents field-dipole interaction, and $\Phi_{\delta F-\mu}$ represents field gradient-quadrupole interaction. The dominance of a specific interaction depends on the nature of adsorbate molecule and surface of the adsorbent. For a given adsorbent, the non-electrostatic energies are essentially proportional to polarizability of the adsorbate molecules [3]. The forces involved in chemisorption, however, are much stronger and involve a substantial degree of electron transfer or electron sharing, as in the formation of a chemical bond. As a result, chemisorption is highly specific and the adsorption energies are generally substantially greater than those for physical adsorption.

Several different models have been suggested to describe physical adsorption in microporous adsorbents. A more detailed discussion of the reliability of these models for different adsorbate-adsorbent systems can be found elsewhere [4]. Among these mathematical interpretations, the simplest one is single-site Langmuir model [4]:

$$C_A = \frac{C'_{H,A} b_A p_A}{1 + b_A p_A} \tag{2.13}$$

Where p_A is gas-phase equilibrium pressure (bar), C_A is the sorption capacity (mmol/g), $C'_{H,A}$ is the capacity constant (mmol/g), and b is the affinity constant (1/bar). In the pressure range where the product of affinity constant and equilibrium pressure is negligible compared with unity, single-site Langmuir model can be reduced to the Henry's law:

$$C_A = C'_{H,A} b_A p_A = K_A p_A \tag{2.14}$$

Where K_A is the Henry's constant, mmol/(g·bar).

Sorption in glassy polymer can be described by the dual mode model accounting for sorption in the densified region and non-equilibrium microvoids, which are usually referred to as the free volume. Sorption in the densified region can be described by the Henry's law and sorption in the free volume can be described by the Langmuir model. Therefore, dual mode model can be written as [1]:

$$C_A = C_{D,A} + C_{H,A} = k_{D,A} p_A + \frac{C'_{H,A} b_A p_A}{1 + b_A p_A} \tag{2.15}$$

Where $C_{D,A}$ accounts for sorption in the densified region and $C_{H,A}$ represents sorption in the microvoids. $k_{D,A}$ is the Henry's constant characterizing sorption in the densified region.

2.2.3 Diffusion

According to IUPAC, pores are classified into different categories based on their dimension [5]: macropores (d>50 nm), mesopores (2 nm<d<50 nm), micropores (d<2 nm), and ultramicropores (d<0.7 nm). Diffusion in porous adsorbents may be dominated by one or more of the following mechanisms: viscous flow, molecular diffusion, Knudsen diffusion, and activated diffusion [2]. The diffusion mechanism depends on the pore diameter relative to the size of diffusing molecules.

Diffusion in micropores and ultramicropores is usually an activated process, in which size of the diffusing molecule is comparable with dimension of the pore and gaseous phase transport is not limiting. Inside these tiny pores, diffusion proceeds by a sequence of jumps. Since diffusing molecules never escape from the force field of pore surface atoms, the fluid within these pores can be considered as a single adsorbed phase [2]. Diffusion of this type is called intracrystalline diffusion or micropore diffusion. Its diffusivity can be referred to as intracrystalline diffusivity or micropore diffusivity.

It is transport diffusion (or diffusive transport) that leads to net transfer of mass inside a porous adsorbent, which is based on chemical potential gradient and should be

distinguished from self-diffusion, in which movement of molecules occur by random (Brownian) motion without the need of an external driving force. Transport diffusivity in microporous adsorbents is dependent on loading of the diffusing molecule [6]:

$$D = D_0 \frac{d \ln p}{d \ln C(p)} \tag{2.16}$$

where D (cm^2/s) is the loading-dependent transport diffusivity, D_0 (cm^2/s) is the thermodynamically corrected diffusivity, $C(p)$ (mmol/g) is the amount adsorbed, and p (bar) is the gas-phase equilibrium pressure. Therefore, D/D_0 is dependent on the non-linearity of the adsorption isotherm. Generally, assuming that the adsorption isotherm is described using the Langmuir model (equation 2.13), it will be easy to obtain the following relationship [6]:

$$D = \frac{D_0}{1-\theta} \tag{2.17}$$

Where $\theta = C(p)/C_s$ is the surface fractional coverage.

Unlike microporous adsorbents, no permanent pores exist in dense glassy polymer membranes, and diffusion is based on random jumps of penetrant molecules through thermally activated transient gaps in the polymer matrix. Diffusion in in dense glassy polymers is illustrated in Figure 2.2.

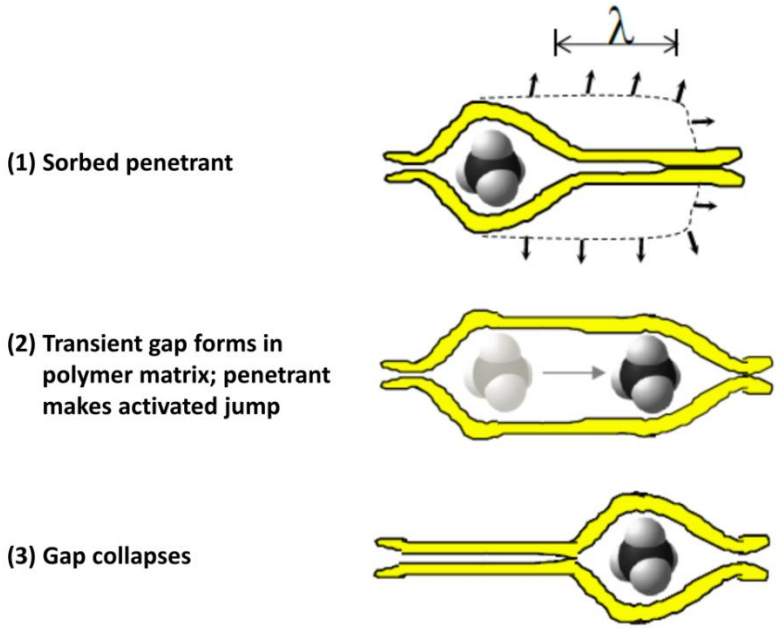

Figure 2.2: Schematic illustration of diffusion in polymer by transient gap formation. λ is the average length of diffusion jump [7].

2.2.4 Transport in Mixed-Matrix Materials

Reliable estimation of permeability in mixed-matrix materials is crucial to proper selection of mixed-matrix membrane materials, i.e., the polymer and molecular sieve. The Maxwell model is probably the simplest and most widely used mathematical description of gas transport in mixed-matrix materials. The model was initially derived by James C. Maxwell in 1867 to describe dielectric properties in a conducting dilution suspension of identical particles, and is used to describe gas transport in mixed-matrix materials based on the close analogy between electrical conduction and gas permeation. Maxwell model is given by [8]:

$$P_{MMM} = P_p \left[\frac{P_s + 2P_p - 2\Phi_s(P_p - P_s)}{P_s + 2P_p + \Phi_s(P_p - P_s)} \right] \tag{2.18}$$

where P_{MMM} is permeability in the mixed matrix material; P_p is permeability in the polymer matrix; P_s is permeability in dispersed molecular sieve particles; and Φ_s is volume fraction of molecular sieve particles in the mixed matrix material.

The Maxwell model provides a simplified description based on the assumption that a dilute suspension of spherical particles is uniformly dispersed in the matrix so that diffusion around any particle is not disturbed by the presence of others. This assumption may seem to be very limiting in mixed-matrix membranes, and there have been substantial investigations on more sophisticated models accounting for high particle loading and non-ideal particle-matrix interfaces [9]. Recent computational studies by Minelli and co-workers showed that the Maxwell model could be quite reliable at particle loading far beyond the value limited by its assumptions. And it will be experimentally demonstrated in Chapter 5 and 6 that the Maxwell model is indeed quite useful to design mixed-matrix membranes by predicting transport properties.

2.3 Zeolites and Zeolitic Imidazolate Frameworks

Aluminosilicate zeolites and their structural analogs (e.g. aluminophosphates, silicoaluminophosphates, and titanosilicates, etc.) represent an extremely important class of crystalline porous materials that is of particular interest for the petrochemical industry. Zeolites are composed of TO_4 tetrahedra (T=Si, Al) linked together by sharing Oxygen ions. Replacement of Si with Al makes the framework negatively charged and therefore

requires the introduction of extra-framework cations such as sodium, potassium, magnesium, and calcium [2].

The heterogeneously charged surface of aluminosilicates offers them unique adsorption properties that have been taken advantage of for equilibrium selectivity-based separations. For example, Lithium cation-exchanged zeolite X adsorbs nitrogen much stronger than oxygen due to interaction between quadrupole moments of nitrogen molecules and charge gradient on surface of the zeolite [3]. In addition to unique surface chemistry, zeolite's ordered crystal network and uniform microporous or ultramicroporous structure offer them great opportunities for size/shape-selective separations. Based on the pore size, zeolites and their analogs are categorized into large pore twelve ring zeolites (e.g. zeolite X and Y), medium pore ten ring zeolites (e.g. zeolite MFI), and small pore eight ring zeolites (e.g. zeolite A and DDR) [6]. As the zeolite pore size approaches the dimension of the diffusing molecule, activated diffusion becomes the dominant mechanism for mass transfer inside the zeolite network and the intracrystalline diffusivity is strongly dependent on the size and shape of the diffusing molecule. Remarkable and in some cases, infinite diffusion selectivity can be achieved for molecules that are slightly different in size and shape. Studies on transport and self-diffusivities in zeolites were reviewed by Karger et al [6, 2].

Metal-organic frameworks (MOFs) are a new class of crystalline porous materials comprising metal ions or metal oxide clusters coordinated by organic linkers to form one, two, or three-dimensional porous networks. Zeolitic imidazolate frameworks (ZIFs) are a

subclass of MOFs constructed by tetrahedrally coordinated transition metal ions (M, e.g. Zn and Co) bridged by imidazole linkers (IM). Since the angle of M-IM-M of ~145^{o} is close to the angle of T-O-T found in zeolites, ZIFs are able to follow different zeolitic topologies (such as SOD, LTA, and CHA) [10-11]. Compared with zeolites, ZIFs' more diversified building units (transition metal and imidazole linkers) offer them flexibility to be tailored for a particular separation.

Literature on the topic of MOFs/ ZIFs has expanded rapidly in the last few years focusing on material synthesis, structure-property relationships and their potential applications for gas and vapor separations [12-33]. Zeolitic imidazolate framework-8 ($Zn(MeIM)_2$, MeIM=2-methylimidazole) is one of the most extensively studied ZIF material that features excellent thermal and chemical stability [10]. Its structure and building units are shown in Figure 2.3 together with its zeolitic counterpart sodalite. While ZIF-8 and zeolitic sodalite share the same framework topology (SOD), ZIF-8's larger and flexible six-ring aperture enables the sorption of many practical gases, and consequently many opportunities for gas separations and purifications.

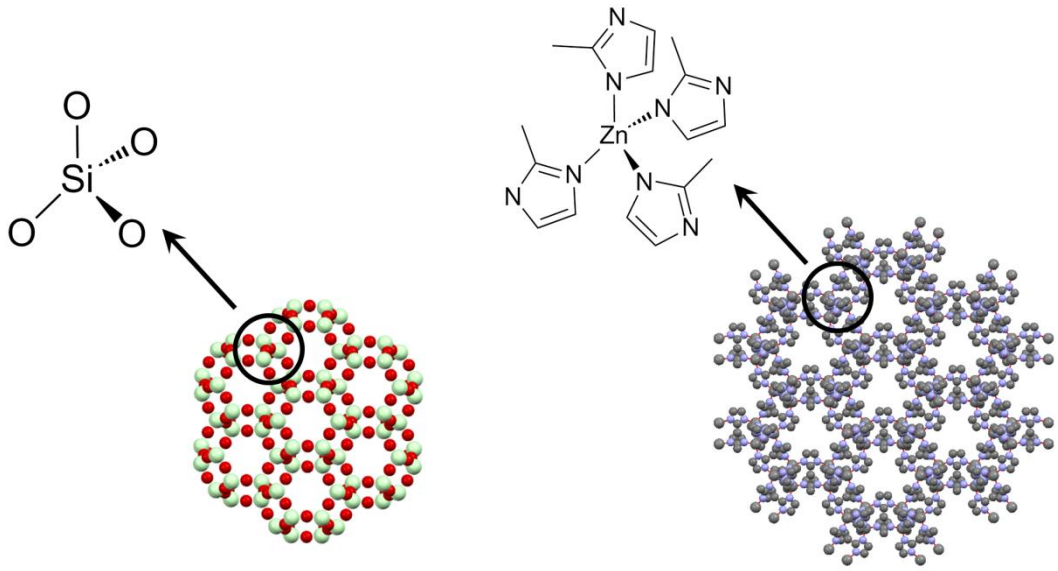

Figure 2.3: Crystal structure of sodalite zeolite (left) and ZIF-8 (right).

2.4 Asymmetric Hollow Fiber Membrane

Practical gas separations require membrane area that is orders of magnitude larger than what can be synthesized in standard labs. This is especially true for bulk separations in the refinery/petrochemical industry. The olefin/paraffin processing capacity of a typical olefin plant can be as high as 500 million scfd [34]. To get the challenging task done with reasonable membrane production costs and minimized equipment footprints, this huge membrane area must be efficiently packed into membrane modules. Hollow fiber is the most desirable membrane geometry in terms of membrane packing efficiency. Depending on outer diameter (OD) of the fiber, the packing density of hollow fiber modules, as shown in Figure 2.4, can be at least one order of magnitude higher than the less desired plate-frame and spiral wound modules.

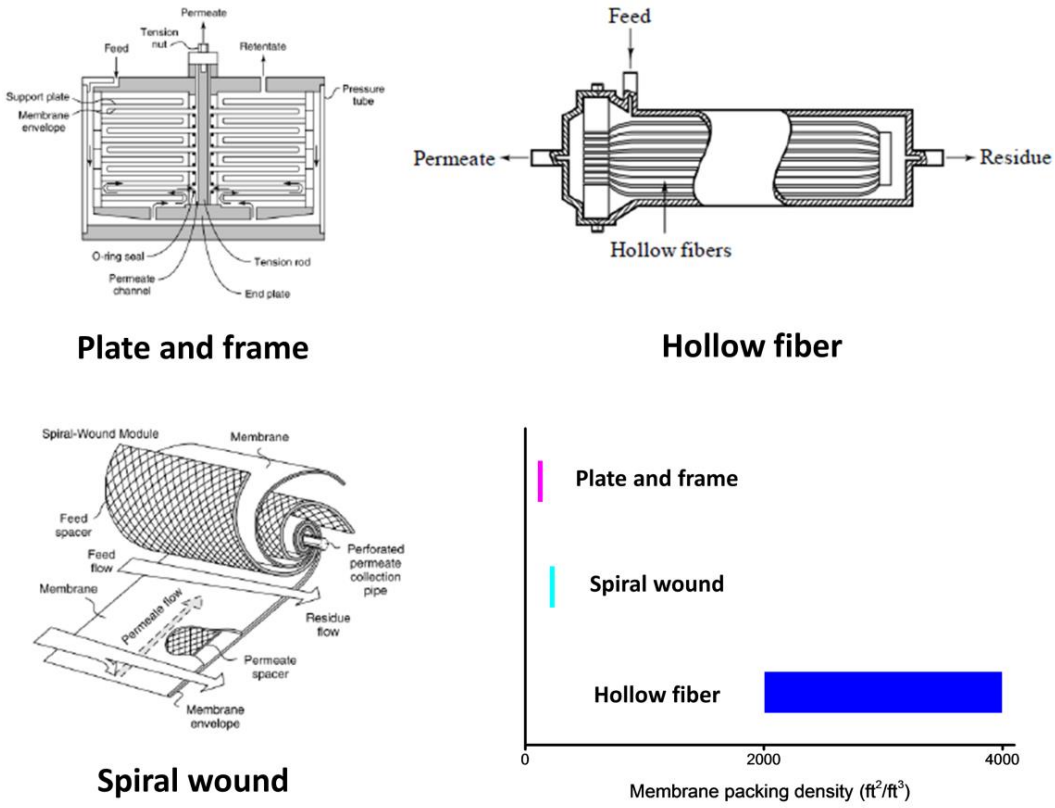

Figure 2.4: Schematic illustration of several membrane modules [34] and comparison of membrane packing density [7].

The asymmetric structure of polymeric hollow fiber membrane is shown in Figure 2.5, which is composed of a dense and thin skin layer at the outside surface supported by underneath porous substrate. The dense skin layer is nonporous and is the selective part of the hollow fiber with a thickness that is usually less than 1% of the fiber wall thickness. The much thicker porous substrate provides structural integrity of the device and preferably should not add significant mass transfer resistances to gas transport. Hollow fiber membrane can be either single-layer (monolithic hollow fiber) or dual-layer (composite hollow fiber). Single-layer hollow fibers are formed by coextruding the

spinning dope and the bore fluid using a monolithic spinneret with two annular channels (dope channel and bore fluid channel). Consequently, the dense skin layer and porous substrate layer are made of the same type of polymer.

Dual-layer hollow fibers are spun by coextruding two spinning dopes (sheath dope and core dope) and the bore fluid from a composite spinneret with three annular channels (sheath dope channel, core dope channel, and bore fluid channel). If the sheath layer polymer is inexpensive, the core layer polymer is usually the same type of polymer. In the case that sheath layer polymer is too expensive to constitute the entire fiber, a different polymer, usually commercially available and inexpensive should be used to form the core layer. Such composite structure lowers the material cost of the device and also allows the possibility to individually tailor the properties of selective skin layer and porous substrate [35]. The inside core spinning dope may be optimized to obtain excellent spinnability and desirable fiber macroscopic properties. The outside sheath dope may be formulated for skin formation, and if necessary, with somewhat compromised spinnability.

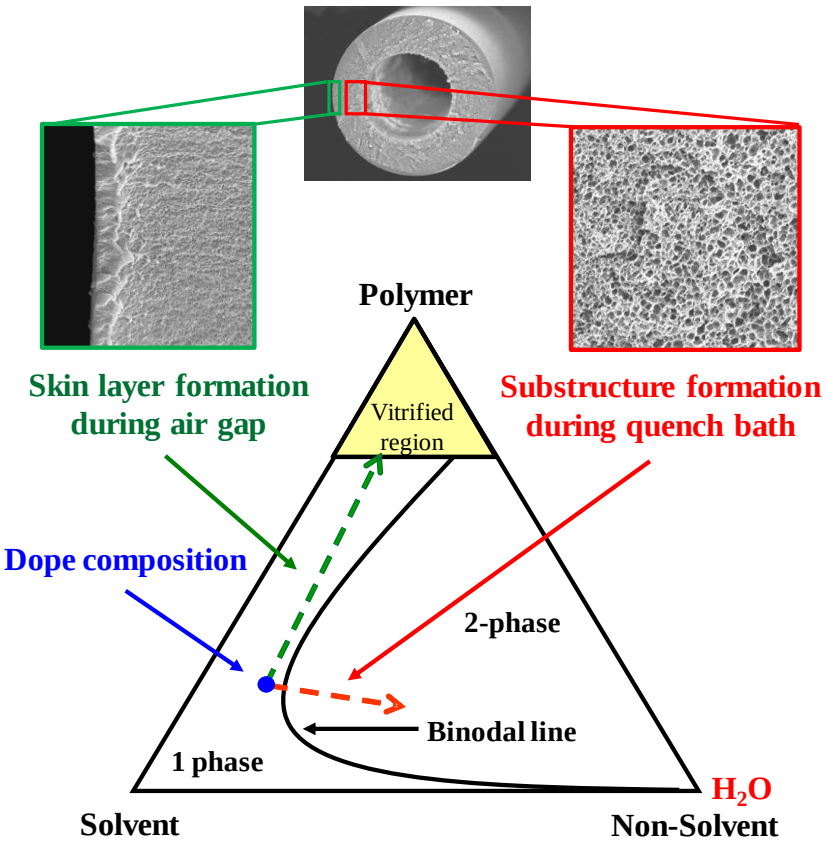

Figure 2.5: Structural illustration of ternary diagram showing formation of asymmetric hollow fiber membrane.

The dual-layer configuration is particularly attractive in the case that the polymer of the separation layer is expensive, and using an inexpensive polymer as the substrate will significantly reduce membrane cost without compromising membrane separation performance. Formation of dual-layer hollow fibers is, however, more complex than single-layer hollow fibers and special attention needs to be paid to the compatibility of the sheath layer polymer and core layer polymer to avoid undesirable interfacial delamination that may undermine the device's mechanical properties.

2.4.1 Formation of Asymmetric Hollow Fiber Membranes

Asymmetric hollow fiber membranes can be formed by the dry-jet/wet-quench spinning process. The set-up to spin single-layer hollow fibers is illustrated in Figure 2.6. Polymer solutions (dopes) and bore fluid are coextruded through a spinneret into the air gap (dry-jet) and then into an aqueous quench bath (wet quench) where polymer solution solidifies due to phase separation prior to being collected on a take-up drum.

The spinning parameters that determine the morphologies and transport properties of the hollow fiber membranes were extensively discussed by previous researchers [35-38] and are listed in Table 2.1. Generally, higher spinning temperature, lower environment humidity, longer air gap residence time, cooler quench bath, and higher concentration of volatile in the spinning dope tend to aid the formation of dense fiber skin with minimized defects.

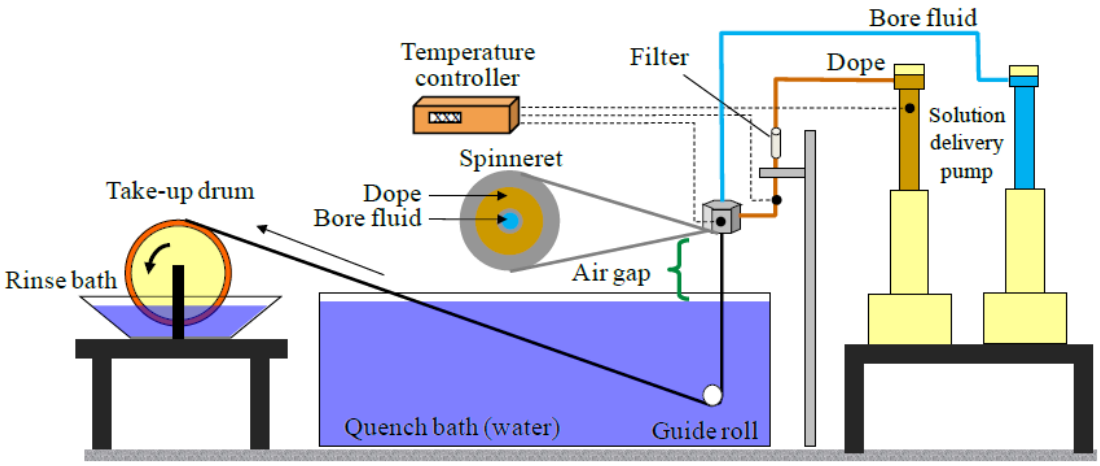

Figure 2.6: Dry-jet/wet-quench set-up for spinning single-layer hollow fiber membranes [7].

Fiber spinning dopes usually comprise polymer, solvent, and non-solvent. In the case of mixed-matrix fiber spinning, adsorbent particles are added as well. The qualitative dope composition trajectories during the skin layer and the substructure formation are shown on the thermodynamic isothermal ternary phase diagram in Figure 2.5. The ternary phase diagram is usually constructed via the cloud point technique by using a chosen dope polymer concentration with increasing non-solvent amounts (and accordingly decreasing solvents amount) to achieve a constant polymer weight fraction to avoid changing too many variables [39]. In this technique, with increasing non-solvent amount, the final dope can be seen to change from one-phase into two-phase. The compositions at different polymer concentrations on the phase boundary are called "cloud points", and these points together form the binodal line. The dope composition should be in the one phase region and close to the binodal line to facilitate rapid phase separation in the quench bath. In the meantime, sufficiently high viscosity is required for the spinning dope so that it can withstand high extensional forces when being drawn at high take-up rates. Such property is usually referred to as "spinnability".

Table 2.1: Factors that determine the quality of hollow fiber membrane [7]

Dope compositions	Air gap height
Environment humidity	Fiber take-up rate
Flow rate of dopes	Spinning temperature
Quench bath temperature	Quench bath composition

When the dope is extruded through the air gap, evaporation of the volatile solvents and non-solvents causes the composition of the outermost region to approach the vitrified region. This composition pathway is believed to assist skin formation. When the fiber reaches the quench bath, water (non-solvent) diffuses into the nascent fiber and brings the composition of the underlying substrate into the two phase region where the dope phase separates and forms a porous substructure without causing vitrified skin layer defects [7]. The fiber take-up rate is usually larger than the linear extrusion rate of the spinning dope and allows the fibers to be drawn down to significantly smaller dimension than the size of the spinneret orifice [35]. The bore of the hollow fiber is created by extruding a bore fluid along with the dope. The bore fluid is a neutral fluid which takes up space and prevents the nascent fiber from collapsing during spinning. In this way, dry-jet/wet-quench spinning results in the desirable asymmetric morphology, a dense selective skin layer with a porous substructure underneath.

2.4.2 Formation of Dual-Layer Mixed-Matrix Hollow Fiber Membrane

Mixed-matrix hollow fiber membrane can be formed by the same dry-jet/wet-quench technique discussed above, however, with several critical modifications. Mixed-matrix hollow fiber membrane is best to be realized on the platform of the above mentioned dual-layer hollow fibers with molecular sieve particles dispersed only in the sheath layer as illustrated in Figure 2.7 (C). This is because that in the single-layer hollow fiber configuration shown in Figure 2.7 (B), the majority of the expensive molecular sieve particles will be wasted since they cannot enhance membrane separation performance in the porous substrate. The polymer used for the sheath is usually a high-

performance polymer with superior gas separation performance, which is usually more expensive. Since the porous core layer only provides mechanical strength of the fiber, it can be formed with a relative inexpensive commercial polymer such as cellulose acetate or Matrimid®.

Mixed-matrix hollow fiber membrane is not to be confused with hollow fiber sorbents [40] shown in Figure 2.7 (A), which are also formed by dispersing adsorbent particles in a polymeric hollow fiber matrix. Hollow fiber sorbents are a type of sorbent realized in the hollow fiber geometry and is not a membrane. Despite that hollow fiber sorbents are spun using the similar set-up shown in Figure 2.6, the spinning dope and spinning parameters are manipulated so that no dense skin forms at fiber surface and the entire fiber is porous. Also the polymer used for hollow fiber sorbents are usually inexpensive commercial polymer since the polymer matrix only provides mechanical support for the device.

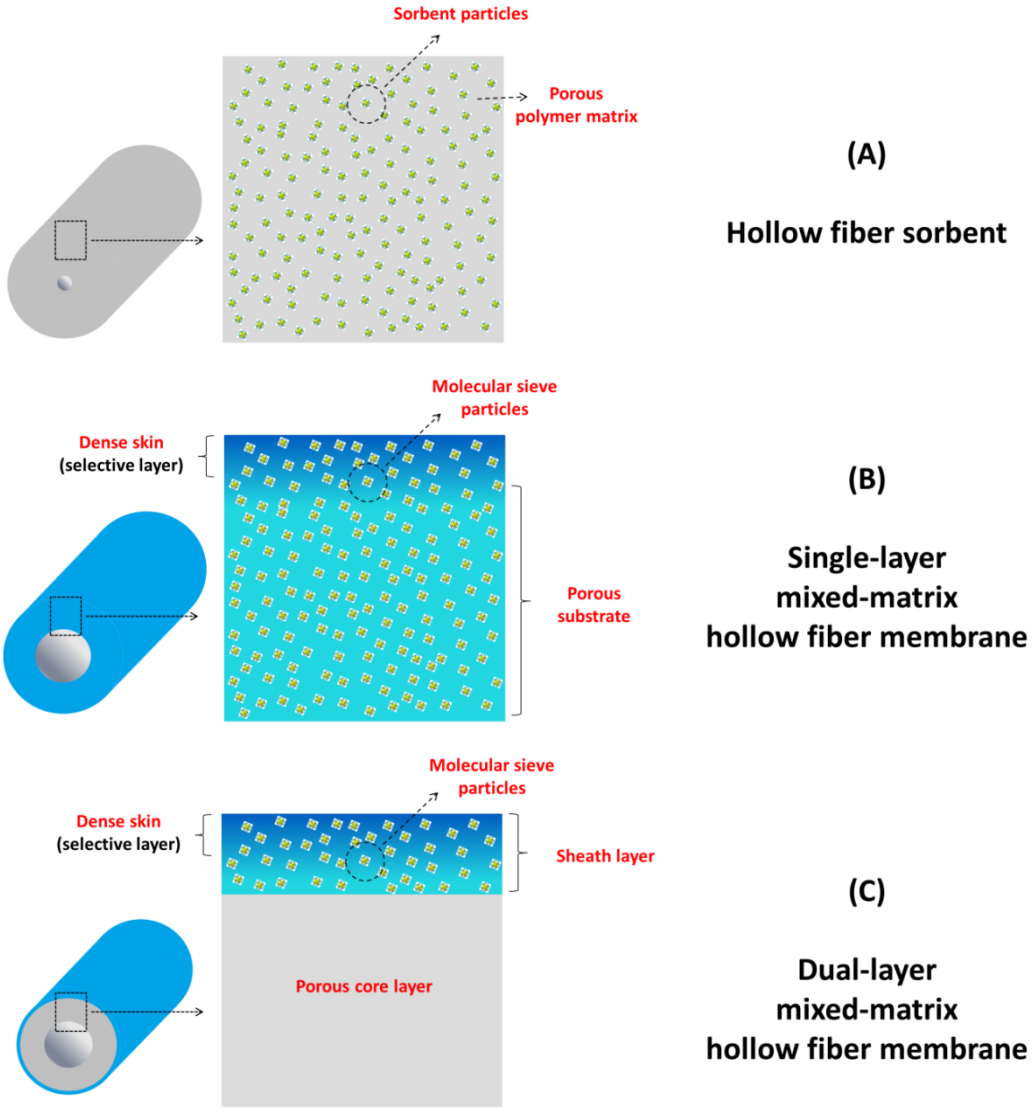

Figure 2.7: Structural illustration of (A) hollow fiber sorbent, (B) single-layer mixed-matrix hollow fiber membrane, and (C) dual-layer mixed-matrix hollow fiber membrane. The blue region indicates a high-performance and expensive polymer. The grey region suggests a commercially available polymer that is usually inexpensive. For hollow fiber sorbent, the entire fiber is porous. For hollow fiber membrane, the skin layer is dense and the rest of the structure is porous. The bore of hollow fiber sorbent is smaller to maximize sorbent loading.

The thickness of the sheath layer can be adjusted by controlling the relative flow rate of the sheath dope and core dope during fiber extrusion. Ideally, to minimize the membrane materials cost, the sheath layer should consist of a very small portion (<10%) of the fiber wall, usually only several microns. To make this possible, nano-sized molecular sieve particles are preferred over micron-sized molecular sieve particles. Figure 2.8 illustrates the set-up for dual-layer mixed-matrix hollow fiber membrane. A composite spinneret with three annular channels (sheath dope channel, core dope channel, and bore fluid channel) must be used. Compared with the set-up in Figure 2.6, a third pump was added to pump the sheath dope into the spinneret.

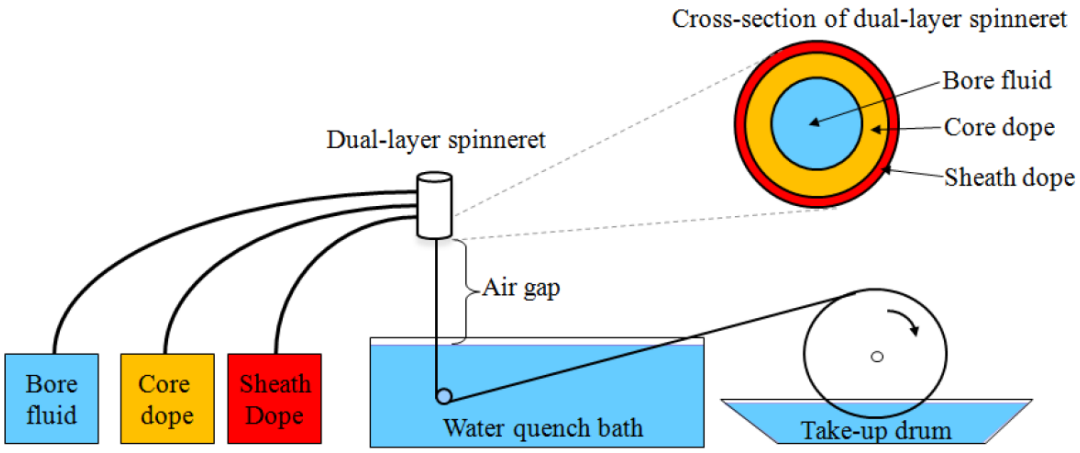

Figure 2.8: Dry-jet/wet-quench set-up for spinning dual-layer hollow fiber membranes [41].

The sub-micron skin of mixed-matrix hollow fibers is formed at the surface of the sheath layer as volatile components in the sheath dope evaporate in the air gap. The spinning parameters should be manipulated so that the thickness of the dense skin layer is

no larger than the thickness of the sheath layer. This is because that selectivity of the core layer polymer is usually inferior to that of the mixed-matrix sheath layer and any mass transfer resistance from the core layer will undermine the overall selectivity of the membrane. Composition of the sheath dope containing molecular sieve particles is critical to formation of high-quality dual-layer mixed-matrix hollow fiber membrane with integral skin layer and desirable separation performance. The dope composition, however, cannot be conveniently optimized using the above mentioned cloud point technique since the dispersed particles make the dope opaque even in the one phase region. An empirical approach was used in this research to determine the composition of the mixed-matrix sheath dope, which will be discussed with detail in Chapter 7.

2.5 Challenges to Develop Scalable Mixed-Matrix Membranes

Figure 2.9 shows the critical issues that must be addressed to provide a commercially viable membrane product for gas separations, i.e. material selection, membrane formation, module design and system configurations. Membrane scientists/engineers are in charge of material selection and membrane formation, while the job of module design and system configuration often falls into the responsibility of mechanical and process engineers. Proper selection of membrane materials with superior intrinsic permeability and selectivity is certainly crucial to achieve this goal. Additionally, the raw membrane materials must be fabricated into a defect-free membrane with practical permeance in a geometry that can be economically scaled up for commercial implementations.

The first decade of 21st century has seen significant progress in the development of advanced membrane materials for gas separations, many of which have demonstrated lab-scale performance that are either superior to commercialized membrane separators or promising to open new opportunities such as hydrocarbon separations and CO_2 capture. However, the update rate of commercial membranes is unparalleled with fast development on membrane materials and today's gas separation membrane market is still limited to air separation, acid gas removal from natural gas, H_2 purification, and organic vapor recovery. This is due partially to the conservative nature of the industry and partially to many technical challenges to economically scale up the advanced membranes with consistent and stable separation performance under realistic operating conditions.

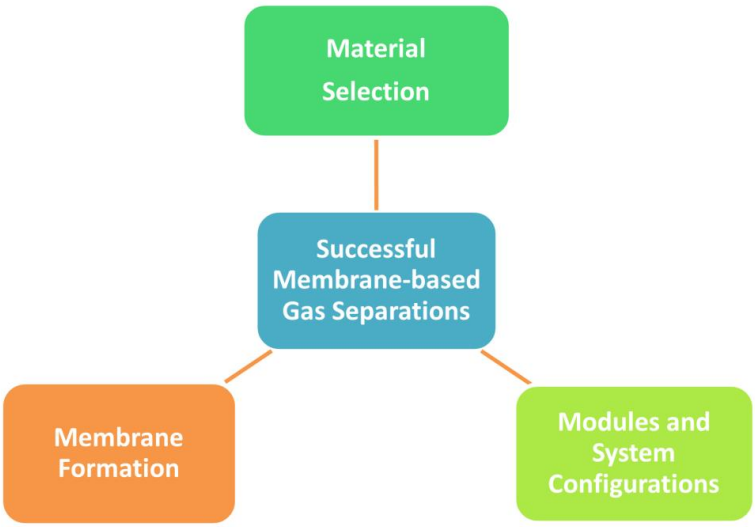

Figure 2.9: Critical issues controlling successful membrane-based gas separation [1].

Research on mixed-matrix membranes has been continuing since the 1980's and received increasing attention in the last couple of years, as shown by the statistics in Figure 2.10. Although material selection represents a very important aspect of membrane research, processing the materials to fabricate hollow fiber membranes constitutes another important aspect. However, the majority of research work on mixed-matrix membranes has been strongly focusing on membrane materials and making small dense films. Much less efforts were made to fabricate the mixed-matrix materials into practical membrane geometry with only a few studies extended to hollow fibers. Accordingly, today no commercial mixed-matrix membrane exists for gas separation applications.

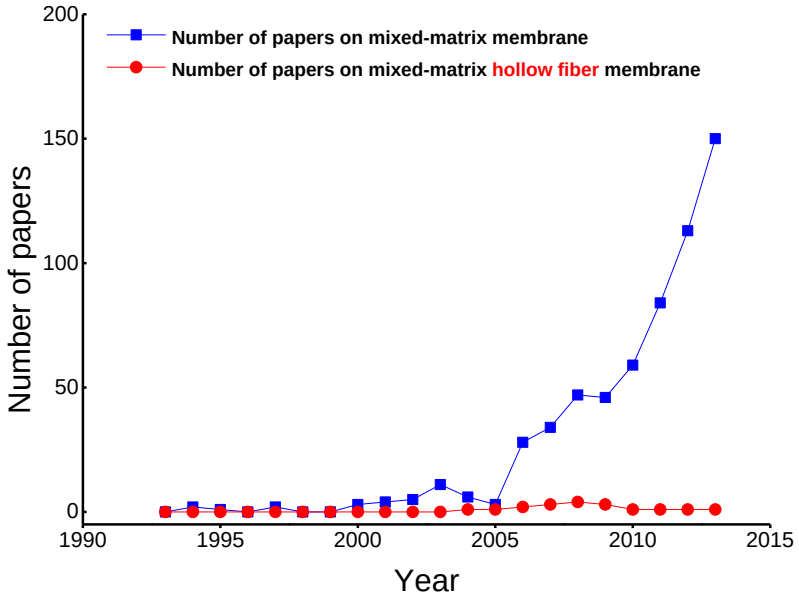

Figure 2.10: Statistics of research articles on the subject of mixed-matrix membranes. (Data from Science Citation Index)

This research identifies desirable properties of practical mixed-matrix membranes realized in the hollow fiber geometry. For a simple proof-of-concept, the mixed-matrix hollow fiber membrane should possess the following basic properties to show consistent selectivity with dense film membrane and to be "*conceptually feasible*":

(1) Dual-layer hollow fiber with particles only in the sheath layer

(2) Excellent particle-polymer adhesion

(3) Generally well-dispersed particles with minimal agglomerations

(4) Integral skin layer with minimal skin defects

(5) Uniform fiber wall thickness with porous substrate free of macrovoids

Additionally, in order to make the mixed-matrix hollow fiber membranes *"economically attractive"*, some additional features that are more challenging must be achieved beyond items (1)-(5):

(6) Generally well-dispersed nano-sized particles with minimal agglomerations

(7) Sufficiently high particle loading to show economically attractive selectivity

(8) Minimized skin thickness (<200-500 nm) to enable higher permeance and minimized sheath layer thickness (<1-5 micron) to minimize membrane material cost

(9) Inexpensive polymer as fiber core layer with excellent inter-layer adhesion between sheath layer and core layer

(10) Hollow fine fibers (fiber outer diameter (OD)<150-300 micron) collected at high take-up rates (>50 m/min) to achieve higher membrane packing density

As shown in Figure 2.10, only a few journal articles and patents reported fabrication of mixed-matrix hollow fiber membranes. Several pioneering works explored items (1)-(5) and (9) using commercial polyimides [42-44]. The particle loading in these mixed-matrix hollow fibers was generally low (up to 15 wt %) and moderately enhanced selectivity was achieved for separation of CO_2/CH_4 and O_2/N_2. No data on olefin/paraffin separations were reported. Due to limited breakthroughs in items (1)-(5), the more advanced items (6)-(10) have essentially remained untouched (except item (9)). The major technical challenges to form high-performance, high-loading mixed-matrix hollow fiber membranes satisfying items (1)-(10) are discussed below:

(1) The challenge to achieve ideal particle-polymer interfacial adhesion.

Ideal particle-matrix interface refers to adsorption of polymer chains on particle surface with interfacial polymer chain packing density identical with the bulk polymer phase. Ideally, with properly selected polymer matrix and molecular sieve and this ideal particle-matrix interface, the hybrid membrane is supposed to become both more permeable and more selective than the polymer matrix. However, any deviations from the ideal particle-matrix interface may lead to non-idealities and experimental transport properties that are inconsistent with theoretical values. These non-idealities have been studied and categorized by previous researchers, which are (1) sieve in a cage (2) leaky interface (3) matrix rigidification (4) plugged sieve.

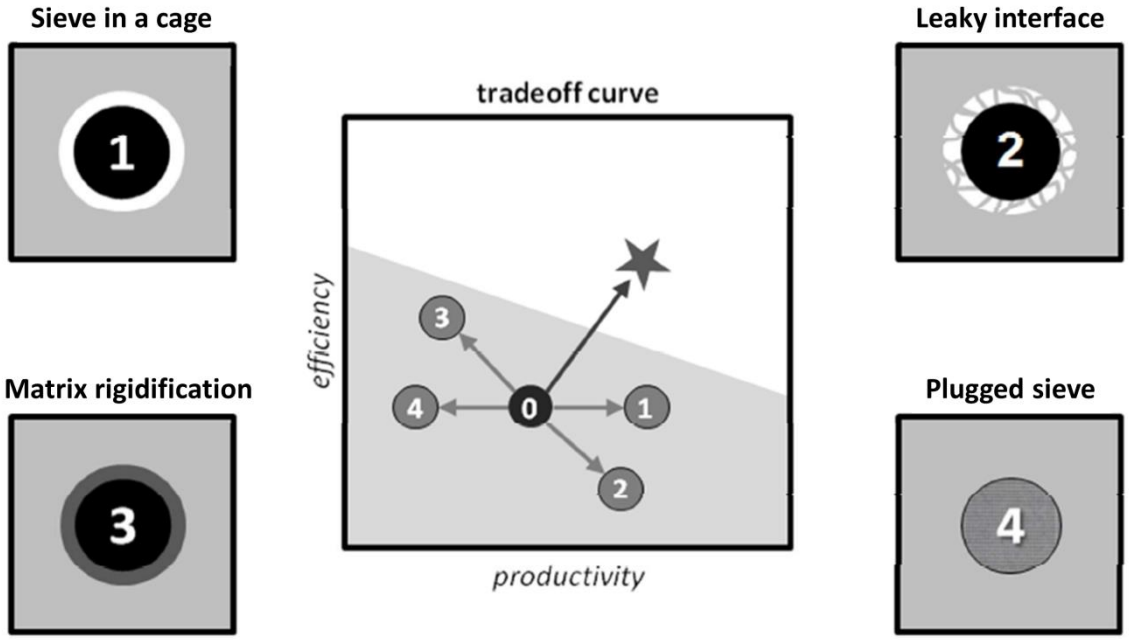

Figure 2.11: Non-ideal interfacial morphologies of mixed-matrix materials and their influences on membrane transport properties.

Schematic illustration and typical permeation behaviors introduced by these non-ideal situations are shown in Figure 2.11. "Plugged sieve" happens when the sieve particles are not properly activated or the aperture of the sieve particles is so small that penetrants molecules are totally excluded from their internal network. This typically results in a hybrid membrane with permeability lower than the polymer matrix with unchanged selectivity. "Matrix rigidification" applies to the case that polymer chains pack more densely at the particle surface than in the bulk polymer. When this happens, permeability of the hybrid membrane becomes lower than the theoretical value.

On the contrary, a "leaky interface" happens if polymer chains pack less densely at the particle surface than in the bulk polymer, and selectivity of the hybrid membrane

will become lower than the theoretical value. This is because that the dilated region around the particles is much less selective than the bulk polymer phase. An extreme case of "leaky interface" is named "sieve in a cage". This applies when polymers chains are completed peeled off from the particle surface to create an essentially void area around the particles. These voids, although non-selective, add no mass transfer resistance to permeation, therefore they will not affect selectivity of the polymer matrix. The "sieve in a cage" morphology had been the largest obstacle to advance mixed-matrix membranes into practical applications. It had been spotted in many, if not all, mixed-matrix membranes based on zeolites and high T_g glassy polymers. The backbones of high T_g glassy polymers are very rigid, and their hydrocarbon-based chemistry makes them poorly compatible with the inorganic zeolite's hydrophilic surfaces. A SEM image of "sieve in a cage" morphology is shown in Figure 2.12.

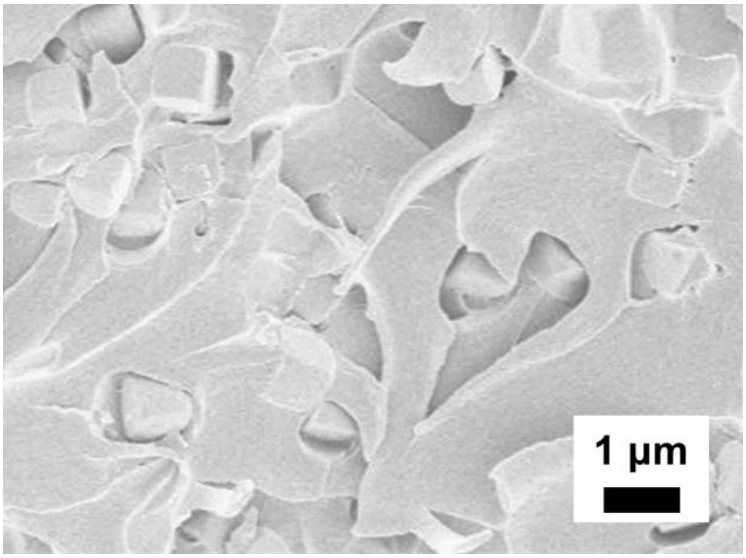

Figure 2.12: "Sieve in a cage" morphology observed in zeolite 4A/6FDA-6FpDA mixed-matrix membrane.

A great deal of efforts has been made to eliminate the "sieve in a cage" morphology by improving the compatibility between hydrophilic zeolite particles and hydrophobic glassy polymers with rigid backbones, such as silanation treatment [43, 38] and Grignard surface treatment [38, 45, 8]. In some cases, the surface treatment works quite well to improve the particle-matrix adhesion and to enhance the selectivity of the mixed-matrix membrane. However, these additional steps usually make the membrane preparation process very complex and may not be practical for large-scale applications. Also, it appeared that the effectiveness of these surface treatments is highly sensitive to surface chemistry of the particles [45] and a universally effective surface treatment approach has not been identified. In this research, the problem of non-ideal "sieve in a cage" morphology was successfully addressed, however not by treating the surface of the inorganic zeolite particles, but by using a new type of molecular sieve that can perfectly adhere with glassy polymer without any surface treatment. ZIFs are organic-inorganic hybrid materials with organic moieties in the framework. Consequently, ZIFs' partially hydrocarbon-based chemistry makes them intrinsically compatible with organic glassy polymers.

(2) The challenge to uniformly disperse high concentration of nano-sized particles in the polymer matrix.

To form a mixed-matrix membrane, the molecular sieve particles are usually dispersed in an organic solvent before being mixed with polymer powders or a polymer dope. Nano-sized particles are preferred to micron-sized particles for the purpose of minimizing membrane thickness. However, nano-sized particles, especially at high concentrations, tend to agglomerate more seriously due to their much higher surface

energy. The agglomerates in the fiber spinning dope, if sufficiently large, may plug the narrow channel of spinneret and result in ununiformed fibers. If ended up in the fiber skin layer, they can be detrimental to selectivity of the membrane by introducing skin defects, in the case that their dimension is larger than or comparable with the thickness of fiber skin layer. Figure 2.13 shows formation of fiber skin defects caused by large particle agglomerates.

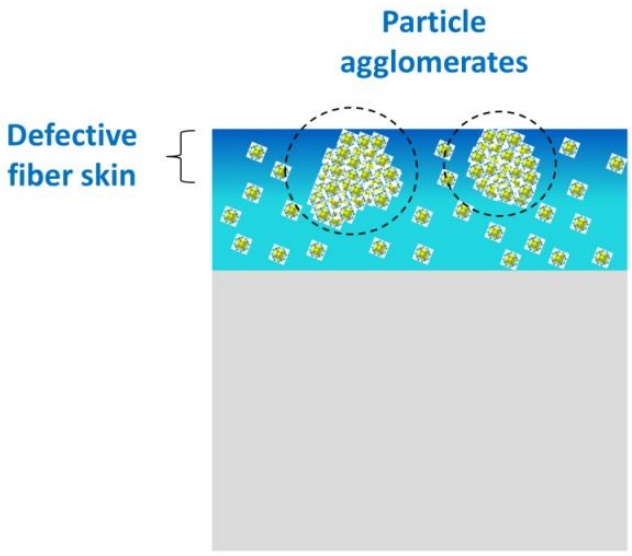

Figure 2.13: Schematic illustration of skin defects formation caused by large particle agglomerates.

The concentration of particle agglomerates can be reduced by applying high shear forces (using high shear mixer) or vibrational forces (using sonication bath or horn) to the particle dispersion [46]. However, at times, agglomerates formed by small nano-particles are quite difficult to be broken even under high shear or vibrational forces. Additionally, intensive sonication may undesirably change the morphology of the particles (e.g. Ostwald ripening [47]), if the heat generated by the sonication is not efficiently removed

from the system. In addition to high shear and vibrational forces, a multistep polymer addition procedure (usually referred to as "priming") [48] can be used to stabilize the particle dispersion and reduce agglomerations. In priming, a very dilute polymer solution is added to the particle dispersion to coat a very thin layer of polymer on particle surface to keep them from "stick" with each other.

(3) The challenge to spin high-loading mixed-matrix hollow fiber membranes and to minimize fiber skin thickness without creating undesirable defects.

As mentioned above, a few studies succeeded in formation of mixed-matrix hollow fiber membranes with moderate selectivity enhancements, at low particle loadings. Without significant advancements in materials science, high-loading mixed-matrix hollow fiber membrane with more aggressive selectivity enhancements must be made to be commercially attractive and competitive with other separation options. Formation of high-quality, high-loading mixed-matrix hollow fiber membrane is quite challenging, and actually, has never been reported. Generally, it is believed that sufficiently high polymer concentration in the spinning dope is necessary to form of an integral skin with minimized defects and consistent selectivity [43]. This poses a challenge to the processability of mixed-matrix hollow fiber membranes since the addition of particles, especially at high concentration, significantly increase the viscosity of the fiber spinning dope. This will not only make it more difficult to make the dope homogeneous during dope preparation, but also requires a higher spinning temperature to extrude the dope from the spinneret [2].

Theoretically, by reducing fiber skin thickness, a highly productive and highly selective hollow fiber membrane can be formed using a highly selective polymer with moderate or even low permeability. However, practically, there is a limitation of the minimum skin layer thickness. As the fiber skin becomes thinner, the probability of fiber skin defects increase dramatically [1]. For high-loading mixed-matrix hollow fiber membrane, it is even more challenging to optimize fiber skin layer thickness. Fiber skin formation is a very complicated process involving many variables and the effects of particles on skin formation is still not very well understood. Obviously the skin has to be at least thicker than the dimension of a single particle. Also, while the number of particle agglomerates can be reduced, they can hardly be completed eliminated. Actually even the particles are uniformly dispersed in the spinning dope, they may agglomerate during dope extrusion from the narrow spinneret channels, owing to high shear stress [43].

(4) The challenge to balance fiber microscopic properties with macroscopic properties

Among the fiber properties described above, item (2)-(4) and (6)-(8) are related to fiber skin formation and are referred to as fiber *microscopic* properties. On the other hand, item (1), (5), (9), and (10) are referred to as fiber *macroscopic* properties. These properties are determined by spinning dope compositions and spinning parameters. It is difficult to isolate one variable from others since there is a complex interplay between dope rheology, mass transfer, and thermodynamics [35].

Very often changing one variable may lead to more desirable microscopic properties but will limit the degree of freedom to tune macroscopic properties, and vice versa. For example, it was suggested that [49] longer air gap residence time and cooler quench batch will help to achieve more desirable sheath/core inter-layer adhesion. However, this will inevitably increase fiber skin thickness and limit the maximum fiber take-up speed and minimum fiber OD. For neat polymer hollow fiber membrane, this conflict may be conveniently resolved by optimizing spinning dope composition (such as adding $LiNO_3$ and increasing volatile component concentration) and other spinning parameters (such as increasing spinneret temperature). However, for mixed-matrix hollow fiber membranes, especially at high particle loading, fiber skin integrity may be more sensitive to changes in these variables. Accordingly, the "window" allowed to tailor fiber skin thickness and control fiber skin integrity is smaller, and it may be more challenging to obtain simultaneously desired fiber microscopic and macroscopic properties.

2.6 References

[1] W. J. Koros and G. K. Fleming, "Membrane-based gas separation" *Journal of Membrane Science* **1993**, *83*, 1-80.

[2] J. Karger, D. M. Ruthven and D. N. Theodorou, *Diffusion in Nanoporous Materials*, John Wiley & Sons, Ltd, **2012**

[3] R. T. Yang, *Adsorbents: Fundamentals and Applications*, John Wiley & Sons, Inc., **2003**

[4] H. G. Karge and J. Weitkamp, *Adsorption and Diffusion*, Springer-Verlag Berlin Heidelberg, **2008**

[5] G. Leofanti, M. Padovan, G. Tozzola and B. Venturelli, "Surface area and pore texture of catalysts" *Catalysis Today* **1998**, *41*, 207-219.

[6] J. Karger and D. M. Ruthven, *Diffusion in Zeolites and Other Microporous Solids.*, John Wiley & Sons, Inc., **1991**

[7] C.-C. Chen, PhD Dissertation, Georgia Institute of Technology, 2011.

[8] S. Shu, PhD Dissertation, Georgia Institute of Technology, 2007.

[9] H. Vinh-Thang and S. Kaliaguine, "Predictive Models for Mixed-Matrix Membrane Performance: A Review" *Chemical Reviews* **2013**, *113*, 4980-5028.

[10] K. S. Park, Z. Ni, A. P. Cote, J. Y. Choi, R. Huang, F. J. Uribe-Romo, H. K. Chae, M. O'Keeffe and O. M. Yaghi, "Exceptional chemical and thermal stability of zeolitic imidazolate frameworks" *Proc. Natl. Acad. Sci. U. S. A.* **2006**, *103*, 10186-10191.

[11] A. Phan, C. J. Doonan, F. J. Uribe-Romo, C. B. Knobler, M. O'Keeffe and O. M. Yaghi, "Synthesis, Structure, and Carbon Dioxide Capture Properties of Zeolitic Imidazolate Frameworks" *Acc. Chem. Res.* **2010**, *43*, 58-67.

[12] C. O. Ania, E. García-Pérez, M. Haro, J. J. Gutiérrez-Sevillano, T. Valdés-Solís, J. B. Parra and S. Calero, "Understanding Gas-Induced Structural Deformation of ZIF-8" *The Journal of Physical Chemistry Letters* **2012**, *3*, 1159-1164.

[13] U. Böhme, B. Barth, C. Paula, A. Kuhnt, W. Schwieger, A. Mundstock, J. Caro and M. Hartmann, "Ethene/Ethane and Propene/Propane Separation via the Olefin and Paraffin Selective Metal–Organic Framework Adsorbents CPO-27 and ZIF-8" *Langmuir* **2013**, *29*, 8592-8600.

[14] N. C. Burtch, H. Jasuja, D. Dubbeldam and K. S. Walton, "Molecular-level Insight into Unusual Low Pressure CO2 Affinity in Pillared Metal–Organic Frameworks" *Journal of the American Chemical Society* **2013**, *135*, 7172-7180.

[15] J. A. Gee, J. Chung, S. Nair and D. S. Sholl, "Adsorption and Diffusion of Small Alcohols in Zeolitic Imidazolate Frameworks ZIF-8 and ZIF-90" *The Journal of Physical Chemistry C* **2013**, *117*, 3169-3176.

[16] Z. R. Herm, E. D. Bloch and J. R. Long, "Hydrocarbon Separations in Metal–Organic Frameworks" *Chemistry of Materials* **2013**.

[17] H. Jasuja, N. C. Burtch, Y.-g. Huang, Y. Cai and K. S. Walton, "Kinetic Water Stability of an Isostructural Family of Zinc-Based Pillared Metal–Organic Frameworks" *Langmuir* **2012**, *29*, 633-642.

[18] R. Krishna and J. M. van Baten, "Investigating the Relative Influences of Molecular Dimensions and Binding Energies on Diffusivities of Guest Species Inside Nanoporous Crystalline Materials" *The Journal of Physical Chemistry C* **2012**, *116*, 23556-23568.

[19] G. Kumari, K. Jayaramulu, T. K. Maji and C. Narayana, "Temperature Induced Structural Transformations and Gas Adsorption in the Zeolitic Imidazolate Framework ZIF-8: A Raman Study" *The Journal of Physical Chemistry A* **2013**, *117*, 11006-11012.

[20] H. T. Kwon and H.-K. Jeong, "In Situ Synthesis of Thin Zeolitic–Imidazolate Framework ZIF-8 Membranes Exhibiting Exceptionally High Propylene/Propane Separation" *Journal of the American Chemical Society* **2013**, *135*, 10763-10768.

[21] W. Morris, C. J. Stevens, R. E. Taylor, C. Dybowski, O. M. Yaghi and M. A. Garcia-Garibay, "NMR and X-ray Study Revealing the Rigidity of Zeolitic Imidazolate Frameworks" *The Journal of Physical Chemistry C* **2012**, *116*, 13307-13312.

[22] A. U. Ortiz, A. Boutin, A. H. Fuchs and F.-X. Coudert, "Investigating the Pressure-Induced Amorphization of Zeolitic Imidazolate Framework ZIF-8: Mechanical Instability Due to Shear Mode Softening" *The Journal of Physical Chemistry Letters* **2013**, *4*, 1861-1865.

[23] E. Pantatosaki, G. Megariotis, A.-K. Pusch, C. Chmelik, F. Stallmach and G. K. Papadopoulos, "On the Impact of Sorbent Mobility on the Sorbed Phase Equilibria and Dynamics: A Study of Methane and Carbon Dioxide within the Zeolite Imidazolate Framework-8" *The Journal of Physical Chemistry C* **2011**, *116*, 201-207.

[24] D. Peralta, G. Chaplais, A. Simon-Masseron, K. Barthelet, C. Chizallet, A.-A. Quoineaud and G. D. Pirngruber, "Comparison of the Behavior of Metal–Organic Frameworks and Zeolites for Hydrocarbon Separations" *Journal of the American Chemical Society* **2012**, *134*, 8115-8126.

[25] J. A. Thompson, C. R. Blad, N. A. Brunelli, M. E. Lydon, R. P. Lively, C. W. Jones and S. Nair, "Hybrid Zeolitic Imidazolate Frameworks: Controlling Framework Porosity and Functionality by Mixed-Linker Synthesis" *Chemistry of Materials* **2012**, *24*, 1930-1936.

[26] J. A. Thompson, N. A. Brunelli, R. P. Lively, J. R. Johnson, C. W. Jones and S. Nair, "Tunable CO2 Adsorbents by Mixed-Linker Synthesis and Postsynthetic Modification of Zeolitic Imidazolate Frameworks" *The Journal of Physical Chemistry C* **2013**, *117*, 8198-8207.

[27] L. B. Vilhelmsen, K. S. Walton and D. S. Sholl, "Structure and Mobility of Metal Clusters in MOFs: Au, Pd, and AuPd Clusters in MOF-74" *Journal of the American Chemical Society* **2012**, *134*, 12807-12816.

[28] H. Wu, T. Yildirim and W. Zhou, "Exceptional Mechanical Stability of Highly Porous Zirconium Metal–Organic Framework UiO-66 and Its Important Implications" *The Journal of Physical Chemistry Letters* **2013**, *4*, 925-930.

[29] C. Zhang, R. P. Lively, K. Zhang, J. R. Johnson, O. Karvan and W. J. Koros, "Unexpected Molecular Sieving Properties of Zeolitic Imidazolate Framework-8" *The Journal of Physical Chemistry Letters* **2012**, *3*, 2130-2134.

[30] K. Zhang, R. P. Lively, C. Zhang, R. R. Chance, W. J. Koros, D. S. Sholl and S. Nair, "Exploring the Framework Hydrophobicity and Flexibility of ZIF-8: From Biofuel Recovery to Hydrocarbon Separations" *The Journal of Physical Chemistry Letters* **2013**, *4*, 3618-3622.

[31] K. Zhang, R. P. Lively, C. Zhang, W. J. Koros and R. R. Chance, "Investigating the Intrinsic Ethanol/Water Separation Capability of ZIF-8: An Adsorption and Diffusion Study" *The Journal of Physical Chemistry C* **2013**, *117*, 7214-7225.

[32] K. Zhang, L. Zhang and J. Jiang, "Adsorption of C1–C4 Alcohols in Zeolitic Imidazolate Framework-8: Effects of Force Fields, Atomic Charges, and Framework Flexibility" *The Journal of Physical Chemistry C* **2013**, *117*, 25628-25635.

[33] L. Zhang, Z. Hu and J. Jiang, "Sorption-Induced Structural Transition of Zeolitic Imidazolate Framework-8: A Hybrid Molecular Simulation Study" *Journal of the American Chemical Society* **2013**, *135*, 3722-3728.

[34] R. W. Baker, "Future directions of membrane gas separation technology" *Industrial & Engineering Chemistry Research* **2002**, *41*, 1393-1411.

[35] S. B. Carruthers, PhD Dissertation, The University of Texas at Austin, 2001.

[36] D. T. Clausi, PhD Dissertation, The University of Texas at Austin, 1998.

[37] O. M. Ekiner and G. Vassilatos, "Polyaramide hollow fibers for hydrogen/methane separation — spinning and properties" *Journal of Membrane Science* **1990**, *53*, 259-273.

[38] S. Husain, PhD Dissertation, Georgia Institute of Technology, 2006.

[39] L. Xu, PhD Dissertation, Georgia Institute of Technology, 2012.

[40] R. P. Lively, R. R. Chance, B. T. Kelley, H. W. Deckman, J. H. Drese, C. W. Jones and W. J. Koros, "Hollow Fiber Adsorbents for CO2 Removal from Flue Gas" *Industrial & Engineering Chemistry Research* **2009**, *48*, 7314-7324.

[41] C. Ma, PhD Dissertation, Georgia Institute of Technology, 2012.

[42] Y. Dai, J. R. Johnson, O. Karvan, D. S. Sholl and W. J. Koros, "Ultem®/ZIF-8 mixed matrix hollow fiber membranes for CO2/N2 separations" *J. Membr. Sci.* **2012**, *401–402*, 76-82.

[43] O. M. Ekiner and S. S. Kulkarni, Process for Making Hollow Fiber Mixed Matrix Membranes. US Patent 6663805, 2003.

[44] S. Husain and W. J. Koros, "Mixed matrix hollow fiber membranes made with modified HSSZ-13 zeolite in polyetherimide polymer matrix for gas separation" *Journal of Membrane Science* **2007**, *288*, 195-207.

[45] J. Liu, PhD Dissertation, Georgia Institute of Technology, 2010.

[46] E. M. V. Hoek and V. V. Tarabara *Encyclopedia of Membrane Science and Technology*, Oxford University Press Inc., **2013**

[47] J. A. Thompson, K. W. Chapman, W. J. Koros, C. W. Jones and S. Nair, "Sonication-induced Ostwald ripening of ZIF-8 nanoparticles and formation of ZIF-8/polymer composite membranes" *Microporous Mesoporous Mater.* **2012**, *158*, 292-299.

[48] C. M. Zimmerman, A. Singh and W. J. Koros, "Tailoring mixed matrix composite membranes for gas separations" *Journal of Membrane Science* **1997**, *137*, 145-154.

[49] C. Ma and W. J. Koros, "High-performance ester-crosslinked hollow fiber membranes for natural gas separations" *Journal of Membrane Science* **2013**, *428*, 251-259.

CHAPTER 3

MATERIALS AND METHODS

3.1 Overview

This chapter describes the materials and experimental methods. Section 3.2 describes the polymer and molecular sieve. Section 3.3 discusses formation of dense films and asymmetric hollow fiber membranes. Section 3.4 outlines characterization techniques including membrane permeation measurements and sorption measurements, etc.

3.2 Materials

3.2.1 Polymer

The 6FDA-DAM polymer was synthesized using a step growth polymerization method with details described elsewhere [1]. The monomers 6FDA (2,2-bis (3,4-carboxyphenyl) hexafluoropropane dianhydride) and DAM (diaminomesitylene) were purchased from Sigma-Aldrich and purified by sublimation before polymerization. The molecular weight (Mw) of the synthesized 6FDA-DAM was 165-192 kDa, depending on the batch.

3.2.2 ZIF-8

ZIF-8 samples with different crystal sizes were used in this research to prepare mixed-matrix membranes and to study the ZIF's adsorption properties as well as

framework flexibility. Detailed synthesis procedures of ZIF-8 samples will be described in section 4.2. A commercially available ZIF-8 sample (Basolite Z1200, BASF) referred to as "BASF ZIF-8" was obtained from Sigma-Aldrich and used to form mixed-matrix dense film membranes. SEM image of as-received BASF ZIF-8 sample is shown in Figure 3.1.

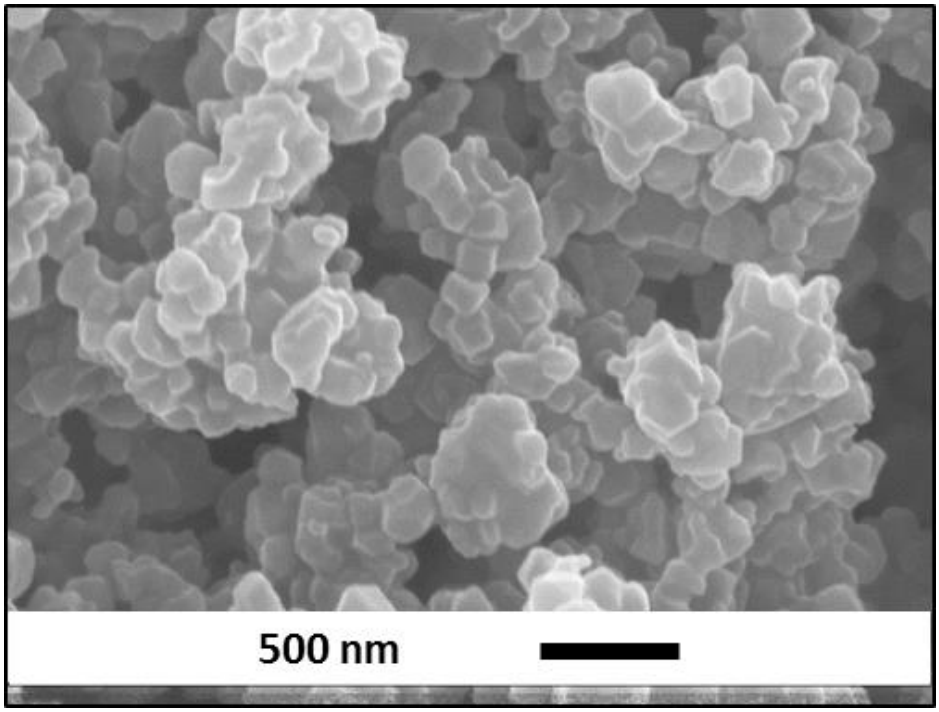

Figure 3.1: SEM image of as-received BASF ZIF-8 sample.

3.3 Membrane Formation

3.3.1 Formation of Dense Film Membranes

Powders of 6FDA-DAM were dried in a convection oven at 110 ℃ overnight before being dissolved in dichloromethane in a 20 ml vial (vial A) to form the polymer solution (dope). The dope was mixed on a rolling mixer overnight to dissolve the

polymer. Pure 6FDA-DAM dense film was formed by casting the polymer dope in a dichloromethane saturated glove bag using the method described elsewhere [2]. For mixed-matrix dense film formation, as-received BASF ZIF-8 crystals were dried in a vacuum oven at 200 ^{o}C overnight before being dispersed in dichloromethane in a 20 ml vial (Vial B) with the help of a sonication horn (Vibra-Cell, Sonics & Materials Inc.). The milky ZIF-8 dispersion in vial B was added to vial A to form the mixed-matrix dope. Excess solvent in the mixed-matrix dope was removed by purging the vial slowly with dry nitrogen. ZIF-8/6FDA-DAM mixed-matrix dense films were formed by casting the mixed-matrix dope in the same condition with the pure 6FDA-DAM dense film.

Pure 6FDA-DAM dense film and ZIF-8/6FDA-DAM mixed-matrix dense films were dried in a vacuum oven at 210 ^{o}C for 20 hours before permeation tests. ZIF-8 loadings in mixed-matrix dense films were controlled by changing the mass ratio of ZIF-8 to 6FDA-DAM in the mixed matrix dope. Three ZIF-8/6FDA-DAM mixed matrix dense films (DAMZ_1, DAMZ_2, and DAMZ_3) with low (16.4 wt%), medium (28.7 wt%), and high (48.0 wt%) ZIF-8 loadings were prepared. ZIF-8 loadings in mixed-matrix dense films were determined by TGA, which will be described with more details in Appendix B.

3.3.2 Formation of Asymmetric Hollow Fiber Membranes

3.3.2.1 Preparation of Mixed-Matrix Sheath Spinning Dopes

Two dopes (sheath dope and core dope) were used to spin dual-layer mixed-matrix hollow fiber membranes. The core dope contained polymer, solvents, non-solvents and was free of particles. The core dope was prepared following the conventional dope preparation technique, which can be found elsewhere [3].

This research has identified the key to form ZIF/polymer mixed-matrix hollow fiber membranes with minimized particle agglomerations, which is to avoid drying ZIF particles before mixing with other components in the mixed-matrix sheath spinning dope. After being dried, either under atmosphere or vacuum with or without heat, ZIF-8 particles mostly exist as particle agglomerations and are very difficult to re-disperse in solvents even with strong sonication.

The mixed-matrix sheath spinning dope was prepared with the following procedure. 6FDA-DAM polyimide was dried under vacuum at 100 ^{o}C for at least 12 hours to remove condensables. 15 wt% of the total dried polyimide was dissolved in 30 wt% of the total solvents to form a dilute "priming" dope A. After being washed with methanol, ZIF-8 particles (without being dried) were washed with NMP overnight to extract the residual methanol from the particles. After the NMP/methanol mixture is separated from the ZIF-8 particles by centrifuge, non-solvent (ethanol) and 70 wt% of the total solvents were added to the centrifuge vials. After being shaken overnight, the slurry

was transferred from the centrifuge vials to a sealed 400 mL glass jar and sonicated for at least 1 hour using a sonication bath (Elmasonic P30H). After ZIF-8 particles were re-dispersed, dope A was added under constant stirring. A white and homogeneous paste containing ZIF-8 particles, solvents, non-solvent, and polyimide was formed. The remaining (85 wt%) of the total dried polyimide was added to the above mentioned paste under constant stirring. Finally, the jar was sealed and placed on a rolling mixer for at least two weeks until a very viscous and homogeneous white paste was formed.

3.3.2.2 Formation of Asymmetric Hollow Fiber Membranes

Dual-layer mixed-matrix hollow fiber membranes were formed using the dry-jet/wet-quench fiber spinning technique as described previously in section 2.4.2. A composite spinneret (Recessed I) was used for fiber spinning. The spinneret, tubing and connections were cleaned by NMP in a sonication bath for at least 12 hrs. The homogenous sheath and core dopes were transferred into two Isco syringe pumps and allowed to degas at least for ~12 hrs at 50-60 ℃. A 500 ml Isco syringe pump was used for the core dope and a 100ml Isco syringe pump was used for the sheath dope. A bore fluid mixture of 90/10 (wt%) NMP/water was loaded into another 100mL Isco syringe pump.

The sheath dope, core dope, and bore fluid were filtered in-line between the Isco delivery pumps and the spinneret with 140 μm, 90 μm and 2 μm sintered metal filters, respectively. Three thermocouples were attached to the dope delivery pumps and the spinneret, and another one was immersed in the core dope stream prior to the filter block.

The spinning was carried out at desired temperature by heating the entire system including the dope delivery pump, tubing, dope filter and spinneret using multiple heating tapes controlled by temperature controllers. The dopes and bore fluid were co-extruded through an adjustable air gap into the water quench bath (height = 1 m), passed over a Teflon guide in the quench bath and collected on a polyethylene rotating take-up drum (diameter = 0.32 m). The take-up drum was partially immersed in a separate water bath at room temperature. The fiber take-up rate used in this research ranged from 5 to 50 m/min.

Once cut off from the take-up drum, the fibers were soaked sequentially in at least four separate water baths for 3 days to remove residual organic solvents, and then solvent-exchanged with sequential 1 hr baths of methanol and hexane. After air-drying in the fume hood for 1 hr, the fibers were dried in the vacuum oven at 120 ℃ for ~3 hrs. The obtained fibers are referred to as as-spun fibers.

3.3.2.3 Post-treatment of Asymmetric Hollow Fiber Membranes

The surface of as-spun fibers was coated with polydimethylsiloxane (PDMS) and/or polyaramid to seal fiber skin defects, if existing. To coat the fiber surface with PDMS, the as-spun fibers were contacted with a solution of 2 wt% PDMS in iso-octane [4]. After 30 mins, the solution was drained and the residual iso-octane was removed from the fiber by degassing the fiber at 80 ^{o}C overnight in a vacuum oven. The obtained fibers are referred to as PDMS-coated fibers.

To coat the fiber surface only with polyaramid, the as-spun fibers were contacted with a solution of 0.2 wt% diethyltoluene diamine (DETDA) in iso-octane for 30 mins and the solution was drained. The fibers were then further contacted with a second solution of 0.2 wt% trimesoyl chloride (TMC) in iso-octane for 30 mins and the solution was drained [5]. The residual iso-octane was removed from the fiber by degassing the fiber at 80 ^{o}C overnight in a vacuum oven. The obtained fibers are referred to as polyaramid-coated fibers.

To coat the fiber surface with both PDMS and polyaramid[5], the as-spun fibers were contacted with a solution of 0.2 wt% diethyltoluene diamine (DETDA) in iso-octane for 30 mins and the solution was drained. The fibers were then further contacted with a second solution of 0.2 wt% trimesoyl chloride (TMC) and 2 wt% PDMS in iso-octane for 30 mins and the solution was drained. The residual iso-octane was removed from the fiber by degassing the fiber at 80 ^{o}C overnight in a vacuum oven. The obtained fibers are referred to as PDMS/polyaramid-coated fibers.

3.4 Characterizations

3.4.1 Membrane Permeation Measurements

3.4.1.1 Permeation Measurements of Dense Film Membranes

Both single-gas and mixed-gas permeation measurements were performed at 35 ^{o}C following procedures described in details elsewhere [2]. Two film samples were tested

at each ZIF-8 loading to get average permeation results in single-gas studies. Single-gas permeation was done with upstream pressure of ~29.4 psia (~2 bars).

Mixed-gas permeation was done with a 50/50 (vol%) C_3H_6/C_3H_8 mixture at upstream pressures around 20, 40, 60, and 80 psia with single film sample at each ZIF-8 loading. In all cases the uncertainties were smaller than the observed differences between single and mixed-gases. For mixed-gas measurements, permeate compositions were analyzed with a Varian-450 gas chromatograph (GC). The stage cut, which is the percentage of feed that permeates through the membrane, was kept less than 1% to avoid concentration polarization.

3.4.1.2 Permeation Measurements of Asymmetric Hollow Fiber Membranes

Permeation measurements of hollow fiber membranes were performed at 35 ^oC using the constant volume method. A detailed description of making hollow fiber membrane modules can be found elsewhere [4]. Permeation of C_3H_6/C_3H_8 was done with mixed-gas feed while O_2/N_2 was done with single-gas feed. The upstream pressure was ~29.4 psia (~2 bars) for O_2/N_2; and was ~20 psia for C_3H_6/C_3H_8. Since 6FDA-DAM-based materials were quite permeable, only one or two fibers were used in each hollow fiber membrane module. During the permeation measurements, the feed was in contact with the shell side of the fiber while permeate was collected from the bore side of the fiber. For mixed-gas measurements, permeate compositions were analyzed with a Varian-450 gas chromatograph (GC). The stage cut was again kept less than 1% to avoid concentration polarization.

3.4.2 Sorption Measurements

Equilibrium sorption isotherms and kinetic uptake curves in ZIF-8 were measured at 35 ^{o}C using the pressure-decay sorption method (piezometric method). Illustration of the pressure decay sorption set-up, experimental procedures, and calculation of sorption capacity were described with great detail elsewhere [1]. It should be noted, though, that the ZIF-8 powder sample was sealed in a sintered stainless steel filter (0.5 μm) by an aluminum foil. The sample was degassed at 100 ^{o}C for 12 hrs prior to being loaded into the sample chamber. Compressibility factor equations were calculated using the NIST SUPERTRAPP software and listed in Appendix A.

3.4.3 Complementary Characterization Techniques

3.4.3.1 Scanning Electron Microscopy (SEM)

All samples were sputter-coated with a gold coating before being transferred to a LEO 1530 field emission scanning electron microscope (LEO Electron Microscopy, Cambridge, UK). Film and fiber samples were fractured in liquid nitrogen before being mounted to the sample holder. Energy dispersive X-ray spectroscopy (EDX) was used to analyze the TGA residues of ZIF-8 and mixed-matrix membrane samples.

3.4.3.2 Transmission Electron Microscopy (TEM)

Samples were prepared by dispersing the ZIFs in methanol, sonicating for ten minutes, dropping the solution on a carbon coated grid, and drying the grid in a 60 ℃

oven for 3 hrs. Imaging was done using a FEI Tecnai F30 high resolution TEM at 300 kV.

3.4.3.3 Cryogenic (77K) N_2 Physisorption

Surface area and micropore volume of ZIF-8 samples were measured by analyzing N_2 physisorption isotherms at 77K, which were obtained using an ASAP 2020 instrument (Micromeritics, Norcross, GA). Samples were degassed at 120-150 ^{o}C for 12-16 hrs prior to measurements.

3.4.3.4 Thermogravimetric Analysis (TGA)

Samples were activated in a vacuum oven at 150 ^{o}C for 12 hrs prior to analysis in a Netzsch STA 409 TGA instrument.

3.4.3.5 Powder X-ray Diffraction (PXRD)

PXRD data were collected on a Phillips X'Pert X-Ray Diffractometer (using Cu Kα radiation, λ=0.154 nm at 45 kV and 40 mA). Experiments were carried out scanning from 2θ =5-40 °.

3.4.3.6 Elemental Analysis

Elemental analysis of the mixed-matrix hollow fiber samples were done by ALS Environmental. Carbon, nitrogen, hydrogen, and oxygen were analyzed by combustion/IR. Fluorine was analyzed by combustion/IC. Zinc analysis was done by total dissolution.

3.5 References

[1] J. Liu, PhD Dissertation, Georgia Institute of Technology, 2010.

[2] M. Das, PhD Dissertation, Georgia Institute of Technology, 2009.

[3] L. Xu, PhD Dissertation, Georgia Institute of Technology, 2012.

[4] C.-C. Chen, PhD Dissertation, Georgia Institute of Technology, 2011.

[5] O. M. Ekiner, R. A. Hayes and P. Manos, Reactive Post Treatment for Gas Separation Membrane. US Patent 5091216, 1992.

CHAPTER 4

SYNTHESIS AND CHARACTERIZATIONS OF ZIF-8 WITH CONTOLLABLE CRYSTAL SIZE

4.1 Overview

This chapter described synthesis of ZIF-8 samples with controllable crystal size, which enables reliable and convenient study of adsorption and diffusion properties that will be discussed in Chapter 5. Further, the ZIF-8 samples were characterized by SEM, PXRD, and N_2 physisorption. The crystal-size dependent N_2 physisorption was discussed.

4.2 Synthesis and Characterizations

Eight ZIF-8 samples with distinct crystal size (average equivalent crystal radius: 5nm, 9nm, 26nm, 47nm, 270nm, 516nm, 1.7 micron, and 3.8 micron) were synthesized at room temperature in methanol using $Zn(NO_3)_2 \bullet 6H_2O$ and 2-methylimidazole with or without the presence of a modulating ligand. Another two ZIF-8 samples (7.9 micron and 162 micron) were synthesized solvothermally at 90 ^oC.

Cravillon and co-workers [1-3] studied the reaction mechanism of ZIF-8 formation, which follows the steps of (1) complex formation (2) deprotonation, and (3) ligand exchange. An excess of 2-methylimidazole relative to Zn results in a high nucleation rate and consequently small nano-sized crystals. Modulating ligands can be used to control the nucleation rate and the size of the ZIF-8 crystals. For room

temperature synthesis, addition of basic modulating ligands (e.g. n-butylamine) accelerates the nucleation and ZIF-8 crystals as small as 5 nm can be obtained. On the contrary, the nucleation is slowed down in the presence of less basic modulating ligands such as 1-methylimidazole and sodium formate. When this happens, large micron crystals as large as 3.8 micron were formed.

For solvothermal synthesis, however, the role of modulating ligands such as sodium formate was found to be quite different with the case of room temperature synthesis [3]. At 90 ^{o}C, sodium formate functions as a base in deprotonation equilibria rather than a competitive ligand in coordination equilibria and its presence actually accelerates instead of slowing down the nucleation.

5 nm ZIF-8 sample 588 mg (1.977 mmol) $Zn(NO_3)_2 \cdot 6H_2O$ was dissolved in 40 ml methanol. 648 mg (7.897 mmol) 2-methylimidazole and 0.78 ml (7.897 mmol) n-butylamine were dissolved in 40 ml methanol. The molar ratio of Zn/MeIM/amine/MeOH was 1:4:4:1000. The latter solution was poured into the former solution under stirring with a magnetic bar. Stirring was stopped upon mixing. After 24 hours, the gel-like solids were separated from the dispersion by centrifugation, followed by extensive washing with methanol. The product was dried at room temperature under vacuum.

9 nm ZIF-8 sample 588 mg (1.977 mmol) $Zn(NO_3)_2 \cdot 6H_2O$ was dissolved in 40 ml methanol. 648 mg (7.897 mmol) 2-methylimidazole and 0.39 ml (3.947 mmol) n-

butylamine were dissolved in 40 ml methanol. The molar ratio of Zn/MeIM/amine/MeOH was 1:4:2:1000. The latter solution was poured into the former solution under stirring with a magnetic bar. Stirring was stopped upon mixing. After 24 hours, the gel-like solids were separated from the dispersion by centrifugation, followed by extensive washing with methanol. The product was dried at room temperature under vacuum.

26 nm ZIF-8 sample 588 mg (1.977 mmol) $Zn(NO_3)_2 \cdot 6H_2O$ and 811mg (9.883 mmol) 2-methylimidazole were each dissolved in 40 ml methanol. The molar ratio of Zn/MeIM/MeOH was 1:5:1000. The latter solution was poured into the former solution under stirring with a magnetic bar. Stirring was stopped after 7 min, and then the white solids were separated from the milky colloidal dispersion by centrifugation, followed by extensive washing with methanol. The product was dried at room temperature under vacuum.

46 nm ZIF-8 sample 588 mg (1.977 mmol) $Zn(NO_3)_2 \cdot 6H_2O$ and 648 mg (7.897 mmol) 2-methylimidazole were each dissolved in 40 ml methanol. The molar ratio of Zn/MeIM/MeOH was 1:4:1000. The latter solution was poured into the former solution under stirring with a magnetic bar. Stirring was stopped after mixing. After 24 hours, the white solids were separated from the dispersion by centrifugation, followed by extensive washing with methanol. The product was dried at room temperature under vacuum.

270 nm ZIF-8 sample 588 mg (1.977 mmol) $Zn(NO_3)_2 \cdot 6H_2O$ was dissolved in 40 ml methanol. 648 mg (7.897 mmol) 2-methylimidazole and 648 mg (7.897 mmol) 1-methylimidazole were dissolved in 40 ml methanol. The molar ratio of Zn/2-MeIM/1-MeIM/MeOH was 1:4:4:1000. The latter solution was poured into the former solution under stirring with a magnetic bar. Stirring was stopped after mixing. After 12 mins, the white solids were separated from the dispersion by centrifugation, followed by extensive washing with methanol. The product was dried at room temperature under vacuum.

516 nm ZIF-8 sample 588 mg (1.977 mmol) $Zn(NO_3)_2 \cdot 6H_2O$ was dissolved in 40 ml methanol. 648 mg (7.897 mmol) 2-methylimidazole and 648 mg (7.897 mmol) 1-methylimidazole were dissolved in 40 ml methanol. The molar ratio of Zn/2-MeIM/1-MeIM/MeOH was 1:4:4:1000. The latter solution was poured into the former solution under stirring with a magnetic bar. Stirring was stopped after mixing. After 45 mins, the white solids were separated from the dispersion by centrifugation, followed by extensive washing with methanol. The product was dried at room temperature under vacuum.

1.7 µm ZIF-8 sample 588 mg (1.977 mmol) $Zn(NO_3)_2 \cdot 6H_2O$ was dissolved in 40 ml methanol. 648 mg (7.897 mmol) 2-methylimidazole and 648 mg (7.897 mmol) 1-methylimidazole were dissolved in 40 ml methanol. The molar ratio of Zn/2-MeIM/1-MeIM/MeOH was 1:4:4:1000. The latter solution was poured into the former solution under stirring with a magnetic bar. Stirring was stopped after mixing. After 24 hours, the white solids were separated from the dispersion by centrifugation, followed by extensive washing with methanol. The product was dried at room temperature under vacuum.

3.8 μm ZIF-8 sample 588 mg (1.977 mmol) $Zn(NO_3)_2 \cdot 6H_2O$ was dissolved in 40 ml methanol. 648 mg (7.897 mmol) 2-methylimidazole and 538 mg (7.908 mmol) sodium formate were dissolved in 40 ml methanol. The molar ratio of Zn/MeIM/$NaHCO_2$/MeOH was 1:4:4:1000. The latter solution was poured into the former solution under stirring with a magnetic bar. Stirring was stopped after mixing. After 24 hours, the white solids were separated from the dispersion by centrifugation, followed by extensive washing with methanol. The product was dried at room temperature under vacuum.

7.9 μm ZIF-8 sample 588 mg (1.977 mmol) $Zn(NO_3)_2 \cdot 6H_2O$ was dissolved in 40 ml methanol. 324 mg (3.954 mmol) 2-methylimidazole and 538 mg (7.908 mmol) sodium formate were dissolved in 40 ml methanol. The molar ratio of Zn/MeIM/$NaHCO_2$/MeOH was 1:2:4:1000. The latter solution was poured into the former solution under stirring with a magnetic bar. Stirring was stopped after mixing. The solution was heated at 90℃ for 24 hours in a sealed glass jar. The crystals were recovered by centrifugation, followed by extensive washing with methanol. The product was dried at room temperature under vacuum.

162 μm ZIF-8 sample 3.528 g (11.862 mmol) $Zn(NO_3)_2 \cdot 6H_2O$ was dissolved in 40 ml methanol. 1.944 g (23.724 mmol) 2-methylimidazole and 0.807 g (11.862 mmol) sodium formate were dissolved in 40 ml methanol. The molar ratio of Zn/MeIM/$NaHCO_2$/MeOH was 1:2:1:166.5. The latter solution was poured into the former solution under stirring with a magnetic bar. Stirring was stopped after mixing. The solution was heated at 90℃ for 24 hours in a sealed glass jar. The large crystals on the wall of the jar were collected

and washed extensively with methanol. The product was dried at room temperature under vacuum.

SEM images of synthesized ZIF-8 nano- and microcrystals are shown in Figure 4.1, and reveal (truncated) rhombic dodecahedron shaped micro-crystals. The nano-crystals have a spherical shape. PXRD patterns of the synthesized ZIF-8 samples are shown in Figure 4.2 and match well with the simulated one.

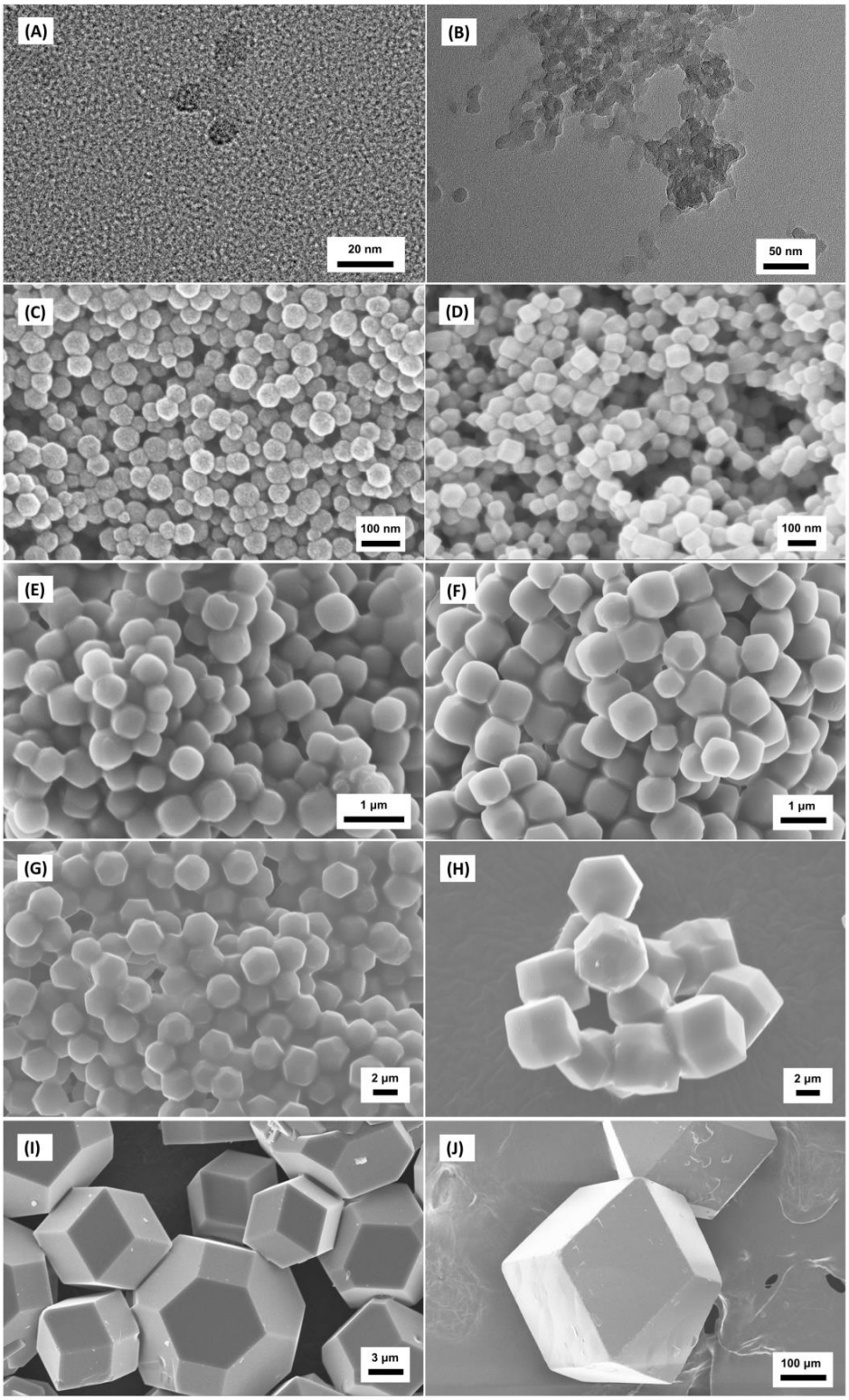

Figure 4.1: Scanning electron microscopy (SEM) images of synthesized ZIF-8 samples (A) 5 nm (B) 9 nm (C) 26 nm (D) 46nm (E) 270 nm (F) 516 nm (G) 1.7 micron (H) 3.8 micron (I) 7.9 micron (J) 162 micron

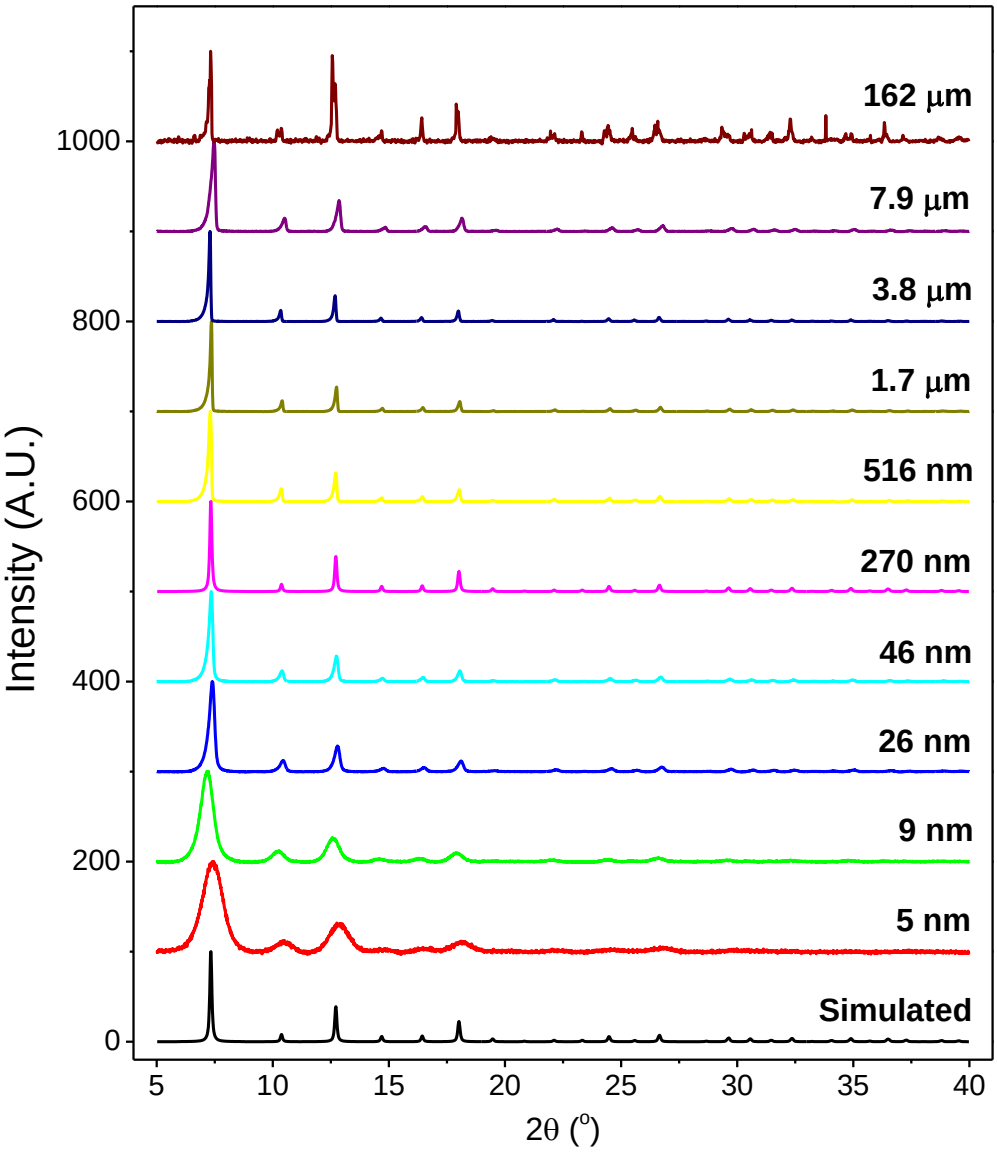

Figure 4.2: Powder X-ray diffraction (PXRD) patterns of synthesized ZIF-8 samples. The simulated pattern is shown for reference.

4.3 Crystal-Size Dependent N_2 Physisorption at Cryogenic Temperature (77K)

4.3.1 N_2 Physisorption Isotherms

N_2 sorption and desorption isotherms of the synthesized ZIF-8 samples were measured at 77K and plotted in Figure 4.3. At low relative pressure ($P/P_0<0.01$), N_2 molecules sorb in the ultramicropores through the multilayer formation and micropore filling mechanism, as shown by the dramatic increase in the sorption capacity. As the relative pressure increases, sorption continues on crystal external surface. A "plateau" is observed for large micron-sized crystals due to negligible external surface area. However, a sharp increase in sorption capacity occurs for nano-sized crystals in the region close to the saturation pressure (1 atm or $P/P_0=1$), which can be explained by capillary condensation in the mesopores and macropores that were formed by agglomeration of nano-sized crystals.

Table 4.1 summarizes surface area and pore volume of the synthesized ZIF-8 samples. Surface area was calculated using the Brunauer–Emmett–Teller (BET) theory based on the consistency criteria [4]. Values of micropore volume were obtained with the t-plot method. They were both in good agreement with the commercial sample. Two exceptions are the 5 nm and 9 nm samples, whose reduced BET surface area and micropore volume are due to much larger portion of atoms on crystal external surface.

Table 4.1: Surface area and micropore volume of synthesized ZIF-8 samples. Values of the commercial sample are shown as well for reference.

ZIF-8 sample	BET surface area (m^2/g)	t-plot micropore volume (cm^3/g)	Range of relative pressure (P/P_0) for BET analysis
5 nm	1172	0.290	0.0004-0.07
9 nm	1247	0.399	0.0004-0.005
26 nm	1374	0.582	0.0004-0.004
47 nm	1475	0.661	0.0004-0.005
270 nm	1303	0.603	0.0004-0.004
516 nm	1377	0.645	0.0004-0.005
1.7 μm	1390	0.658	0.0004-0.004
3.8 μm	1436	0.681	0.0004-0.004
7.9 μm	1364	0.650	0.0004-0.005
162 μm	1377	0.659	0.0004-0.004
Commercial sample	1327	0.625	0.0004-0.004

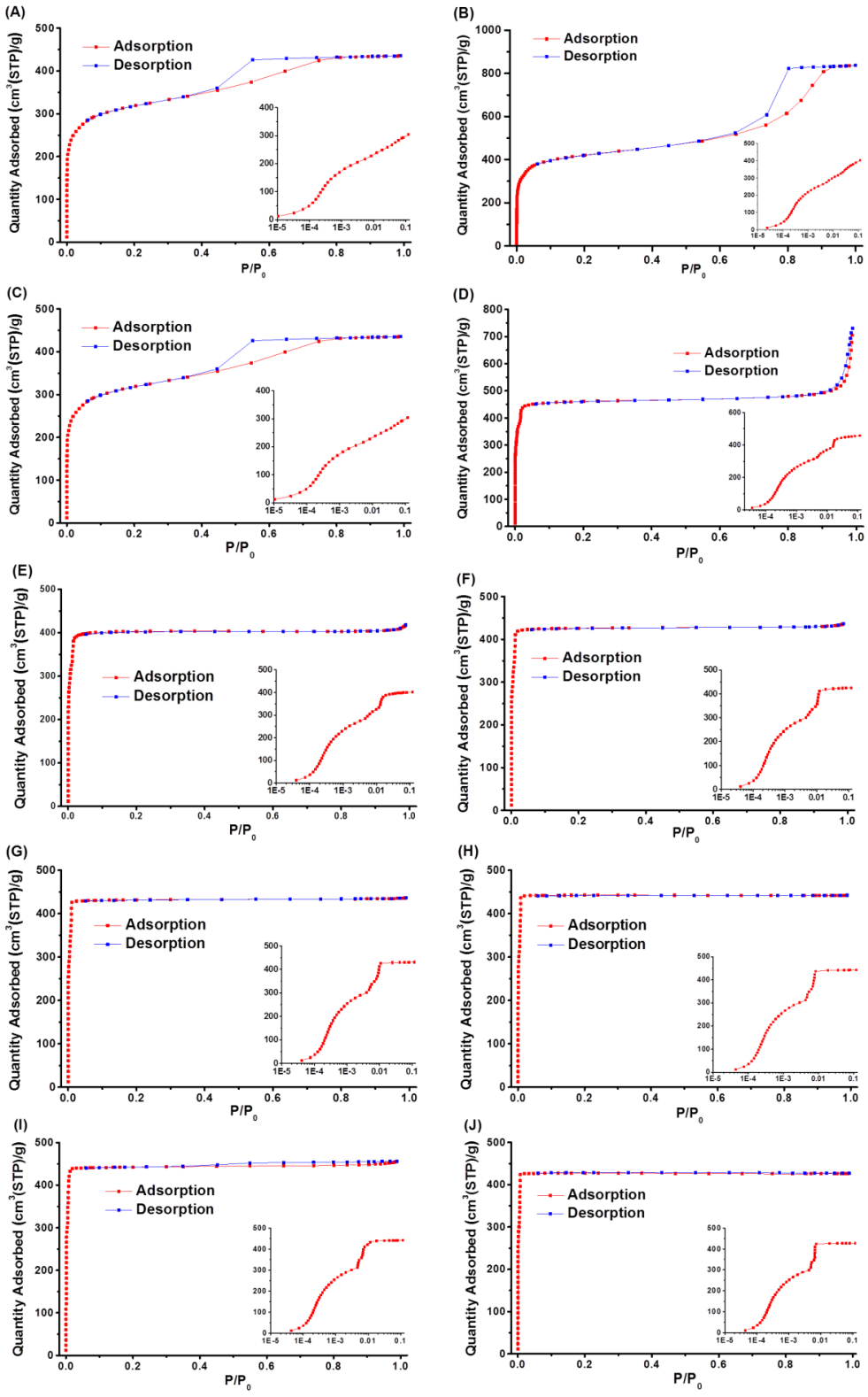

Figure 4.3: N_2 physisorption isotherms (77K) of synthesized ZIF-8 samples (A) 5 nm (B) 9 nm (C) 26 nm (D) 46 nm (E) 270 nm (F) 516 nm (G) 1.7 micron (H) 3.8 micron (I) 7.9 micron (J) 162 micron

4.3.2 Crystal-Size Dependence of N_2 Physisorption Isotherm

The low pressure regions ($P/P_0<0.01$) of each N_2 physisorption isotherm are shown in the semi-log plots in Figure 4.3. It was interesting to see that several "sub-steps" were observable at the low pressure region of the isotherm before N_2 molecules start to adsorb on the particle's external surface ($P/P_0=0.008$-0.02). This phenomenon was consistent with the observations made by Park and co-workers on micron-sized ZIF-8 crystals [5]. However, for the first time, this research demonstrated the interesting fact that the shape of the "sub-steps" and the threshold pressure of each step are strongly dependent on the size of the ZIF-8 crystal.

The "sub-steps" and threshold pressure of each step were illustrated in Figure 4.4 with the example of 3.8 micron ZIF-8 sample, showing that the isotherm can be divided into four regions (I, II, III, and IV) with threshold pressures A, B, and C. Region I represents formation of mono and multilayers in the ultramicropores. This region also includes the part of the isotherm that was used for calculation of BET surface area, which is shown by red data points. Region II and III are two "sub-steps" characterized by sharp increases in sorption capacity. Sorption possibly still happens in the ultramicropores for these two regions. Region IV represents sorption on crystal external surfaces (for all samples) and mesopores (only for nano-sized crystals). Transition A, B, and C represents the threshold pressure from region I to II, II to III, and III to IV, respectively.

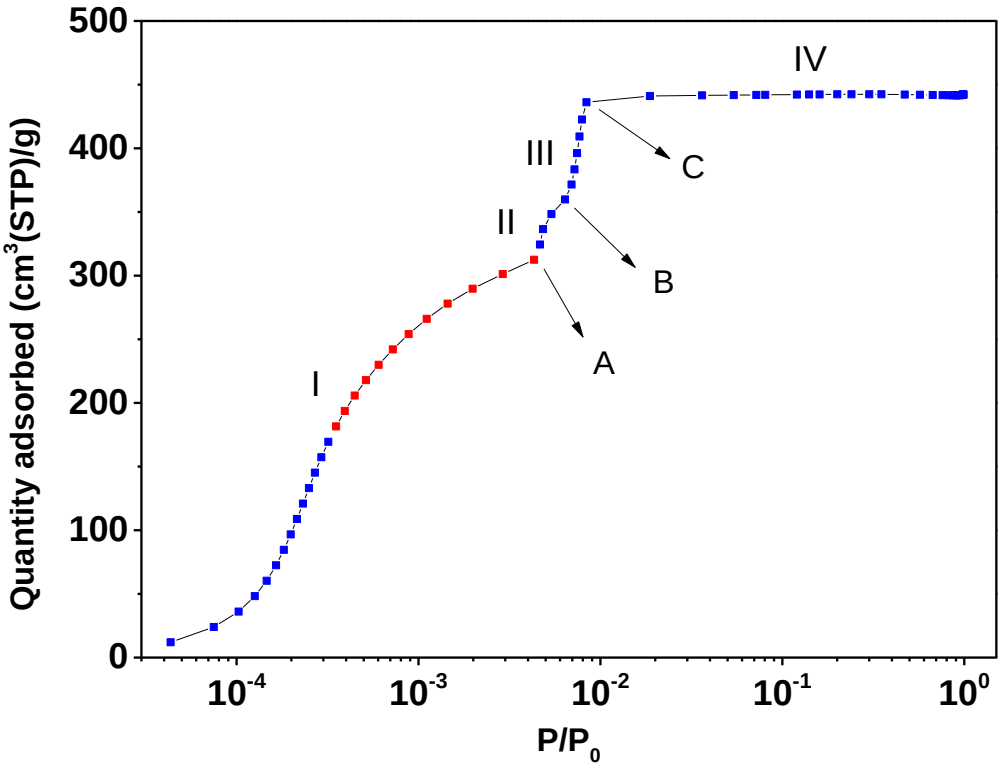

Figure 4.4: Illustration of different regions (I, II, III, and IV) and transition pressures (A, B, and C) of a typical N_2 physisorption isotherm in ZIF-8 (3.8 micron sample). Red data points indicate the part of the isotherm that satisfies the BET consistency criteria and was used for analysis of BET surface area.

The interesting evolution of the "sub-steps" with sample crystal size can be seen from Figure 4.5 and 4.6. As the crystal size decreases: (1) Region III and IV become more and more stretched and separated. (2) The slopes of region III and IV both decrease. (3) The threshold pressure B and C both shifted to higher values, while threshold pressure A essentially remains constant. For the smallest crystal (5 nm), region II and III are completely stretched and it is not possible to distinguish between region I, II, and III

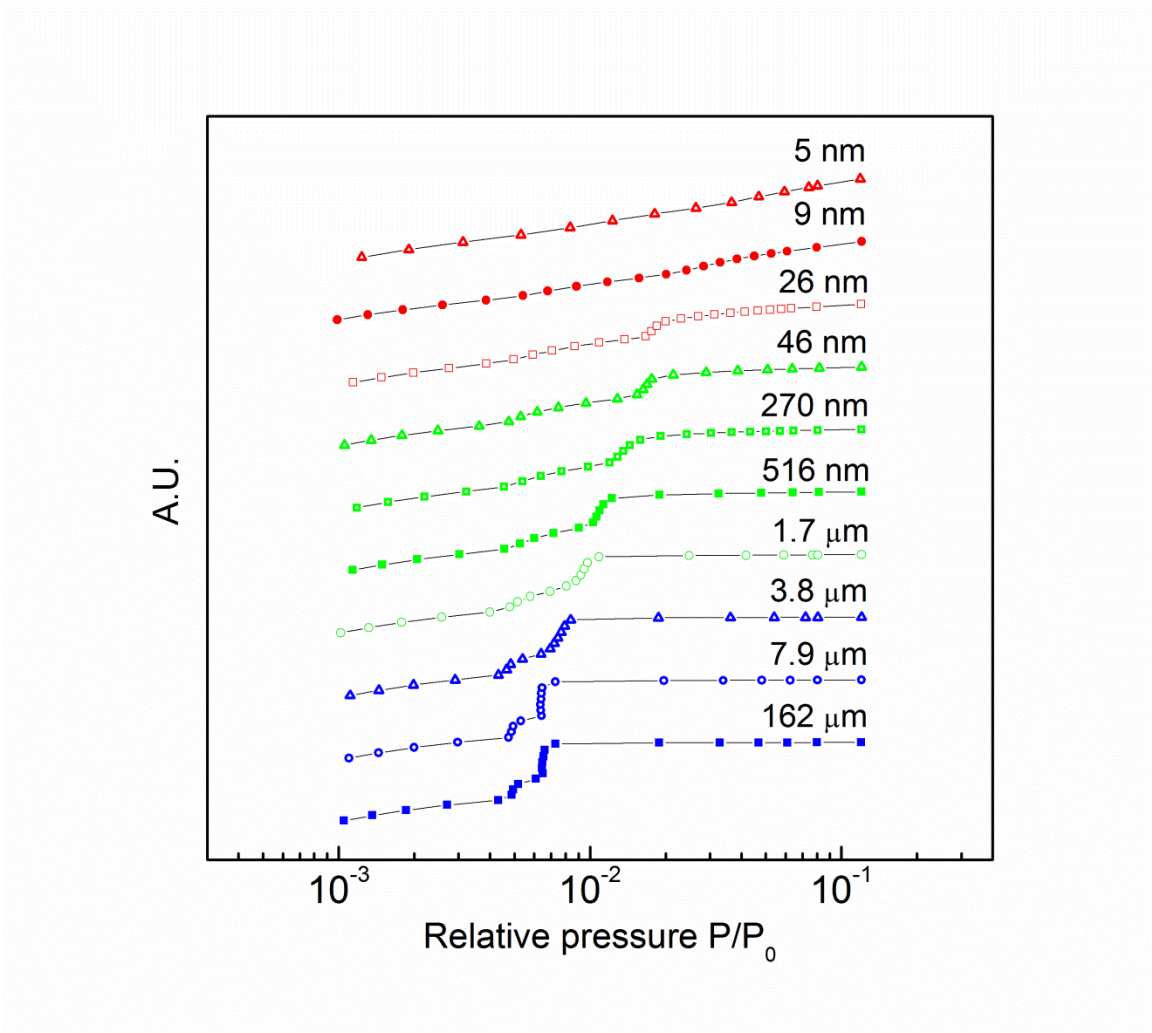

Figure 4.5: Evolution of sorption isotherm "sub-steps" (region II and III of Figure 4.4) with decreasing sample crystal size.

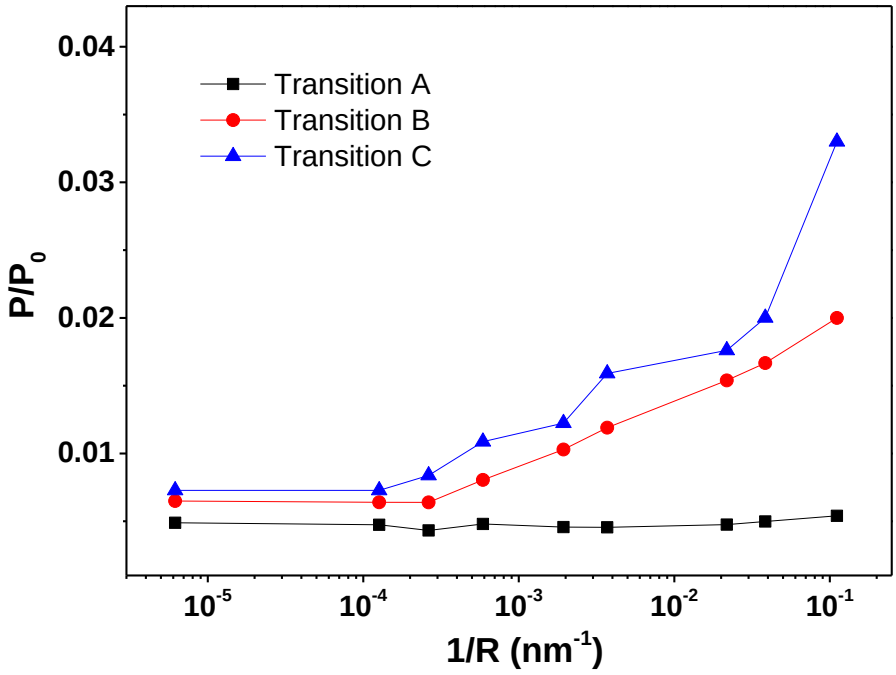

Figure 4.6: Evolution of sorption isotherm "sub-steps" (region II and III of Figure 4.4) with decreasing sample crystal size. Data of the 5 nm sample were not shown since the transitions were not observable.

The similar "sub-steps" shown in Figure 4.4 were observed for N_2 physisorption isotherms in MFI zeolites with high Si/Al ratio, and was believed to be a result of adsorbate phase transition [6]. We hypothesize that the crystal-size dependent behavior in Figure 4.5 may be due to framework flexibility of the ZIF. A parallel work is being done by Professor David Sholl group at Georgia Tech using atomically-detailed modeling. We hypothesize that the behavior shown in Figure 4.5 may be due to structural transition of the ZIF that was affected by crystal size.

4.4 Summary and Conclusions

Chapter 4 discussed synthesis and characterization of ten ZIF-8 samples with distinct crystal radii: 5 nm, 9 nm, 26 nm, 46 nm, 270 nm, 516 nm, 1.7 μm, 3.8 μm, 7.9 μm, and 162 μm. The crystal size was controlled by the ratio of reactant concentration and choice of modulating ligand. PXRD patterns of the synthesized ZIF-8 samples matched well with the simulated one. N_2 physisorption showed comparable BET surface area and porosity for micron-sized samples and most nano-sized samples. Interesting crystal-size dependent N_2 physisorption isotherms were discovered and discussed. The ability to control crystal size enabled reliable and convenient study of adsorption and diffusion, which will be discussed in subsequent chapters.

4.5 References

[1] J. Cravillon, S. Munzer, S.-J. Lohmeier, A. Feldhoff, K. Huber and M. Wiebcke, "Rapid Room-Temperature Synthesis and Characterization of Nanocrystals of a Prototypical Zeolitic Imidazolate Framework" *Chem. Mater.* **2009**, *21*, 1410-1412.

[2] J. Cravillon, R. Nayuk, S. Springer, A. Feldhoff, K. Huber and M. Wiebcke, "Controlling Zeolitic Imidazolate Framework Nano- and Microcrystal Formation: Insight into Crystal Growth by Time-Resolved In Situ Static Light Scattering" *Chem. Mater.* **2011**, *23*, 2130-2141.

[3] J. Cravillon, C. A. Schröder, H. Bux, A. Rothkirch, J. Caro and M. Wiebcke, "Formate modulated solvothermal synthesis of ZIF-8 investigated using time-resolved in situ X-ray diffraction and scanning electron microscopy" *CrystEngComm* **2012**, *14*, 492.

[4] K. S. Walton and R. Q. Snurr, "Applicability of the BET Method for Determining Surface Areas of Microporous Metal−Organic Frameworks" *Journal of the American Chemical Society* **2007**, *129*, 8552-8556.

[5] K. S. Park, Z. Ni, A. P. Cote, J. Y. Choi, R. Huang, F. J. Uribe-Romo, H. K. Chae, M. O'Keeffe and O. M. Yaghi, "Exceptional chemical and thermal stability of zeolitic imidazolate frameworks" *Proc. Natl. Acad. Sci. U. S. A.* **2006**, *103*, 10186-10191.

[6] P. L. Llewellyn, J. P. Coulomb, Y. Grillet, J. Patarin, G. Andre and J. Rouquerol, "Adsorption by MFI-type zeolites examined by isothermal microcalorimetry and neutron diffraction. 2. Nitrogen and carbon monoxide" *Langmuir* **1993**, *9*, 1852-1856.

CHAPTER 5

SELECTION OF MEMBRANE MATERIALS VIA INVESTIGATING ADSORPTION AND DIFFUSION PROPERTIES OF ZEOLITIC IMIDAZOLATE FRAMEWORK-8

5.1 Overview

Chapter 5 discusses selection of membrane materials by studying the fundamental adsorption and diffusion properties of ZIF-8. The capability to control ZIF-8 crystal size enabled reliable and convenient adsorption measurements. Equilibrium sorption isotherms were used to calculate sorption coefficients and sorption selectivity. Analysis of adsorption kinetics was employed to estimate diffusivities and diffusion selectivity. Finally, a polymer matrix was selected to form mixed-matrix membrane with ZIF-8 based on Maxwell modeling results.

5.2 Equilibrium Adsorption

While the target separation of this research was C_3H_6/C_3H_8, the adsorption study was extended to include other gases to fully evaluate the potential of ZIF-8 for gas separations, and also to fundamentally understand adsorption and diffusion in flexible frameworks. Equilibrium adsorption in ZIF-8 was studied using the pressure-decay sorption technique at 35 ^oC. Isotherms for CO_2, N_2, CH_4, C_2H_4, C_2H_6, C_3H_6, C_3H_8, 1-C_4H_8 and n-C_4H_{10} were obtained using the commercial BASF ZIF-8 sample with gas phase equilibrium pressure up to 4 bars, as shown in Figure 5.1 (a). Isotherms for He, H_2,

and O_2 were obtained using the BASF ZIF-8 sample with gas phase equilibrium pressure up to 50 bars, as shown in Figure 5 (b). Diffusion of iso-C_4H_8 and iso-C_4H_{10} was extremely slow and cannot be conveniently measured on the 200 nm BASF ZIF-8 sample. Therefore, a ZIF-8 sample having much smaller crystal size (the 26 nm sample described in section 4.2) with much faster uptake was used to measure isotherms of these branched hydrocarbons, and the results are shown in Figure 5.1 (c). Isotherms for n-C_4H_{10} were measured on both the BASF ZIF-8 and 7.9 μm synthesized ZIF-8 sample (described in section 4.2) and illustrated in Figure 5.1 (d), showing almost identical adsorption capacities. Isotherms in Figure 5.1 were fit using the Langmuir model (equation 2.13) or Henry's law (equation 2.14), and the fitting parameters are listed in Table 5.1.

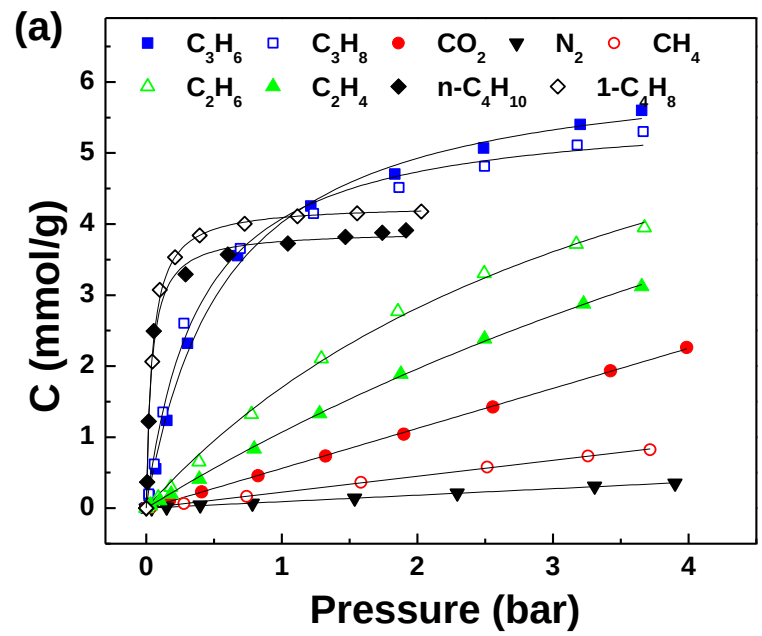
(a)
C3H6
C3H8
CO2
N2
CH4
C2H6
C2H4
n-C4H10
1-C4H8
C (mmol/g)
Pressure (bar)
0
1
2
3
4
5
6

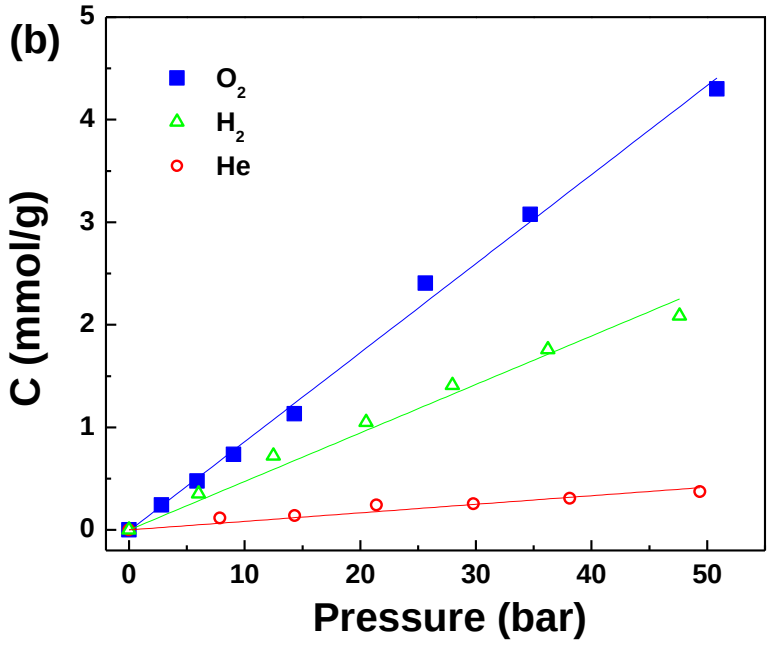
(b)
O2
H2
He
C (mmol/g)
Pressure (bar)
0
10
20
30
40
50
1
2
3
4
5

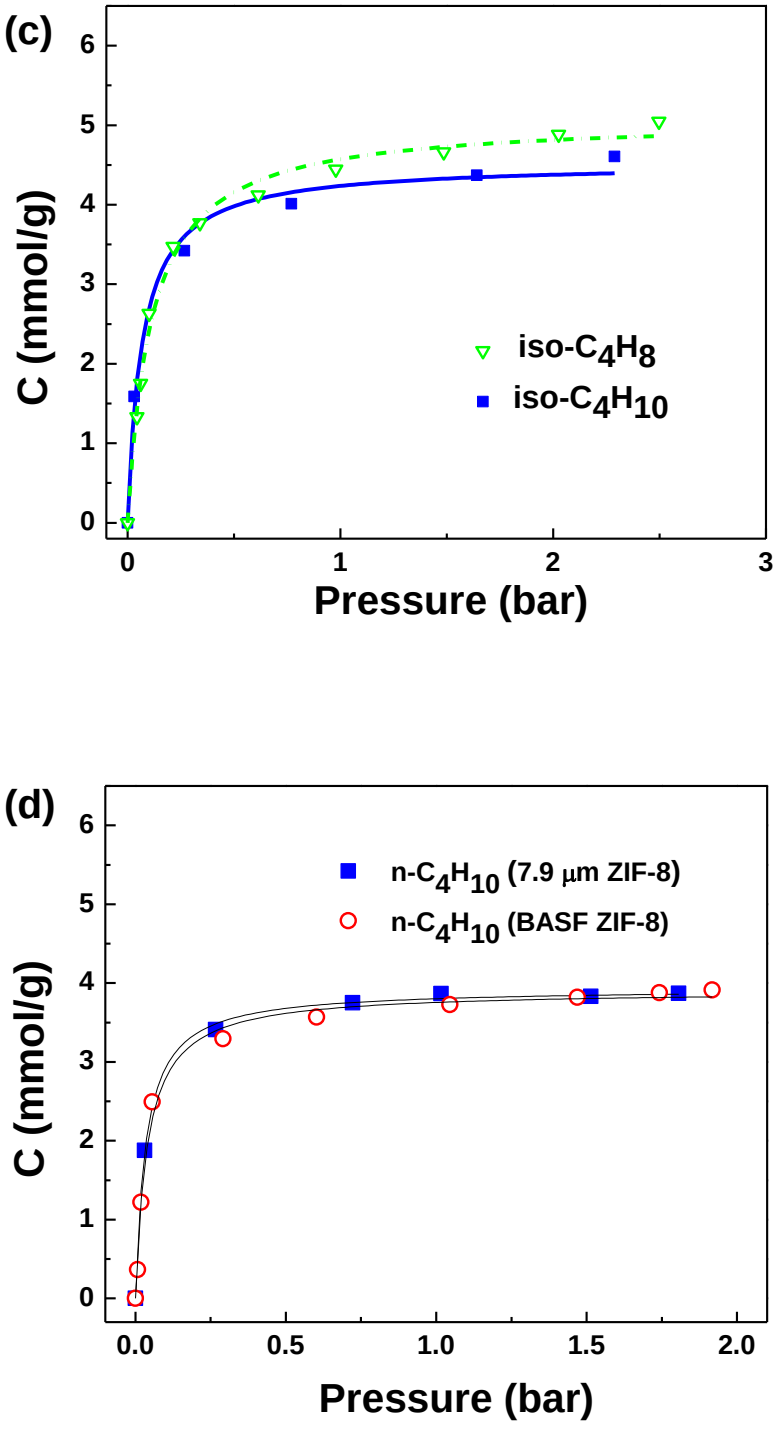

Figure 5.1: (a) & (b) Adsorption isotherms on the BASF ZIF-8 sample at 35 ^{o}C (c) Adsorption isotherms of iso-C_4H_8 and iso-C_4H_{10} on the 26 nm synthesized ZIF-8 sample at 35 ^{o}C (d) Adsorption isotherms of n-C_4H_{10} on the BASF ZIF-8 and 7.9 μm synthesized ZIF-8 samples at 35 ^{o}C

Table 5.1: Langmuir model parameters and Henry's constants at 35 ^{o}C.

Adsorbate	C_S (mmol/g)	b (1/bar)	K (mmol/(g bar))	Polarizability [1] (10^{-24} cm^3)
He	N/A	N/A	0.013	0.21
H_2	N/A	N/A	0.039	0.80
CO_2	N/A	N/A	0.563	2.91
O_2	N/A	N/A	0.087	1.58
N_2	N/A	N/A	0.091	1.74
CH_4	N/A	N/A	0.224	2.59
C_2H_4	11.8	0.10	1.18	4.25
C_2H_6	8.25	0.26	2.15	4.47
C_3H_6	6.36	1.72	10.9	6.26
C_3H_8	5.65	2.59	14.6	6.29
1-C_4H_8	4.28	22.4	95.9	8.52
n-C_4H_{10}*	3.91	24.9	97.4	8.20
iso-C_4H_8**	5.08	9.0	45.7	8.29
iso-C_4H_{10}**	4.53	14.6	66.1	8.14

*Fit using the isotherm on the BASF ZIF-8 sample
** Fit using isotherms on the 26 nm synthesized ZIF-8 sample

Table 5.1 suggests that ZIF-8 was not attractive for equilibrium selectivity-based separations. The selectivity of olefin over corresponding paraffin was scarcely above unity and significantly lower than cationic zeolites [2]. At ambient temperature and low surface coverage (Henry's law region), the isosteric heat of adsorption ΔH (J/mol) is related to the interaction potential energy ϕ (J/mol) between adsorbate molecules and the adsorbent surface, as described by equation 2.12. For a given adsorbent, the non-electrostatic energies are essentially proportional to the polarizability of adsorbate

molecules. Unlike cationic aluminosilicate zeolites (e.g. zeolite A and X) with surface electric charges, the surface of ZIF-8 is non-polar and absent of free charges. Therefore, the interaction potentials in ZIF-8 should be dominated by non-electrostatic energies and the isosteric heats of adsorption in ZIF-8 are expected to be proportional to adsorbate polarizabilities. Due to time constraints, equilibrium adsorption data were not collected at multiple temperatures in our study, and therefore, the value of ΔH cannot be determined experimentally. Nevertheless, as shown by Figure 5.2, the logarithm of Henry's constants ($\ln K$) on ZIF-8 at 35 ^{o}C is generally linearly correlated to adsorbate polarizabilities. While it does not necessarily indicates the absence of any field-dipole and field gradient-quadrupole interactions, the good correlation strongly suggests that the interaction potentials between the studied adsorbate molecules and ZIF-8 surface are dominated by non-electrostatic energies. While the quardupole moment of N_2 is almost three times larger than O_2 (-5.0×10^{-40} vs. -1.3×10^{-40} C m^2), N_2 adsorbs slightly stronger than O_2 on ZIF-8 merely due to its marginally higher polarizability.

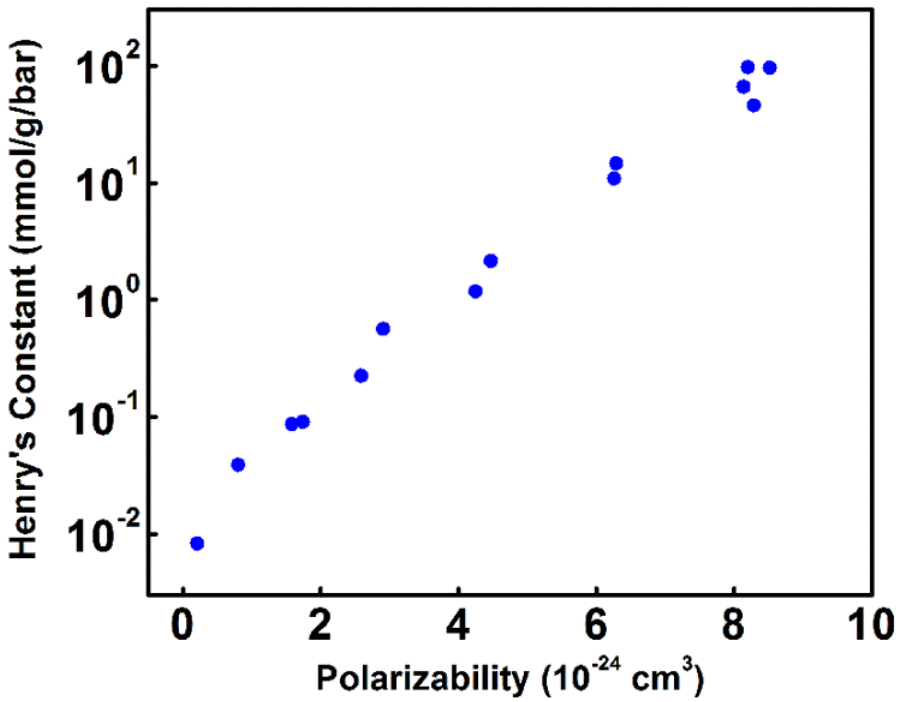

Figure 5.2: Henry's constants in ZIF-8 (35 ^{o}C) versus adsorbate polarizability.

5.3 Adsorption Kinetics and Diffusivity Calculations

5.3.1 Measurements of Kinetic Adsorption

Measurements of kinetic adsorption have been among the oldest and most reliable techniques to estimate transport diffusivities in micropores of microporous materials such as zeolites, carbon molecular sieves, and MOFs/ZIFs [3]. The kinetic uptake curve can be obtained by monitoring either the decreasing rate of sample chamber pressure (piezometric) or increasing rate of sample weight (gravimetric) during adsorption.

Illustration of the pressure decay adsorption device employed for gas kinetic uptake measurements can be found elsewhere [4]. After thermal equilibrium was obtained in the reservoir, the valve connecting the sample chamber and reservoir was opened shortly (typically ~ 1 sec) and then closed. The initial data points (typically 5~20 seconds) after closing the valve were not used to plot the experimental uptake curve since they were influenced by response of the pressure transducer as well as rapid expansion of gases upon opening of the valve [5]. The actual sample chamber pressure right after closing the valve (t=0) was calculated by mass balance using the reservoir pressure (after closing the valve) and the known volumes of the sample chamber and reservoir, in order to obtain the entire uptake curve. Typical pressure profiles of pressure-decay sorption and the corresponding kinetic uptake curve are shown in Figure 5.3.

The ability to manipulate crystal size as discussed in Chapter 4 enabled the possibility of using kinetic adsorption to study intracrystalline diffusion phenomena in ZIF-8. As will be shown later, transport diffusivities of C_3 and C_4 hydrocarbons differ by ten orders of magnitude in ZIF-8 and hence it was impractical to reliably and conveniently measure diffusivities of all the studied adsorbates in a ZIF-8 sample with a particular crystal size. The 26 nm, 7.9 μm, and 162 μm ZIF-8 sample described in section 4.2 were used for kinetic uptake rate measurements, in which uptake of iso-C_4H_8/iso-C_4H_{10}, 1-C_4H_8/n-C_4H_{10}, and C_3H_6/C_3H_8, respectively, was sufficiently slow to permit reliable estimates of intracrystalline diffusivity at 35^{o}C. The kinetic uptake curves are shown in Figure 5.4.

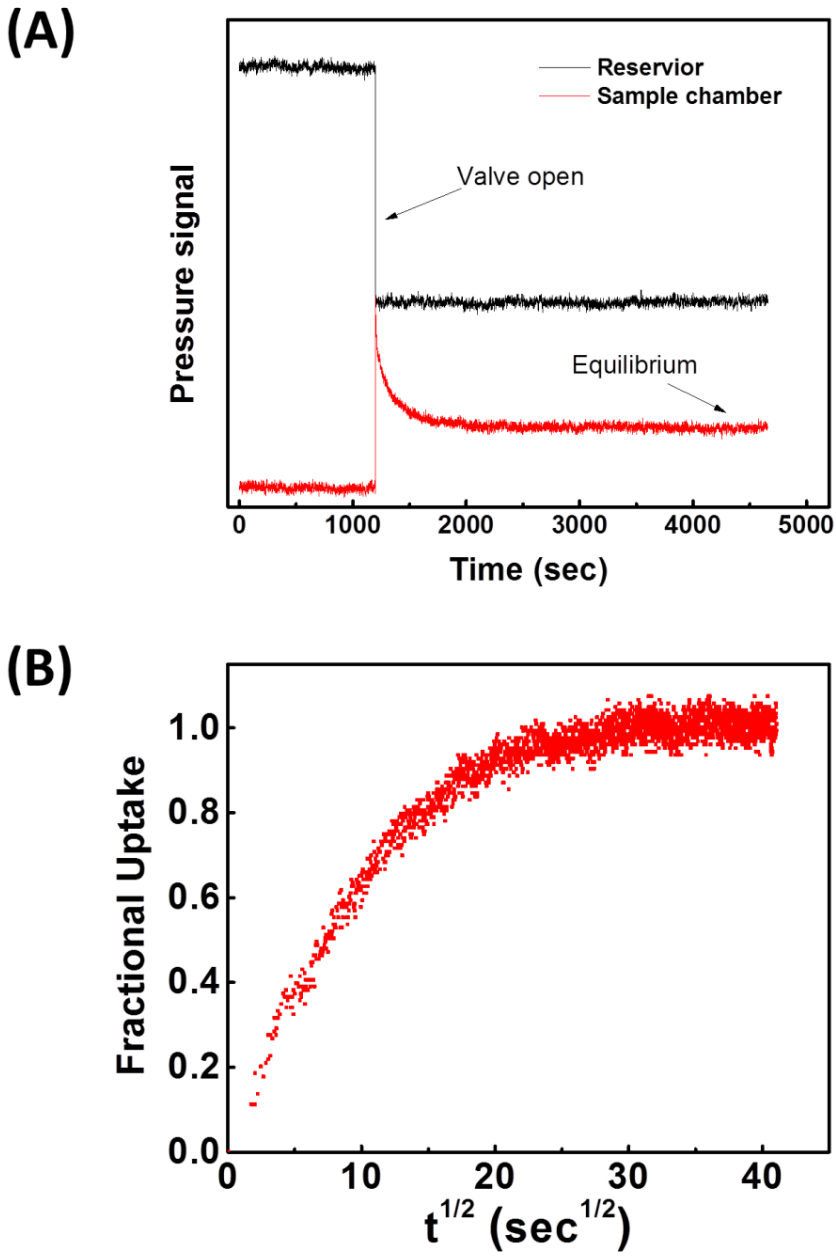

Figure 5.3: (A) Typical pressure profiles of pressure-decay sorption measurements. (B) The corresponding kinetic uptake curve.

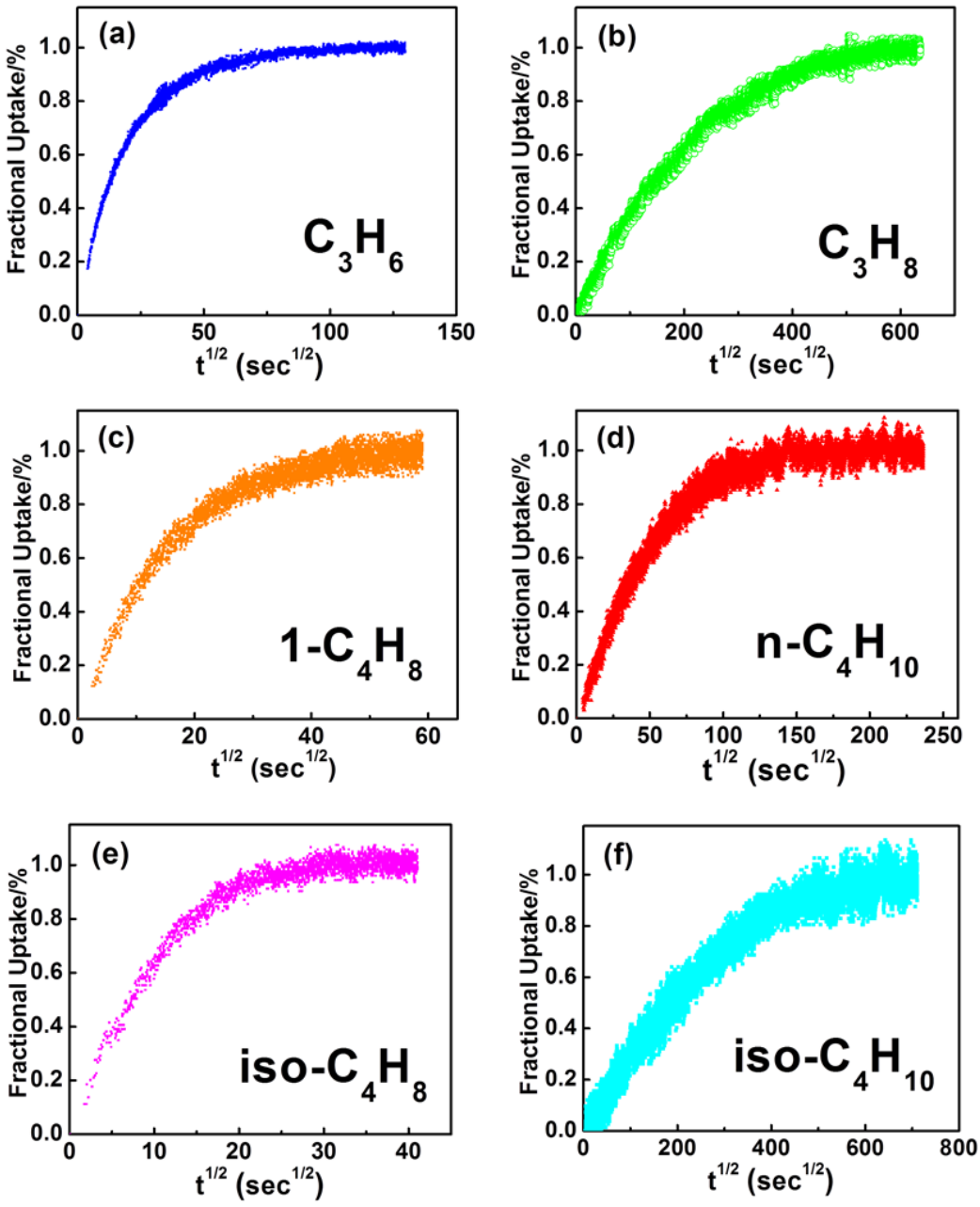

Figure 5.4: Kinetic uptake curves in ZIF-8 at 35 ^{o}C (a) Kinetic uptake curve of C_3H_6 in the 162 μm sample (b) Kinetic uptake curve of C_3H_8 in the 162 μm sample (c) Kinetic uptake curve of 1-C_4H_8 in the 7.9 μm sample (d) Kinetic uptake curve of n-C_4H_{10} in the 7.9 μm sample (e) Kinetic uptake curve of iso-C_4H_8 in the 26 nm sample (f) Kinetic uptake curve of iso-C_4H_{10} in the 26 nm sample.

In Figure 5.4, diffusivities measured from ZIF-8 samples with significantly different crystal sizes (nano- and microcrystals) were compared, based on the knowledge that Fickian diffusivity is not a function of crystal size. This assumption has been shown to be valid for zeolite 5A with relatively rigid frameworks [6]. On the other hand, it has been suggested that vapor transport in polymers can involve a relaxation process due to swelling of polymer chains in addition to Fickian diffusion. For these systems, the shape of kinetic uptake curves may deviate from Fickian type responses depending on the type of polymer, vapor phase activities, as well as polymer sample sizes, etc [7-8]. The framework of ZIF-8 is locally flexible due to rotation of MeIM ligand [9], however; long-range flexibility does not exist in the ZIF-8 framework that is constructed by covalently bonded Zn and MeIM. Therefore, swelling effects are not expected in ZIF-8 and the assumption that Fickian diffusivity of a particular adsorbate is irrelevant of sample size should be valid for this research.

5.3.2 Diffusivity Calculations by Analyzing Adsorption Kinetics

Generally, the effective intracrystalline transport diffusivity D_e can be calculated by fitting the experimental kinetic uptake curves ($M_t / M_\infty \sim t^{1/2}$) in Figure 5.4 with the theoretical uptake curve derived from the analytical solution to the model of transient diffusion with intracrystalline diffusion control [10-11]. For a spherical particle subject to a step change in adsorbate concentration at its external surface at time zero, the fractional uptake is equal to [12]:

$$\frac{M_t}{M_\infty} = 1 - \frac{6}{\pi}\sum_{n=1}^{\infty}\frac{1}{n^2}\exp(-\frac{n^2\pi^2 Dt}{R^2}) \qquad (5.1)$$

where M_t (mmol) and M_∞ (mmol) are moles adsorbed during time t and as $t \to \infty$, D (cm^2/s) is the transport diffusivity, R (cm) is the equivalent spherical crystal radius of the adsorbent particle. In the short time region, the kinetic uptake curve is essentially linear and approximated by [12]:

$$\frac{M_t}{M_\infty} \approx \frac{6}{\sqrt{\pi}}\sqrt{\frac{Dt}{R^2}} \qquad (5.2)$$

In our study, a collection of crystals with non-uniform crystal sizes (Figure 4.1) instead of a single crystal were used for adsorption rate measurements. It was suggested by Ruthven and co-workers [11] that it was not possible to obtain reliable intracrystalline diffusivity data using the average equivalent spherical crystal radius, if the individual crystal sizes are widely distributed. Instead, their study showed that relatively reliable diffusivities can be determined by taking into account the crystal size distribution. For a collection of particles with a size distribution, Equation 5.1 and 5.2 can be re-written as:

$$\frac{M_t}{M_\infty} = \sum_i X_i(\frac{M_t}{M_\infty})_i = 1 - \frac{6}{\pi}\sum_i\sum_{n=1}^{\infty} X_i\frac{1}{n^2}\exp(-\frac{n^2\pi^2 Dt}{R_i^2}) \qquad (5.3)$$

$$\frac{M_t}{M_\infty} = \sum_i X_i(\frac{M_t}{M_\infty})_i \approx \frac{6}{\sqrt{\pi}}\sum_i X_i\sqrt{\frac{Dt}{R_i^2}} \qquad (5.4)$$

Where X_i is the weight fraction of particles with a radius of R_i.

The effective transport diffusivity D_e obtained by matching the experimental kinetic uptake curves in Figure 5.4 with equation 5.4 will be equal to the corrected diffusivity D_0 only if [3] (1) the uptake is controlled by intracrystalline diffusion (2) the temperature of the adsorbent particle is constant during the uptake, i.e. isothermal adsorption (3) the adsorbate concentration is constant during the uptake in the ambient of the particle (4) the concentration in the adsorbent particle is sufficiently low and the concentration change is differential.

In our study, pure gases were introduced into the sample chamber without a carrier gas and hence transport is only limited by intracrystalline diffusion in the ultramicropores. For kinetic uptake curves shown in Figure 5.4, the adsorption rate was sufficiently slow compared to heat dissipation and therefore the assumption of isothermal adsorption should be valid. However, since the adsorption rate was measured by decreasing pressure in the sample chamber, a deviation from the third assumption was inevitable. Hence, instead of using equation 5.4 to calculate diffusivities, a modified model taking into account the non-constant boundary concentration was used to calculated transport diffusivity of the studied C_3 and C_4 hydrocarbons in ZIF-8. Moreover, the fourth assumption was not satisfied either. The adsorption isotherm of the strongly adsorbed C_3 and C_4 hydrocarbons are non-linear during the uptake, and therefore the loading dependence was also taken into account for diffusivity calculations, which will be shown later.

In the short time region, transient diffusion in a spherical particle with decreasing adsorbate concentration in the ambient can be described as:

$$\frac{M_t}{M_\infty} \approx (1+\alpha)\left[1-\frac{\gamma_1}{\gamma_1+\gamma_2}\,eerfc\left\{\frac{3\gamma_1}{\alpha}\left(\frac{Dt}{R^2}\right)^{1/2}\right\}-\frac{\gamma_2}{\gamma_1+\gamma_2}\,eerfc\left\{\frac{3\gamma_2}{\alpha}\left(\frac{Dt}{R^2}\right)^{1/2}\right\}\right] \quad (5.5)$$

$$\alpha = \frac{1}{\Lambda} - 1 \quad (5.6)$$

$$eerfc(z) \equiv \exp\left(z^2\right) \times erfc(z) \quad (5.7)$$

Where Λ is the fraction of adsorbate added in the step that is finally adsorbed by the adsorbent particle, γ_1 and γ_2 are functions of α. Similarly to equation 5.2, for a collection of particles with a size distribution, equation 5.7 can be re-written as:

$$\frac{M_t}{M_\infty} = \sum_i X_i \left(\frac{M_t}{M_\infty}\right)_i \approx \sum_i X_i (1+\alpha) \times\left[1-\frac{\gamma_1}{\gamma_1+\gamma_2}\,eerfc\left\{\frac{3\gamma_1}{\alpha}\left(\frac{Dt}{R_i^2}\right)^{1/2}\right\}-\frac{\gamma_2}{\gamma_1+\gamma_2}\,eerfc\left\{\frac{3\gamma_2}{\alpha}\left(\frac{Dt}{R_i^2}\right)^{1/2}\right\}\right] \quad (5.8)$$

In our work, effective diffusivities of the studied C_3 and C_4 hydrocarbons were obtained by matching the initial region of the experimental uptake curves ($0 < M_t / M_\infty < 0.2$) in Figure 5.4 to the theoretical uptake curve derived from equation 5.8 for a collection of particles.

For less strongly adsorbed species (i.e. He, H_2, CO_2, O_2, N_2, and CH_4), the isotherm is essentially linear in the studied pressure range. According to equation 2.17, D will be essentially identical to D_0. For more strongly adsorbed species (i.e. C_2H_4, C_2H_6, C_3H_6, C_3H_8, 1-C_4H_8, n-C_4H_{10}, iso-C_4H_8, and iso-C_4H_{10}), however, D/D_0 will be non-negligible even at low pressures due to curvature of the adsorption isotherm. Therefore, to study the molecular sieving behavior of ZIF-8, it is more meaningful to compare the thermodynamically corrected diffusivity D_0 instead of the loading-dependent transport diffusivity D_e.

For macroscopic kinetic uptake rate measurements, it is preferred to have differential concentration change during the uptake. However, in our study, the size of the concentration step was limited by the sensitivity of the pressure transducer. The studied C_3 and C_4 hydrocarbons adsorb very strongly on ZIF-8 and the isotherms were not linear during the uptake. Therefore, the effective diffusivity obtained previously was actually an averaged value [10]:

$$\frac{D_e}{D_0} = \frac{5}{3}\frac{1}{(\theta_\infty^{5/3} - \theta_0^{5/3})}\int_{\theta_0}^{\theta_\infty} \theta^{2/3} f(\theta) d\theta \qquad (5.9)$$

Where θ_0 and θ_∞ are surface fractional coverage at the beginning and the end of the uptake. If the adsorption isotherm is Langmuir type, equation 5.9 can be further written as [10]:

$$\frac{D_e}{D_0}=\frac{5}{U_\infty^5-U_0^5}\{\frac{1}{6}\ln\left[\frac{(1+U_\infty+U_\infty^2)}{(1-U_\infty)^2}\frac{(1-U_0)^2}{(1+U_0+U_0^2)}\right] \\ -\frac{1}{\sqrt{3}}\tan^{-1}\left(\frac{1+2U_\infty}{\sqrt{3}}\right)+\frac{1}{\sqrt{3}}\tan^{-1}\left(\frac{1+2U_0}{\sqrt{3}}\right)-\frac{U_\infty^2}{2}+\frac{U_0^2}{2}\} \tag{5.10}$$

Where $U_0=\theta_0^{1/3}$ and $U_\infty=\theta_\infty^{1/3}$.

Uncertainties of diffusivity data obtained from kinetic uptake rate measurements may arise from approximating the polyhedral microcrystals to be spherical particles. It has been suggested [3] that the crystal shape has negligible effects on the slope of uptake curve in its initial region, as long as the crystal size is approximated by the equivalent spherical radius. In my study, since diffusivities were obtained from the initial region of the experimental uptake curves, the uncertainties arising from crystal shape should be quite limited.

The corrected transport diffusivities of the studied C_3 and C_4 hydrocarbons in ZIF-8 are shown in Table 5.2. D_{ES-4} is the effective transport diffusivity obtained by matching the region of $0<M_t/M_\infty<0.2$ of the uptake curve in Figure 4 with equation 5.4, using the average crystal radii $\bar{R}$. D_{ES-8} is the effective transport diffusivity obtained by matching the region ($0<M_t/M_\infty<0.2$) of the uptake curve in Figure 4 with equation 5.8. For the studied C_3 and C_4 hydrocarbons, a comparison of D_{ES-4} and D_0 shows that neglecting the fact of non-constant boundary concentration and the loading dependence of transport diffusivity will lead to significantly overestimated values.

Table 5.2: Corrected diffusivities of the studied C_3 and C_4 hydrocarbons in ZIF-8 at 35 ^oC ($\theta_0 = 0$ for all cases).

	$D_{ES\text{-}4}$ (cm^2/s)	$D_{ES\text{-}8}$ (cm^2/s)	Λ	θ_∞	D_e/D_0	D_0 (cm^2/s)
C_3H_6	4.6×10^{-8}	3.3×10^{-8}	0.16	0.18	1.13	2.9×10^{-8}
C_3H_8	3.1×10^{-10}	2.2×10^{-10}	0.213	0.13	1.09	2.0×10^{-10}
1-C_4H_8	1.4×10^{-10}	1.9×10^{-11}	0.66	0.51	1.52	1.3×10^{-11}
n-C_4H_{10}	1.2×10^{-11}	8.0×10^{-12}	0.20	0.43	1.40	5.7×10^{-12}
iso-C_4H_8	3.8×10^{-15}	5.2×10^{-16}	0.65	0.29	1.23	4.2×10^{-16}
iso-C_4H_{10}	4.3×10^{-18}	2.7×10^{-18}	0.15	0.22	1.16	2.3×10^{-18}

The six-ring β-cage aperture of ZIF-8 was determined to be 3.4 Å by single-crystal XRD [13]. However, the above adsorption study clearly showed that C_3 and C_4 hydrocarbons with significantly larger molecular size were able to diffuse into ZIF-8's ultramicroporous network. This suggests that unlike zeolites with more rigid structures, ZIF-8's framework is flexible at ambient temperature, presumably due to rotation of the MeIM ligand upon pressure or introduction of guest molecules [9]. As a result, sharp molecular sieving "cut-off" does not exist at its crystallographic aperture size.

Usually, a flexible structure is undesirable for a molecular sieving material to be capable for molecular size/shape-based separations. However, the flexible nature of ZIF-8's framework can be used to take advantage for separation of C_3 and C_4 hydrocarbons, which were not supposed to adsorb in ZIF-8 if the framework is rigid. For the species shown in Table 5.2, ZIF-8's ultramicroporous network is flexible enough to enable adsorption, yet is sufficiently rigid to achieve molecular size/shape-based separations.

Uptake of He, H_2, CO_2, O_2, N_2, CH_4, C_2H_4, and C_2H_6 in the largest ZIF-8 crystals were still too fast to permit reliable diffusivity estimates. Instead of pursuing the synthesis of ZIF-8 samples with even larger crystal sizes (which are of less practical importance), I used mixed matrix membrane permeation as an alternative to obtain the transport diffusivities of these faster diffusing gases in ZIF-8, which will be discussed in Chapter 6.

5.4 Evaluation of ZIF-8 for Adsorptive Separation and Membrane Separation

5.4.1 Evaluation of ZIF-8 for Adsorptive Separation

Based on the adsorption study discussed in sections 5.2 and 5.3, I further evaluated the potential of ZIF-8 as an adsorbent and membrane material for separation of binary hydrocarbon mixtures, i.e. C_3H_6/C_3H_8, 1-C_4H_8/n-C_4H_{10}, iso-C_4H_8/iso-C_4H_{10}, 1-C_4H_8/iso-C_4H_8, and n-C_4H_{10}/iso-C_4H_{10}. The low-molecular weight olefins and iso-paraffins are essential ingredients to the alkylation process for production of premium motor fuels with high-octane values [14-15].

The molecular sieving nature of ZIF-8 makes it a potential candidate for kinetic selectivity-based adsorptive separations, in which separation of a gas mixture by passing through an adsorbent bed is achieved based on the difference in diffusion rates rather than adsorption strength. For separation of butane isomers (n-C_4H_{10}/iso-C_4H_{10}) and butylene isomers (1-C_4H_8/iso-C_4H_8), the slower diffusing branched hydrocarbons (iso-C_4H_8 or iso-C_4H_{10}) are usually more valuable products. Their enrichment in the raffinate could be

efficiently achieved on a ZIF-8 adsorbent bed thanks to large differences in diffusion rates between linear and branched hydrocarbons. For olefin/paraffin separations (i.e. C_3H_6/C_3H_8, $1\text{-}C_4H_8/n\text{-}C_4H_{10}$, and $iso\text{-}C_4H_8/iso\text{-}C_4H_{10}$), however, the faster and more adsorbed olefin is the desired product, which has to be recovered as desorbate streams from the ZIF-8 adsorbent bed by applying temperature swing or displacement desorption process. Since paraffins adsorb in ZIF-8 simultaneously, the purity of olefins in the desorbate stream is dependent not only on the relative diffusion rate of olefin/paraffin, but also on their relative adsorption strength [2]:

$$s = \frac{K_O}{K_P}\sqrt{\frac{D_O}{D_P}} \tag{5.11}$$

$$Y = \frac{s}{1+s} \times 100\% \tag{5.12}$$

Where s is the separation factor, Y (%) is the purity of olefins in the desorbate stream, K_O and K_P (mmol/g/bar) are Henry's constants of olefin and paraffin, D_O and D_P (cm^2/s) are diffusivity of olefin and paraffin. The square root dependence on D_O/D_P appears due to the transient uptake relationship in a time varying PSA process. Since paraffin is the more strongly adsorbed species on ZIF-8, K_O/K_P is smaller than unity. This suggests that in a PSA process, the effective diffusion selectivity of olefin/paraffin on ZIF-8 is offset by the stronger adsorbed paraffins. Table 5.3 shows that in a PSA process, as a kinetically selective adsorbent, ZIF-8 is ideally capable of enriching 90% C_3H_6 and 90% $iso\text{-}C_4H_8$ streams from binary mixtures of C_3H_6/C_3H_8 and $iso\text{-}C_4H_8/iso\text{-}$

C_4H_{10}, respectively. While the diffusion rate of C_3H_6 is 2~4 orders of magnitude higher, ZIF-8 as a kinetically selective adsorbent is not competitive with small pore eight-ring zeolite in terms of product purity, in which desorbate streams with 99% C_3H_6 purity was expected [2].

Table 5.3: Evaluation of ZIF-8 as kinetically-selective adsorbents for olefin/paraffin separations.

	K_O/K_P	D_O/D_P	s	Y /%
C_3H_6/C_3H_8	0.77	140*	9.1	90%
1-C_4H_8/n-C_4H_{10}	1.0	2.3	1.5	60%
iso-C_4H_8/iso-C_4H_{10}	0.67	180	8.9	90%

5.4.2 Evaluation of ZIF-8 for Membrane Separation

On the other hand, the following analysis shows that efficient separation of hydrocarbon mixtures may be realized by membranes fabricated with ZIF-8. Moreover, forming membranes from zeolites or using them in hybrid materials is much more challenging vs. the case with ZIF-8. Assuming Langmuir sorption isotherm, equation 5.13 can be derived based on equation 2.4-2.6 to calculate permeability in a pure ZIF-8 membrane under upstream pressure of p_1 and downstream pressure of p_2:

$$P = \tilde{D} \times \tilde{S} = \frac{D_0 C_s}{p_2 - p_1} \ln \frac{C_s - C_1}{C_s - C_2} = \frac{D_0 C_s}{p_2 - p_1} \ln\left(\frac{1 + bp_2}{1 + bp_1}\right) \qquad (5.13)$$

If vacuum exists at the membrane downstream, equation 5.13 can be simplified to:

$$P = \tilde{D} \times \tilde{S} = \frac{D_0 C_s}{p_2} \ln \frac{C_s}{C_s - C_2} = \frac{D_0 C_s}{p_2} \ln(1 + bp_2) \tag{5.14}$$

Table 5.4 and 5.5 show the pure component permeability and selectivity of C_3 and C_4 hydrocarbons on a pure ZIF-8 membrane operated at 35^{o}C and 2 bars upstream pressure (vacuum in the downstream). The calculations were done with equation 5.14 using parameters (C_s, b, and D_0) in Table 5.1 and 5.2. For separation of C_3H_6/C_3H_8 and iso-C_4H_8/iso-C_4H_{10}, a membrane is obviously the more favorable option over adsorption in terms of product purity. The estimated pure component permselectivity of C_3H_6/C_3H_8 and iso-C_4H_8/iso-C_4H_{10} on a pure ZIF-8 membrane were 130 and 180, respectively, which are promising to produce high purity olefin in the permeate. However, it should be noted that in the case of iso-C_4H_8/iso-C_4H_{10} separation, the permeability of iso-C_4H_8 was so low that an unreasonably thin ZIF-8 layer would have to be fabricated to achieve a practical productivity at 35 ^{o}C.

The potential of using ZIF-8 as a membrane material for separation of C_3H_6/C_3H_8 mixtures was compared with that of small pore (~3.8 Å) eight-ring zeolites in Table 5.6, whose apertures are relatively rigid. While the C_3H_6/C_3H_8 kinetic selectivity (10^4-infinity) of these rigid molecular sieves are much higher than that of ZIF-8 with flexible structure, the diffusion rates of C_3H_6 in these small pore zeolites are 10^2-10^4 times lower. Therefore, ZIF-8 is obviously the preferred membrane material in terms of overall process economics since a membrane with C_3H_6/C_3H_8 permselectivity over 35 is high

enough to replace the C_3 splitter in the configuration of a three-stage membrane separator [16].

Table 5.4: Estimated permeability on a pure ZIF-8 membrane operated at 35 ^{o}C and 2 bars upstream pressure.

Separation	Permeability (Barrer)
C_3H_6	390*
C_3H_8	2.9*
1-C_4H_8	0.30
n-C_4H_{10}	0.12
iso-C_4H_8	8.8E-6
iso-C_4H_{10}	5.0E-8

Table 5.5: Estimated ideal permselectivity on a pure ZIF-8 membrane operated at 35 ^{o}C and 2 bars upstream pressure.

Separation	Permselectivity
Olefin/paraffin separations	
C_3H_6/C_3H_8	130
1-C_4H_8/n-C_4H_{10}	2.5
iso-C_4H_8/iso-C_4H_{10}	180
Isomer separations	
1-C_4H_8/iso-C_4H_8	3.4×10^4
n-C_4H_{10}/iso-C_4H_{10}	2.4×10^6

Table 5.6: Comparison of ZIF-8 with small pore eight-ring zeolites for C_3H_6/C_3H_8 separations at 35 ^oC.

Molecular sieve	D_{C3H6} (cm^2/s)	P_{C3H6} (Barrer)	$\alpha(C_3H_6/C_3H_8)$
ZIF-8	3×10^{-8}	390	130
AlPO-14 [17]	4×10^{-10}	<1.5	$>10^4$
SiCHA [2]	7×10^{-11}	<0.5	$>10^4$
DD3R [2]	5×10^{-12}	<0.5	$>10^4$
4A [2]	1×10^{-12}	<0.5	$>10^4$

It should be noted that the above analysis was based on pure component adsorption and permeation measurements. In realistic conditions with mixture feeds, the mobility of faster diffusing component might be reduced, which may result in a decreased kinetic selectivity and permselectivity.

Testing permeation properties of a pure molecular sieving membrane with probe penetrants could be used to study its molecular sieving properties, as long as differences in adsorption capacities of the penetrants can be taken into account. This approach, however, is less reliable for large penetrants with very slow permeation rates. Due to intrinsic limitations of permeation tests (e.g. system leaking rate and gas chromatography sensitivity), membrane defects, and possible grain boundaries, it is impractical to unbiasedly determine the actual permeation flux of these slowly diffusing penetrants. Tomita and co-workers [18] reported pure gas permeances of zeolite DDR membrane that was formed on a porous alumina substrate. The reported “permeance-kinetic diameter”

curve flattened out for n-C_4H_{10}, iso-C_4H_{10}, and SF_6, which may potentially be attributed to few defects on the membrane. Similarly, Pan and co-workers [19] reported C_3H_6/C_3H_8 permselectivity of ~15 and almost identical permeances of n-C_4H_{10} and iso-C_4H_{10} on a ZIF-8/α-alumina composite membrane, which were inconsistent with the values that we obtained from kinetic uptake measurements (Table 5.5). These inconsistencies were probably due to the defective nature of the pure ZIF-8 layer, which was confirmed by their later work [20] reporting much higher C_3H_6/C_3H_8 permselectivities. Unfortunately, permeation results of C_4 hydrocarbons were not reported in their later work.

5.5 Selection of Polymer Matrix and Estimation of Mixed-Matrix Membrane Performance

Based on estimated permeability and selectivity of pure ZIF-8 material, a polymer matrix may be selected to form mixed-matrix materials with attractive C_3H_6/C_3H_8 separation performance. Ideally, the polymer should be a high performance glassy polymer close to or on the polymer "permeability-selectivity" trade-off curve with desirable spinnability that enables the potential to be formed into hollow fibers. Moreover, the polymer matrix should be "matched" with the molecular sieve in terms of C_3H_6 permeability. Figure 5.5 shows the chemical structures of several high-performance polyimides that were considered to for mixed-matrix membrane fabrication. The C_3H_6/C_3H_8 transport properties of these polymers are summarized in Table 5.7.

Polymer	Chemical structure
6FDA-DAM	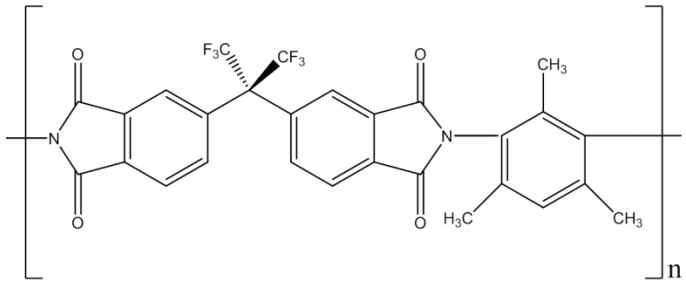
6FDA/BPDA-DAM	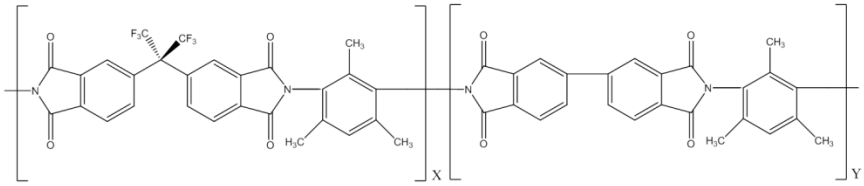
6FDA-6FpDA	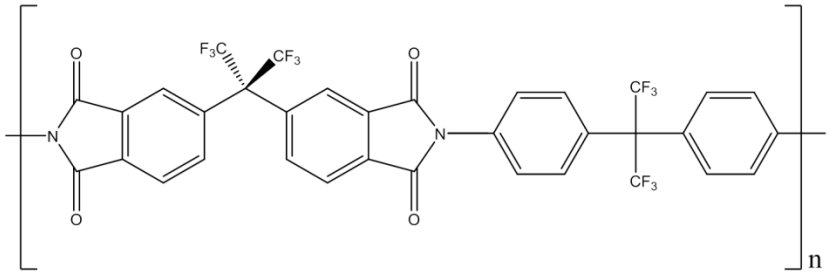
Matrimid®	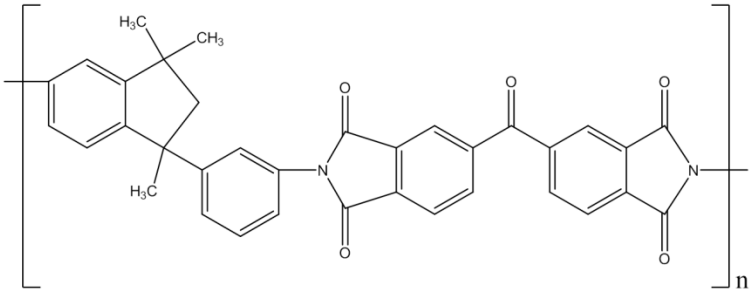

Figure 5.5: Chemical structures of several polyimides considered for mixed-matrix membrane fabrication.

Table 5.7: C_3H_6/C_3H_8 separation performance of the polyimides shown in Figure 5.5. Permeation in Matrimid was done at 26 ^oC and 2-3 bars upstream pressure. Others were done at 35 ^oC and 2 bars upstream pressure.

Molecular sieve	P_{C3H6} (Barrer)	$\alpha(C_3H_6/C_3H_8)$
6FDA-DAM	15.7	12.4
6FDA/BPDA-DAM	10.4	14
6FDA-6FpDA[17]	0.7	19
Matrimid®[21]	0.1	16

Figure 5.6 shows how the C_3H_6 permeability and C_3H_6/C_3H_8 selectivity of the ZIF-8-based mixed-matrix membrane should change with different polymer matrices. The calculations were done by Maxwell model (equation 2.18) based on the assumptions that (1) the molecular sieve was ZIF-8 with C_3H_6 permeability of 390 Barrer and C_3H_6/C_3H_8 selectivity of 130 as shown in Table 5.4 and 5.5. (2) The polymer matrix was on the polymer "permeability-selectivity" trade-off curve. (3) The volume percentage of ZIF-8 particles was 60%. Apparently, as the polymer matrix becomes more permeable and less selective, the mixed-matrix material becomes more permeable. On the contrary, there existed an optimal permeability (~60 Barrer) for the polymer matrix, by which a maximum selectivity (~44) was obtained for the mixed-matrix material. Unfortunately, a high-performance upper-bound polymer with C_3H_6 permeability of 60 Barrer is not available at the moment of this research. Therefore, 6FDA-DAM, which is the most permeable upper-bound glassy polyimide with a C_3H_6 permeability of 15.7 Barrer was used as the polymer matrix to form mixed-matrix membrane with ZIF-8.

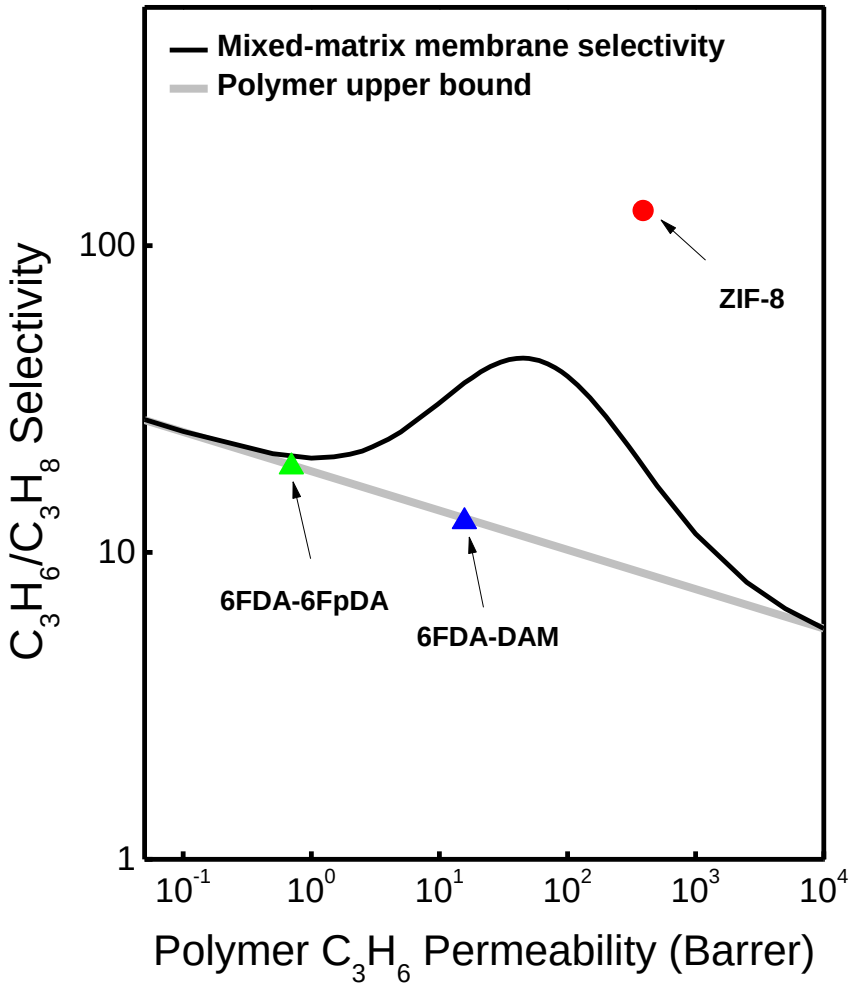

Figure 5.6: Dependence of permeability and selectivity of mixed-matrix materials on permeability of polymer matrix.

For a given dispersed molecular sieve, the more selective polymer matrix may not result in a mixed-matrix material that is more selective. An example is given in Figure 5.7 by comparing two high-performance polyimides 6FDA-DAM and 6FDA-6FpDA. 6FDA-6FpDA is more selective (19 vs. 12.4) than 6FDA-DAM. Attractive enhancements

in C_3H_6/C_3H_8 selectivity were seen in AlPO-14/6FDA-6FpDA mixed-matrix dense film membranes [17]. However, the C_3H_6 permeability of 6FDA-6FpDA (0.7 Barrer) is not as well-matched with ZIF-8 as the more permeable 6FDA-DAM (15.7 Barrer). As a result, ZIF-8 is expected to be more effective to enhance separation performance of 6FDA-DAM than 6FDA-6FpDA. As shown in Figure 5.7, much higher enhancements in C_3H_6/C_3H_8 selectivity would be achieved in ZIF-8/6FDA-DAM than ZIF-8/6FDA-6FpDA at each ZIF-8 loading (30, 45, and 60 vol%). An increase of 158% in C_3H_6/C_3H_8 selectivity is expected for ZIF-8/6FDA-DAM mixed-matrix material with 60 vol% particle loading over neat 6FDA-DAM material. However, for ZIF-8/6FDA-6FpDA, the two materials would be so poorly matched with each other that the selectivity enhancement would be negligible (~6 %) even at 60 vol% particle loading.

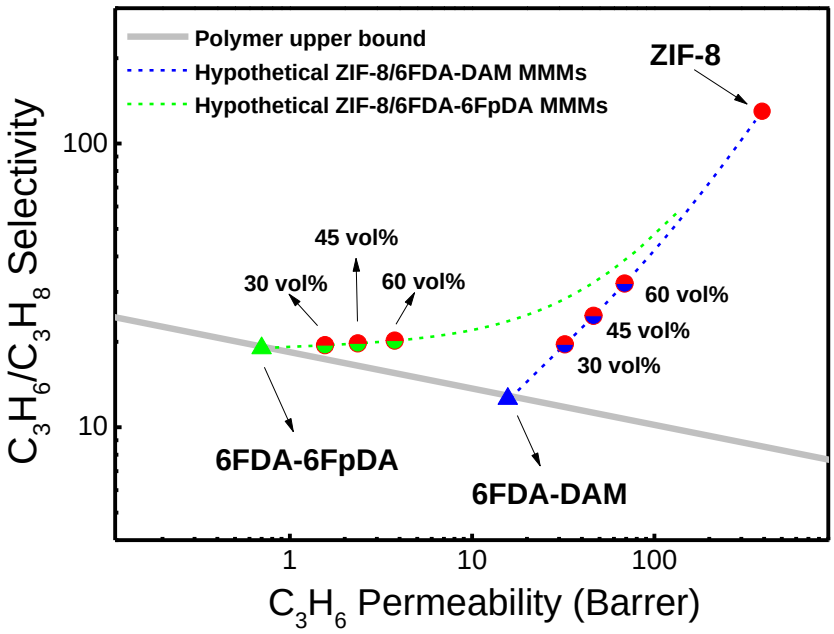

Figure 5.7: Estimated C_3H_6/C_3H_8 transport properties in hypothetical ZIF-8/6FDA-DAM and ZIF-8/6FDA-6FpDA mixed-matrix materials.

5.6 Summary and Conclusions

In this chapter, adsorption and diffusion properties of ZIF-8 were systematically studied to evaluate its potential for adsorptive and membrane separations. Equilibrium sorption showed that ZIF-8 was not particularly attractive for equilibrium selectivity-based separations. Transport diffusivities were obtained by analyzing adsorption kinetics, which demonstrated that ZIF-8 was highly kinetically selective for C_3 and C_4 hydrocarbons. Consequently, ZIF-8 was selected to form mixed-matrix membrane due to its attractive C_3H_6/C_3H_8 separation performance with a C_3H_6 permeability of 390 Barrer and C_3H_6/C_3H_8 selectivity of 130. The Maxwell model was used to estimate transport properties of hypothetical mixed-matrix materials. Based on calculation results, 6FDA-DAM, a high performance upper-bound polyimide, was selected as the continuous polymer matrix to form mixed-matrix membrane with ZIF-8.

5.7 References

[1] D. R. Lide, *Handbook of Chemistry and Physics, 87th Edition*, CRC Press, LLC, **2006**

[2] D. M. Ruthven and S. C. Reyes, "Adsorptive separation of light olefins from paraffins" *Microporous Mesoporous Mat.* **2007**, *104*, 59-66.

[3] J. Karger and D. M. Ruthven, *Diffusion in Zeolites and Other Microporous Solids.*, John Wiley & Sons, Inc., **1991**

[4] J. R. Johnson, PhD Dissertation, Georgia Institute of Technology, 2010.

[5] H. G. Karge and J. Weitkamp, *Adsorption and Diffusion*, Springer-Verlag Berlin Heidelberg, **2008**

[6] H. Yucel and D. M. Ruthven, "DIFFUSION IN 5A-ZEOLITE - STUDY OF THE EFFECT OF CRYSTAL SIZE" *J. Chem. Soc., Faraday Trans.* **1980**, *76*, 71-83.

[7] A. R. Berens and H. B. Hopfenberg, "Diffusion and relaxation in glassy polymer powders: 2. Separation of diffusion and relaxation parameters" *Polymer* **1978**, *19*, 489-496.

[8] D. J. Enscore, H. B. Hopfenberg and V. T. Stannett, "Effect of particle size on the mechanism controlling n-hexane sorption in glassy polystyrene microspheres" *Polymer* **1977**, *18*, 793-800.

[9] D. Fairen-Jimenez, S. A. Moggach, M. T. Wharmby, P. A. Wright, S. Parsons and T. Duren, "Opening the Gate: Framework Flexibility in ZIF-8 Explored by Experiments and Simulations" *J. Am. Chem. Soc.* **2011**, *133*, 8900-8902.

[10] D. M. Ruthven, "Sorption kinetics for diffusion-controlled systems with a strongly concentration-dependent diffusivity" *Chem. Eng. Sci.* **2004**, *59*, 4531-4545.

[11] D. M. Ruthven and K. F. Loughlin, "The effect of crystallite shape and size distribution on diffusion measurements in molecular sieves" *Chem. Eng. Sci.* **1971**, *26*, 577-584.

[12] J. Crank, *The Mathematics of Diffusion*, Oxford University Press Inc., **1975**

[13] K. S. Park, Z. Ni, A. P. Cote, J. Y. Choi, R. Huang, F. J. Uribe-Romo, H. K. Chae, M. O'Keeffe and O. M. Yaghi, "Exceptional chemical and thermal stability of zeolitic imidazolate frameworks" *Proc. Natl. Acad. Sci. U. S. A.* **2006**, *103*, 10186-10191.

[14] J. H. Gary and G. E. Handwerk, *Petroleum Refinning Technology and Economics*, MARCEL DEKKER, INC., **1975**

[15] J. Liu, PhD Dissertation, Georgia Institute of Technology, 2010.

[16] C. W. Colling, G. A. Huff Jr and J. V. Bartels, Process Using Solid Perm-selective Membranes in Multiple Groups for Simultaneous Recovery of Specified Products from a Fluid Mixture. 2004.

[17] M. Das, PhD Dissertation, Georgia Institute of Technology, 2009.

[18] T. Tomita, K. Nakayama and H. Sakai, "Gas separation characteristics of DDR type zeolite membrane" *Microporous Mesoporous Mat.* **2004**, *68*, 71-75.

[19] Y. Pan and Z. Lai, "Sharp separation of C2/C3 hydrocarbon mixtures by zeolitic imidazolate framework-8 (ZIF-8) membranes synthesized in aqueous solutions" *Chem. Commun.* **2011**, *47*, 10275.

[20] Y. Pan, T. Li, G. Lestari and Z. Lai, "Effective separation of propylene/propane binary mixtures by ZIF-8 membranes" *J. Membr. Sci.* **2012**, *390-391*, 93-98.

[21] R. L. Burns and W. J. Koros, "Defining the challenges for C3H6/C3H8 separation using polymeric membranes" *Journal of Membrane Science* **2003**, *211*, 299-309.

CHAPTER 6

DEVELOPMENT OF ZIF-BASED MIXED-MATRIX DENSE FILM MEMBRANES

6.1 Overview

In Chapter 6, mixed-matrix dense film membranes were prepared using the membrane materials (ZIF-8 and 6FDA-DAM) selected in Chapter 5. Membrane morphology was studied and membrane separation performance was extensively evaluated. Permeabilities and diffusivities in pure ZIF-8 phase were estimated based on permeation results of mixed-matrix dense film membranes using the Maxwell model. Molecular sieving properties of ZIF-8 were studied by analyzing the results of adsorption measurements and mixed-matrix dense film permeation. Physical aging of mixed-matrix dense film membrane was discussed as well.

6.2 Hydrophobicity of ZIF-8

The hydrophobicity of ZIF-8 was compared with zeolite LTA, a molecular sieve that has been extensively used as a selective adsorbent in adsorptive separation as well as molecular sieving material in mixed-matrix membrane preparation. Zeolite LTA is well-known for its hydrophilic nature as a moisture adsorbent. It has been used as hydrophilic filler in fabrication of thin film composite reverse osmosis membranes to enhance their water flux [1]. Previous researchers prepared mixed-matrix membrane with zeolite LTA and glassy polymers for CO_2/CH_4 and n/i-butane separations finding that zeolite LTA

was poorly compatible with rigid backbones of glassy polymers, and good polymer-sieve adhesion could not be achieved without inconvenient surface treating of the zeolite [2-3].

The hydrophobicity of ZIF-8 and zeolite 5A was compared using TGA. Crystals of BASF ZIF-8 and zeolite 5A (Sigma-Aldrich, 2 microns) were heated to 400 ^{o}C below their decomposition temperatures with a constant heating rate of 5 ^{o}C /min in a nitrogen atmosphere. Samples were pre-treated with saturated water vapor for 24 hours before the TGA measurements. As shown in Figure 6.1, at 400 ^{o}C, zeolite 5A lost 21.2 % of its weight while ZIF-8 only lost 3.0 % of its weight, showing that ZIF-8 sorbes much less moisture, thereby reflecting the hydrophobic nature of ZIF-8 as compared to zeolite 5A. This marked difference was probably due to the presence of organic imidazolate linkers in the framework, which should make ZIF-8 more compatible with polymers. Such a characteristic could mean that little or no surface treatment is required to achieve good polymer-sieve adhesion.

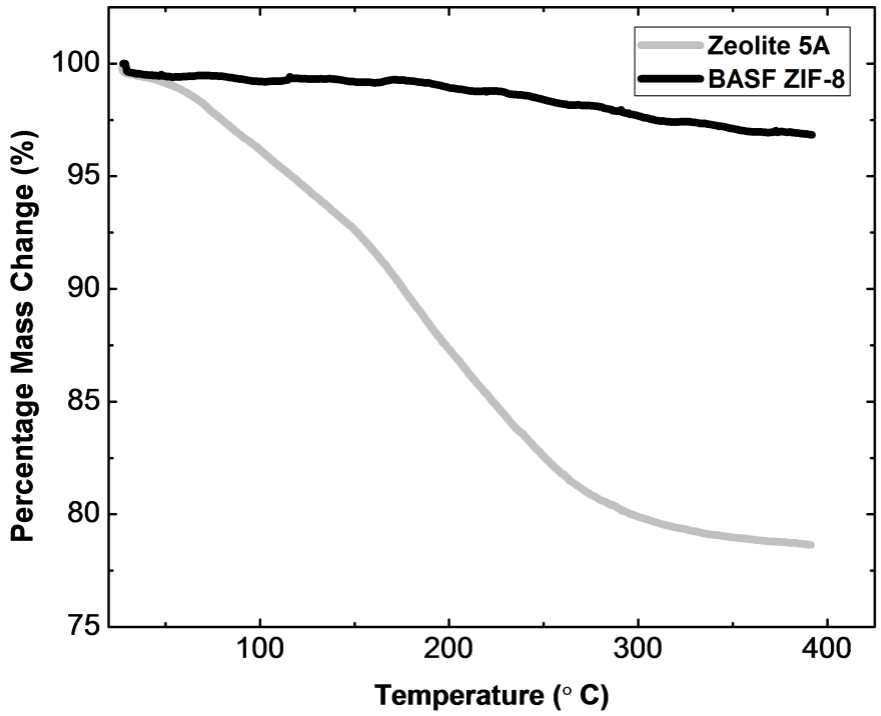

Figure 6.1: TGA analysis results of zeolite 5A and BASF ZIF-8 in a nitrogen atmosphere.

6.3 Morphology of Mixed-Matrix Dense Film Membrane

Three mixed-matrix dense films were prepared with low (DAMZ_1, 16.4 wt%), medium (DAMZ_2, 28.7 wt%), and high (DAMZ_3, 48.0 wt%) ZIF-8 loading. TGA was used to determine accurate ZIF-8 loadings (Appendix B). Figure 6.2 shows SEM images of ZIF-8/6FDA-DAM mixed-matrix dense films, which indicate good contact of bare ZIF-8 to the 6FDA-DAM matrix without the "sieve in a cage" morphology described in section 2.5. It is noteworthy that the good contact was achieved without any surface treatment of the sieve due to the hydrophobicity nature of ZIF-8.

SEM images show that other than well-dispersed 200 nm ZIF-8 particles, there also existed many non-ideal large clusters of ZIF-8 with size ranging from 500 nm to several microns, which was more than an order of magnitude larger than single ZIF-8 particles. Also, the volume fraction of large ZIF-8 clusters in the matrix increased with increasing ZIF-8 loading. Unlike agglomerations of molecular sieve particles that have been previously reported in mixed matrix membranes prepared with other molecular sieves, the surface of these large ZIF-8 clusters as revealed in Figure 6.2 looks fairly smooth. Also, almost no defects were observed for these clusters among all the ZIF-8/6FDA-DAM dense film samples. Since film samples were randomly fractured for SEM analysis, we believe that the mostly non-defective feature of these large ZIF-8 clusters shown in Figure 6.2 is representative of their interior structures. Thompson and co-workers [4] studied the influence of sonication intensity on morphology of ZIF-8 and believed that the formation of this type of "clusters" was a result of Ostwald ripening effects. Despite likely detrimental impacts on the selectivity of the mixed-matrix membrane, significant C_3H_6/C_3H_8 selectivity enhancements were observed by permeation tests for DAMZ_2 and DAMZ_3 with high volume fractions of ZIF-8 clusters, which will be discussed in the following section.

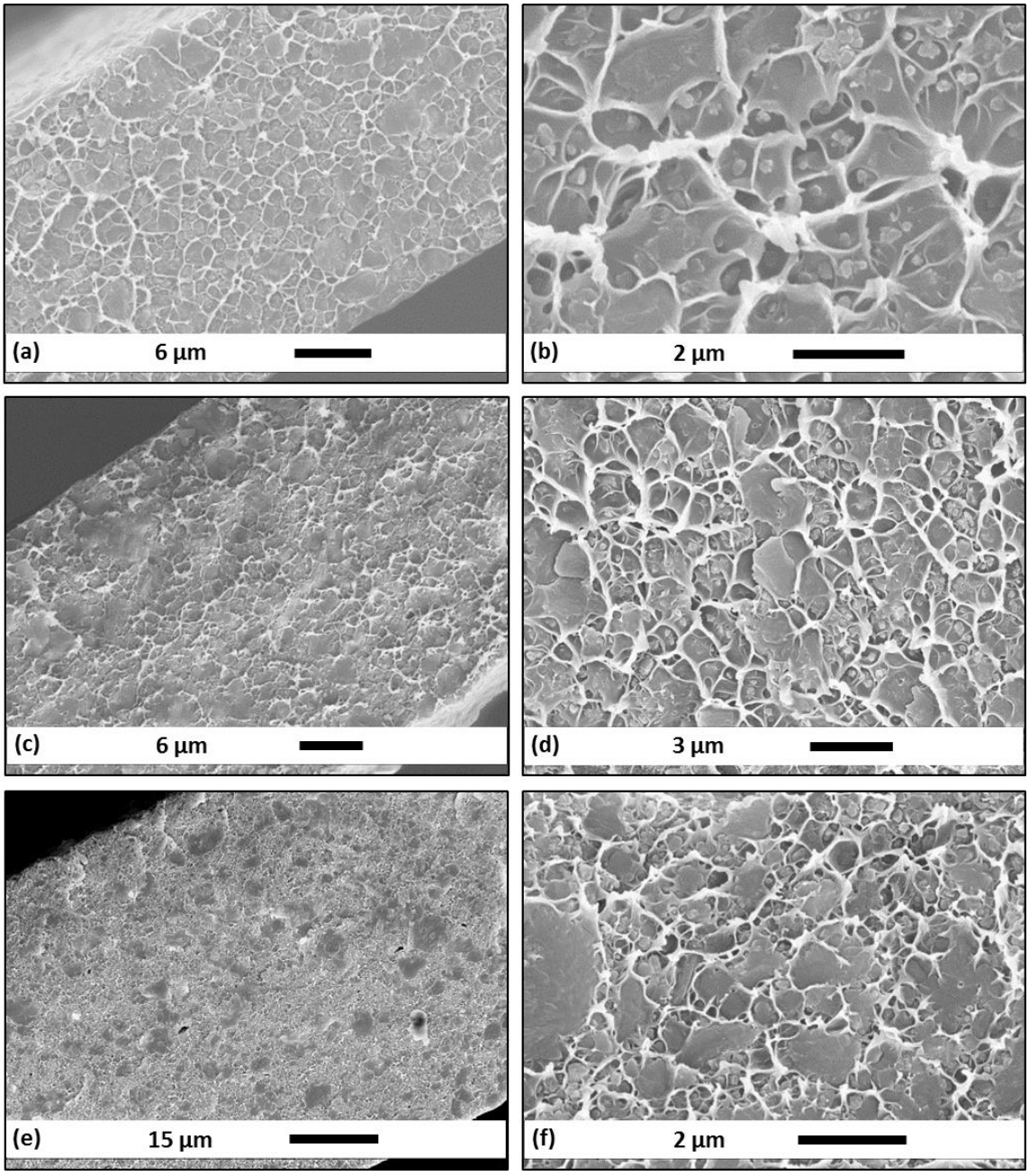

Figure 6.2: SEM images of ZIF-8/6FDA-DAM mixed matrix membrane. (a) & (b) DAMZ_1, (c) & (d) DAMZ_2, (e) & (f) DAMZ_3.

6.4 Separation Performance of Mixed-Matrix Dense Film Membrane

The gas separation performance of neat 6FDA-DAM dense film and ZIF-8/6FDA-DAM mixed-matrix dense films were characterized with singe-gas permeation (He, H_2, CO_2, O_2, N_2, CH_4, C_2H_4, C_2H_6, C_3H_6, and C_3H_8) as well as mixed-gas permeation (50/50 vol% C_3H_6/C_3H_8) at 35 ^oC. The pressure dependence of C_3H_6 permeability and C_3H_6/C_3H_8 was also studied with mixed-gas feed.

6.4.1 Single-Gas Permeation

Permeation properties of neat 6FDA-DAM dense film and ZIF-8/6FDA-DAM mixed-matrix dense films were characterized with He, H_2, CO_2, O_2, N_2, CH_4, C_2H_4, C_2H_6, C_3H_6, and C_3H_8 single gases at 35 ^oC and 2 bars upstream pressure. Permeabilities are summarized in Table 6.1 and plotted in Figure 6.3 with their molecular size. Permeabilities of all components increased with increasing particle loading. Since SEM images have suggested good particle-polymer interfacial adhesion, the increases in permeabilities were believed to be higher intrinsic permeability in ZIF-8 rather than non-ideal interfacial morphologies or membrane defects.

Table 6.1: Permeabilities of neat 6FDA-DAM and ZIF-8/6FDA-DAM mixed-matrix dense film membranes at 35 ^{o}C and 2 bars upstream pressure.

Membrane	Loading (vol %)	P_{He} (Barrer*)	P_{H2} (Barrer)	P_{CO2} (Barrer)	P_{O2} (Barrer)	P_{N2} (Barrer)	P_{CH4} (Barrer)	P_{C2H4} (Barrer)	P_{C2H6} (Barrer)	P_{C3H6} (Barrer)	P_{C3H8} (Barrer)
6FDA-DAM	0	339±17	483	512±25	103±5	27.9±2.5	22.6±2.1	39.4±1.5	12.0±0.2	15.7±1.1	1.27±0.05
DAMZ_1	16.4	621±5	899	781±3	186±4	48.5±0.6	41.2±0.5	72.9±2.5	22.8±0.8	27.6±1.6	1.47±0.13
DAMZ_2	28.7	N/D	N/D	1155±17	N/D	81.3±1.1	72.6±0.6	N/D	N/D	39.8±0.2	1.63±0.01
DAMZ_3	48.0	1590	2600	1590±92	492	143±11	129±9	253±16	86±4	56.2±1.9	1.81±0.08

Table 6.2: Ideal selectivities of neat 6FDA-DAM and ZIF-8/6FDA-DAM mixed-matrix dense film membranes at 35 ^{o}C and 2 bars upstream pressure.

Membrane	Loading (vol %)	α (O_2/N_2)	α (CO_2/CH_4)	α (CO_2/N_2)	α (C_2H_4/C_2H_6)	α (C_3H_6/C_3H_8)	α (H_2/N_2)	α (H_2/CO_2)	α (H_2/CH_4)	α (H_2/C_3H_8)
6FDA-DAM	0	3.9±0.4	22.6±0.9	18.3±0.9	3.3±0.2	12.4±0.5	17.3±1.7	0.95±0.05	21.4±0.6	380±16
DAMZ_1	23.8	4.0±0.1	19.0±0.3	16.1±0.3	3.2±0.2	18.8±0.6	18.5±0.3	1.15	21.8±0.3	612±59
DAMZ_2	39.0	N/D	15.9±0.4	14.2±0.4	N/D	24.4±0.3	N/D	N/D	N/D	N/D
DAMZ_3	59.5	3.5±0.2	12.4±0.6	11.2±1.5	3.0±0.3	31.0±0.4	18.3±1.4	1.6±0.1	20.3±1.4	1440±64

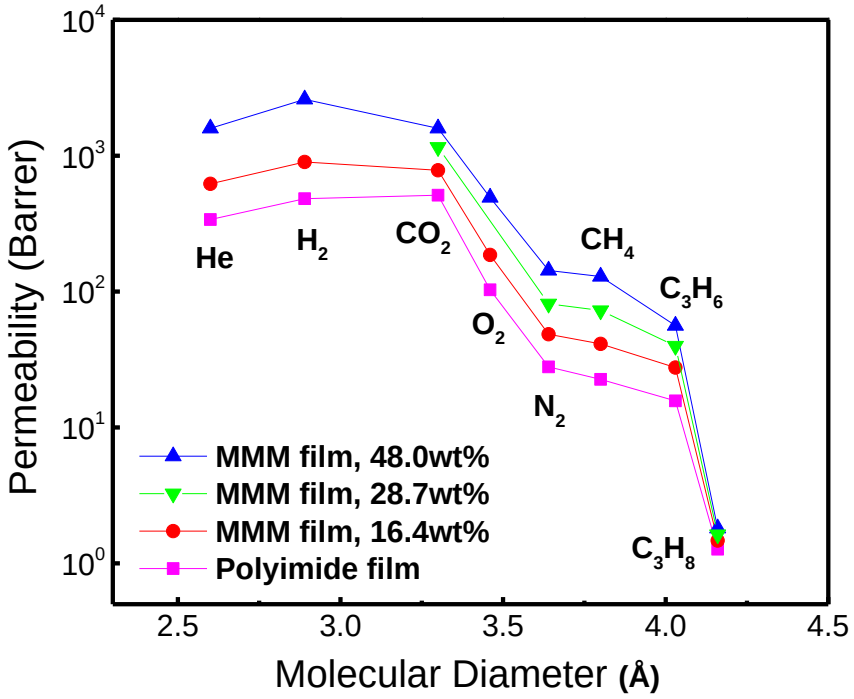

Figure 6.3: Permeabilities of neat 6FDA-DAM dense film membrane and ZIF-8/6FDA-DAM mixed-matrix dense film membranes.

C_3H_6/C_3H_8 ideal selectivities were plotted with C_3H_6 permeability in Figure 6.4, with the "single-gas" upper bound plot of pure polymeric materials for C_3H_6/C_3H_8 separation [5]. The permeability of C_3H_6 was increased greatly relative to C_3H_8 in the mixed-matrix membrane, resulting in significantly enhanced C_3H_6/C_3H_8 ideal selectivity. Since SEM images have suggested good particle-polymer interfacial adhesion, the increases in C_3H_6/C_3H_8 ideal selectivity were believed to be higher intrinsic C_3H_6/C_3H_8 selectivity in ZIF-8 than the neat 6FDA-DAM polymer, which was also consistent with the results of adsorption study in section 5.3.2. For the mixed-matrix dense film

membrane with the highest ZIF-8 loading (DAMZ_3, 48.0 wt%), C_3H_6 permeability was enhanced by 258 % while C_3H_6/C_3H_8 ideal selectivity was enhanced by 150 % compared to the neat 6FDA-DAM film. This was among the highest separation performance enhancements that have ever been seen in mixed-matrix materials. The polymer upper bound was overcome with the incorporation of ZIF-8 particles by simultaneously making the membrane more permeable and more selective.

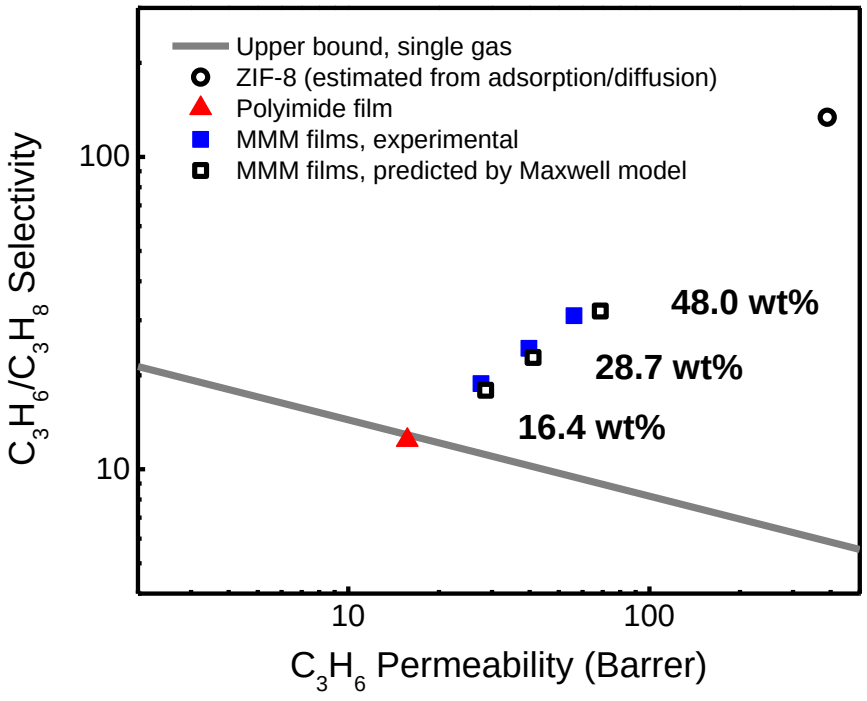

Figure 6.4: Enhanced C_3H_6/C_3H_8 separation performance in ZIF-8/6FDA-DAM mixed-matrix dense film membranes.

Experimental C_3H_6 permeability and C_3H_6/C_3H_8 ideal selectivities in ZIF-8/6FDA-DAM dense films were compared with the values predicted by the Maxwell model, using estimated C_3H_6/C_3H_8 transported properties in ZIF-8 obtained in section 5.4. As can be seen from Figure 6.4 and Table 6.3, excellent agreements were obtained between experimental and predicted transport properties, even at ZIF-8 loading as high as 48 wt% (60 vol%). This further suggests that with ideal interfacial adhesion, the Maxwell model may be reliable to estimate permeability in mixed-matrix materials at particle loading far beyond the value limited by its assumption.

Table 6.3: Comparison of experimental C_3H_6/C_3H_8 permeation results with the values predicted by the Maxwell model.

Membrane	ZIF-8 loading (wt%)	P_{C3H6} (Barrer)		C_3H_6/C_3H_8	
		Experimental	Predicted	Experimental	Predicted
6FDA-DAM	0	15.7 ±1.1	N/A	12.4 ±0.5	N/A
DAMZ_1	16.4	27.6 ±1.6	28.6	18.8 ±0.6	17.9
DAMZ_2	28.7	39.8 ±0.2	41.1	24.4 ±0.3	22.8
DAMZ_3	48.0	56.2 ±1.9	68.7	31.0 ±0.4	32.1

In addition to C_3H_6/C_3H_8 separation, Figure 6.5 shows the potential of ZIF-8/6FDA-DAM mixed-matrix material for several other economically important separations. Unlike C_3H_6/C_3H_8, separation efficiency of CO_2/N_2, CO_2/CH_4, O_2/N_2, and C_2H_4/C_2H_6 cannot be enhanced by adding ZIF-8. Selectivities of CO_2/N_2 and CO_2/CH_4 dropped significantly with increasing ZIF-8 loading. However, Figure 6.5 (E)-(H) show that ZIF-8 may be able to improve H_2 separation performance of the mixed-matrix

membrane. A four-fold increase in H_2 permeability was achieved for DAMZ_3 with 48 wt% ZIF-8 loading over the neat 6FDA-DAM dense film. In the meantime, selectivity of H_2/CO_2, H_2/CH_4, and H_2/N_2 almost stay unchanged and the upper bounds were overcome. In the case of H_2/C_3H_8 separation, molecular sieving was observed, possibly due to large size difference between H_2 and C_3H_8 molecules. Therefore, similar to separation of C_3H_6/C_3H_8, simultaneous enhancements in H_2 permeability and H_2/C_3H_8 selectivity were seen as ZIF-8 loading increased. The upper bound of H_2/C_3H_8 was not studied by Robeson and few permeation data were found in literature. As a result the upper bound was not shown in Figure 6.5 (H).

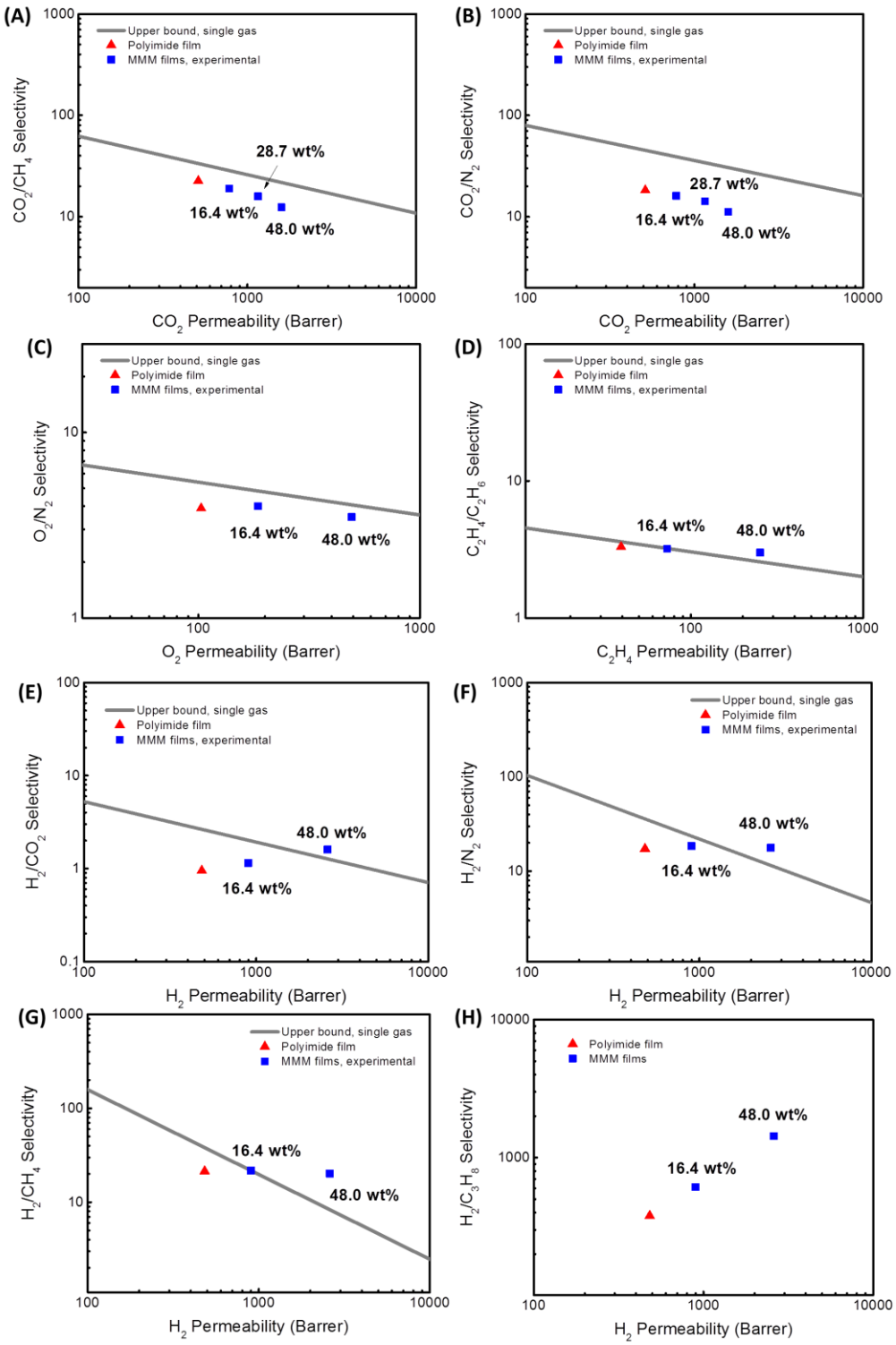

Figure 6.5: Separation performance of ZIF-8/6FDA-DAM mixed-matrix dense film membranes (A) CO_2/CH_4 (B) CO_2/N_2 (C) O_2/N_2 (D) C_2H_4/C_2H_6 (E) H_2/CO_2 (F) H_2/N_2 (G) H_2/CH_4 (H) H_2/C_3H_8. Upper bounds in (A), (B), (C), (E), (F), (G) were drawn based on the work of Robeson [6]. The upper bound in (D) was drawn by Rungta and co-workers [7].

6.4.2 Mixed-Gas Permeation

Mixed-gas permeation tests were performed at 35 ^{o}C with an equimolar C_3H_6/C_3H_8 mixture at C_3H_6 partial pressures around 10, 20, 30, and 40 psia. Dependences of permeability and selectivity on C_3H_6 partial pressure are shown in Figure 6.6 and tabulated in Table 6.4.

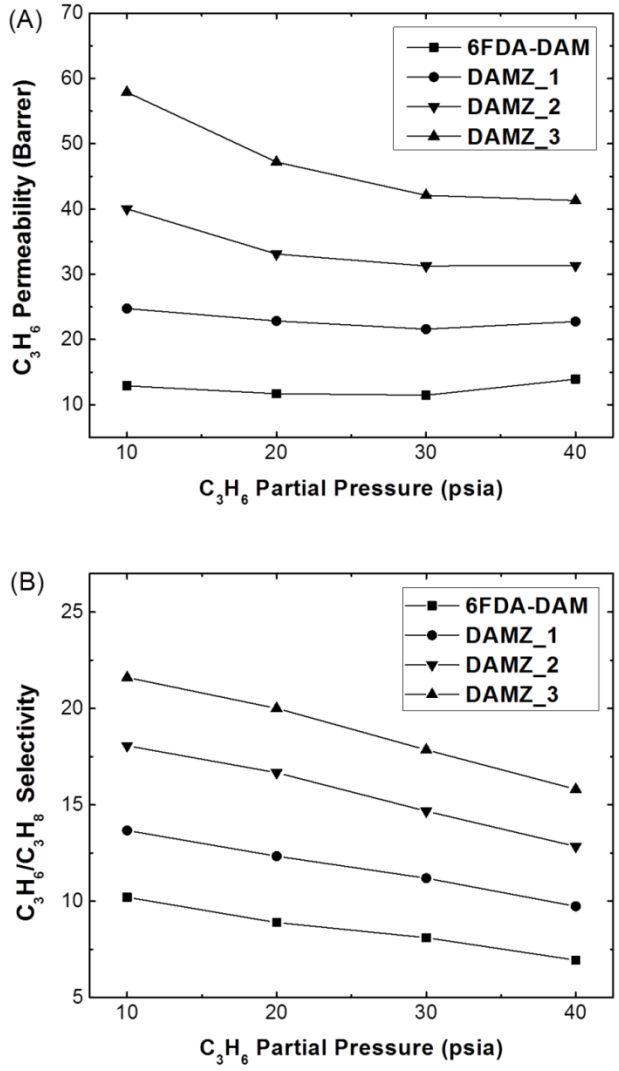

Figure 6.6: (A) C_3H_6 permeability and (B) C_3H_6/C_3H_8 selectivity in neat 6FDA-DAM dense film and ZIF-8/6FDA-DAM mixed-matrix dense films with an equimolar C_3H_6/C_3H_8 mixture.

Table 6.4: C_3H_6/C_3H_8 mixed-gas permeation results of neat 6FDA-DAM dense film and ZIF-8/6FDA-DAM mixed-matrix dense films. The permeability was given in the unit of Barrer and pressure was given in the unit of psia.

Pressure	6FDA-DAM		DAMZ_1		DAMZ_2		DAMZ_3	
	P_{C3H6}	C_3H_6/C_3H_8	P_{C3H6}	C_3H_6/C_3H_8	P_{C3H6}	C_3H_6/C_3H_8	P_{C3H6}	C_3H_6/C_3H_8
20	12.9	10.2	24.8	13.7	40	18.1	57.7	21.6
40	11.7	8.9	22.8	12.3	33.1	16.7	46.8	19.7
60	11.5	8.1	21.6	11.2	31.3	14.7	42	17.9
80	13.9	6.9	22.8	9.8	31.4	12.8	41.3	15.5

The "single-gas" upper bound plot of pure polymeric materials for C_3H_6/C_3H_8 separation was developed by Burns and Koros [5]. In this research, a "mixed-gas" upper bound plot of pure polymeric materials was constructed for C_3H_6/C_3H_8 separation using mixed-gas permeation data in the literature from temperatures between 35 and 50 ^oC and total feed pressures between 1 and 4 bars as well as the current study, as shown in Figure 6.7. The mixed-gas permeation data used to construct the "mixed gas" upper bound plot comprised the value for 6FDA/BPDA (1:1)-DDBT [8] and the value for 6FDA-DAM in the current study. The work of Visser and Wessling [9] was not considered to for the construction since their study was for asymmetric membranes and hence only permeance, rather than actual permeability data were available.

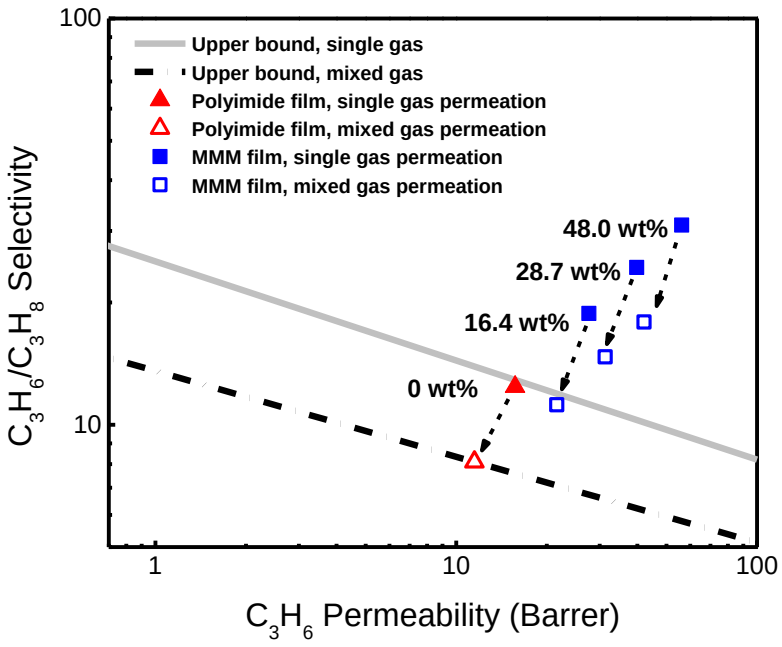

Figure 6.7: Comparison of single-gas and mixed-gas permeation properties at 35 ^{o}C and C_3H_6 feed pressure of ~2 bars.

Permeation properties of C_3H_6 and C_3H_8 in single-gas and mixed-gas environment are compared in Figure 6.7, with plots of "single-gas" and "mixed-gas" upper bounds. As expected, C_3H_6 permeability in the mixed-gas environment was lower than that with single-gas feed, and there was also a decrease in mixed-gas selectivity compared with single-gas selectivity for both neat 6FDA-DAM dense film and ZIF-8/6FDA-DAM mixed-matrix dense films. These decreases were presumably due to competitive sorption and diffusion effects in both the matrix and dispersed particles [10-11]. In any case, under mixed-gas feed, there were still significant enhancements in C_3H_6 permeability and C_3H_6/C_3H_8 separation factor with increasing ZIF-8 loading, which was consistent with

single-gas permeation results. These results also show that caution must be made when comparing single-gas performance in any modeling of achievable energy savings.

6.5 Attractive Molecular Sieving Properties of ZIF-8

6.5.1 Calculation of Diffusivity Based on Dense Film Permeation

Permeabilities of He, H_2, CO_2, O_2, N_2, CH_4, C_2H_4, C_2H_6, C_3H_6 and C_3H_8 in the pure ZIF-8 phase were back-calculated using single-gas permeation data of the neat 6FDA-DAM dense film and the ZIF-8/6FDA-DAM mixed-matrix dense films with 23.8 vol% ZIF-8 loading (DAMZ_1) by the Maxwell model. Uncertainties in experimental dense film permeabilities (Table 6.1) were taken into account for calculation of permeabilities (average of physically possible numbers) in the pure ZIF-8 phase. The results are shown in Table 6.5. We believe that the assumptions of the Maxwell model were essentially satisfied for our calculations, since (1) excellent adhesion was achieved between ZIF-8 particles and the 6FDA-DAM matrix at all ZIF-8 loadings, and (2) the ZIF-8 volume fraction of the film (23.8 vol.%) used for permeability calculation was sufficiently low and determined quantitatively by TGA (Appendix B).

Equation 5.14 was used to calculate corrected diffusivities (Table 6.5) of C_2H_4, C_2H_6, C_3H_6 and C_3H_8, whose adsorption isotherms follow Langmuir model under the studied pressure (2 bars). To calculate corrected diffusivities of He, H_2, CO_2, O_2, N_2, and CH_4, whose adsorption isotherms follow Henry's law, equation 6.1 was used:

$$P = \tilde{D} \times \tilde{S} = D_0 C_s b = D_0 K \tag{6.1}$$

Table 6.5: Estimated permeabilities and corrected diffusivities of pure ZIF-8 phase at 35 ^{o}C.

	He	H_2	CO_2	O_2	N_2	CH_4	C_2H_4	C_2H_6	C_3H_6	C_3H_8
P (Barrer)	$2.7 \pm 2.2 \times 10^{4}$	2.2×10^{4}	$3.3 \pm 0.8 \times 10^{3}$	$2.5 \pm 1.3 \times 10^{3}$	$1.0 \pm 0.8 \times 10^{3}$	270 ± 26	$1.1 \pm 0.5 \times 10^{3}$	430 ± 130	210 ± 95	2.5 ± 1.1
D_0 (cm^2/s)	$6.5 \pm 5.2 \times 10^{-4}$	2.0×10^{-4}	$2.1 \pm 0.5 \times 10^{-6}$	$1.0 \pm 0.5 \times 10^{-5}$	$4.0 \pm 3.0 \times 10^{-6}$	$4.0 \pm 0.4 \times 10^{-7}$	$3.6 \pm 1.6 \times 10^{-7}$	$8.8 \pm 2.7 \times 10^{-8}$	$1.6 \pm 0.3 \times 10^{-8}$	$1.7 \pm 0.8 \times 10^{-10}$

Due to uncertainties in measurements of dense film permeabilities, the resulting uncertainties in permeabilities and diffusivities in the pure ZIF-8 phase as shown in Table 6.5 were large, however, were reliable on their order of magnitude. As suggested by Table 6.5, for the pure ZIF-8 phase, the selectivity of CO_2/CH_4 and CO_2/N_2 were both lower than that of neat 6FDA-DAM polymer. This explains the reduced selectivity in mixed-matrix dense films, as shown in Figure 6.5 (A) and (B). The calculated selectivity of H_2/C_3H_8 was significantly higher than the reported separation factors of a pure ZIF-8 membrane grown above a porous α-alumina support [12], which were measured in a mixed-gas feed environment. While competitive adsorption and diffusion in mixed-gas environmental contribute to the discrepancies somewhat, it is possible that even very small defects in the pure ZIF-8 membrane could lead to separation factors that are significantly lower than the intrinsic values.

Bux and co-workers [13-14] reported transport diffusivity of CO_2 ($\sim 1.5\times10^{-6}$ cm^2/s), CH_4 ($\sim 1.0\times10^{-6}$ cm^2/s), C_2H_4 ($\sim 5\times10^{-7}$ cm^2/s), and C_2H_6 ($\sim 1\times10^{-7}$ cm^2/s) in ZIF-8 at low concentrations using the IR-Microscopy method, which were respectively on the same order of magnitude to the corrected diffusivities shown in Table 6.5. Pantatosaki and co-workers [15] reported self-diffusivity of CO_2 and CH_4 in ZIF-8 at higher concentrations determined by the PFG-NMR technique, which were both in the range of $1\sim2\times10^{-6}$ cm^2/s. These suggest that if the assumptions of the Maxwell model can be satisfied, mixed-matrix membrane permeation could be an approach with order of magnitude reliability to obtain transport diffusivity in the dispersed molecular sieving phase. It is necessary to mention that the IR-Microscopy and PFG-NMR measurements

were done at a slightly lower temperature (~300 K). We believe that a justification of comparison could be made since the effect of 10 K temperature difference on the diffusivities should be trivial considering that the diffusional activation energies for these fast diffusing gases are expected to be low.

6.5.2 Estimation of Penetrant Molecular Size

In order to estimate the effective molecular sieving aperture size of ZIF-8, it is essential to have knowledge of the dimension of probe molecules. A variety of scales have been used to characterize molecular dimensions [16-18] (e.g. kinetic diameter, van der Waals diameter, Lennard-Jones diameter, CPK diameter, and critical molecular diameter). Unfortunately, none of these scales is capable of satisfactorily characterizing molecular dimensions with respect to the relative diffusion rates for all the studied penetrants.

The scale of kinetic diameters by Breck [16] was adopted for this study with a few modifications. This scale, which was based on the minimum equilibrium cross-sectional diameters, was capable of explaining the molecular sieving behavior of zeolites for simple diffusing molecules (e.g. adsorption of CO_2 with exclusion of N_2 on zeolite 3A) as well as linear and branched paraffins (e.g. adsorption of n-C_4H_{10} with exclusion of iso-C_4H_{10} on zeolite 5A). However, according to Breck [16], the kinetic diameters of linear paraffin C_3H_8 and n-C_4H_{10} (both listed as ~4.3 Å) are smaller than those of linear olefins C_3H_6 and 1-C_4H_8 (both listed as ~4.5 Å). This has been shown to be questionable

on the basis of faster diffusion of linear olefins than the corresponding linear paraffins in both microporous molecular sieves and polymers [19-21, 18]. On the other hand, the scale of van der Waals diameter suggested by Ruthven [17] was able to reflect the subtle size differences of linear olefin/paraffin molecules (C_3H_6/C_3H_8 and 1-C_4H_8/n-C_4H_{10}) , which is given by:

$$b = \frac{4}{3}\pi\left(\frac{\sigma_0}{2}\right)^3 \times 4 \qquad (6.2)$$

where σ_0 (Å) is the van der Waals diameter, b (Å^3) is the van der Waals co-volume, which can be calculated from fluid critical parameters [22]. Ruthven [17] correlated diffusional activation energies in zeolite LTA and carbon molecular sieves with van der Waals diameters for simple molecules as well as linear hydrocarbons. In our study, however, the scale of van der Waals diameter was not adopted for all the penetrants. N_2 is smaller than CO_2 in the scale of van der Waals diameters. However, as mentioned before, CO_2 can adsorb on zeolite 3A but N_2 is excluded. Another limitation of this scale is that it cannot explain slower diffusion of iso-C_4H_{10} than n-C_4H_{10} in many systems [23, 19]. Therefore, we believe that a hybrid molecular dimension scale based on kinetic diameter and the van der Waals diameter will be most appropriate for our study.

Table 6.6: Estimated molecular diameters for the studied probe molecules.

	Kinetic diameter (Å)	van der Waals diameter (Å)
He	2.6	2.66
H_2	2.89	2.76
CO_2	3.3	3.24
O_2	3.46	2.94
N_2	3.64	3.13
CH_4	3.8	3.25
C_2H_4	3.9	3.59
C_2H_6	N/A	3.72
C_3H_6	4.5	4.03
C_3H_8	4.3	4.16
1-C_4H_8	4.5	4.41
n-C_4H_{10}	4.3	4.52
iso-C_4H_8	4.8	4.42
iso-C_4H_{10}	5.0	4.52

6.5.3 Molecular Sieving Properties of ZIF-8

ZIF-8's attractive molecular sieving properties were discovered after plotting the diffusivity data from Table 5.2 and Table 6.5 in Figure 6.8 with the penetrants' molecular diameters. Similarly, permeabilities were plotted in Figure 6.9 with molecular diameter using data from Table 5.4 and Table 6.5. From He (2.6 Å) to iso-C_4H_{10} (5.0 Å), the corrected diffusivity drops by fourteen orders of magnitude. Since larger and slower

diffusing molecules generally adsorb stronger, permeability decreases by eleven orders of magnitude. The C_3H_6 and C_3H_8 diffusivities obtained from kinetic uptake rate measurements (2.9×10^{-8} and 2.0×10^{-10} cm^2/s) match well with the values ($1.6\pm0.3\times10^{-8}$ and $1.7\pm0.8\times10^{-10}$ cm^2/s) estimated by the Maxwell model, using permeation results of mixed-matrix dense film and equilibrium sorption measurements described in Chapter 5.

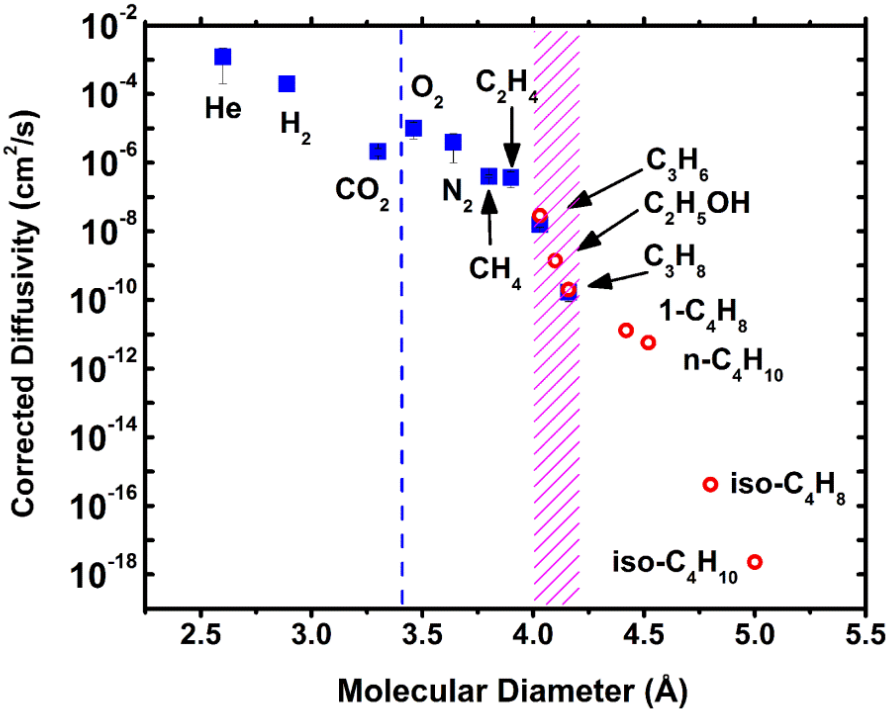

Figure 6.8: Corrected diffusivities in ZIF-8 at 35 ^oC vs. molecular diameter of probe molecules. (Solid blue squares: diffusivities estimated from mixed-matrix membrane permeation. Hollow red circles: diffusivities calculated from kinetic uptake rate measurements. Dashed blue line: single-XRD derived aperture size of ZIF-8 [24]. Dashed magenta region: effective aperture size range of ZIF-8.)

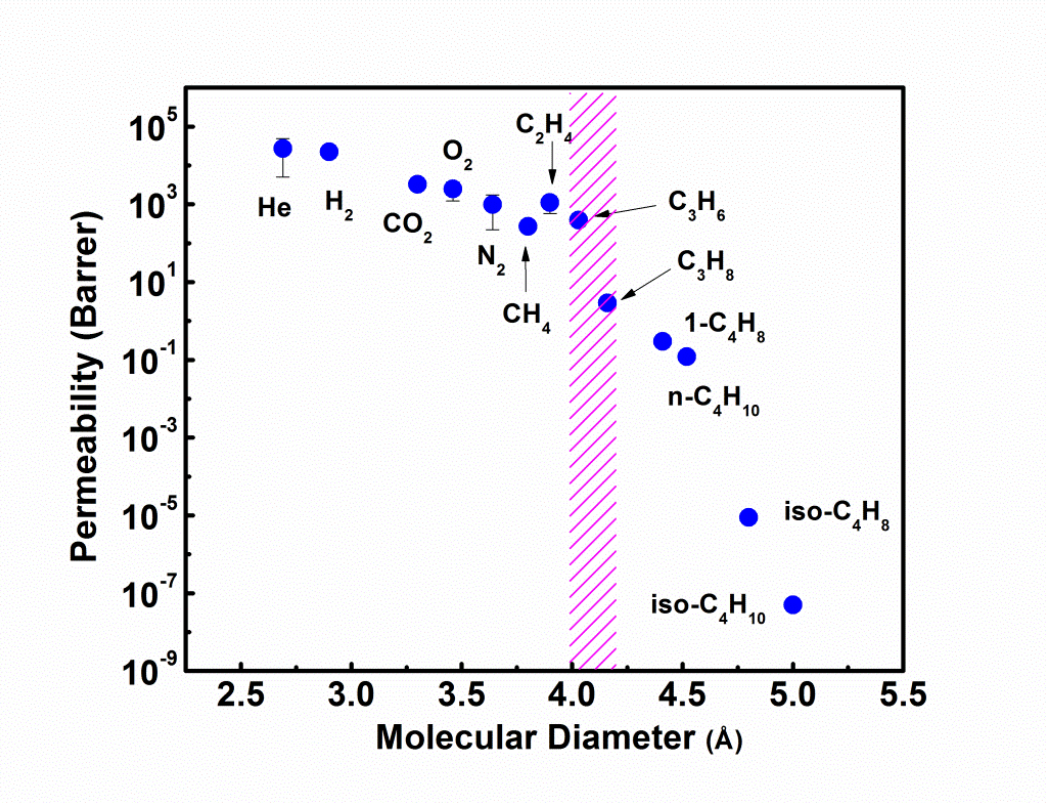

Figure 6.9: Estimated permeabilities in a pure ZIF-8 membrane operated at 35 ^{o}C and 2 bars upstream pressure. (Dashed magenta region: effective aperture size range of ZIF-8.)

The molecular sieving properties of ZIF-8 are unexpected and may be compared with the well-studied small pore aluminosilicate zeolite A. The α-cage aperture size of zeolite 5A determined by crystallographic analysis (4.2 Å) matches satisfactorily with its effective aperture size (4.3-4.4 Å) estimated by complete exclusion of CF_2Cl_2 (4.4 Å) and larger probe molecules [16]. For ZIF-8, however, a similar sharp "cut-off" phenomenon does not exist, so we have defined the effective aperture size to be in the range (4.0-4.2 Å) where the slope of "corrected diffusivity vs. molecular diameter" curve (Figure 6.8) starts to drop. This size range is considerably larger than the single-XRD derived value (3.4 Å) [24]. In addition, while the α-cage aperture of zeolite A dilates with temperature,

it is rather rigid at room temperature as evidenced by complete exclusion of C_3H_8 and iso-C_4H_{10} by 4A and 5A, respectively [16, 25-26]. On the other hand, the β-cage aperture of ZIF-8 appears to be somewhat flexible at the studied temperature (35 ^oC). All the studied C_4 hydrocarbon molecules that are considerably larger than the effective aperture size range diffuse into the micropores of ZIF-8 with remarkably high adsorption capacities, albeit slowly.

For molecules with diameters no larger than the effective aperture size (i.e. He, H_2, CO_2, O_2, N_2, CH_4, C_2H_4, and C_2H_6), micropore diffusion is not significantly constrained by steric hindrance. When this happens, ZIF-8 is not particularly size/shape selective and cannot enhance selectivity of the mixed-matrix membrane, as discussed in section 6.4.1. For example, linear CO2 (3.3 Å) diffuses only ~5 times as fast as the larger, spherical CH_4 (3.8 Å), though the "rigid" pore aperture assumption would predict a dramatic diffusion selectivity between these two molecules. Nonetheless, as the molecular diameters are within or become larger than the effective aperture of the freely mobile ZIF-8 (i.e. C_3H_6, C_3H_8, 1-C_4H_8, n-C_4H_{10}, iso-C_4H_8, and iso-C_4H_{10}), the diffusivity drops remarkably by ten orders of magnitude over molecular diameter difference of merely 1.0 Å (from C_3H_6 to iso-C_4H_{10}) and thus molecular sieving is truly realized. Therefore, as long as one penetrant (H_2/C_3H_8) or both penetrants (C_3H_6/C_3H_8) become larger than this effective size range, ZIF-8 becomes fairly size selective and the mixed-matrix membrane selectivity may be substantially improved.

We hypothesize that the aperture of ZIF-8 does not show unlimited flexibility at a fixed temperature, so there should exist a limiting aperture size above which sufficiently large molecules are totally excluded. The identification of such a limiting aperture size was not pursued in this work, which requires knowledge of adsorption properties of even larger probe molecules than iso-C_4H_{10} (e.g. di-branched paraffins and aromatics). Even if they diffuse into micropores of ZIF-8, conveniently measuring adsorption of these larger molecules are expected to be challenging at ambient temperatures even in the smallest ZIF-8 nano-crystals described in section 4.2 due to extremely slow diffusion rates as predicted by Figure 6.8. A recent paper [27] reported significant uptake of para-xylene by ZIF-8 at an elevated temperature (100 ^{o}C). Although the large para-xylene molecules might be unable to diffuse into micropores of ZIF-8 at 35 ^{o}C, the combination of aperture flexibility and dilation at the high temperature may explain the uptake noted by Peralta and co-workers. Even the aperture of more rigid zeolite A dilates at elevated temperatures to admit molecules that are unable to adsorb at lower temperatures [16, 26].

6.6 Physical Aging of Mixed-Matrix Dense Film Membrane

Glassy polymers are not in a state of true equilibrium. As the polymer is cooled from the rubbery state to the glassy state, excess free volume may be created and trapped in the polymer. As the polymer ages and approaches equilibrium state, the un-relaxed volume will be diffusing out and the polymer becomes more densified. As a result, permeation properties of glassy polymer-based membranes are usually time-dependent.

Physical aging of neat glassy polymers has been studied by previous researchers [28-31]. Usually, reduced permeability and increased selectivity are seen due to more densified structure. Figure 6.10 shows the time-dependent O_2/N_2 permeation properties of neat 6FDA-DAM dense film membrane [30]. As suggested by the figure, O_2 permeability dropped ~80% after being aged for ~3000 hrs with a ~30 % increase in O_2/N_2 selectivity.

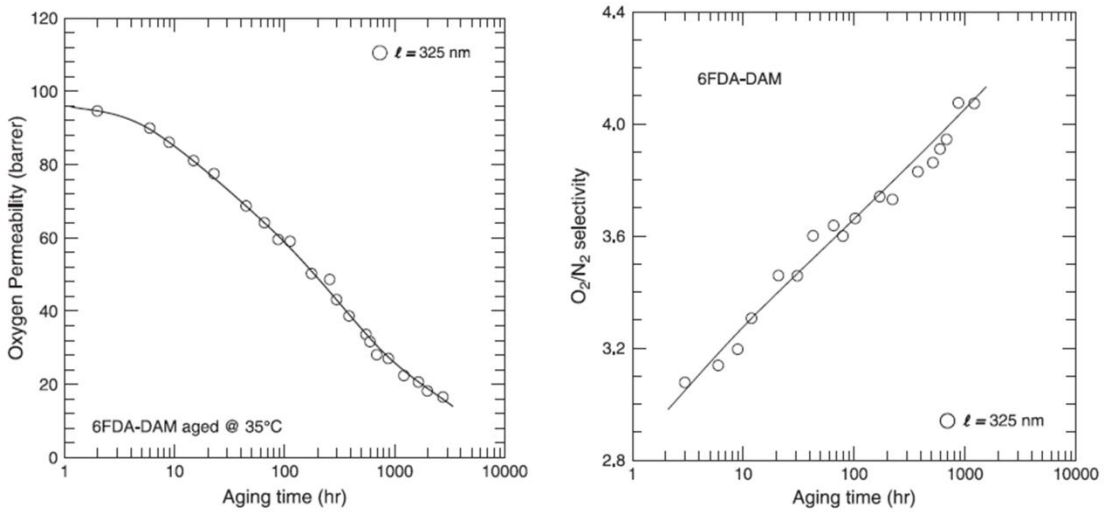

Figure 6.10: Time-dependent O_2/N_2 permeation properties of neat 6FDA-DAM dense film membrane [30].

Transport properties of mixed-matrix materials are determined by the polymer and dispersed molecular sieve particles. Consequently, transport properties of glassy polymer-based mixed-matrix materials may change as the polymer matrix ages. A schematic illustration of physical aging-induced structural change is shown in Figure 6.11. To our best knowledge, physical aging of mixed-matrix membranes has never been studied. In this research, a neat 6FDA-DAM and a ZIF-8/6FDA-DAM mixed-matrix dense film with 48 wt% ZIF-8 loading (DAMZ_3) were aged at room temperature in dry

air for ~3000 hrs. The films were then tested for C_3H_6/C_3H_8 single-gas permeation at 35 ^oC and 2 bars upstream pressure. The results are shown in Figure 6.12 and compared with data of new (un-aged) dense film membranes.

Figure 6.11: Schematic illustration of physical aging-induced structural change of glassy polymer-based mixed-matrix material.

For the neat 6FDA-DAM dense film, C_3H_6 permeability dropped and C_3H_6/C_3H_8 selectivity increased after aging, which was not surprising. In the case of ZIF-8/6FDA-DAM mixed-matrix dense film, however, the aging behavior was quite unusual. Both C_3H_6 permeability and C_3H_6/C_3H_8 selectivity dropped after the film was aged. Since moisture uptake of ZIF-8 was very low, we hypothesized that the decrease in selectivity was not due to adsorption of moisture during storage.

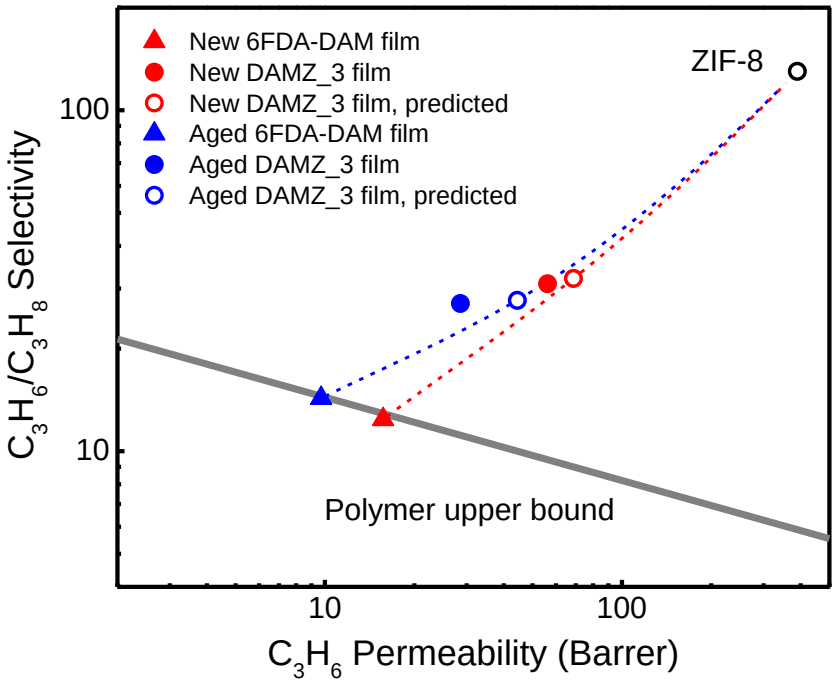

Figure 6.12: Permeation properties (35 ^{o}C and 2 bars upstream pressure) of neat 6FDA-DAM dense film and DAMZ_3 before and after being aged for ~3000 hrs in dry air at room temperature. The dotted lines indicate Maxwell model-predicted permeability/selectivity of mixed-matrix materials made with ZIF-8 and un-aged (red) and aged (blue) 6FDA-DAM.

To explain such unexpected aging behavior, permeability/selectivity in aged DAMZ_3 mixed-matrix dense films was calculated using the Maxwell model and permeability data of aged 6FDA-DAM, assuming that permeability in ZIF-8 was unchanged during aging and densification of the matrix. As shown in Figure 6.12, the Maxwell model successfully predicted that selectivity of the mixed-matrix membrane would be reduced with aged polymer matrix. The fact that the Maxwell model underestimated the drop in C_3H_6 permeability may be due to accelerated polymer

densification in the presence of particles. While measuring the glass transition temperature of the aged DAMZ_3 may be able to support this hypothesis, such work is beyond the scope of this study.

6.7 Summary and Conclusions

In this Chapter, ZIF-8/6FDA-DAM mixed-matrix dense film membranes with particle loading up to 48 wt% were successfully fabricated with desirable interfacial adhesion. TGA was used to confirm the hydrophobicity of ZIF-8. Significant enhancements in C_3H_6/C_3H_8 selectivity and C_3H_6 permeability were simultaneously achieved under both single-gas and mixed-gas feeds. The experimental separation performance of the mixed-matrix dense films was in good agreement with the values predicted by the Maxwell model. The unusual physical aging behavior of mixed-matrix dense film was studied and explained by the Maxwell model.

ZIF-8's attractive molecular sieving properties were discovered after analyzing diffusivity data obtained from adsorption measurements and mixed-matrix dense film permeation. From Helium (2.6 Å) to iso-C_4H_{10} (5.0 Å), the corrected diffusivity drops fourteen orders of magnitude. The results further suggest that the effective aperture size of ZIF-8 for molecular sieving is in the range of 4.0-4.2 Å, which is significantly larger than the XRD-derived value (3.4 Å) and between the well-known aperture size of zeolite 4A (3.8 Å) and 5A (4.3 Å). These unexpected molecular sieving properties open up new opportunities for ZIF materials for separations which cannot be economically achieved by traditional microporous adsorbents such as synthetic zeolites.

6.8 References

[1] B.-H. Jeong, E. M. V. Hoek, Y. Yan, A. Subramani, X. Huang, G. Hurwitz, A. K. Ghosh and A. Jawor, "Interfacial polymerization of thin film nanocomposites: A new concept for reverse osmosis membranes" *Journal of Membrane Science* **2007**, *294*, 1-7.

[2] S. Husain and W. J. Koros, "Mixed matrix hollow fiber membranes made with modified HSSZ-13 zeolite in polyetherimide polymer matrix for gas separation" *Journal of Membrane Science* **2007**, *288*, 195-207.

[3] J. Liu, PhD Dissertation, Georgia Institute of Technology, 2010.

[4] J. A. Thompson, K. W. Chapman, W. J. Koros, C. W. Jones and S. Nair, "Sonication-induced Ostwald ripening of ZIF-8 nanoparticles and formation of ZIF-8/polymer composite membranes" *Microporous Mesoporous Mater.* **2012**, *158*, 292-299.

[5] R. L. Burns and W. J. Koros, "Defining the challenges for C3H6/C3H8 separation using polymeric membranes" *Journal of Membrane Science* **2003**, *211*, 299-309.

[6] L. M. Robeson, "The upper bound revisited" *J. Membr. Sci.* **2008**, *320*, 390-400.

[7] M. Rungta, C. Zhang, W. J. Koros and L. Xu, "Membrane-based ethylene/ethane separation: The upper bound and beyond" *AIChE Journal* **2013**, *59*, 3475-3489.

[8] M. Yoshino, S. Nakamura, H. Kita, K.-i. Okamoto, N. Tanihara and Y. Kusuki, "Olefin/paraffin separation performance of asymmetric hollow fiber membrane of 6FDA/BPDA–DDBT copolyimide" *Journal of Membrane Science* **2003**, *212*, 13-27.

[9] T. Visser and M. Wessling, "Auto and mutual plasticization in single and mixed gas C3 transport through Matrimid-based hollow fiber membranes" *Journal of Membrane Science* **2008**, *312*, 84-96.

[10] M. Das, PhD Dissertation, Georgia Institute of Technology, 2009.

[11] J. Karger, D. M. Ruthven and D. N. Theodorou, *Diffusion in Nanoporous Materials*, John Wiley & Sons, Ltd, **2012**

[12] H. Bux, A. Feldhoff, J. Cravillon, M. Wiebcke, Y.-S. Li and J. Caro, "Oriented Zeolitic Imidazolate Framework-8 Membrane with Sharp H2/C3H8 Molecular Sieve Separation" *Chem. Mater.* **2011**, *23*, 2262-2269.

[13] H. Bux, C. Chmelik, R. Krishna and J. Caro, "Ethene/ethane separation by the MOF membrane ZIF-8: Molecular correlation of permeation, adsorption, diffusion" *J. Membr. Sci.* **2011**, *369*, 284-289.

[14] H. Bux, C. Chmelik, J. M. van Baten, R. Krishna and J. Caro, "Novel MOF-Membrane for Molecular Sieving Predicted by IR-Diffusion Studies and Molecular Modeling" *Adv. Mater.* **2010**, *22*, 4741-4743.

[15] E. Pantatosaki, G. Megariotis, A.-K. Pusch, C. Chmelik, F. Stallmach and G. K. Papadopoulos, "On the Impact of Sorbent Mobility on the Sorbed Phase Equilibria and Dynamics: A Study of Methane and Carbon Dioxide within the Zeolite Imidazolate Framework-8" *J. Phys. Chem. C* **2011**, *116*, 201-207.

[16] D. W. Breck, *Zeolite Molecular Sieves*, Robert E. Krieger Publishing Company, INC., **1973**

[17] D. M. Ruthven, *Principles of Adsorption and Adsorption Processes*, John Wiley & Sons, Inc., **1984**

[18] Y. Yampolskii, I. Pinnau and B. D. Freeman, *Materials Science of Membranes*, John Wiley & Sons Ltd, **2006**

[19] J. Karger and D. M. Ruthven, *Diffusion in Zeolites and Other Microporous Solids.*, John Wiley & Sons, Inc., **1991**

[20] M. Rungta, L. Xu and W. J. Koros, "Carbon molecular sieve dense film membranes derived from Matrimid® for ethylene/ethane separation" *Carbon* **2012**, *50*, 1488-1502.

[21] L. R. Xu, M. Rungta and W. J. Koros, "Matrimid (R) derived carbon molecular sieve hollow fiber membranes for ethylene/ethane separation" *J. Membr. Sci.* **2011**, *380*, 138-147.

[22] D. R. Lide, *Handbook of Chemistry and Physics, 87th Edition*, CRC Press, LLC, **2006**

[23] O. Esekhile, W. Qiu and W. J. Koros, "Permeation of butane isomers through 6FDA-DAM dense films" *J. Polym. Sci., Part B: Polym. Phys.* **2011**, *49*, 1605-1620.

[24] K. S. Park, Z. Ni, A. P. Cote, J. Y. Choi, R. Huang, F. J. Uribe-Romo, H. K. Chae, M. O'Keeffe and O. M. Yaghi, "Exceptional chemical and thermal stability of zeolitic imidazolate frameworks" *Proc. Natl. Acad. Sci. U. S. A.* **2006**, *103*, 10186-10191.

[25] J. Padin, S. U. Rege, R. T. Yang and L. S. Cheng, "Molecular sieve sorbents for kinetic separation of propane/propylene" *Chem. Eng. Sci.* **2000**, *55*, 4525-4535.

[26] R. T. Yang, *Adsorbents: Fundamentals and Applications*, John Wiley & Sons, Inc., **2003**

[27] D. Peralta, G. Chaplais, A. Simon-Masseron, K. Barthelet and G. D. Pirngruber, "Separation of C6 Paraffins Using Zeolitic Imidazolate Frameworks: Comparison with Zeolite 5A" *Industrial & Engineering Chemistry Research* **2012**, *51*, 4692-4702.

[28] L. Cui, W. Qiu, D. R. Paul and W. J. Koros, "Physical aging of 6FDA-based polyimide membranes monitored by gas permeability" *Polymer* **2011**, *52*, 3374-3380.

[29] J. H. Kim, W. J. Koros and D. R. Paul, "Effects of CO2 exposure and physical aging on the gas permeability of thin 6FDA-based polyimide membranes - Part 1. Without crosslinking" *Journal of Membrane Science* **2006**, *282*, 21-31.

[30] J. H. Kim, W. J. Koros and D. R. Paul, "Physical aging of thin 6FDA-based polyimide membranes containing carboxyl acid groups. Part I. Transport properties" *Polymer* **2006**, *47*, 3094-3103.

[31] B. W. Rowe, B. D. Freeman and D. R. Paul, "Influence of previous history on physical aging in thin glassy polymer films as gas separation membranes" *Polymer* **2010**, *51*, 3784-3792.

CHAPTER 7

DEVELOPMENT OF DUAL-LAYER ZIF/POLYIMIDE MIXED-MATRIX HOLLOW FIBER MEMBRANES

7.1 Overview

The potential economic "scalability" of mixed-matrix membranes makes them attractive when compared with inorganic zeolite membranes and even CMS membranes. However, limited efforts and progress have been made to form mixed-matrix membranes into scalable hollow fibers to prove that mixed-matrix membranes can actually deliver on this potential.

With solid performance enhancements demonstrated in Chapter 6 for mixed-matrix dense films, Chapter 7 uses the same materials (ZIF-8 and 6FDA-DAM polyimide) to form mixed-matrix hollow fiber membranes. Dual-layer mixed-matrix hollow fibers with ZIF-8 particle loading of 17 wt%, 30 wt%, and 40 wt% were spun and evaluated for gas separations. The effects of fiber post-treatments on fiber transport properties were investigated. The challenge to spin high-quality hollow fiber membrane for hydrocarbon separations was identified. The effects of polymer molecular weight and non-solvent strength on hollow fiber spinning were discussed.

7.2 Challenges to Form High Quality Hollow Fiber Membranes for Hydrocarbon Separations

Formation of asymmetric hollow fiber membranes with thin skin layer is highly desirable for the purpose of achieving high membrane productivity. Unfortunately, as the fiber skin becomes thinner, the probability of fiber skin defects increases dramatically. Diffusion in these defects usually follows the Knudsen diffusion mechanism with selectivity that is substantially lower than the membrane material itself.

The influence of fiber skin defects on fiber transport properties results from even minute ($<10^{-5}$) area fraction of such defects. Fiber skin defects usually affect the relative flux of slower permeating gas pairs more than that of faster permeating gases. Indeed, for slower permeating hydrocarbons, a much larger portion of penetrant molecules may permeate through the unselective defects, even if the percentage of defects is low, rendering the membrane unattractive for separation of such mixtures. As a rule of thumb, if the selectivity of the as-spun fiber is within 90 % of the intrinsic value measured with dense film, the fiber can be considered as "defect-free" [1].

While fiber skin defects can be minimized, they are hardly to avoid completely, especially when manufactured at large scale. To solve this problem, industry uses a "caulking" technique [2-4] to cover and/or fill the skin defects by coating the surface of as-spun fibers with a second layer of polymer. With this additional layer, diffusion in the fiber skin defects is reduced, and fiber selectivity may approach the intrinsic selectivity of the membrane material. A schematic illustration of "caulking" will be shown later.

PDMS is often used to seal fiber skin defects [4], and permeability data in PDMS and 6FDA-DAM polyimide are plotted in Figure 7.1 with penetrant molecular size. Permeation in rubbery polymer is controlled by solubility, and permeability increases as the penetrant becomes more condensable. On the contrary, permeation in glassy polyimides is controlled by diffusion, and permeability decreases with increasing penetrant molecular size. Consequently, the permeability ratio between PDMS and 6FDA-DAM increases dramatically as the penetrant molecule becomes larger and more condensable. For example, the ratio of H_2 permeability is only ~3, while the ratio of n-C_4H_{10} is over 6×10^4.

Figure 7.2 shows the effectiveness of PDMS to seal fiber skin defects for separation of O_2/N_2, CO_2/CH_4, C_3H_6/C_3H_8, and n-C_4H_{10}/iso-C_4H_{10}. The X axis is the fractional area (percentage) of fiber skin defects. The Y axis is the normalized selectivity of the coated fiber relative to the intrinsic selectivity of the fiber skin material. Calculations were based on the assumptions that (1) PDMS forms a uniform coating on the surface of the fiber with thickness that was 1% of the fiber skin. (2) PDMS also fills the defects. (3) Permeation in the therefore coated fiber follows the resistance model suggested by Henis and Tripodi [3]. Varying the thickness ratio of PDMS layer vs fiber skin may change the results but the trend should stay the same.

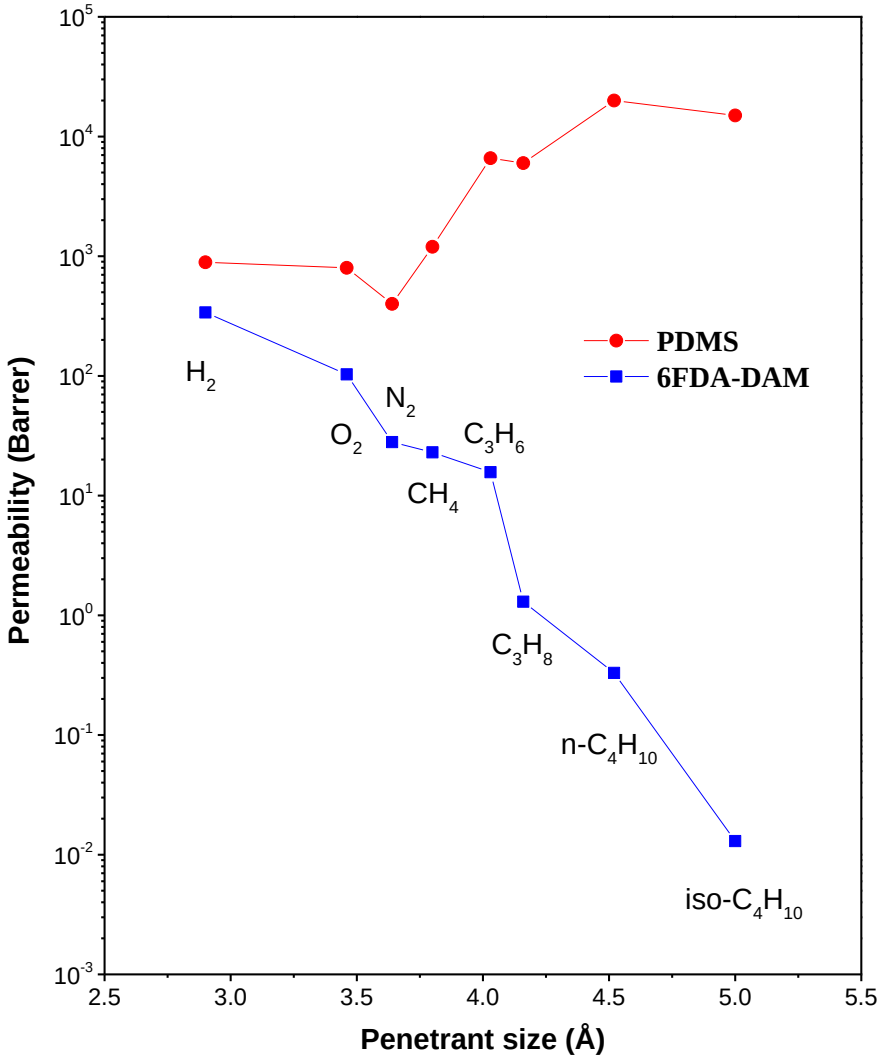

Figure 7.1: Permeability data in PDMS and 6FDA-DAM. Permeabilities of H_2, O_2, N_2, CH_4, C_3H_6, and C_3H_8 in 6FDA-DAM were measured at 35 ^oC in this work (Table 6.1). Permeability data of H_2, O_2, N_2, and CH_4 in PDMS at 35 ^oC were reported by Freeman and co-workers [5]. Permeabilities of C_3H_6 and C_3H_8 at 50 ^oC were reported by Tanaka and co-workers [6]. Permeability of n-C_4H_{10} and iso-C_4H_{10} in were calculated based on permeation data at 100 ^oC and permeation activation energy [7-8].

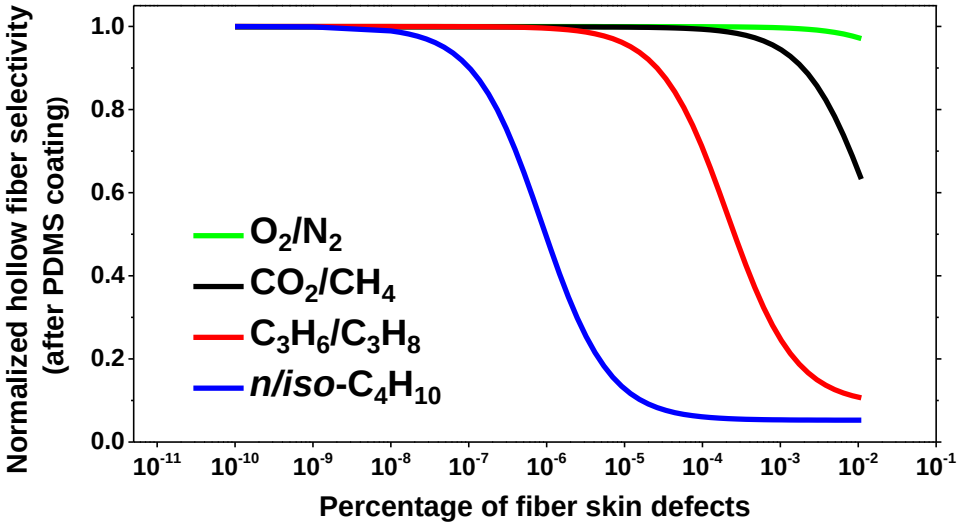

Figure 7.2: Normalized selectivity of PDMS-coated 6FDA-DAM hollow fiber vs. percentage of fiber skin defects. It is assumed that PDMS fills the defects as well as forms a continuous layer on top of the fiber surface.

Figure 7.2 also shows that even with PDMS coating, it is much more challenging to obtain high-quality hollow fiber membranes that demonstrate desirable hydrocarbon selectivity that is consistent with dense film membrane. For PDMS-coated 6FDA-DAM hollow fibers, percentage of fiber skin defects has to be below 2×10^{-5} to show defect-free (90 %) C_3H_6/C_3H_8 selectivity. For n-C_4H_{10}/iso-C_4H_{10}, the required percentage is even lower (8×10^{-8}).

The effectiveness of a coating material to seal fiber skin defects depends on the relative permeability of the permeating gas in the coating material and the membrane material that comprises the fiber skin. In the case that the coating material is several orders of magnitude more permeable than the membrane, it may not be able to effectively

seal fiber skin defects and improve membrane selectivity. Clearly, PDMS as a coating layer material is more effective to seal fiber skin defects for separation of less condensable, permanent gases than highly condensable hydrocarbons. For example, assuming 0.1 % fiber skin defects, selectivities of O_2/N_2, CO_2/CH_4 were within 95 % of the intrinsic selectivity after PDMS coating. Whereas C_3H_6/C_3H_8 and n-C_4H_{10}/iso-C_4H_{10} selectivities of the PDMS-coated fiber were only less than 30 % and 10 % of the intrinsic selectivity, respectively.

In addition to mismatch in hydrocarbon permeability, another limitation of PDMS as a defect-sealing material is illustrated in Figure 7.3 (B). As described in section 3.3.2.3, the extended network of PDMS has already been formed before being contacted with the as-spun fiber. As a result, PDMS is only capable of filling those defects that are sufficiently large to accommodate PDMS's long chains but cannot effectively plug smaller defects.

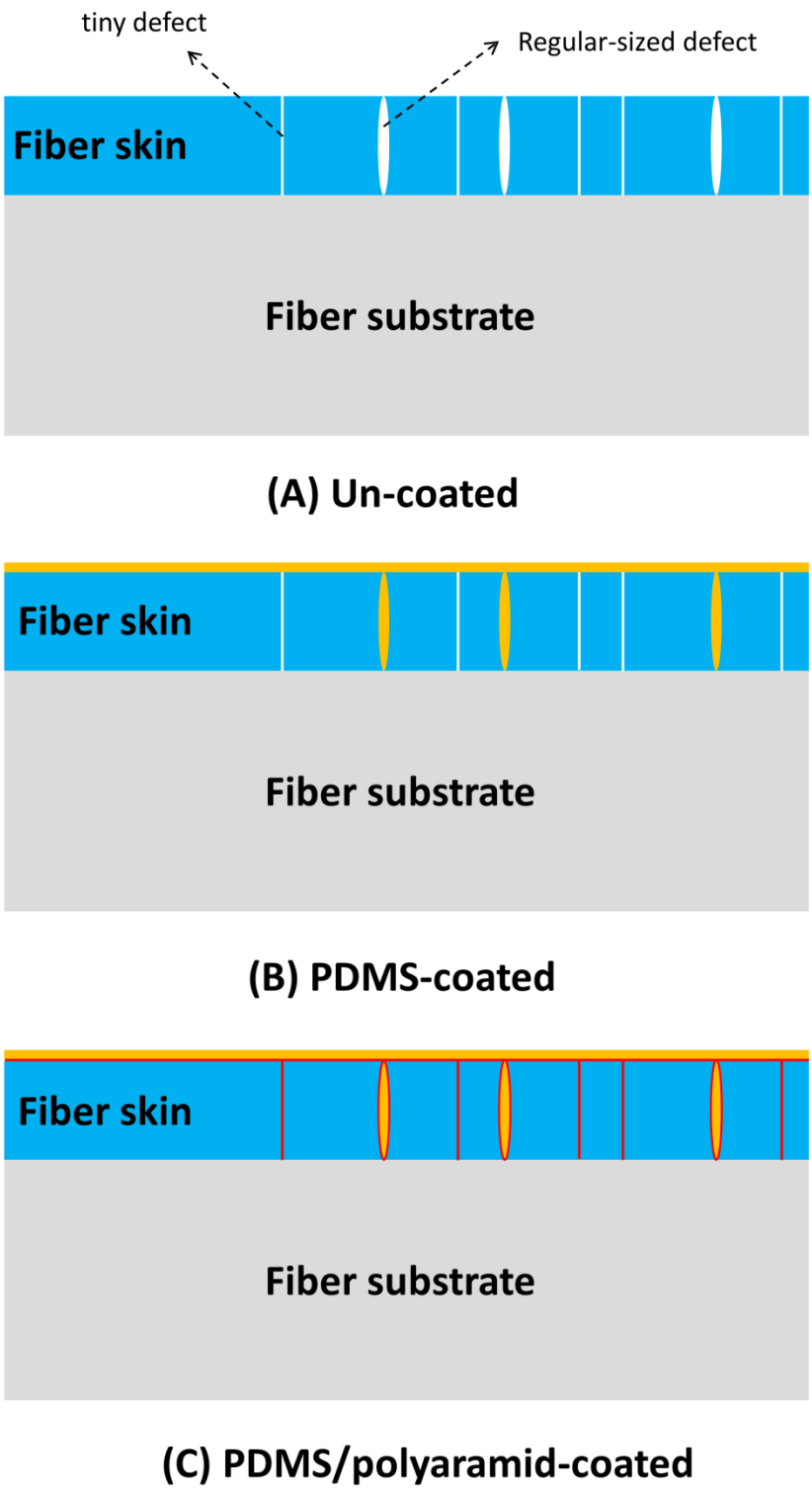

Figure 7.3: Schematic illustration of sealing fiber skin defects. (A) un-coated fiber (B) PDMS-coated fiber (C) PDMS/polyaramid-coated fiber. The orange region indicates PDMS coating, whereas the red region indicates polyaramid coating.

Other than PDMS, another coating material that has been used to seal fiber skin defects is polyaramid [2]. Such materials are glassy, and tend to be much less permeable than PDMS, and therefore may be more effective to slow down Knudsen diffusion of hydrocarbons in fiber skin defects. Also, the diamine and acryl chloride monomer molecules may be small enough to diffuse into and polymerize inside smaller defects, providing small interstitial seals that cannot be realized by bulkier PDMS. This is illustrated in Figure 7.3 (C). The picture shows that PDMS and polyaramid exist as distinct layers. However, in the actual case, the two polymers may be well-mixed with each other where they co-exist.

7.3 Single-layer 6FDA-DAM Hollow Fiber Membrane

7.3.1 Hollow Fiber Spinning

Polymer molecular weight may play an important role in formation of defect-free fiber skin. Carruthers studied fiber skin formation using Matrimid® polyimides with different molecular weights [1]. It was found that lower molecular polymer had difficulty being formed into defect-free fibers.

Xu [9] successfully spun defect-free 6FDA-DAM hollow fiber membranes using a high-molecular weight (526 kDa) 6FDA-DAM sample. In this research, initial efforts were made to reproduce Xu's work, however, using a 6FDA-DAM sample with lower molecular weight (192 kDa). The spinning employed the same dope composition and similar spinning parameters as described by Xu [9]. All the permeation tests in this

spinning indicated defective fibers, showing the importance of polymer molecular weight for promoting defect-free spinning. It was observed that the dope made from 192 kDa 6FDA-DAM was much less viscous than the dope made from 526 kDa, and was more prone to phase separation instead of dense skin formation, possibly, leading to defects during exposure to humid air gap.

Based on the above hypothesis, the dope formulation for the 192 kDa 6FDA-DAM sample was adjusted based on Xu's work, as shown in Table 7.1, by increasing polymer concentration (and therefore viscosity), to promote the skin formation. Correspondingly, the concentrations of non-solvents, in this case, ethanol and lithium nitrate, were decreased. The spinning conditions are listed in Table 7.2.

Table 7.1: Spinning dope composition of 6FDA-DAM hollow fibers using the 192 kDa 6FDA-DAM sample. The dope composition used by Xu [9] is shown for reference.

Component	Concentration (wt%)	
	Xu	This work
6FDA-DAM	18	25
NMP	50.5	49.5
THF	10	10
Ethanol	15	12
$LiNO_3$	6.5	3.5

Table 7.2: Spinning parameters of 6FDA-DAM hollow fibers using the 192 kDa 6FDA-DAM sample. The dope composition used by Xu [9] is shown for reference.

Component	Value	
	Xu	This work
Dope flow rate (cc/hr)	180	180
Bore fluid flow rate (cc/hr)	60	60
Quench bath temperature (^{o}C)	25-50	25
Spinneret temperature (^{o}C)	70	70
Air gap height (cm)	5-30	10
Take-up rate (m/min)	20-50	10

7.3.2 Hollow Fiber Characterizations

SEM was used to examine the morphology of single-layer 6FDA-DAM hollow fibers spun using 192 kDa polymer with adjusted dope composition. Figure 7.4 (A) shows the overall cross-section of a hollow fiber; Figure 7.4 (B) shows the morphology of the fiber wall; Figure 7.4 (C) shows the side view of fiber skin layer; and Figure 7.4 (D) shows the top view of the fiber skin layer. The fiber displayed quite desirable macroscopic properties: uniform wall thickness, substrate with open pore structure, and free of macrovoids. Due to relatively slow take-up rate (10 m/min) and therefore longer air gap residence time, fiber skin layer was quite thick, which was ~4 μm as shown by Figure 7.4 (C).

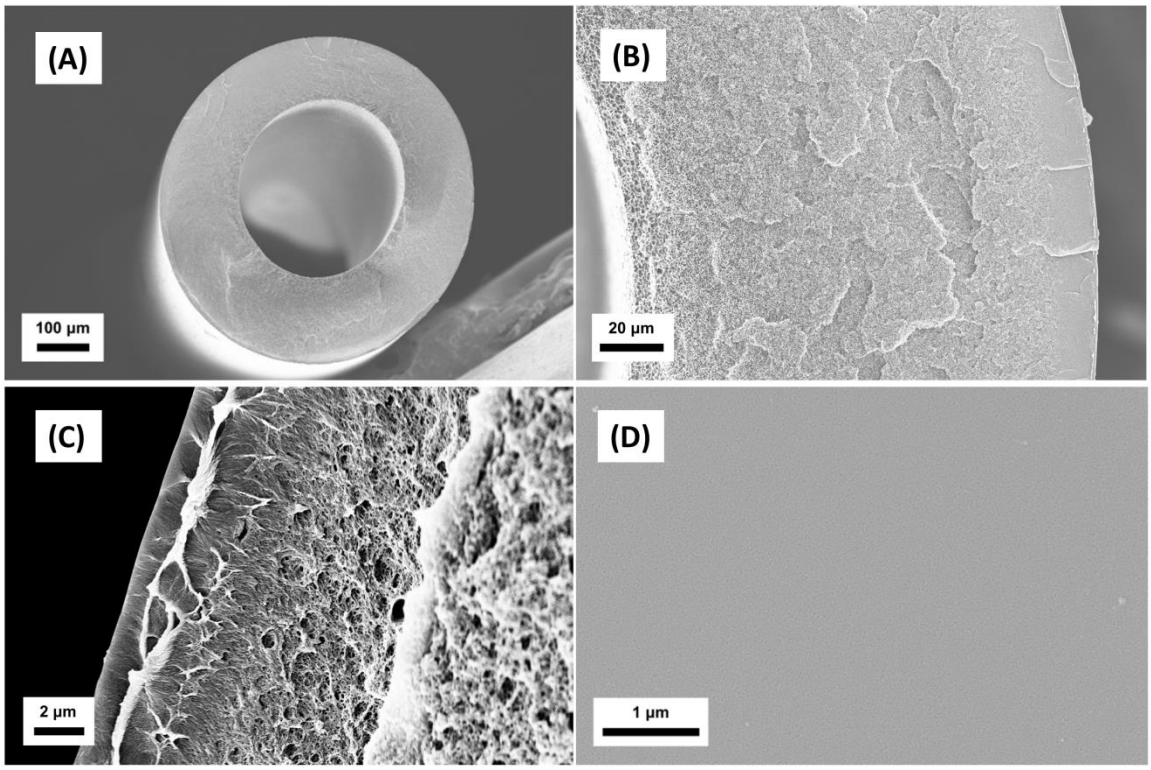

Figure 7.4: SEM images of single-layer 6FDA-DAM hollow fiber membranes. (A) fiber overview (B) fiber substrate (C) fiber skin layer side view (D) fiber skin layer top view.

7.3.3 Evaluation of Separation Performance

Separation performance of as-spun and coated 6FDA-DAM hollow fiber membranes was evaluated with O_2/N_2 single-gas permeation and C_3H_6/C_3H_8 mixed-gas permeation. The results are shown in Table 7.3. O_2/N_2 selectivity of the as-spun fiber agreed perfectly with that of neat 6FDA-DAM dense films. C_3H_6/C_3H_8 selectivity of the as-spun fiber was ~80% of the value (10.2) measured under the same conditions using neat 6FDA-DAM dense films. As mentioned in section 7.2, fiber skin defects affect hydrocarbon selectivities more than smaller gases. In this case, the tiny defects have negligible impact on O_2/N_2 selectivity but apparently affected C_3H_6/C_3H_8 selectivity. The

fiber may be considered as "defect-free" in terms of O_2/N_2 selectivity, but was slightly defective in terms of C_3H_6/C_3H_8 selectivity. The fiber skin thickness was estimated using O_2 permeability of the neat 6FDA-DAM dense film (103 Barrer) and permeance of the neat 6FDA-DAM hollow fiber (87.5 GPU) based on equation 2.3. The calculated skin thickness was ~1.2 μm, which was smaller than the value determined by SEM; however, ambiguity usually exists with SEM-based selective layer estimates.

Table 7.3: Permeation results of single-layer 6FDA-DAM hollow fibers. Permeation of O_2/N_2 was done with single gases at 35 ^oC and 2 bars upstream pressure. Permeation of C_3H_6/C_3H_8 was done with 50/50 vol% mixed-gas at 35 ^oC and 20 psia upstream pressure.

Fiber	Permeance (GPU)		Selectivity	
	O_2	C_3H_6	$\frac{O_2}{N_2}$	$\frac{C_3H_6}{C_3H_8}$
As-spun fiber	87.5	9.3	4.2	8.0
PDMS-coated fiber	78.0	7.3	4.2	8.5
PDMS/polyaramid-coated fiber	6.3	0.38	6.3	16.3

After coating fiber surface with PDMS, O_2 permeance decreased by 10 % with no changes in O_2/N_2 selectivity. The reduced O_2 permeance was possibly due to additional mass transfer resistance in the coated PDMS layer. Table 7.3 shows that the PDMS coating was not able to restore C_3H_6/C_3H_8 to the intrinsic value (10.2) of the membrane material, presumably due to the reasons discussed in section 7.2. After coating the surface of as-spun fibers with both PDMS and polyaramid, C_3H_6/C_3H_8 selectivity and O_2/N_2 selectivity substantially increased to 16.3 and 6.3, which are both higher than the intrinsic

selectivity of 6FDA-DAM. Strikingly, C_3H_6 permeance decreased by ~95 % to only 0.38 GPU. It appears that the quite impermeable polyaramid not only sealed the defects, but also added significant resistance to permeation. The fact that the PDMS/polyaramid-coated fiber showed higher O_2/N_2 and C_3H_6/C_3H_8 selectivities than the membrane itself was possibly because the polyaramid was more selective than the membrane material itself. Indeed, polyaramid has been commercialized for H_2 separations and shown H_2/CH_4 selectivity as high as 4000 [3].

7.3.4 Effect of Non-solvent Strength on Phase Behaviors of Fiber Spinning Dopes

Carruthers [1] compared skin morphology of Matrimid® fibers formed with ethanol, methanol, acetone, and water as spinning dope non-solvents. It was found that the dope with water as the non-solvent resulted in fiber skin with a nodular morphology rather than a densely packed skin. Carruthers hypothesized that it may be due to water's relatively lower volatility.

In addition, water may be overly strong as a non-solvent for spinning dope development. In this research, two phase diagrams were constructed via the cloud point technique, one with water being the only non-solvent, the other one with water/6.5 wt% $LiNO_3$ being non-solvents. The results were compared with Xu's work [9], which used ethanol and ethanol/6.5 wt% $LiNO_3$ as non-solvents. At a fixed 6FDA-DAM concentration, the dope was seen to change from one-phase into two-phase with increasing water amount. The compositions at different selected polymer concentrations on the phase boundary are called "cloud points", and these points together form the

binodal line. The constructed phase diagrams with water and water/6.5 wt% $LiNO_3$ as non-solvents are shown in Figure 7.5 and Figure 7.6. It is clear that water is much stronger than ethanol as a non-solvent. In both diagrams, the water binodal lines are much closer to the polymer-solvent axis than the ethanol binodal lines.

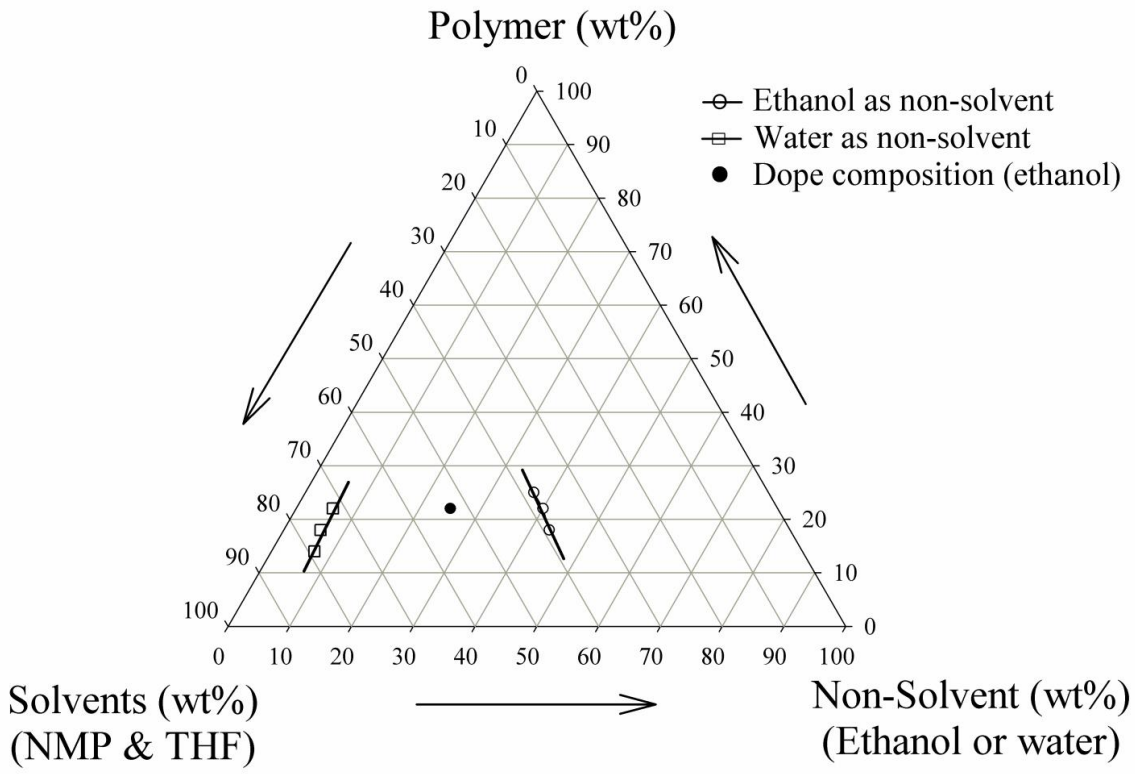

Figure 7.5: Ternary phase diagram of 6FDA-DAM (without $LiNO_3$). Open circle (○): compositions on the phase boundary, with ethanol as the non-solvent; open square (□): compositions on the phase boundary, with water as the non-solvent; solid circle (●): spinning dope composition [9] with ethanol as the non-solvent.

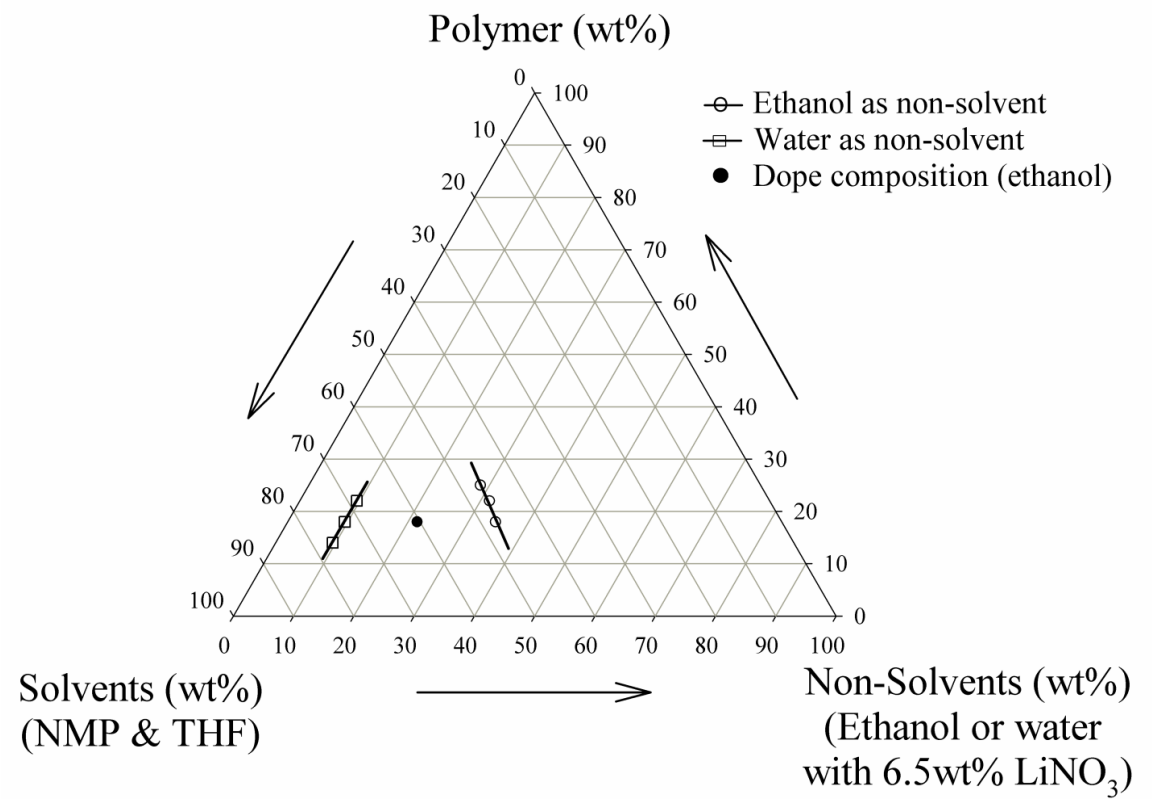

Figure 7.6: Ternary phase diagram of 6FDA-DAM (with 6.5 wt% $LiNO_3$). Open circle (○): compositions on the phase boundary, with ethanol and $LiNO_3$ as non-solvents; open square (□): compositions on the phase boundary, with water and $LiNO_3$ as non-solvents; solid circle (●): spinning dope composition [9] with ethanol and $LiNO_3$ as non-solvents.

Figure 7.7 shows an example of how sensitive the phase behavior was with a slight change in water concentration across the binodal line. The polymer concentration of the small-scale dopes was fixed at 18 wt% with increasing water concentration (4, 5, 6, and 7 wt%) balanced by solvents (NMP and 10 wt% THF). At 4 and 5 wt%, the dope looked perfectly transparent and was apparently in a single phase. Strikingly, the dope turned from transparent to completely opaque with increasing water concentration by just 1 wt%. When water concentration reached 7 wt%, a single-phase dope cannot be obtained with a solid phase on top of the vial and a liquid phase on the bottom.

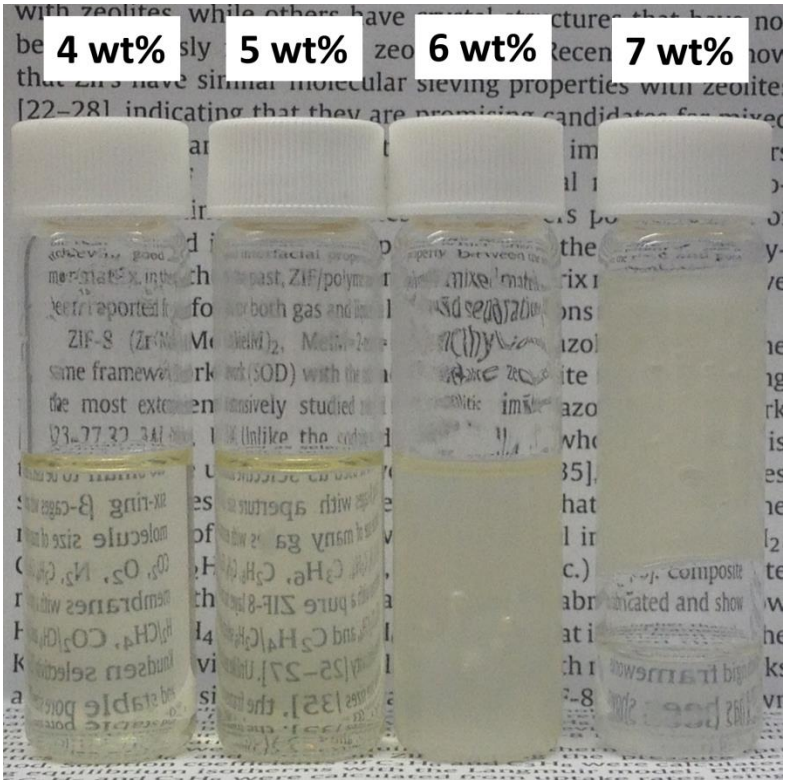

Figure 7.7: Photographs of small-scale dopes with varying water concentration.

For the ethanol case in Xu's work [9], ~40 wt% of ethanol is required for the dope to turn cloudy. That is to say, water is about 6-7 times stronger than ethanol. The operating window is very small if water is used as the non-solvent for dope formulation as compared to ethanol. For lower free volume polymers such as Matrimid® and Ultem®, the operating window is expected to be even smaller, since they are less non-solvent resistant [10-11]. The issues may exist as the instability during dope processing and volatile evaporation in air gap. In dope preparation, the composition of the dope preparation should be carefully adjusted, since even the moisture in air may cause early phase separation either during mixing or dope loading into delivery pumps. In the air gap,

the evaporation of volatile solvent THF and the absorption of moisture in high humidity case may enable the dope composition to cross the phase boundary and cause phase separation. Early phase separation causes defects in the skin layer of hollow fiber membranes. Therefore, water should be avoided as the non-solvent in dope formulation compared to ethanol and other less strong non-solvents. Nevertheless, water is still an excellent option as the coagulant in quench bath to ensure rapid fiber solidification.

7.4 Dual-layer ZIF-8 (17 wt%)/6FDA-DAM Hollow Fiber Membrane

7.4.1 Hollow Fiber Spinning

As a notable advancement over previous research that used micron-sized particles for mixed-matrix hollow fiber spinning [12-14], this research formed mixed-matrix hollow fibers with nano-sized particles. The 46 nm ZIF-8 sample described in section 4.2 was chosen over other nano-sized samples as the yield of this recipe was the highest. As discussed in Chapter 2, ideally an inexpensive commercial polymer should be used to form the fiber core layer. However, as a proof of concept study, this research used 6FDA-DAM as the core layer polymer to avoid possible sheath-core inter-layer adhesion problem that may complicate the analysis of fiber spinning results.

The above mentioned could point technique cannot be used to determine dope compositions for mixed-matrix hollow fiber membranes, since the added particles would make the dope opaque even in the one-phase region. In this research, a systematic empirical approach was employed to develop dope composition for ZIF-8/6FDA-DAM

mixed-matrix hollow fiber membranes, based on the established dope composition of neat 6FDA-DAM hollow fiber membrane in Table 7.1.

$LiNO_3$ was originally added in the spinning dope of neat 6FDA-DAM hollow fibers to accelerate phase separation and to improve fiber spinnability; however, it has been shown that it may be hard to control fiber skin integrity in the presence of $LiNO_3$ [8]. For dual-layer mixed-matrix hollow fibers, the sheath layer usually comprises a very small amount of the entire fiber. As a result, fiber spinnability and phase separation rate are largely determined by the core dope. In this research, $LiNO_3$ was removed from the sheath spinning dope of mixed-matrix hollow fibers to avoid unnecessary complexities.

Based on the spinning dope of neat 6FDA-DAM hollow fibers, sheath spinning dope (Table 7.4) of dual-layer ZIF-8(17 wt%)/6FDA-DAM mixed-matrix hollow fibers was developed by making a few adjustments. The polymer concentration was fixed around 25 wt% (in this case 26 wt%). Concentration of ZIF-8 in the dope was then determined based on the desired particle loading (17 wt%, close to DAMZ_1 in Chapter 6) in the solidified fiber sheath layer. Ethanol concentration was reduced so that the total non-solvent (ethanol and ZIF-8) concentration was comparable between these two dopes (15.5 wt% for neat polymer fiber spinning dope vs. 14.2 wt% for mixed-matrix fiber spinning dope). To assist fiber skin formation, THF concentration was increased to 16 wt%. A wide range of spinning parameters was used, which were listed in Table 7.5. A different composition was employed for the core spinning dope. Polymer concentration was decreased to obtain a more open substrate with minimal mass transfer resistance.

$LiNO_3$ was added to improve dope spinnability and accelerate nascent fiber phase separation.

Table 7.4: Dope compositions for ZIF-8 (17 wt%)/6FDA-DAM mixed-matrix hollow fiber spinning.

Component	Concentration (wt%)	
	Sheath dope	Core dope
6FDA-DAM	26	20.5
NMP	43.8	48
THF	16	10
Ethanol	9	15
$LiNO_3$	N/A	6.5
ZIF-8	5.2	N/A

Table 7.5: Spinning parameters for ZIF-8 (17 wt%)/6FDA-DAM mixed-matrix hollow fiber spinning. Spinning parameters of the spinning state (CZ-9_ST-6) showing promising separation performance is shown as well.

Spinning parameter	Value	CZ-9_ST-6
Sheath dope flow rate (cc/hr)	15-30	15
Core dope flow rate (cc/hr)	150-300	150
Bore fluid flow rate (cc/hr)	55-100	55
Quench bath temperature (^oC)	25-50	25
Spinneret temperature (^oC)	50-60	60
Air gap height (cm)	7-30	10
Take-up rate (m/min)	5-20	10

7.4.2 Hollow Fiber Characterizations

SEM images of dual-layer ZIF-8(17 wt%)/6FDA-DAM mixed-matrix hollow fibers are shown in Figure 7.8. The fiber was free of macrovoids; however, was slightly non-concentric due to misaligned spinneret. This problem was successfully solved by aligning the spinneret during spinning of 40 wt% mixed-matrix fiber, which will be shown in section 7.6. The fiber showed slight delamination between the outside sheath and underlying core layer. While fiber inter-layer delamination usually undermines the fibers' mechanical strength under high pressure, it appeared that it did not negatively affect transport properties under the testing conditions utilized in this research. In any case, this issue was corrected by using a spinneret with modified design when the 30 wt% and 40 wt% loading mixed-matrix fibers were spun ,which will be shown in section 7.5 and 7.6.

Striking differences were observed between fiber skin surface of neat 6FDA-DAM fiber in Figure 7.4 (D) and mixed-matrix fiber in Figure 7.8 (D). While the skin surface of neat 6FDA-DAM fiber appeared to be completely smooth without any observable features, skin surface of the mixed-matrix fiber displayed many small "nodules" with dimensions close to the size of individual ZIF-8 nanoparticles (diameter ~100 nm). It should be noted that these "nodules" need to be distinguished from those described by Carruthers [1] and Liu [15], which were characteristic of fiber skin morphologies subject to early phase separation.

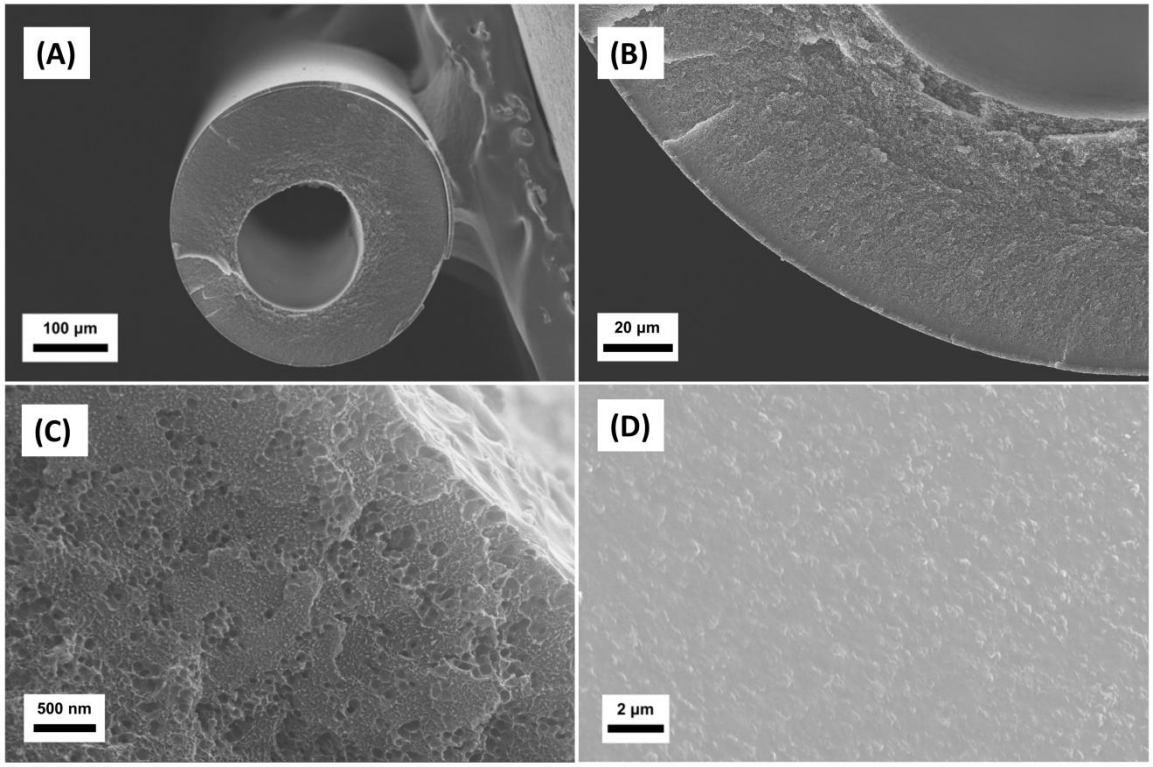

Figure 7.8: SEM images of dual-layer ZIF-8 (17 wt%)/6FDA-DAM mixed-matrix hollow fiber membranes. (A) fiber overview (B) fiber substrate (C) fiber skin layer side view (D) fiber skin layer top view.

Some spherical sockets with diameter of ~100 nm can be seen in the fiber skin cross section in Figure 7.8 (C). We hypothesize that this is due to ZIF-8 particles "popping out" from the fiber upon fracturing the fiber sample in liquid nitrogen and therefore is not an indication of fiber skin defects. Due to these sockets, the transition from fiber dense skin and the underlying porous region was unclear. As a result, it was hard to unambiguously estimate skin layer thickness of mixed-matrix hollow fiber membranes simply based on SEM imaging. The presence of ZIF-8 particles in the fiber sheath layer was further confirmed by elemental analysis. As shown in Figure 7.9, Zn weight fraction agreed very well with the theoretical value.

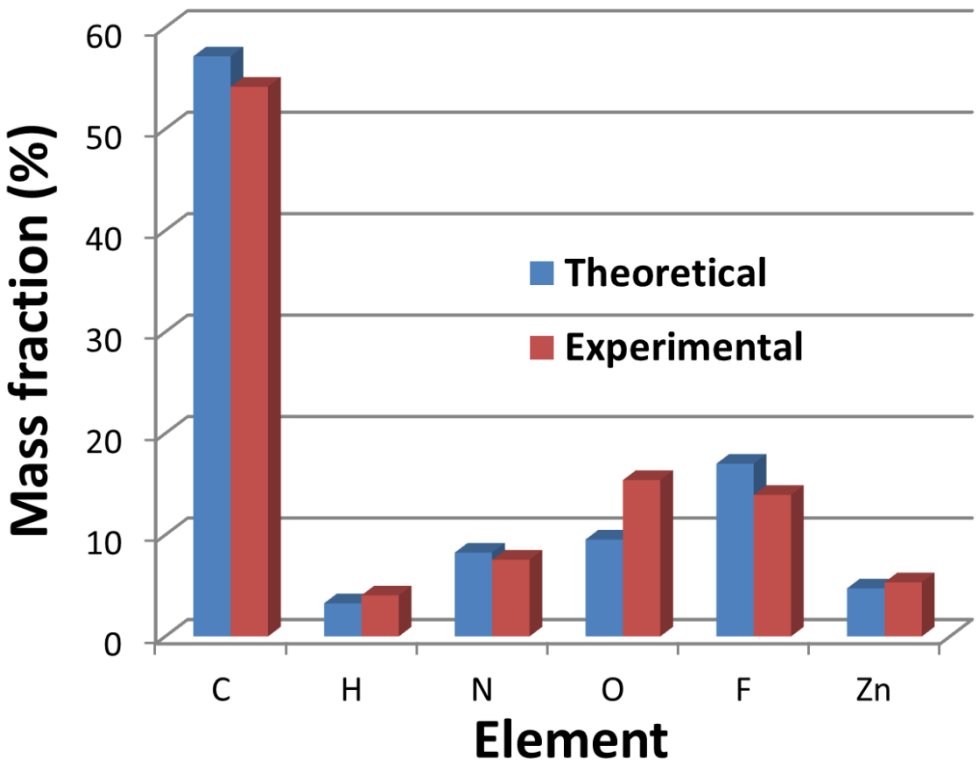

Figure 7.9: Elemental analysis results of ZIF-8(17 wt%)/6FDA-DAM mixed-matrix hollow fibers (sheath layer only).

7.4.3 Evaluation of Separation Performance

Spinnability of the dope was excellent. Using 50 ^{o}C quench batch, the dual-layer mixed-matrix fibers can be collected continuously at drawing speed as high as 50 m/min, which resulted in fine fibers with OD as small as ~260 μm. However, initial permeation tests with O_2/N_2 single-gases suggested that those states spun using cooler quench batch (25 ^{o}C) and lower drawing speed (10 m/min) generally had better selectivities. This was probably due to the thicker fiber skin formed with longer air gap residence time and slower phase separation in the quench bath.

The state with the highest O_2/N_2 selectivity was CZ-9_ST-6, whose spinning parameters are shown in Table 7. Permeation results of this state are shown in Table 7.5. An O_2/N_2 selectivity of 4.5 was obtained for as-spun fibers, which was slightly higher than the value (4.0) of mixed-matrix dense film with similar loading (DAMZ_1). The fiber skin thickness was estimated using O_2 permeability of DAMZ_1 (186 Barrer) and permeance of the as-spun mixed-matrix fiber (69.3 GPU) based on equation 2.3. The calculated skin thickness was ~2.7 μm.

Table 7.6: Permeation results of dual-layer ZIF-8(17 wt%)/6FDA-DAM hollow fibers. Permeation of O_2/N_2 was done with single gases at 35 ^oC and 2 bars upstream pressure. Permeation of C_3H_6/C_3H_8 was done with 50/50 vol% mixed-gas at 35 ^oC and 20 psia upstream pressure.

Fiber	Permeance (GPU)		Selectivity	
	O_2	C_3H_6	$\frac{O_2}{N_2}$	$\frac{C_3H_6}{C_3H_8}$
As-spun fiber	69.3	2.4	4.5	16.5
PDMS-coated fiber	66.5	2.2	4.5	17.7
PDMS/polyaramid-coated fiber	25.3	0.68	7.7	21.1

C_3H_6/C_3H_8 mixed-gas permeation showed that the as-spun fiber had good C_3H_6/C_3H_8 separation performance with C_3H_6 permeance of 2.4 GPU and C_3H_6/C_3H_8 selectivity of 16.5. It was surprising, yet obviously desirable to see, that the C_3H_6/C_3H_8 selectivity of the mixed-matrix hollow fiber membrane exceeded the value (13.7) of mixed-matrix dense film at similar loading (DAMZ_1). It was hypothesized that this was

because of better particle dispersion achieved in mixed-matrix fiber than the mixed-matrix dense film. It was also possible due to polymer chain orientations resulting from extensional forces applied on the nascent fiber. In any case, this suggested successful formation of high-quality mixed-matrix fiber with minimized skin defects. To my best knowledge, this was among the few studies that mixed-matrix hollow fiber membranes showed consistent selectivity with the mixed-matrix dense film. It was also the first that mixed-matrix hollow fiber membrane showed enhanced selectivity for challenging hydrocarbon separations.

Coating fiber surface with PDMS slightly enhanced C_3H_6/C_3H_8 selectivity to 17.7 with a minor drop of C_3H_6 permeance to 2.2 GPU. This indicates that tiny defects still existed, although apparently their impacts on C_3H_6/C_3H_8 selectivity were minimal. Since the as-spun fibers were close to being defect-free, coating with both PDMS and polyaramid seemed to be unnecessary. As shown in Table 7.6, the added polyaramid layer significantly decreased C_3H_6 permeance while only slightly improved C_3H_6/C_3H_8 selectivity.

7.5 Dual-layer ZIF-8 (30 wt%)/6FDA-DAM Hollow Fiber Membrane

7.5.1 Hollow Fiber Spinning

With successful spinning of 17 wt% mixed-matrix hollow fiber, efforts were further made to spin high-loading mixed-matrix hollow fibers with 30 wt% ZIF-8. The spinning still employed 46 nm ZIF-8 as the dispersed molecular sieve and was still

realized on the dual-layer hollow fiber platform with 6FDA-DAM as the core layer polymer. It should be noted that such high particle loading has never been reported before in the literature for mixed-matrix hollow fibers.

The sheath dope composition of the dual-layer ZIF-8(30 wt%)/6FDA-DAM mixed-matrix hollow fiber was set on the basis of the sheath dope composition of 17 wt% ZIF-8 loading. If the polymer concentration was fixed at 26 wt%, ZIF-8 concentration had to be above 11 wt% to reach the desired loading in the solidified sheath layer. This was found to be very challenging to practice since high concentration of polymer, and high concentration of particles would make the dope extremely viscous and more difficult to process [13].

To solve this problem, polymer concentration was decreased to 20 wt% and therefore the required ZIF-8 concentration dropped to 8.5 wt%. The resulting sheath dope was very viscous, but still processable. With increasing concentration of ZIF-8, ethanol concentration was decreased to 7.5 wt%. Since lowering polymer concentration tend to produce defective fiber skin, THF concentration was significantly increased from 16 wt% to 44 wt% to remedy this problem. Again, a wide range of spinning parameters was used. With the knowledge that lower quench batch temperature may produce thicker and less defective skin, a cooler quench bath (12 ^{o}C) was used. This was probably wise, since particle agglomerations may be more serious for the high-loading mixed-matrix fiber.

Table 7.7: Dope compositions for ZIF-8 (30 wt%)/6FDA-DAM mixed-matrix hollow fiber spinning.

Component	Concentration (wt%)	
	Sheath dope	Core dope
6FDA-DAM	20	20.5
NMP	20	48
THF	44	10
Ethanol	7.5	15
$LiNO_3$	N/A	6.5
ZIF-8	8.5	N/A

Table 7.8: Spinning parameters for ZIF-8 (30 wt%)/6FDA-DAM mixed-matrix hollow fiber spinning. Spinning parameters of the spinning state (CZ-12_ST-10) gave the highest selectivity is shown as well.

Spinning parameter	Value	CZ-12_ST-10
Sheath dope flow rate (cc/hr)	15-30	15
Core dope flow rate (cc/hr)	150-180	150
Bore fluid flow rate (cc/hr)	55-60	55
Quench bath temperature (^oC)	12-25	12
Spinneret temperature (^oC)	50-60	60
Air gap height (cm)	2-30	2
Take-up rate (m/min)	5-20	10

7.5.2 Hollow Fiber Characterizations

SEM images of dual-layer ZIF-8(30 wt%)/6FDA-DAM mixed-matrix hollow fibers are shown in Figure 7.10. The fiber was again slightly non-concentric. By using a spinneret with modified design, the delamination problem seen for 17 wt% mixed-matrix was successfully solved. Figure 7.10 (B) shows excellent adhesion between fiber sheath and core layer. The "nodules" shown on skin surface of 30 wt% mixed-matrix fiber appeared to be more densely packed than the 17 wt% mixed-matrix fiber, reflecting its higher particle loading. Excellent consistency was again obtained by elemental analysis between experimental and theoretical Zn weight concentrations (Figure 7.11).

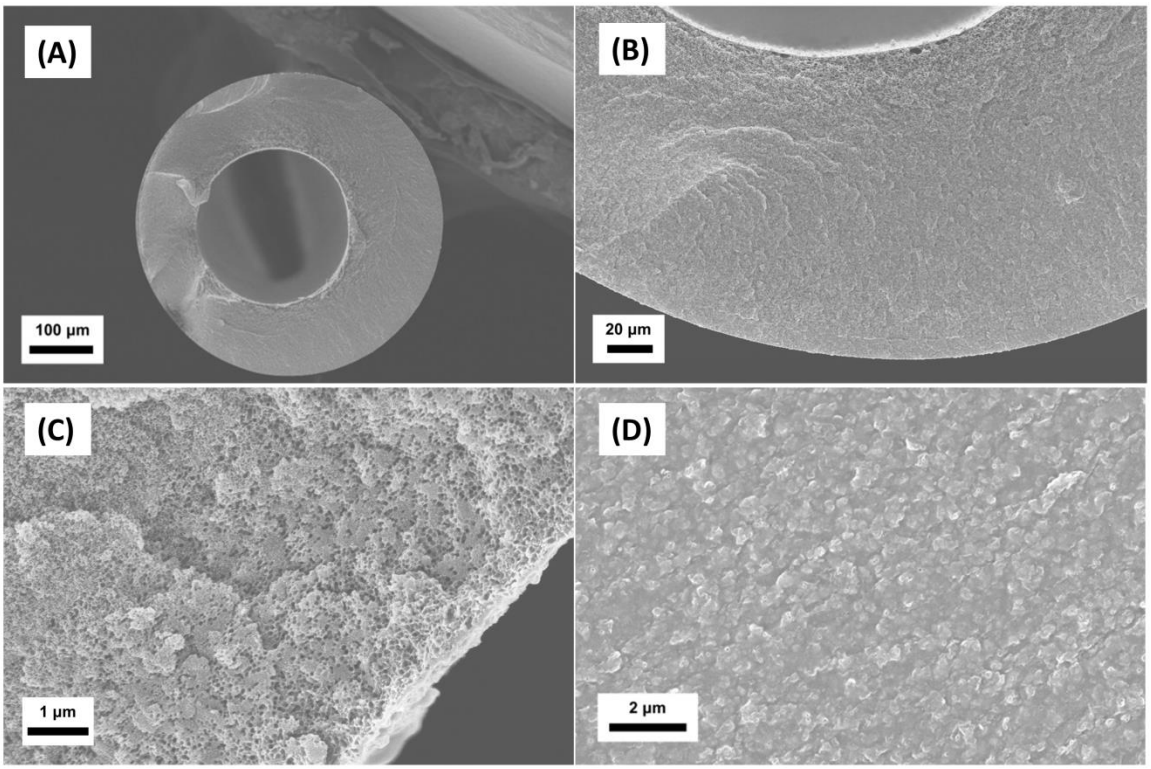

Figure 7.10: SEM images of dual-layer ZIF-8 (30 wt%)/6FDA-DAM mixed-matrix hollow fiber membranes. (A) fiber overview (B) fiber substrate (C) fiber skin layer side view (D) fiber skin layer top view.

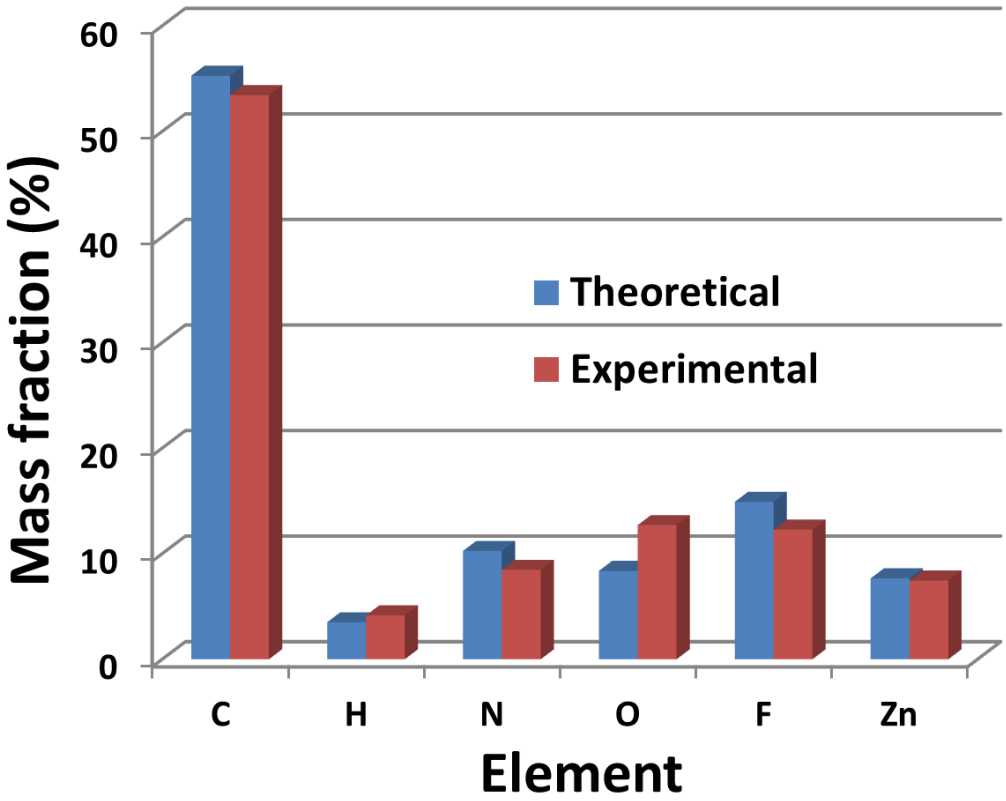

Figure 7.11: Elemental analysis results of ZIF-8 (30 wt%)/6FDA-DAM mixed-matrix hollow fibers (sheath layer only).

7.5.3 Evaluation of Separation Performance

Separation performance of the as-spun mixed-matrix hollow fibers was first evaluated with O_2/N_2 single-gas permeation. It was found that those states spun with lower quench batch temperature (12 ^oC) generally gave higher O_2/N_2 selectivity, probably due to thicker fiber skin. Spinning parameters of the state (CZ-12_ST-10) having the highest O_2/N_2 selectivity (4.0) are shown in Table 7.8. This state was further taken for C_3H_6/C_3H_8 mixed-gas permeation. The C_3H_6/C_3H_8 selectivity of the as spun fiber was only 6.6, which was significantly lower than the value (18.1) of mixed-matrix dense film membrane with similar loading (DAMZ_2). The unattractive C_3H_6/C_3H_8 selectivity

suggests that the as-spun fibers were defective at the levels noted in section 7.2, which caused difficulties for this lower permeability pair. And as a result, fiber skin thickness estimation cannot be estimated with acceptable reliability.

Table 7.9: Permeation results of dual-layer ZIF-8(30 wt%)/6FDA-DAM hollow fibers. Permeation of O_2/N_2 was done with single gases at 35 ^oC and 2 bars upstream pressure. Permeation of C_3H_6/C_3H_8 was done with 50/50 vol% mixed-gas at 35 ^oC and 20 psia upstream pressure.

Fiber	Permeance (GPU)		Selectivity	
	O_2	C_3H_6	$\frac{O_2}{N_2}$	$\frac{C_3H_6}{C_3H_8}$
As-spun fiber	73.9	10.1	4.0	6.6
PDMS-coated	59.5	6.0	4.2	16.4
PDMS/polyaramid-coated fiber	7.3	0.27	7.0	27.5

Since O_2 permeability was unavailable for DAMZ_2, skin thickness of 30 wt% loading mixed-matrix fiber was estimated using the dense film's N_2 permeability (81.3 Barrer, Table 6.1) and permeance of the as-spun fiber (18.5 GPU) based on equation 2.3. The calculated skin thickness was ~4.4 μm. It should be noted that this number may underestimate the actual skin layer thickness as the fiber was partially defective. This suggests that the adjustments made on sheath spinning dope composition (increased THF concentration) and spinning parameters (decreased quench bath temperature) indeed increased skin layer thickness (from ~2.7 μm to at least 4.4 μm). However, it is surprising to see that the fiber was partially defective with such thick skin layer. It is hypothesized

that the defects were caused by large particle agglomerates. The sheath dope preparation procedure must be optimized to improve particle dispersion for future efforts.

After coating the fiber surface with PDMS, O_2/N_2 selectivity slightly increased to 4.2 with O_2 permeance dropped by 20 %. In the meantime, C_3H_6 permeance was reduced by 40% with C_3H_6/C_3H_8 selectivity increased to 16.4, which was still lower than the expected value of 18.1. The PDMS/polyaramid-coating, however, enhanced C_3H_6/C_3H_8 selectivity dramatically to 27.5, which was ~50 % higher than the intrinsic value of the dense film. Similar to the case of mixed-matrix fiber with 17 wt% loading, the increase in selectivity should be partially attributed to sealing of skin defects and partially to the intrinsically higher selectivity of the polyaramid. In any case, when C_3H_6/C_3H_8 selectivities are compared between PDMS/polyaramid-coated neat 6FDA-DAM and mixed-matrix fibers with 17 wt% and 30 wt% loading, it can be found that C_3H_6/C_3H_8 selectivity increases nicely with increasing ZIF-8 loading. This was consistent with the trend observed for dense films, which is shown in Figure 7.12.

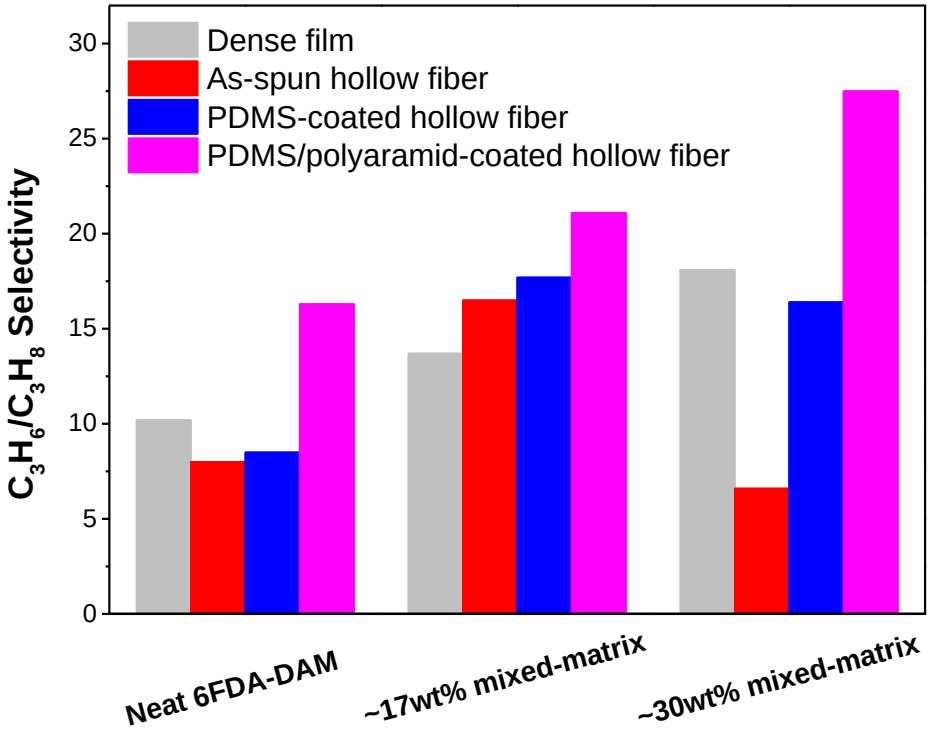

Figure 7.12: Comparison of C_3H_6/C_3H_8 selectivities of dense films, as-spun fibers, and coated fibers.

In chapter 6, transport properties of mixed-matrix dense films were compared with pure polymer's "permeability-selectivity" trade-off curve (Figure 6.4). Such comparison cannot be performed for hollow fiber membranes. Unlike permeability, permeance is not the material's intrinsic property and is dependent on membrane thickness for a given membrane material. Therefore, a trade-off curve between permeance and selectivity of neat polymeric fibers does not make any sense unless the fiber skin layer thickness is the same, which is neither realistic nor necessary to practice.

7.6 Dual-layer ZIF-8 (40 wt%)/6FDA-DAM Hollow Fiber Membrane

7.6.1 Hollow Fiber Spinning

With attractive C_3H_6/C_3H_8 selectivity seen for 30 wt% mixed-matrix hollow fiber, efforts were further made to spin ZIF-8 (40 wt%)/6FDA-DAM mixed-matrix hollow fibers. The spinning still employed 46 nm ZIF-8 as the dispersed molecular sieve and was still realized on the dual-layer hollow fiber platform with 6FDA-DAM as the core layer polymer. Such high particle loading was expected to be very challenging for hollow fiber membranes. Actually, such high particle loading has been scarcely reported for mixed-matrix dense film membranes.

Based on that of 30 wt% mixed-matrix fiber, the sheath dope composition of 40 wt% was developed with a few adjustments (Table 7.10). To accommodate the increased particle loading, polymer concentration was reduced by 2 wt% to 18 wt%. Ethanol concentration was decreased to 1 % due to significantly increased ZIF-8 concentration (12 wt%). A wide range of spinning parameters was tried (Table 7.11). The temperature of quench batch was as low as 8 ^{o}C.

Table 7.10: Dope compositions for ZIF-8 (40 wt%)/6FDA-DAM mixed-matrix hollow fiber spinning.

Component	Concentration (wt%)	
	Sheath dope	Core dope
6FDA-DAM	18	20.5
NMP	46	48
THF	23	10
Ethanol	1	15
$LiNO_3$	N/A	6.5
ZIF-8	12	N/A

Table 7.11: Spinning parameters for ZIF-8 (40 wt%)/6FDA-DAM mixed-matrix hollow fiber spinning.

Spinning parameter	Value
Sheath dope flow rate (cc/hr)	15-30
Core dope flow rate (cc/hr)	150
Bore fluid flow rate (cc/hr)	55
Quench bath temperature (^oC)	8-25
Spinneret temperature (^oC)	60
Air gap height (cm)	1-30
Take-up rate (m/min)	5-10

7.6.2 Hollow Fiber Characterizations

Again, SEM images (Figure 7.13) showed perfect inter-layer adhesion. By using a well-aligned spinneret, the fiber showed uniform wall thickness and good concentricity.

The “nodules” became even more densely packed on the skin surface of 40 wt% mixed-matrix fiber due to its higher loading. Excellent consistency was again obtained by elemental analysis between experimental and theoretical Zn weight concentrations (Figure 7.14).

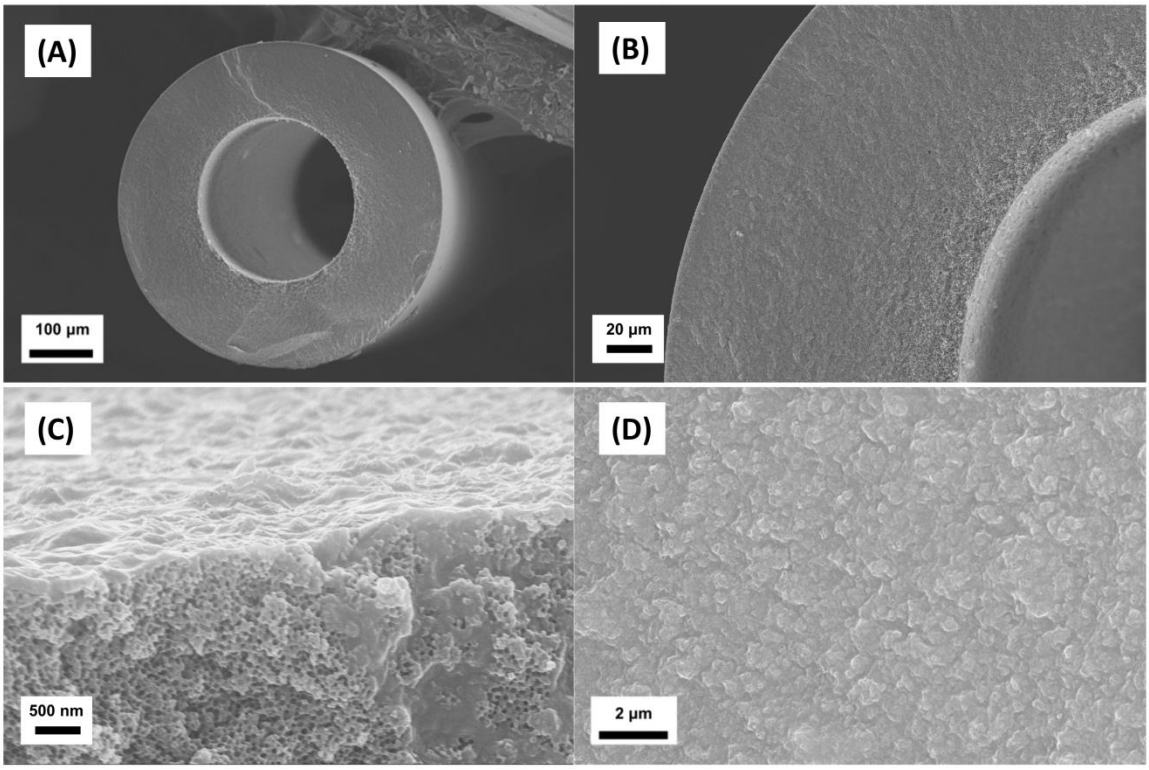

Figure 7.13: SEM images of dual-layer ZIF-8 (40 wt%)/6FDA-DAM mixed-matrix hollow fiber membranes. (A) fiber overview (B) fiber substrate (C) fiber skin layer side view (D) fiber skin layer top view.

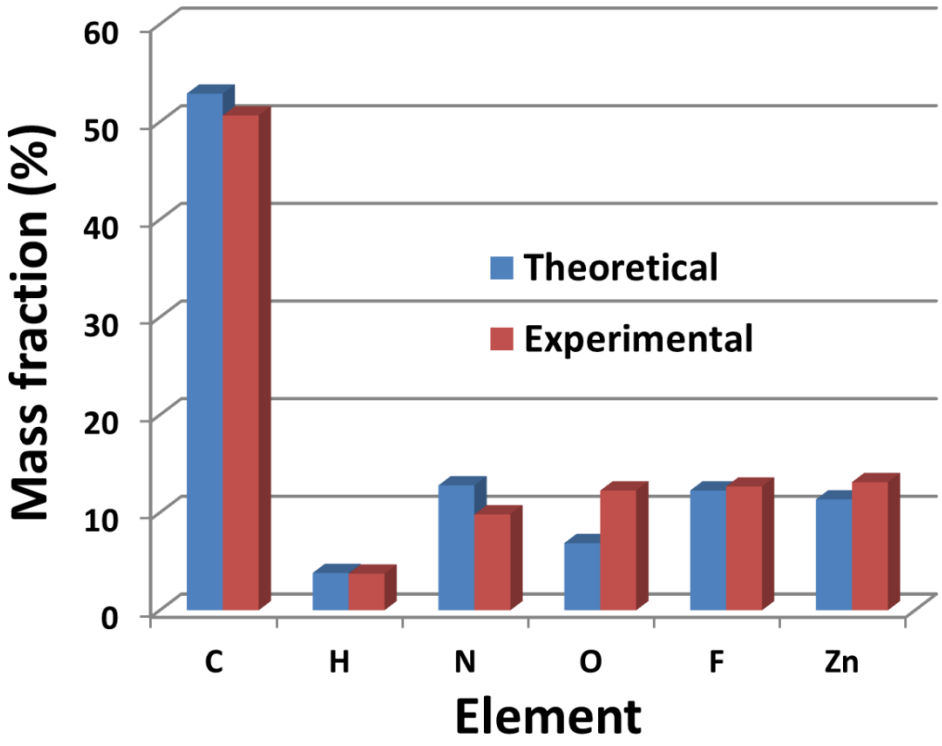

Figure 7.14: Elemental analysis results of ZIF-8 (40 wt%)/6FDA-DAM mixed-matrix hollow fibers (sheath layer only).

7.6.3 Evaluation of Separation Performance

Selected states were tested for O_2/N_2 and C_3H_6/C_3H_8 permeation. All the tested as-spun fibers were seriously defective showing Knudsen selectivity. After coating the fiber surface with PDMS and polyaramid, O_2/N_2 selectivity increased to ~2 while C_3H_6/C_3H_8 selectivity almost stay unchanged. It is hypothesized that some of the fiber skin defects grew so large that polyaramid chains were not able to locally extend the entire over-sized defects and slow down the unselective Knudsen diffusion. Optimizing polycondensation reaction conditions may increase the polyaramid molecular weight and its capability to seal larger defects, but will possibly end up with bringing significant

mass transfer resistance to gas permeation and accordingly, unattractive membrane permeance.

The results were a bit surprising, since a wide range of spinning parameters were tried and some of them were manipulated to intentionally form a thicker skin. It was possible that 18 wt% polymer in the spinning dope was not high enough to suppress formation of skin defects under such high loading of particles, regardless of spinning parameters. A higher polymer concentration in the spinning dope may improve the skin integrity, but will inevitably increase particle concentration in the spinning dope and make the dope more viscous and more difficult to process. Increasing the concentration of THF and temperature of the spinneret may also aid skin formation and improve fiber selectivity. In any case, extending to 40 wt% ZIF-8 loading requires more optimization, and is beyond the scope of this study.

7.7 Summary and Conclusions

Analysis suggests that it is intrinsically challenging to form hollow fiber membranes having desirable selectivity for hydrocarbon mixtures. In addition, it was found that polymer molecular weight was a very important factor determining properties of hollow fiber membranes. To spin high-quality hollow fiber membranes with minimized skin defects, higher polymer concentration in the spinning dope is required when lower molecular weight polymer is used. Moreover, plotting ternary phase

diagrams with water as the non-solvent showed that water was overly strong as a non-fsolvent and should be avoided for spinning dope preparation.

This chapter attempted to address the challenges associated with developing scalable mixed-matrix membranes described in Chapter 2, by exploring several aspects that have not been touched by previous researchers. A systematic empirical approach was developed to formulate spinning dope for ZIF-8/6FDA-DAM mixed-matrix hollow fiber membranes. Permeation results of mixed-matrix hollow fiber membranes showed that this approach worked quite well. For the first time, mixed-matrix hollow fiber membranes were spun with nano-sized particles showing attractive selectivity without any defect-sealing post-treatment. Additionally, by successfully achieving 70% enhancement in C_3H_6/C_3H_8 selectivity with high-loading (30 wt%) ZIF-8/6FDA-DAM mixed-matrix hollow fiber membranes, this research proves that mixed-matrix membrane is indeed a practical approach for advanced hydrocarbon separations. It should be noted, though, that membrane permeance was compromised with selectivity enhancements, and substantial optimization is required in the future to obtain simultaneous high permeance and high selectivity. While this should be achievable, it represents a major additional step beyond the scope of the current work.

7.8 References

[1] S. B. Carruthers, PhD Dissertation, The University of Texas at Austin, 2001.

[2] O. M. Ekiner, R. A. Hayes and P. Manos, Reactive Post Treatment for Gas Separation Membrane. US Patent 5091216, 1992.

[3] J. M. S. Henis and M. K. Tripodi, "Composite hollow fiber membranes for gas separation: the resistance model approach" *Journal of Membrane Science* **1981**, *8*, 233-246.

[4] J. M. S. Henis and M. K. Tripodi, Multicomponent Membranes for Gas Separations. US Patent 4230463, 1980.

[5] T. C. Merkel, V. I. Bondar, K. Nagai, B. D. Freeman and I. Pinnau, "Gas sorption, diffusion, and permeation in poly(dimethylsiloxane)" *J. Polym. Sci. Pt. B-Polym. Phys.* **2000**, *38*, 415-434.

[6] K. Tanaka, A. Taguchi, J. Hao, H. Kita and K. Okamoto, "Permeation and separation properties of polyimide membranes to olefins and paraffins" *Journal of Membrane Science* **1996**, *121*, 197-207.

[7] O. Esekhile, PhD Dissertation, Georgia Institute of Technology, 2011.

[8] J. Liu, PhD Dissertation, Georgia Institute of Technology, 2010.

[9] L. Xu, PhD Dissertation, Georgia Institute of Technology, 2012.

[10] D. T. Clausi, PhD Dissertation, The University of Texas at Austin, 1998.

[11] S. Husain, PhD Dissertation, Georgia Institute of Technology, 2006.

[12] Y. Dai, J. R. Johnson, O. Karvan, D. S. Sholl and W. J. Koros, "Ultem®/ZIF-8 mixed matrix hollow fiber membranes for CO2/N2 separations" *J. Membr. Sci.* **2012**, *401–402*, 76-82.

[13] O. M. Ekiner and S. S. Kulkarni, Process for Making Hollow Fiber Mixed Matrix Membranes. US Patent 6663805, 2003.

[14] S. Husain and W. J. Koros, "Mixed matrix hollow fiber membranes made with modified HSSZ-13 zeolite in polyetherimide polymer matrix for gas separation" *Journal of Membrane Science* **2007**, *288*, 195-207.

[15] L. Liu, E. S. Sanders, J. R. Johnson, O. Karvan, S. Kulkarni, D. J. Hasse and W. J. Koros, "Influence of membrane skin morphology on CO2/N2 separation at sub-ambient temperatures" *Journal of Membrane Science* **2013**, *446*, 433-439.

CHAPTER 8

CONCLUSIONS AND FUTURE DIRECTIONS

8.1 Summary and Conclusions

8.1.1 Dissertation Overview

Mixed-matrix membranes have received continuous attention from both academia and industry in the past years; however, like several other advanced membranes described in Chapter 1, they have yet to be proven to be practical for large-scale gas separations due to several challenges that need to be worked out. The largest challenge had been the polymer-zeolite adhesion problem. Instead of attempting to address polymer-zeolite adhesion, this research successfully overcomes this challenge by using ZIFs that are intrinsically compatible with polymers.

The overarching goal of this research was to provide a framework for development of scalable ZIF-based mixed-matrix membrane that is able to deliver attractive transport properties for advanced gas separations. Efforts were made not only to study membrane materials' fundamental transport properties, but also to overcome those challenges associated with translating the attractive properties into workable membrane geometry. While the membrane materials selected in this research were tailored for C_3H_6/C_3H_8 separation, this framework can be extended to design and develop ZIF-based mixed-matrix membranes for separation of other gas mixtures. The objectives described in Chapter 1 are summarized and progress toward these goals is reviewed.

8.1.2 Objective 1

The first objective was to select membrane materials (ZIF and polymer) based on a fundamental understanding of adsorption and diffusion in the ZIF.

The ability to manipulate ZIF-8 crystal size enabled convenient and reliable adsorption measurements of a wide range of permanent gases and condensable hydrocarbons. Adsorption kinetics demonstrated that ZIF-8 was highly kinetically selective for C_3 and C_4 hydrocarbons with olefin/paraffin kinetic selectivity above 100 and hydrocarbon isomer kinetic selectivity on the order of 10^4-10^6. Complemented by equilibrium sorption data, a C_3H_6 permeability of 390 Barrer and C_3H_6/C_3H_8 selectivity of 130 were estimated for pure ZIF-8 material. The Maxwell model was further employed to estimate transport properties of hypothetical mixed-matrix materials. Based on calculation results, 6FDA-DAM was selected from a portfolio of high performance polyimides as the continuous polymer matrix to form mixed-matrix membranes with ZIF-8.

8.1.3 Objective 2

The second objective was to develop ZIF-based mixed-matrix dense film membranes with enhanced separation performance.

Chapter 6 used membrane materials selected in Chapter 5 to form ZIF-8/6FDA-DAM mixed-matrix dense film membranes with particle loadings at 16.4 wt%, 28.7 wt%, and 48 wt%. The largest technical challenge of mixed-matrix membrane was successfully

overcome by achieving adequate adhesion at the ZIF-polymer interface, presumably due to ZIF-8's intrinsic compatibility with polymers. Significant enhancements in C_3H_6/C_3H_8 selectivity and C_3H_6 permeability were simultaneously achieved under both single-gas and mixed-gas feeds, with increasing ZIF-8 loading. At 48 wt% ZIF-8 loading, the mixed-matrix dense film showed C_3H_6 permeability of 56.2 Barrer and C_3H_6/C_3H_8 ideal selectivity of 31.0, which were 258 % and 150 % higher than the neat polymer matrix, respectively. Additionally, experimental permeabilities of mixed-matrix dense films were in good agreement with the values predicted by the Maxwell model. ZIF-8's interesting and unexpected molecular sieving properties were discovered after analyzing diffusivity data obtained from adsorption measurements and mixed-matrix dense film permeation. From Helium (2.6 Å) to iso-C_4H_{10} (5.0 Å), the corrected diffusivity drops fourteen orders of magnitude. The results further suggest that the framework of ZIF-8 is flexible, and the effective aperture size of ZIF-8 for molecular sieving is in the range of 4.0-4.2 Å, which is significantly larger than the XRD-derived value (3.4 Å).

8.1.4 Objective 3

The third objective was to extend the enhanced separation performance realized in mixed-matrix dense film membranes into industrially desirable hollow fiber geometry.

Chapter 7 attempted to address the challenges associated with developing scalable mixed-matrix membranes, by spinning high-loading ZIF-8/6FDA-DAM mixed-matrix hollow fiber membranes with nano-sized ZIF-8 particles. A systematic empirical approach was developed to formulate spinning dopes of mixed-matrix hollow fiber

membranes. The mixed-matrix fibers showed enhanced C_3H_6/C_3H_8 selectivity with increasing ZIF-8 loading up to 30 wt%, which was consistent with dense film results discussed in Chapter 6. More specifically, at lower particle loading (17 wt%), enhanced C_3H_6/C_3H_8 selectivity and attractive C_3H_6 permeance were achievable without any defect-sealing post-treatment. At higher loading (30 wt%), C_3H_6/C_3H_8 selectivity of mixed-matrix hollow fiber membranes was further enhanced, however, with compromised C_3H_6 permeance due to additional mass transfer resistance brought by the applied PDMS/polyaramid coating layer. While substantial optimization is required in the future to improve membrane permeance, as a proof-of-concept study, this research successfully proves that mixed-matrix membrane is indeed a practical approach for advanced hydrocarbon separations.

8.2 Future Directions

8.2.1 Tailoring Molecular Sieving Properties of ZIFs

The ZIF-8/6FDA-DAM mixed-matrix membranes studied in this research showed comparable C_3H_6/C_3H_8 selectivity with CMS membranes [1] only at high particle loadings. However, as suggested by Chapter 7, preparation of high-quality mixed-matrix membranes becomes increasingly challenging as the particle loading rises. An alternative to avoid the problems associated with high-loading mixed-matrix membranes is to develop ZIFs and polymers having more superior separation performance. It is expected that with such materials, similar selectivity can be achieved under lower particle loading.

Figure 8.1 shows C_3H_6/C_3H_8 separation performance of mixed-matrix materials prepared with 6FDA-DAM and a hypothetical molecular sieve "ZIF-YY" with tailored transport properties. It was assumed that ZIF-YY was more selective and less permeable than ZIF-8, with C_3H_6 permeability of 130 Barrer and C_3H_6/C_3H_8 selectivity of 390. C_3H_6 and C_3H_8 permeabilities of hypothetical mixed-matrix materials were calculated by the Maxwell model. While 60 vol.% particle loading was needed for ZIF-8/6FDA-DAM mixed-matrix materials to show a C_3H_6/C_3H_8 selectivity of ~30, the same selectivity could be realized with the ZIF-YY/6FDA-DAM system under much lower particle loading (30 vol.%). It should be noted that membrane permeability was compromised due to the less permeable sieve. Practically this may not be a problem. This is because particle agglomerations are usually easier to be suppressed at lower particle loadings, and as a result minimization of fiber skin layer thickness would be less difficult to achieve equally high or even higher membrane permeance.

ZIFs are a relatively new class of microporous solids and the community has just recently realized their potential as kinetically selective adsorbent and membrane materials. Many opportunities exist to tailor ZIF's flexibility, aperture size and diffusion properties based on their diversified structure and a wide selection of building units. Such fundamental research is beyond the scope of conventional chemical engineering and possibly requires close collaboration with inorganic chemists and material scientists. Several pioneering studies [2-4] have been reported attempting to control the ZIF's structures and transport properties via approaches such as mixed-linker synthesis and post-synthetic linker exchange.

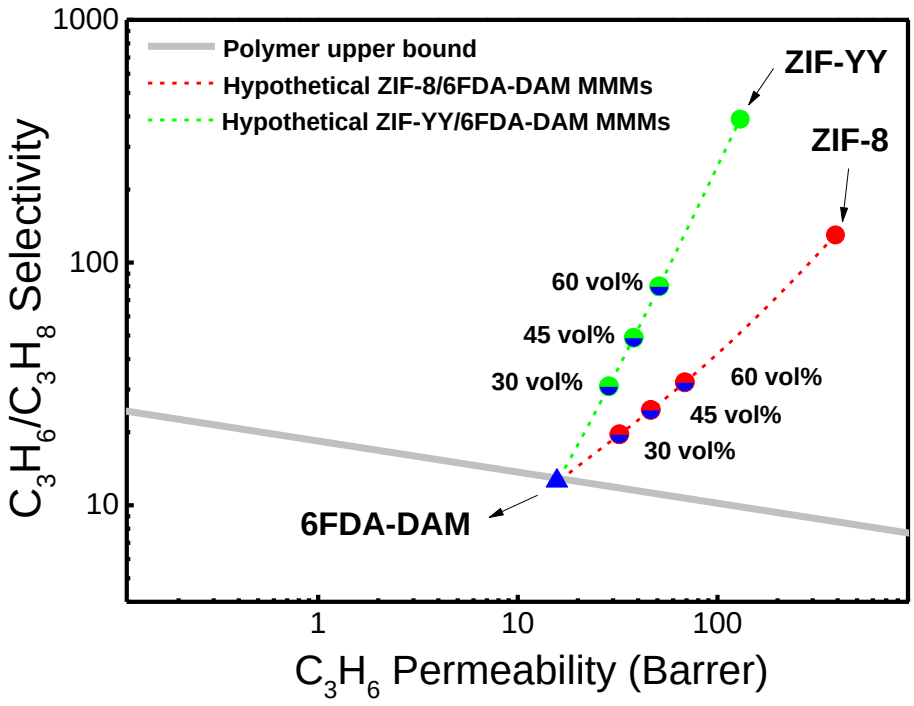

Figure 8.1: Comparison of mixed-matrix membranes fabricated with ZIF-8 and a hypothetical molecular sieve, ZIF-YY.

8.2.2 Exploring More Opportunities for ZIF-Based Membranes and Sorbents

If a generalized approach can be developed to tailor the aperture size and diffusion properties of ZIFs, the material's applicability may not be limited to C_3H_6/C_3H_8 separation. The current work showed that ZIF-8's effective aperture size for molecular sieving was in the range of 4.0-4.2 Å, and was not particularly selective for smaller penetrants. If the ZIF's effective aperture size can be tuned to be slightly smaller, it may become kinetically selective for separation of permanent gases such as CO_2/CH_4 and CO_2/N_2. Indeed, ZIF-7 with larger-sized imidazolate linker (benzimidazole) and therefore

possibly smaller aperture size has already been shown to be able to achieve attractive mixed-matrix membrane CO_2/N_2 selectivity [5].

Chapter 6 mainly investigated C_3H_6/C_3H_8 permeation of ZIF-8-based membranes. As indicated by the kinetic sorption study in Chapter 5, ZIF-8 may be potentially attractive for separation of C_4 hydrocarbon mixtures, such as iso-C_4H_8/iso-C_4H_{10}, 1-C_4H_8/iso-C_4H_8, and n-C_4H_{10}/iso-C_4H_{10}. However, diffusion of these C_4 hydrocarbons in ZIF-8 is quite slow and may not be sufficiently attractive for practical purposes. Enlarging the aperture by substituting 2-methylimidazole with a smaller-sized linker may improve the diffusivity, however, possibly with some compromise in kinetic selectivities.

Separation of C_4 hydrocarbons represents a group of separations with great economic interests. Iso-butane and butadiene are respectively key components for production of premium gasoline blending stock [6] and synthetic rubbers [7]. Figure 8.2 shows how ZIF-8-based membranes can be used to retrofit separation of butane isomer and separation of butadiene from crude C_4s. While sorption kinetics of butadiene was not studied in the current work, it is expected that an attractive kinetic selectivity can be achieved for butadiene over other C_4 components. Van der Waals diameter of the butadiene molecule (~4.3 Å) is smaller than all other C_4 hydrocarbons and the molecule is perfectly planar because of two C=C double bonds.

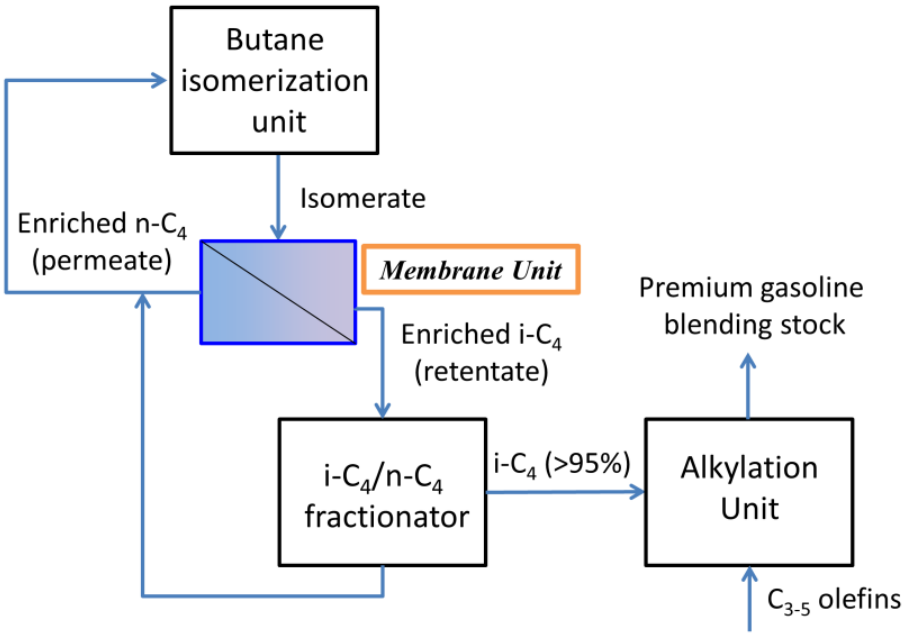

(A) n-C_4H_{10}/iso-C_4H_{10} separation

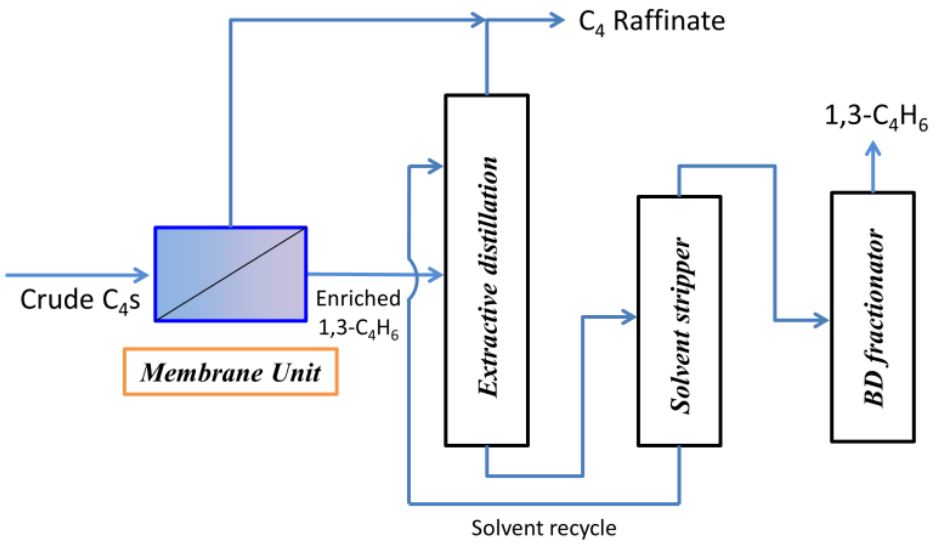

(B) Separation of 1,3-C_4H_6/C_4s

Figure 8.2: Schematic illustrations of distillation-membrane hybrid separation systems for (A) n-C_4H_{10}/iso-C_4H_{10} separation [6] and (B) enrichment of 1,3-C_4H_6 from other C_4 components [7].

Separation of C_4 hydrocarbon mixtures with polymer-based membranes, however, is expected to be more challenging than the C_3H_6/C_3H_8 case. Due to their bulkier sizes, diffusion of C_4 hydrocarbons in rigid glassy polymers is usually slow even at elevated temperatures [6, 8]. Additionally, because of the reasons discussed in section 7.2, fabrication of high-quality hollow fiber membranes with sufficiently low defect density and desirable C_4 hydrocarbon selectivity is intrinsically difficult.

8.2.3 Mixed-Matrix Membranes Based on Plasticization-Resistant Polymers

In this research, membrane permeation measurements were done at relatively mild conditions (under 35 ^{o}C with upstream pressure up to 80 psia). However, the actual conditions under which the membrane will be used in olefin plants may be much more aggressive. The conditions (400 psia and 90 ^{o}C) that Air Liquide chose [9] to test their P84-based hollow fibers may not be universal for every olefin plant, but represent a good example of the typical conditions that the membrane will be subject to. Under such high feed activity, plasticization of the polymer matrix may be a potential problem for mixed-matrix membranes.

For a proof-of-concept study, the plasticization suppression capability of the polymer matrix was not considered for material selection. As shown in Figure 6.6, 6FDA-DAM-based membranes are not expected to display stabilized selectivity at aggressive C_3 pressures. As a result, polymers with adequate plasticization resistance need to be used for the membrane to show stabilized selectivity under realistic operating conditions. The family of crosslink-able polyimides [10-12] that have been developed in

the Koros group may be a good option. Moreover, thermally-rearranged polymers [13] that have demonstrated both attractive separation performance and good plasticization resistance may be potentially used for development of plasticization resistant mixed-matrix membranes.

8.2.4 Optimization of Spinning Mixed-Matrix Hollow Fiber Membranes

Based on the successful proof-of-concept study in Chapter 7, further enhancements in hollow fiber separation performance may be achievable via optimization of hollow fiber spinning. Additionally, while the PDMS/polyaramid coating effectively sealed fiber defects, they apparently brought overly large mass transfer resistance. Optimization of coating conditions such as monomer concentration and reaction time may reduce the coating layer thickness and therefore improve fiber permeance.

In Chapter 7, dual-layer mixed-matrix hollow fibers were spun by using 6FDA-DAM as fiber core layer polymer. If an inexpensive polymer can be used in the core spinning dope, materials cost of hollow fiber spinning is expected to reduce substantially.

While significant insights were gained in Chapter 7 with regard to formulation of spinning dopes for mixed-matrix hollow fibers, a fundamental knowledge at molecular scale is required on formation of mixed-matrix fiber skin layer under elongational forces. The impacts of nano-particles on spinodal decomposition and fiber skin densification, as well as possible shear stress-induced particle migration along radial direction of spinneret channel need to be studied. While these investigations are expected to be complicated,

they are undoubtedly crucial to understand how to control and balance microscopic and macroscopic properties of mixed-matrix hollow fiber membranes.

8.3 References

[1] L. Xu, PhD Dissertation, Georgia Institute of Technology, 2012.

[2] R. Banerjee, H. Furukawa, D. Britt, C. Knobler, M. O'Keeffe and O. M. Yaghi, "Control of Pore Size and Functionality in Isoreticular Zeolitic Imidazolate Frameworks and their Carbon Dioxide Selective Capture Properties" *J. Am. Chem. Soc.* **2009**, *131*, 3875-3877.

[3] X. Liu, Y. Li, Y. Ban, Y. Peng, H. Jin, H. Bux, L. Xu, J. Caro and W. Yang, "Improvement of hydrothermal stability of zeolitic imidazolate frameworks" *Chemical Communications* **2013**, *49*, 9140-9142.

[4] J. A. Thompson, C. R. Blad, N. A. Brunelli, M. E. Lydon, R. P. Lively, C. W. Jones and S. Nair, "Hybrid Zeolitic Imidazolate Frameworks: Controlling Framework Porosity and Functionality by Mixed-Linker Synthesis" *Chem. Mater.* **2012**, *24*, 1930-1936.

[5] T. Li, Y. Pan, K.-V. Peinemann and Z. Lai, "Carbon dioxide selective mixed matrix composite membrane containing ZIF-7 nano-fillers" *Journal of Membrane Science* **2013**, *425–426*, 235-242.

[6] O. Esekhile, PhD Dissertation, Georgia Institute of Technology, 2011.

[7] *Butadiene Stewardship Guidance Manual*; American Chemistry Council: 2002

[8] J. Liu, PhD Dissertation, Georgia Institute of Technology, 2010.

[9] I. C. Roman, J. W. Simmons and O. M. Ekiner, Method of Separating Olefins from Mixtures with Paraffins. US Patent 7399897 B2, 2008.

[10] C.-C. Chen, W. Qiu, S. J. Miller and W. J. Koros, "Plasticization-resistant hollow fiber membranes for CO2/CH4 separation based on a thermally crosslinkable polyimide" *Journal of Membrane Science* **2011**, *382*, 212-221.

[11] A. M. Kratochvil and W. J. Koros, "Decarboxylation-Induced Cross-Linking of a Polyimide for Enhanced CO2 Plasticization Resistance" *Macromolecules* **2008**, *41*, 7920-7927.

[12] W. Qiu, C.-C. Chen, L. Xu, L. Cui, D. R. Paul and W. J. Koros, "Sub-Tg Cross-Linking of a Polyimide Membrane for Enhanced CO2 Plasticization Resistance for Natural Gas Separation" *Macromolecules* **2011**, *44*, 6046-6056.

[13] D. F. Sanders, Z. P. Smith, C. P. Ribeiro Jr, R. Guo, J. E. McGrath, D. R. Paul and B. D. Freeman, "Gas permeability, diffusivity, and free volume of thermally rearranged polymers based on 3,3′-dihydroxy-4,4′-diamino-biphenyl (HAB) and 2,2′-bis-(3,4-dicarboxyphenyl) hexafluoropropane dianhydride (6FDA)" *Journal of Membrane Science* **2012**, *409–410*, 232-241.

APPENDIX A

Compressibility Factor Equations

A.1 Compressibility Factor Equations

Compressibility factors (z) of Helium at T=35 ^{o}C were calculated by extrapolating the data at cryogenic temperatures [1]. Compressibility factor equations of other studied gases at T=35 ^{o}C were calculated using the Peng-Robinson Equation of State and the NIST-SUPERTRAPP program. Pressure (P) was given in the unit of pisa.

1. **He**

$$z = 3.162\times10^{-5}\times P + 1$$

2. **H_2**

$$z = 4.370\times10^{-13}\times P^3 - 4.659\times10^{-9}\times P^2 + 6.705\times10^{-5}\times P + 1$$

3. **O_2**

$$z = 2.686\times10^{-13}\times P^3 + 1.168\times10^{-8}\times P^2 - 5.521\times10^{-5}\times P + 1$$

4. **N_2**

$$z = -9.567\times10^{-13}\times P^3 + 1.546\times10^{-8}\times P^2 - 2.431\times10^{-5}\times P + 1$$

5. **CO_2**

$$z = -1.452\times10^{-10}\times P^3 + 4.904\times10^{-8}\times P^2 - 3.607\times10^{-4}\times P + 1$$

6. CH_4

$$z = 4.762\times10^{-12}\times P^3 + 1.657\times10^{-8}\times P^2 - 1.372\times10^{-4}\times P + 1$$

7. C_2H_4

$$z = -4.922\times10^{-11}\times P^3 - 4.627\times10^{-8}\times P^2 - 4.059\times10^{-4}\times P + 1$$

8. C_2H_6

$$z = -8.357\times10^{-10}\times P^3 + 3.573\times10^{-7}\times P^2 - 5.933\times10^{-4}\times P + 1$$

9. C_3H_6

$$z = -3.107\times10^{-9}\times P^3 - 3.032\times10^{-7}\times P^2 - 8.861\times10^{-4}\times P + 1$$

10. C_3H_8

$$z = -4.130\times10^{-9}\times P^3 - 4.958\times10^{-7}\times P^2 - 9.933\times10^{-4}\times P + 1$$

11. 1-C_4H_8

$$z = -1.010\times10^{-8}\times P^3 - 2.295\times10^{-6}\times P^2 - 1.552\times10^{-3}\times P + 1$$

12. n-C_4H_{10}

$$z = -2.430\times10^{-8}\times P^3 - 3.439\times10^{-6}\times P^2 - 1.927\times10^{-3}\times P + 1$$

13. iso-C_4H_8

$$z = -9.234\times10^{-9}\times P^3 - 2.295\times10^{-6}\times P^2 - 1.542\times10^{-3}\times P + 1$$

14. iso-C_4H_{10}

$$z = -6.720\times10^{-9}\times P^3 - 2.670\times10^{-6}\times P^2 - 1.580\times10^{-3}\times P + 1$$

A.2 Reference

[1] J. E. Jensen, W. A. Tuttle, R. B. Stewart, H. Brechna and A. G. Prodell *Selected Cryogenic Data Notebook*; Brookhaven National Laboratory: 1980

APPENDIX B

Determination of ZIF-8 Loadings in Mixed-Matrix Dense Film Membranes

In order to estimate gas permeability in ZIF-8 using the Maxwell Model, accurate ZIF-8 loading estimates of the mixed-matrix membranes are needed. As shown in Figure 3.1, the as-received BASF ZIF-8 sample consisted of large amount of particle agglomerates. During preparation of mixed-matrix dense films, part of these agglomerates cannot be broken by sonication and they settled in the bottom of vial B (see section 3.3.1). These agglomerates were not transferred to vial A. Accordingly, it was difficult to unambiguously determine ZIF-8 loadings in the mixed-matrix dense films simply based on the mass of dried sieve and dried polymer added to vial B and A.

TGA was used to reliably estimate ZIF-8 loadings in ZIF-8/6FDA-DAM mixed-matrix dense films described in Chapter 6. A small sample of film was first heated at 200 ^{o}C in air for 5 hours to remove most condensable components in the sample. Afterwards, the temperature was increased to 800 ^{o}C in an air atmosphere with a constant heating rate of 10 ^{o}C/min to decompose 6FDA-DAM and ZIF-8, as well as to oxidize all the elements. EDX analysis (Figure B.1) of the final residues showed that zinc and oxygen, with a molar ratio very close to unity, were the only residual elements, indicating that zinc oxide was the only solid oxide in the final residues. The mass percentage of ZIF-8 in the mixed matrix membrane can be back-calculated using the mass of zinc oxide left after

the burn off. TGA curves of the BASF ZIF-8 sample and mixed-matrix dense films are shown in Figure B.2.

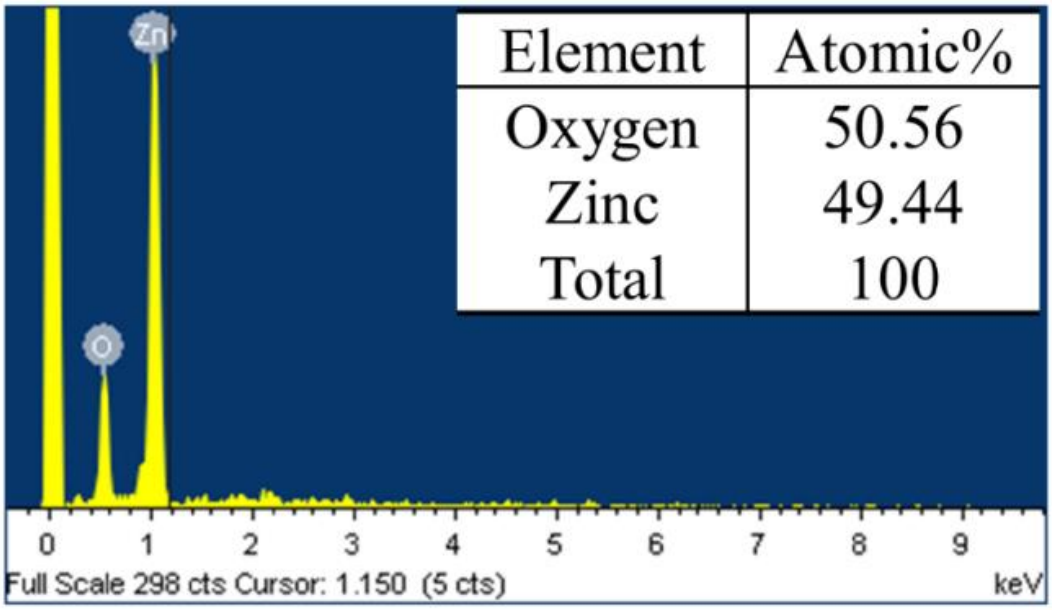

Figure B.1: EDX analysis results of TGA residues of mixed-matrix dense films.

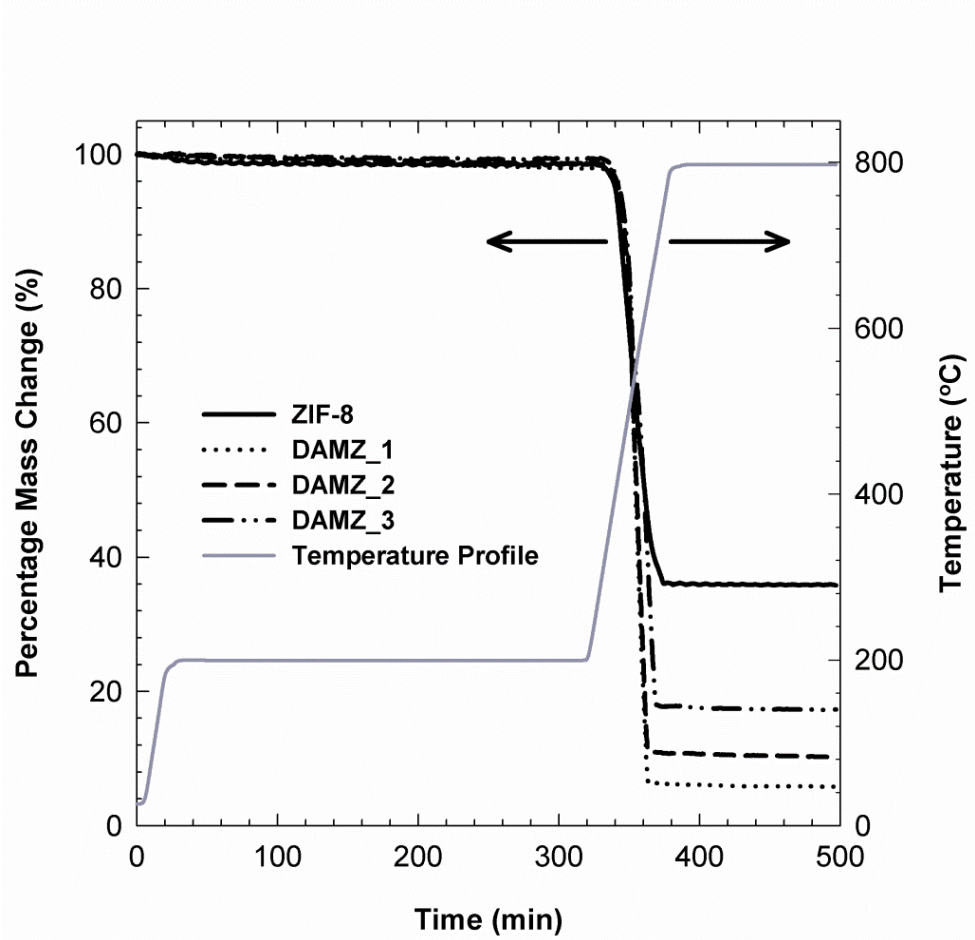

Figure B.2: TGA curves of BASF ZIF-8 and ZIF-8/6FDA-DAM mixed-matrix dense films in an air atmosphere.

The TGA-determined zinc mass percentages and calculated ZIF-8 loadings for each mixed-matrix dense film are shown in Table B.1. The zinc mass percentage of pure ZIF-8 determined by TGA (29.2 %) was close to the theoretical mass percentage calculated by molecular mass (28.5 %). For mixed-matrix dense film samples, higher mass percentage of zinc in the final residues indicates higher ZIF-8 loadings in the membrane. ZIF-8 wt% loadings estimated simply based on the mass of added sieve and polymer are shown in Table B.1 for reference. It is clear that the simple mass ratio approach overestimated ZIF-8 loadings. For example, the TGA-determined ZIF-8 wt%

loading of DAMZ_3 was 48.0 wt%, while the number estimated by the mass ratio approach was 57.1 wt%.

Table B.1: Analysis results of TGA residues and calculated ZIF-8 loadings. The ZIF-8 wt% loadings estimated by mass ratio are shown for reference.

	ZIF-8 wt% loading (by TGA)			ZIF-8 wt% loading
	ZnO wt%	Zn wt%	ZIF-8 wt%	(by mass ratio)
ZIF-8	36.3	29.2	N/A	N/A
DAMZ_1	5.97	4.79	16.4	21.9
DAMZ_2	10.4	8.36	28.7	33.3
DAMZ_3	17.4	14.0	48.0	57.1

APPENDIX C

ZIF-8's Effective Aperture Size Based on the CPK Model

C.1 ZIF-8's Effective Aperture Size Based on the CPK Model

In Chapter 6, effective aperture size of ZIF-8 was determined to be in the range of 4.0-4.2 Å based on the sharply decreased diffusivity between C_3H_6 and C_3H_8 on the "corrected diffusivity-molecular size" plot. Apparently the effective aperture size is affected by the choice of molecular model used to estimate molecular sizes of C_3H_6 and C_3H_8.

The space-filling model, also known as the CPK model, is a type of three-dimensional molecular model where the atoms are represented by spheres whose radii are proportional to the radii of the atoms and whose center-to-center distances are proportional to the distances between the atomic nuclei. Estimated molecular diameters of C_2H_4, C_2H_6, C_3H_6, and C_3H_8 based on the CPK model [1] is listed in Table C.1.

Figure C.1 shows an alternative "corrected diffusivity-molecular size" plot with CPK model-estimated molecular size of C_2H_4, C_2H_6, C_3H_6, and C_3H_8. As suggested by Figure C.1, the effective aperture size of ZIF-8 based on the CPK model is in the range of 3.8-4.0 Å.

Table C.1: Estimated molecular diameters based on the CPK model.

	Molecular diameter (Å)
C_2H_4	3.75
C_2H_6	3.85
C_3H_6	3.82
C_3H_8	3.95

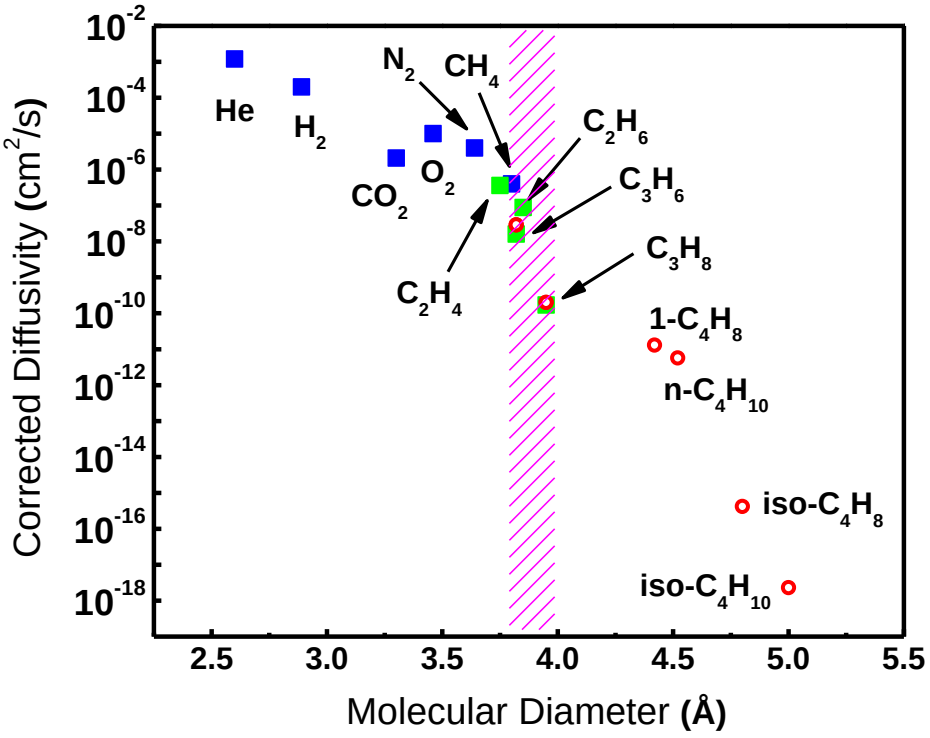

Figure C.1: Corrected diffusivities in ZIF-8 at 35 ^{o}C vs. molecular diameter of probe molecules. (Solid squares: diffusivities estimated from mixed-matrix membrane permeation. The green ones were based on the CPK model. Hollow red circles: diffusivities calculated from kinetic uptake rate measurements. Dashed magenta region: effective aperture size range of ZIF-8.)

C.2 References

[1] M. Rungta, PhD Dissertation, Georgia Institute of Technology, 2012.